Computer Techniques and Computational Methods in Biomechanics

BIOMECHANICAL SYSTEMS
TECHNIQUES AND APPLICATIONS
VOLUME I

EDITED BY
CORNELIUS LEONDES

CRC Press
Boca Raton London New York Washington, D.C.

Library of Congress Cataloging-in-Publication Data

Catalog record is available from the Library of Congress.

Direct all inquiries to CRC Press LLC, 2000 N.W. Corporate Blvd., Boca Raton, Florida 33431.

International Standard Book Number 0-8493-9046-X
Printed in the United States of America 1 2 3 4 5 6 7 8 9 0
Printed on acid-free paper

Preface

Because of rapid developments in computer technology and computational techniques, advances in a wide spectrum of technologies, and other advances coupled with cross-disciplinary pursuits between technology and its applications to human body processes, the field of biomechanics continues to evolve. Many areas of significant progress can be noted. These include dynamics of musculoskeletal systems, mechanics of hard and soft tissues, mechanics of bone remodeling, mechanics of implant-tissue interfaces, cardiovascular and respiratory biomechanics, mechanics of blood and air flow, flow-prosthesis interfaces, mechanics of impact, dynamics of man–machine interaction, and more.

Needless to say, the great breadth and significance of the field on the international scene require several volumes for an adequate treatment. This is the first of a set of four volumes and it treats the area of computer techniques and computational methods in biomechanics.

The four volumes constitute an integrated set that can nevertheless be utilized as individual volumes. The titles for each volume are

Computer Techniques and Computational Methods in Biomechanics
Cardiovascular Techniques
Musculoskeletal Models and Techniques
Biofluid Methods in Vascular and Pulmonary Systems

The contributions to this volume clearly reveal the effectiveness and significance of the techniques available and, with further development, the essential role that they will play in the future. I hope that students, research workers, practitioners, computer scientists, and others on the international scene will find this set of volumes to be a unique and significant reference source for years to come.

The Editor

Cornelius T. Leondes, B.S., M.S., Ph.D., Emeritus Professor, School of Engineering and Applied Science, University of California, Los Angeles has served as a member or consultant on numerous national technical and scientific advisory boards. Dr. Leondes served as a consultant for numerous Fortune 500 companies and international corporations. He has published over 200 technical journal articles and has edited and/or co-authored more than 120 books. Dr. Leondes is a Guggenheim Fellow, Fulbright Research Scholar, and IEEE Fellow as well as a recipient of the IEEE Baker Prize award and the Barry Carlton Award of the IEEE.

Contributors

G. Wayne Brodland
University of Waterloo
Waterloo, Ontario, Canada

Fred Chang
Rochester Hills, Michigan

David A. Clausi
University of Waterloo
Waterloo, Ontario, Canada

Vijay K. Goel
University of Iowa
Iowa City, Iowa

Tawfik B. Khalil
Wayne State University
Detroit, Michigan

Albert I. King
Wayne State University
Detroit, Michigan

M. Parnianpour
The Ohio State University
Columbus, Ohio

Frank A. Pintar
VA Medical Center
Milwaukee, Wisconisn

Jesse S. Ruan
Ford Motor Company
Dearborn, Michigan

Joseph M. Schimmels
Marquette University
Milwaukee, Wisconsin

A. Shirazi-Adl
Ecole Polytechnique
Montreal, Quebec, Canada

Yi Wan
Marquette University
Milwaukee, Wisconsin

Paul P.T. Yang
Southeast Permanente Medical Group
Jonesboro, Georgia

Wen-Jei Yang
The University of Michigan
Ann Arbor, Michigan

Narayan Yoganandan
Medical College of Wisconsin
Milwaukee, Wisconsin

Chun Zhou
Wayne State University
Detroit, Michigan

Contents

1

Finite Element Model Studies in Lumbar Spine Biomechanics

A. Shirazi-Adl
Ecole Polytechnique

M. Parnianpour
The Ohio State University

1.1 Background: Occupational Lower Back Disorders

As many as 85% of adults experience lower back pain that interferes with their work or recreational activity and up to 25% of the people between the ages of 30 to 50 years report low back symptoms when surveyed [1]. Of all lower back patients, 90% recover within six weeks irrespective of the type of treatment received [2]. The remaining 10% who continue to have problems after three months or longer account for 80% of disability costs [1]. Webster and Snook [3] estimated that lower back pain in 1989 incurred at least $11.4 billion in direct workers' compensation costs. Frymoyer and Cats-Baril [4] estimated that direct medical costs of back pain in the U.S. for 1990 exceeded $24 billion, and when indirect costs predominately associated with workers' compensation claims were added, the total cost was estimated to range from $50 billion to $100 billion. One U.S. workers' compensation insurance company incurred costs for lower back pain of about $1 billion per year, whereas the total cost for carpal tunnel syndrome in 1989 was $49 million [5]. Hence, it can be concluded that despite an increasing public attention to cumulative trauma disorders (CTDs) of the upper extremities, occupational low back disorders account for the most significant industrial musculoskeletal disorders (MSDs).

The prevention of low back pain is nearly impossible due to its prevalence. However, occupational safety and ergonomic principles correctly dictate that one should reduce the physical risk factors by worker selection, training, and administrative and engineering controls in order to diminish the risk of severe low back injuries due to overexertions or repetitive cumulative trauma disorder of the low back [6,7]. The fundamental inability to determine "How much of a risk factor is too much?" has been one

of the most critical hindrances toward developing an ergonomics guideline for safe and productive manual material-handling tasks.

Industrial low back disorder (LBD) is a complex multifactorial problem. A full understanding of it can only be gained by considering the personal and environmental risk factors which include both the biomechanical and psychosocial factors; the latter have been identified in the literature in the form of predictors or exacerbators of musculoskeletal disorders [8]. However, careful review [9] of this literature indicates that the results are inconclusive while the following factors are identified to be of significance: monotonous work, high perceived workload, time pressure, low control on the job, and lack of social support. As for the former factors, the results of epidemiological studies have associated six occupational factors with low back pain symptoms. These are (1) physically heavy work, (2) static work postures, (3) frequent bending and twisting, (4) lifting and sudden forceful incidents, (5) repetitive work, and (6) exposure to vibration [10]. In a large retrospective survey, lifting or bending episodes accounted for 33% of all work-related causes of back pain [11]. Troup et al. [12] have identified the combination of lifting with lateral bending or twisting as a frequent cause of back injury in the workplace.

Parnianpour et al. [13], in their study of the fatiguing dynamic movement of the trunk against a set resistance, were the first to report on the combined analysis of triaxial motor output and movement patterns. They showed that during fatiguing trunk flexion and extension, there were significant reductions in the velocity, range of motion, and total angular excursion in the intended (sagittal) plane of motion, and a significant increase in the range of motion and total angular excursion in the accessory (coronal and transverse) planes. The presence of more unintended motion in the accessory planes indicates a loss of coordination and more injury-prone loading conditions for the spine. Numerous studies have demonstrated that soft tissues subjected to repetitive loading show creep and stress relaxation behavior because of their viscoelastic properties [14]. Since the internal stability of the spine is maintained by its passive and active structures, there is an even greater need for muscular control in maintaining a given level of spinal stability after repetitive movements. Hence, the presence of repetitive dynamic trunk exertions increases the risk by adversely affecting the performance of the neuromusculoskeletal system (i.e., diminished control and coordination, reduction in magnitude and rate of tension generation in the muscles, and the reduction in the stiffness of spinal tissues).

Videman et al. [15], based on their prospective cohort study among 5649 nurses, strongly suggested that job-related factors rather than personal characteristics were the major predictors of back disorders among nurses. Bigos et al. [16], in the "Boeing" study, showed that manual handling tasks and falls were associated with 63% and 10% of low back compensation cases, respectively. Burdorf [17] reviewed 81 original papers concerning the LBD in occupational groups and concluded that very few studies provided quantitative measures of the exposures. Punnet et al. [18] showed increased odds ratios of low back disorders (determined from injury records and physical exams) for exposure to awkward postures of the trunk in an industrial setting. The tasks with severe trunk flexion greater than 10% of cycle time had an odds ratio (OR) of 8.9. Marras et al. [19] extended the analysis to include the dynamic components of the trunk motion. It was shown that the mean peak sagittal trunk velocity and acceleration were 49°/sec and 280°/sec^2, respectively, while the maximum peak in the database exceeded 200°/sec and 1300°/sec^2. Furthermore, asymmetric dynamic lifting tasks were found to be more the norm than the exception [20]. The identified risk factors were: lift rates, maximum moment, peak sagittal trunk flexion, and lateral and twisting velocities.

The inability of classical injury models or overexertion phenomena to describe the majority of industrial low back disorders has motivated epidemiologists and biomechanists to search for alternative paradigms. Hansson [21] proposed a biomechanical loading injury model to describe the possible mechanisms for the occurrence of low-back injuries which we have further modified (Fig. 1.1). Biomechanical loads leading to tissue damage can be from overloading (single application of load surpassing the tissue tolerance), repetitive submaximal loading, and prolonged static loading. Repetitive loading, even below the yield stress of the material, may impose microdamage to the structure, depending upon the magnitude, duration, and frequency of the loading. Due to stress relaxation, the resistance of the material will diminish in prolonged loading, and alternative load paths may predispose the spine to higher

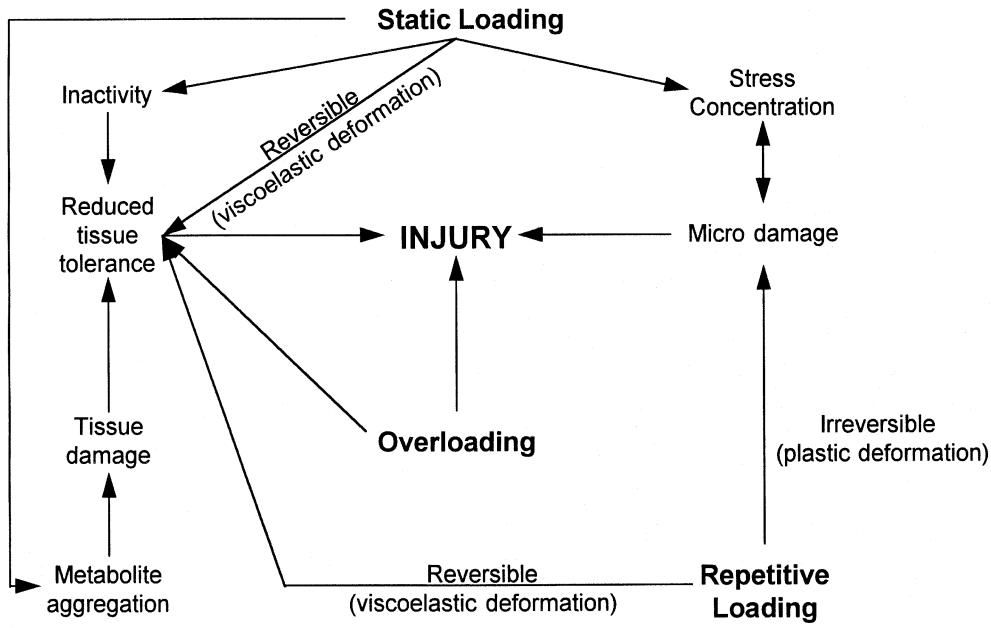

FIGURE 1.1 Possible injury mechanisms for different loadings of the human spine (modified from Hansson [21]).

risk of injury. Hence, the capacity of tolerating external loads could be affected by the time history of loads on the structure. The diminishing capacity of the spine to respond to external loads, due to stress relaxation and loss of stiffness after prolonged loading or cyclic submaximal loading (Fig. 1.1) can alter the loading path within the spine. This alteration of internal loading, in conjunction with diminishing control and coordination, may significantly increase the risk of injury to spine.

In the following sections, some essential features to be incorporated into realistic model studies of the lumbar spine are first discussed. Predicted results of our finite element model studies relating to some important aspects of lumbar spine biomechanics are introduced and discussed in subsequent sections. Finally, models of spinal loading along with our current and future directions in finite element model studies of lumbar spinal biomechanics are presented.

1.2 Finite Element Models of the Lumbar Spine

Computational methods of structural mechanics have long been successfully employed to predict the behavior of complex biological systems [22]. The continuous evolution and availability of affordable powerful computers, the presence of popular computational package programs treating various specific features present in musculoskeletal systems, and recent advances in image analysis and reconstruction have encouraged such applications. The technical difficulties, limitations, and cost involved in experimental *in vitro* and *in vivo* studies as well as ethical concerns have further inspired the use of computer model studies in various branches of orthopedic biomechanics. In view of the widespread presence of similar approaches in different areas of science and technology, the application of computational methods in biomechanics can only become more and more prevalent in future. Naturally, the future challenge is to apply these methods to those areas not yet considered and to further enhance previous models to better take into account the couplings and nonlinearities often present in physical phenomena.

It is imperative to recall that the accuracy of predictions in a model study directly depends on underlying assumptions made in the development of the model including input data and subsequent analysis and interpretation of results. Since it is impossible to develop and analyze a model without any assumption, the importance in knowing the extent of influence of such simplifications on results as well

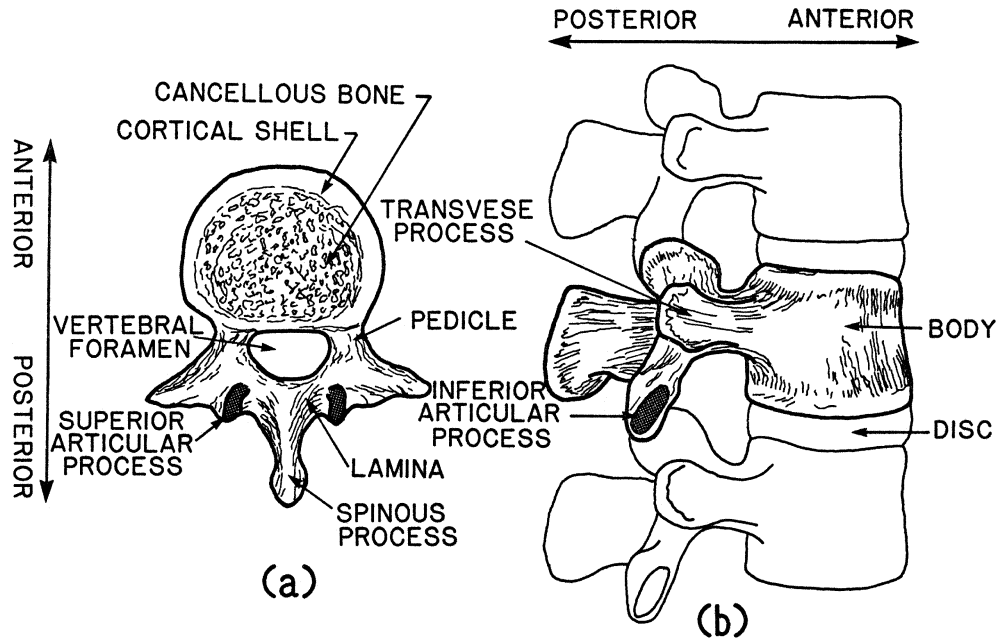

FIGURE 1.2 A typical schema of lumbar vertebrae: (a) a transverse cross-section through the anterior vertebral body; (b) lateral view of three vertebrae with the discs in between. The ligaments are not shown.

as the experience and common sense of the analyst should not be overlooked. Finally, validation of a model by comparison of its predictions with *in vitro* and *in vivo* results should be taken as seriously as the development of the model itself. Such comparisons should be used in fine-tuning a model that replicates the essential features of a biological system as close as possible rather than in validation of one that does not incorporate this essential condition. Experimental data are also required for the adequate development and implementation of constitutive equations as well as the identification of failure modes of biological tissues in order to enhance the accuracy and value of model predictions.

The human spine is a complex system that protects the delicate spinal cord while providing sufficient flexibility and stiffness to adequately perform various activities. With the support and control of muscles, the passive ligamentous column carries loads as low as those in upright standing postures and those under heavy lifting tasks. Due to the difficulty in analyzing the system as a whole, researchers often subdivide it into a number of regions and study them separately. Such attempts, in order to be successful, should realistically account for the boundary conditions between regions. Due to the absence of coupling between various regions, however, such isolated models cannot be expected to manifest all response characteristics present at the global system. In this chapter, finite element model studies of the lumbar functional units or motion segments (each functional unit consists of two adjacent vertebrae with connecting ligaments and intervertebral disc) and the entire ligamentous lumbosacral spine, L1-S1, consisting of five motion segments, are presented in order to study the biomechanics of the human spine.

Due to the three-dimensional irregular geometry, nonhomogeneous material arrangements, large complex loadings and movements, and nonlinear response including contact at facet joints, the finite element method of computational mechanics is the most suitable approach for the analysis of the lumbar spine (Figs. 1.2 and 1.3). Previous finite element models of the lumbar spine have studied the response of the disc-body-disc unit neglecting posterior elements [23-30], the entire motion segment with posterior elements [31-40], multimotion segments, or the whole ligamentous lumbosacral spine [41-49].

For the prediction of reliable results under a specific condition of loading or motion, the model should be realistic enough; that is, features of the structure that play important roles under that specific loading condition should accurately be accounted for in the model. Some of these characteristics are

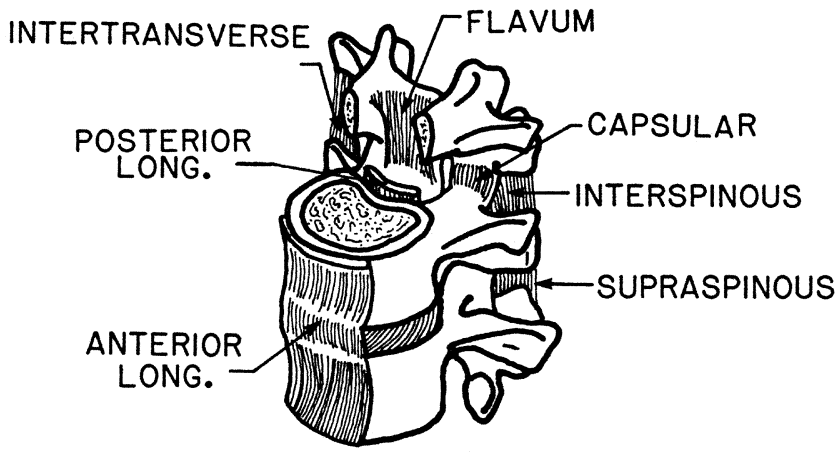

FIGURE 1.3 The ligaments of a lumbar motion segment attaching a vertebral body to the adjacent one.

1. The three-dimensional geometry of the structure including the lordosis, sagittal wedge shape of discs and irregular facet surfaces with their gap distances and likely asymmetry.
2. The nonhomogeneity of disc annulus material as a composite collection of an amorphous matrix (protoglycan and water) reinforced by collagenous fibers (radial variation of the collagen mechanical properties and volume fraction should also be considered).
3. The facet articulation as a large displacement contact problem in which two bodies with spatial articular surfaces could come into contact with each other, slide, and separate during the course of deformation.
4. The nonlinearities: the geometric one is essential due to the likelihood of instability and large displacements/strains even under moderate load levels; the material nonlinearities are essential, particularly for ligaments and disc tissues.
5. The time-dependent response essential when long-term creep or short-term effect of rate of loading are considered. The type of analysis as elastostatic, elastodynamic, viscoelastic, or poroelastic depends on the loading and structural characteristics and response duration sought.
6. The application of load or displacements with consideration of muscle exertions, gravity and external loads, and pelvic tilt.
7. The modification in the structure such as those expected in progressive failure or long-term remodeling studies.

For the study of the effect of annulus material modeling on predicted stresses in both elastic [29, 50] and poroelastic creep [51, 52] conditions, we have used a rather simplified linear axisymmetric model of the disc-body-disc unit. The annulus tissue, nevertheless, is nonhomogeneous as a composite of a matrix and fiber membranes, as shown in Figs. 1.4 and 1.5. Based on direct measurements of an L2-L3 lumbar motion segment, we have developed and extensively used a three-dimensional model of the joint incorporating posterior elements, facets, and ligaments (Fig. 1.6). This model has been employed in our nonlinear elastostatic studies [31-35, 53]; progressive failure studies [54], nonlinear poroelastic creep analyses [40], and nonlinear viscoelstic investigations [39].

More recently, with merging computer-assisted tomography and finite element modeling techniques, the mesh of an entire ligamentous lumbar spine, L1-S1, of a cadaver specimen has been developed [43]. The model has a lordosis angle of about 46° (the angle between the distal L1 end plate and proximal S1 end plate) and exhibits a maximum of about 2 mm lateral deviation along the height as well as facet asymmetries at different levels. The model includes 6 vertebrae, L1 to S1, 5 discs, 10 sets of superior-inferior articulating facet surfaces (2 at each segmental level), and a number of ligaments (supraspinous, interspinous, posterior/anterior longitudinal, flavum, transverse, capsular, iliolumbar, and fascia); see

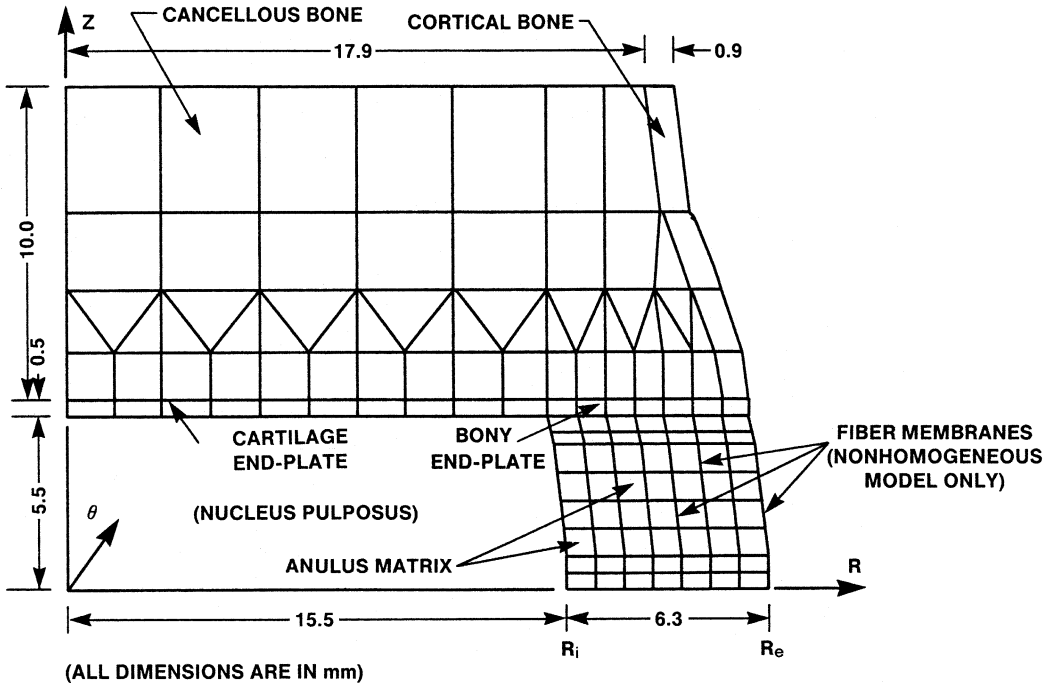

FIGURE 1.4 The finite element mesh of an axisymmetric model of the disc-body-disc unit with symmetry about the mid-disc plane. The disc annulus layers are simulated either as homogeneous orthotropic or nonhomogeneous composite. In both cases, there is a variation in material properties from the innermost layer to the outermost.

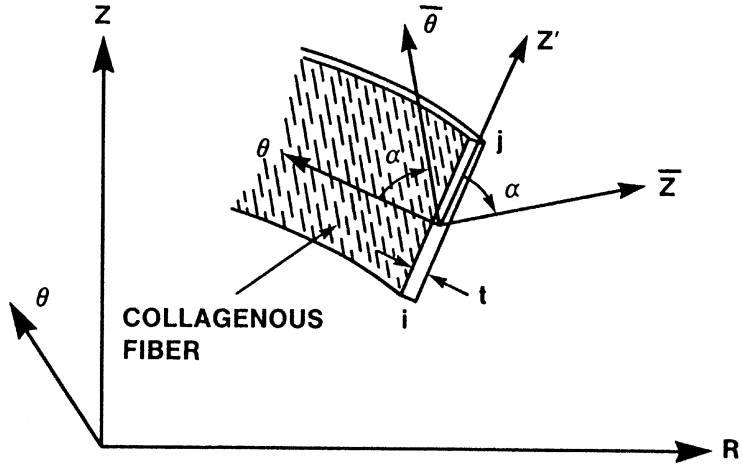

FIGURE 1.5 Details of a fiber membrane in the nonhomogeneous representation of the annulus layers showing the collagen fiber orientations.

Figs. 1.7 and 1.8 for typical views of the mesh. Each vertebra is modeled as two independent rigid bodies, one for the anterior body and the other for the posterior bony elements. These two bodies are attached by two deformable beam elements oriented along the pedicles. This representation of each vertebra as a collection of two rigid bodies attached by two deformable beams has been verified to accurately provide

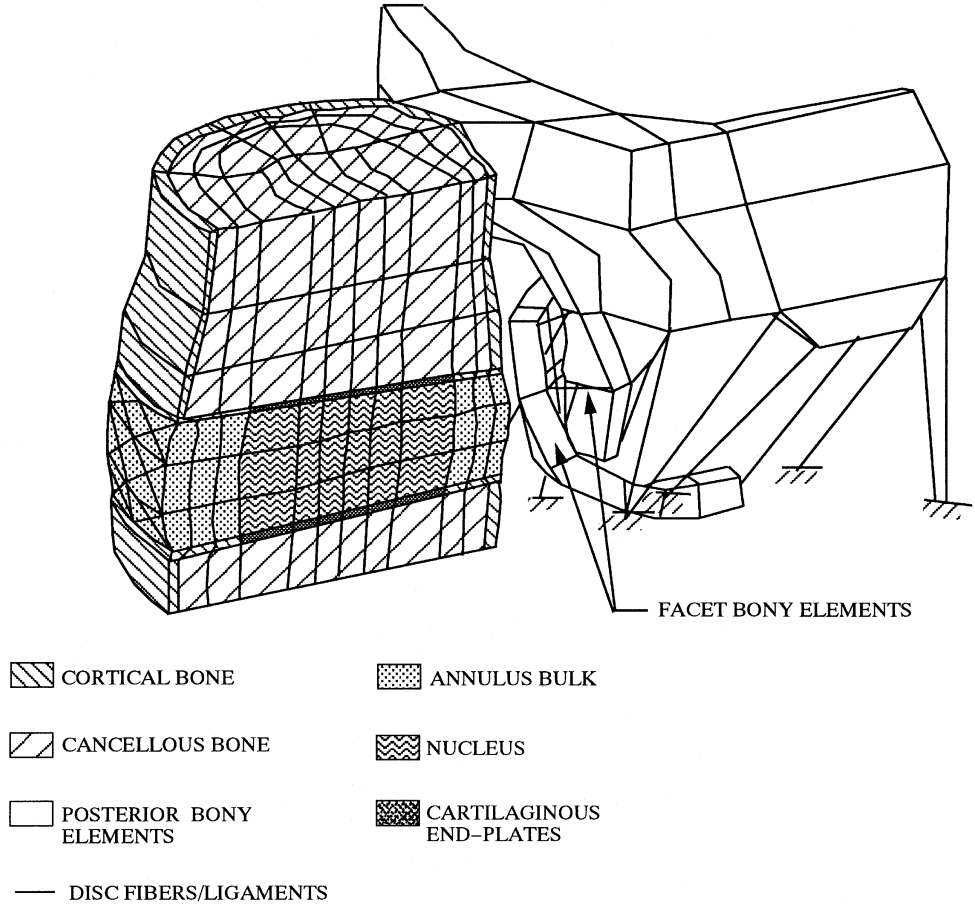

FIGURE 1.6 Three-dimensional finite element model of the entire L2-L3 motion segment with symmetry about the sagittal plane. The loads are applied through the upper vertebra while the lower one remains fixed at the bottom.

for the vertebral compliance while making the analysis cost efficient [55]. Overall, the model contains 1080 eight-node solid elements for the annulus bulk, 5760 three-node membrane shell elements to represent collagenous fibers, 315 two-node uniaxial elements for ligaments, 278 contact points for 10 inferior facet articular surfaces, 685 target triangles for 10 superior articular surfaces, 11 rigid bodies (two for each of L1-L5 vertebrae and one for the S1), 10 beam elements, and a total of 3020 nodal points. The global XYZ coordinate system is set with the Z axis perpendicular to the midplane of the L3-L4 disc, and the X and Y axes are pointed in the sagittal (positive toward posterior) and lateral (positive toward right) directions, respectively.

In the model, the disc annulus is considered as a nonhomogeneous composite with fiber inclinations of about 27° (or 30° in some cases), the nucleus is considered as a compressible or incompressible inviscid fluid with the possibility to prescribe incremental changes in fluid volume or pressure, the ligaments and disc fibers are considered as nonlinear elements with no resistance in compression and a stiffening resistance in tension following some initial slack, and facets are considered as a large-displacement frictionless contact problem accounting for the compliant cartilage layers. The loads are applied at upper levels while the S1 is kept fixed. The model has been used in our nonlinear elastostatic response and stability studies of the entire ligamentous lumbosacral spine under various loads [44-47].

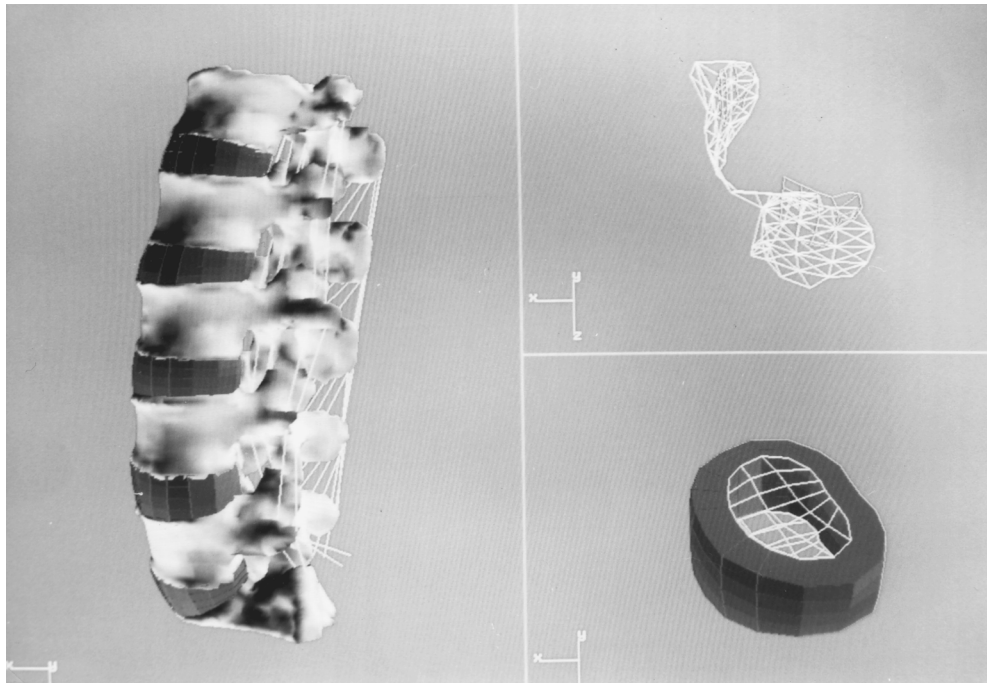

FIGURE 1.7 A typical anterolateral view of the entire lumbar spine model including vertebrae, discs, and ligaments. The finite element meshes for an intervertebral disc and facet contact surfaces at a level are also shown.

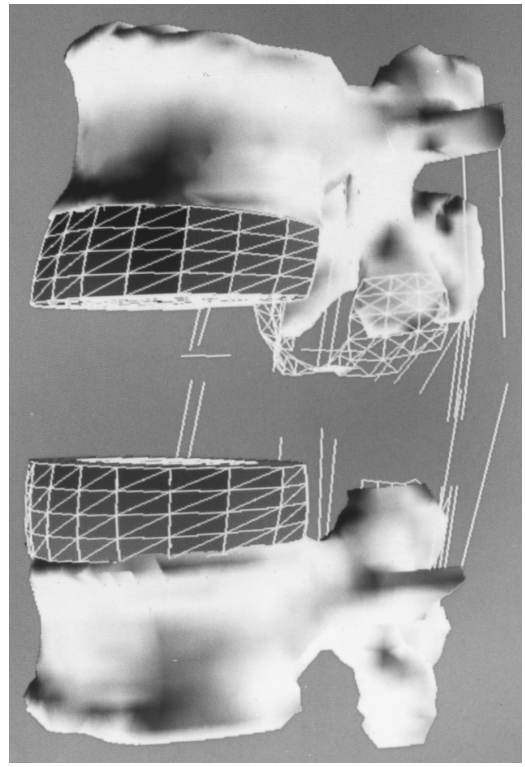

FIGURE 1.8 A typical anterolateral view of two motion segments of the lumbosacral model with the middle vertebra removed. The finite element meshes for discs, ligaments, and facet articular areas are shown.

1.3 Role of Combined Loading

In a linear system, the response under combined loads can be computed easily by superposition of that obtained under each of the applied loads separately. Alteration in magnitude of applied loads does not cause any inconvenience because a simple linear operation needs to be performed. This substantially facilitates the investigation as a repetition of analyses under various load levels and hence combinations are not needed. The lumbar spine, however, exhibits nonlinearity in response even under moderate load magnitudes observed in daily activities, thus requiring individual response analyses for each specific load magnitude and combination. In this section some results related to the lumbar behavior under single loads as compared with combined loads are presented in order to delineate this important feature of the system.

The addition of axial compression has distinct effects on the segmental response (e.g., primary and coupled displacements, intradiscal pressure, facet loads) in flexion, extension, lateral bending, and axial torque. For example, the segmental stiffness decreases in flexion while it increases in extension, axial torque, and lateral moment when an axial compression force is added. Our single-motion segment studies predict that the segmental rotation under 15 N-m moment changes in the presence of a 1000 N compression preload from 6.2° to 6.9° in flexion, 5.3° to 4.5° in extension, 6.7° to 6.2° in lateral moment, and 2.2° to 1.7° in axial torque. The additional flexibility in flexion appears to be mainly due to the anterior horizontal translation of the upper moving vertebra in flexion that generates additional flexion moments in the presence of axial compression force, a nonlinear chain-effect phenomenon referred to as P-effect. The nonlinear coupling between the axial compression and flexion moment increases with increase in compression and/or horizontal displacement. In the remaining moment loadings, the stiffening effect of the addition of axial compression on the segmental rotation is, however, primarily due to the restricting role of facet joints. The stiffening role of facets in extension and lateral moments is such that it even subdues the P-coupling effect that is present similar to the case of flexion moment. The axial compression, in general, has opposite effects on the response; it stiffens the disc by generating initial disc pressure and elongating some disc fibers, whereas it tends to soften the response by slackening ligaments and some disc fibers as a result of shortening in the disc height.

Due primarily to the facet articulations, the presence of axial compression preload tends to markedly increase the intradiscal pressure in flexion, whereas it slightly decreases it in extension [35]; a trend that is supported by direct *in vitro* pressure measurements. The facet and ligament forces influence the net compression force on the disc and, hence, affect the nucleus pressure as is noted in the observation of much greater disc pressure in flexion moment than in extension moment, and the substantial increase in disc pressure after the removal of posterior elements in the extension moment [33,56].

Another example is presented for the model of the entire lumbar spine under right axial torque of 10 N-m applied on the L1 vertebra. The right axial rotation at different levels is predicted under either no compression preload or preloads of 800 N and 2800 N, as shown in Fig. 1.9. In the pure moment case, coupled flexion and lateral rotations are also observed. These coupled rotations are, however, constrained for the cases with the axial compression load in order to avoid compression instability of the system. The results clearly indicate the stiffening effect of the presence of axial compression on rotational rigidity at all lumbar levels and that this effect increases with the magnitude of axial compression load. The increase in the stiffness is primarily caused by the increase in facet effectiveness if applied loads activate facet articulations and by the nonlinear properties of disc fibers and ligaments that offer more resistance as they are further stretched.

1.4 Role of Facets and Facet Geometry

Articulation between different bodies is a common phenomenon in the human musculoskeletal joints. Proper consideration of contact is of prime importance in biomechanical studies of such structures. By constraining and guiding intervertebral motions, facet joints are known to play an important role in the mechanics of spinal segments under various loading conditions. Along with the disc and ligaments, they

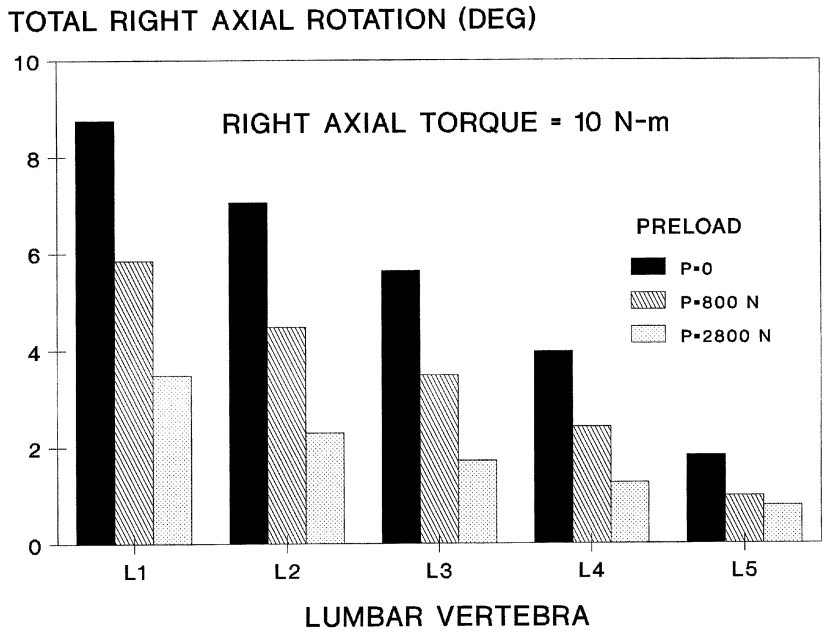

FIGURE 1.9 Effect of various compression preloads, P, on the total right axial rotation at different lumbar levels under 10 N-m right axial torque applied at the L1.

are responsible for transferring loads from one vertebral level to another; i.e., when in contact, facet joints relieve the intervertebral disc by sharing a portion of the applied load. Load-bearing characteristics of facet joints have been determined either indirectly by comparison of segmental response before and after removal of facet joints [33, 53, 56-59] or directly by evaluating the facet contact forces [32, 34, 39, 45-47, 60-66].

Our studies on an L2-L3 motion segment have revealed that, under single loads, axial and extension rotations place considerably larger loads on facets than do flexion and lateral rotations of identical magnitude [32]. Larger flexion rotations beyond 7°, however, initiate contact resulting in relatively large facet forces especially under heavy lifting tasks [32, 34]. Presence of twist and lateral bending in lifting tasks (i.e., asymmetric lifts) substantially increases the load on the compression facet (i.e., the one in contact under the applied axial torque), whereas it relieves the load on the opposite facet joint. In pure axial compression loads of up to 5000 N, the load on each facet varies from 1 to 5% of the applied load depending on the constraint on the coupled sagittal rotation [34].

The geometry of articular surfaces influences the load at which contact first begins as well as the magnitude and direction of contact forces. These are due, respectively, to the initial position of adjacent articular surfaces relative to each other and the spatial orientation of superior articular surfaces. Analysis of regions of contact under various loads suggests three general distinct sets of contact areas (extension, flexion, and torsion) observed primarily under extension, flexion, and torsion loadings, respectively [32]. These contact regions also influence the relative magnitude of contact forces in different directions. In our L2-L3 single-motion segment studies, contact forces in torsion are found to be almost entirely oriented in the lateral direction with negligible axial and sagittal components, while the reverse occurs in extension where the lateral component of the contact force is the smallest one. In flexion, the axial component of the contact forces is negligible, indicating that the resultant contact force is oriented nearly in the horizontal plane.

In the model of the entire lumbar spine, the facet loads vary from one level to another and from one side to the other. The latter variation is due to the geometry of the whole model and the asymmetry in the facets [45]. Results for the whole lumbar spine under a combined load of right axial torque and axial compression are shown in Figs. 1.10 and 1.11. Due to the inherent lumbar instability under compression

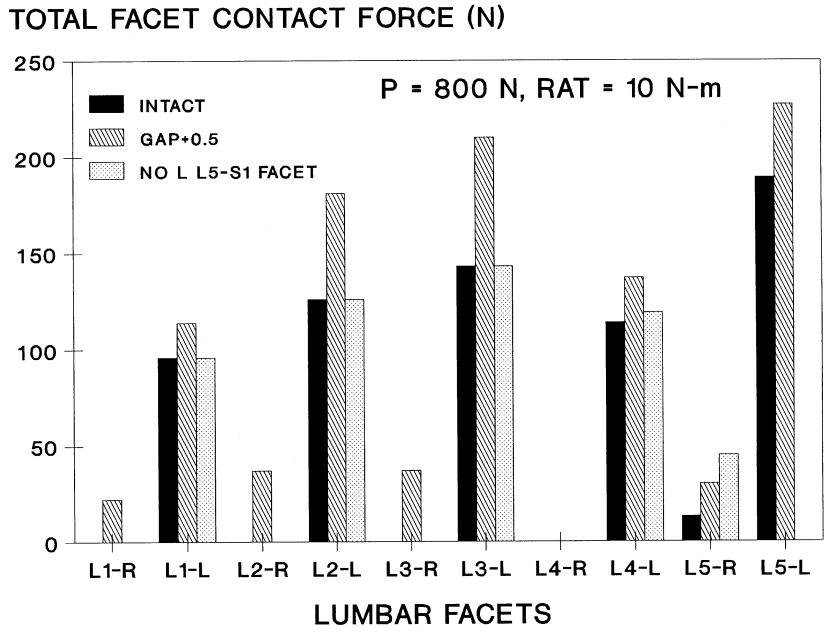

FIGURE 1.10 Total contact force on left, L, and right, R, facets at different segmental levels under combined loading of 800 N axial compression and 10 N-m right axial torque for the intact case, the case with the facet gap limit (i.e., the distance between bodies below which articulation occurs) increased by 0.5 mm at all facet joints, and subsequent to the removal of the left facet at the L5-S1 level.

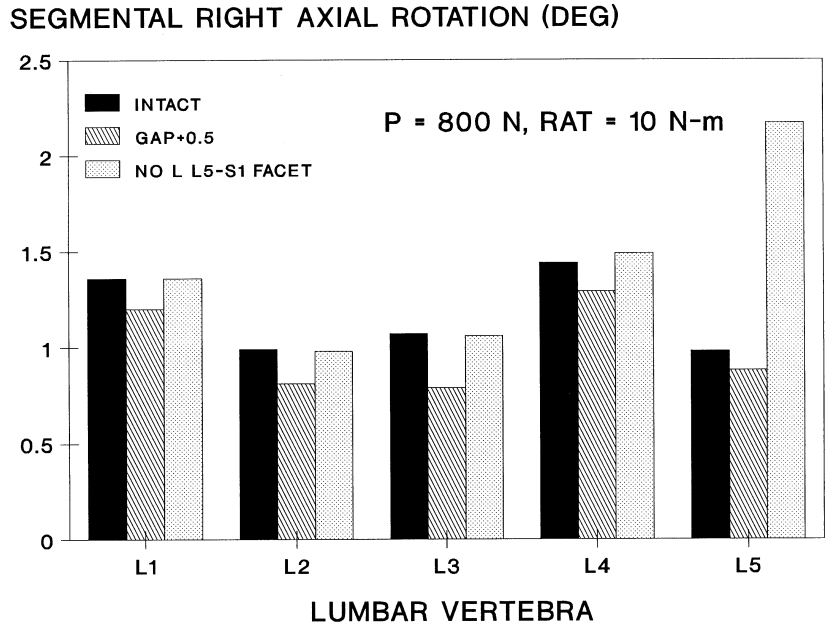

FIGURE 1.11 Segmental right axial rotation at different lumbar levels under combined loading of 800 N axial compression and 10 N-m right axial torque for the intact case, the case with the facet gap limit increased by 0.5 mm at all levels, and when the left L5-S1 facet is removed.

loads of such magnitude, sagittal and lateral rotations at all levels are constrained for all cases. The presence of right axial torque tends to relieve the load on the right facets whereas it increases that on the left facets. As the gap limit (i.e., the distance between articular surfaces below that contact and load transfer initiate in the model) increases, the load on both right and left facets substantially increases as compared to that in the intact model. Removal of the left facets at the distal L5-S1 level markedly increases the load on the opposite right intact facets at the same level with forces on facets of upper levels remaining unchanged. The associated lumbar right axial rotations for these cases under the same combined loading are shown in Fig. 1.11, indicating the variation in intersegmental rotations at different levels and the stiffening effect of more effective facet articulation at all levels when the gap limit is increased. Moreover, removal of left facets at the L5-S1 level significantly increases the joint axial rotational flexibility at the same level, while the rotation at upper proximal levels remains almost unaffected (Fig. 1.11).

The mechanism of articulation at a segmental level is a complex constraint problem affected by many factors such as the initial gap distance, the state of articular cartilage layers, articular surface geometry, loading, coupled motions, and the state of the intervertebral disc at the same level. Our studies have indicated the importance of the interference gap distance in the effectiveness of the lumbar facet joints. As the distance decreases, the resistant contact forces increase and the flexibility decreases [35, 45-47]. The likely association between facet asymmetry and disc failure has been suggested [67], but remains a controversial issue [68, 69]. In recent experimental studies on single-motion segments, the facet geometry has been indicated not to have a significant role in the segmental response in axial torque [68]. In agreement with the latter study, our results suggest that the facet geometry is not the primary factor in determining the segmental response in torsion and, hence, cannot be related to the observed disc ruptures. The articular geometry, however, affects both the direction of resultant forces and subsequent relative movements between articulating bodies. In this manner, the facet geometry likely influences the primary and coupled motions to some minor extents. The facet gap distance and not the facet articular geometry, therefore, appears to be the primary factor affecting the facet forces and the joint response. A smaller gap distance and, hence, a more effective articulation could be produced by additional loads (e.g., compression, torsion, extension), by loss of disc height and disc fluid content occurring especially with long-term loadings (e.g., creep), and by the presence of thick nondegenerated articular cartilaginous layers.

1.5 Role of Bone Compliance

In biomechanical response studies of various joint systems, the bony structures are much stiffer than the remaining tissues and, hence, have occasionally been considered rigid bodies. This consideration suggests that the joint laxity is primarily due to connective soft tissues rather than the bony structures. The rigid simulation of bony elements is also motivated in part by the relative ease in modeling and the cost efficiency of the analysis, particularly in a nonlinear response study. A number of biomechanical studies have modeled bony structures as rigid bodies [45, 46, 70-74]. In the lumbar spine, loads are transmitted from one segment to the adjacent one via soft tissues and bony structures. The latter parts are, however, much stiffer than the former parts and, hence, are expected to play a smaller role in joint flexibility via their internal deformations. Our previous model studies have indicated the deformability of the bony elements and the need for their modeling as deformable solids and not rigid bodies [33, 53]. These studies, however, did not determine the extent by which the vertebral compliance influences the joint biomechanics.

Detailed identification of the role of vertebral compliance in joint biomechanics is essential in areas such as prosthetic replacement of segmental elements, *in vitro* experimental studies, and *in vivo* measurements of joint displacements through bony posterior elements. Changes in bone material properties are also known to occur with aging, remodeling, and osteoporosis [75-77]. The joint biomechanics, as well as degenerative processes, therefore, could be affected by changes in the structure and density of the bony vertebrae. Moreover, rigid simulation of bony elements, if found reliable in yielding accurate results,

significantly reduces the size of the numerical problem to be solved and, hence, allows for the cost-efficient modeling of more complex musculoskeletal systems.

In order to investigate the role of bone compliance in mechanics of motion segments, five models with different representation of bony elements are developed and analyzed under various loads. The modeling of facet joints, intervertebral discs, and ligaments remains identical in these models. The vertebrae of the motion segment are simulated as follows:

1. Bony elements are assumed to be deformable with realistic isotropic material properties; i.e., modulus of elasticity of E = 12000 MPa for the cortical bone, E = 100 MPa for the cancellous bone, and E = 3500 MPa for the bony posterior elements [33, 53].
2. Bony elements are all assumed to be significantly stiffer with homogeneous isotropic properties where E = 26000 Mpa.
3. Each vertebra is modeled as a single rigid body.
4. Each vertebra is modeled as a collection of two rigid bodies attached by two deformable beam elements. The rigid bodies represent the anterior vertebral body and posterior bony elements while deformable beam elements are placed at and oriented along the centroid of pedicles. These beams are expected to somewhat account for the deformability of posterior bony elements. After a number of trials, structural properties of these beams are taken as modulus of elasticity E = 3500 MPa, initial length L = 15 mm, initial cross-sectional area A = 50 mm^2, and moments of inertia Iy = 275 mm^4, Iz = 150 mm^4, and Jx = 500 mm^4, where local rigidly moving axes x, y, and z represent the longitudinal and two cross-sectional principal axes, respectively.
5. Bony material properties of Case (1) are reduced by a factor of 5 to model a marked reduction in bone mechanical properties associated with loss of bone density, for example.

The finite element mesh for all cases with deformable vertebrae is similar to that shown in Fig. 1.6 while that for Case (4) is depicted in Fig. 1.12.

Under axial compression forces up to 5000 N, the predicted axial displacements for various vertebral models and boundary conditions are shown in Fig. 1.13. The segmental axial stiffness increases as the coupled sagittal rotation (TY) is restrained, a trend that further continues when the sagittal translation (DX) is also constrained. The foregoing stiffening effect is due to the articulation at the facets that tends to cause coupled flexion in the unconstrained segment. Use of a rigid body for the whole vertebra (Case 3) is seen to considerably stiffen the segment, whereas the presence of a deformable beam connecting two rigid bodies (Case 4) tends to partially correct the overstiffness due to the rigid modeling of vertebrae. As for the facet forces, not shown here, Cases 1 and 3 yield nearly the same results. The facet forces increase as the coupled motions are constrained and as the vertebral compliance is neglected [55].

During flexion moments, an increase in bone stiffness markedly increases the segmental rotational stiffness and tensile forces in supra/interspinous ligaments. The disc pressure, facet contact forces, and forces in disc fibers are decreased. During extension moments, stiffer bone increases the sagittal stiffness and facet contact forces but decreases the disc pressure. During axial torques, stiffer bone noticeably increases the rotational rigidity. Reverse trends are computed as the bone properties reduce. The predicted segmental rotation under flexion, extension, and torsion moments are shown in Fig. 1.14 for various models of bony vertebrae. Detailed results for various cases at 60 N-m axial torque are listed in Table 1.1, indicating that stiffer bone increases the segmental rigidity and facet contact forces but decreases the disc pressure and forces in disc fibers. Reverse trends are predicted as bone mechanical properties are reduced. The use of deformable beam elements in addition to rigid bodies is found to yield results comparable with those computed with realistic material properties for bony vertebrae.

Alteration in the relative stiffness of bony elements noticeably affects the joint biomechanical response in terms of both the gross response and the state of stress and strain in various components. The extent of change depends on the magnitude and type of applied loads. The results of this investigation suggest that changes in bone properties associated with the aging, remodeling, and osteoporosis could have marked effects on mechanics of the human spine. Alteration in the stress distribution due to changes in

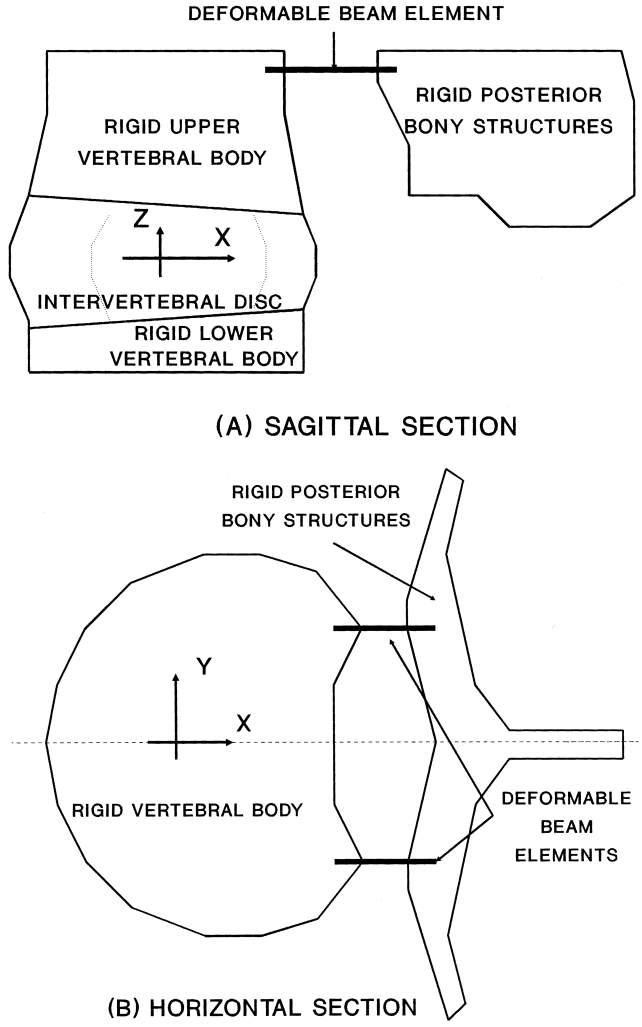

FIGURE 1.12 Two cross-sections showing the finite element model of the motion segment with each vertebra represented as a collection of two rigid bodies attached by two deformable beam elements (model D).

bone properties could initiate a series of action and reaction that may accelerate the process of remodeling and segmental degeneration.

Presence of adjacent vertebrae in a multisegmental model in which ligaments and facet joints of neighboring segments apply opposite forces on the posterior elements of the vertebra in between could diminish the extent of the above predicted changes only if the opposing forces are of nearly the same magnitude. This, however, has been found not to be the case in our model studies of the entire lumbar spine subjected to single moments [45, 46]. Under axial compression force, due primarily to facet articulation, the vertebrae are found to experience rotations at the posterior elements different from those at the anterior body. In compression loads, the difference is much larger in the sagittal plane at the L5 vertebra. Under 800 N axial compression force, the posterior elements of the L5 vertebra rotate 1.4° in flexion in comparison with the L5 anterior body. This difference further increases in a more lordotic posture, in the presence of right axial torque and when the L5-S1 nucleus fluid content is lost. The increase of compression load to 2800 N substantially increases the foregoing difference in rotation at the L5 level to 4.1°; that is, while the L5 anterior body is restrained in sagittal rotation, the L5 posterior elements rotate 4.1° in flexion. Such marked differences in rotations point to the level of stress at the

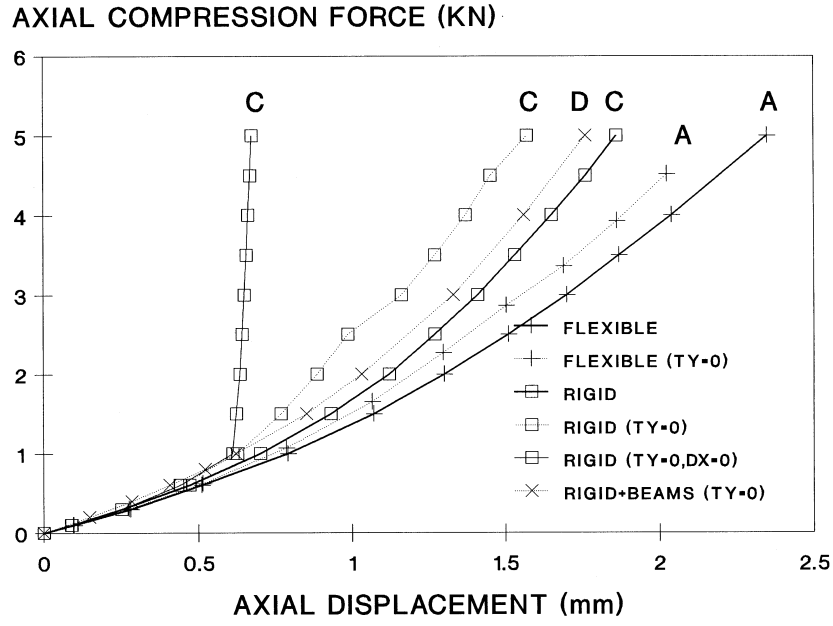

FIGURE 1.13 Effect of vertebral modeling and boundary conditions on the axial response in axial compression force. A: vertebrae with realistic material properties; C: each vertebra as a single rigid body; D: each vertebra as a collection of two rigid bodies attached by two deformable beam elements; TY: coupled sagittal rotation of upper vertebral body; DX: coupled sagittal translation of upper vertebral body.

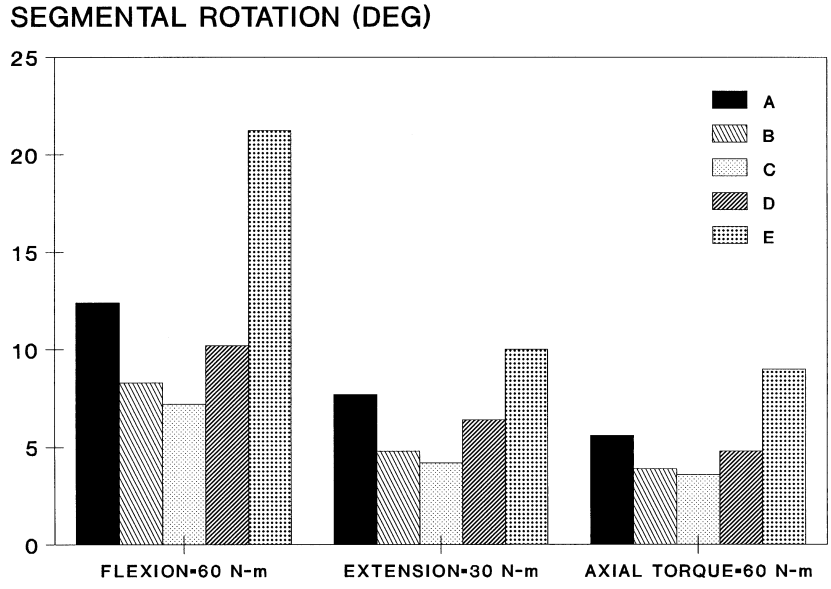

FIGURE 1.14 Effect of vertebral modeling on the segmental response under various moments. A: vertebrae with realistic material properties; B: vertebrae with material properties increased; C: each vertebra as a single rigid body; D: each vertebra as two rigid bodies attached by two deformable beams; E: vertebrae with reduced material properties.

posterior bony elements, particularly in the pars interarticularis and pedicles. These stresses are caused by the facet contact forces as the posterior ligaments are negligibly loaded in neutral postures. In view of the effect of fatigue and creep on bone failure properties [78, 79], prolonged neutral postures, especially

Table 1.1 Predicted Results for Various Cases Under 60 N-m Axial Torque

Case	A	B	C	D	E
Axial rotation (deg)	5.6	3.9	3.6	4.8	9.0
Coupled rotations (deg):					
Lateral	0.7	0.4	0.2	0.6	1.4
Flexion	1.2	1.0	0.9	1.2	0.9
Disc pressure (MPa)	1.02	0.94	0.94	1.05	1.05
Total facet force (N)	892	1140	1153	883	638
Total fiber force (N):					
Innermost	462	455	454	473	454
Outermost	1627	1332	1308	1600	2077

Note: A: realistic deformable material properties for vertebrae; B: much stiffer properties for bony vertebrae; C: a single rigid body for each vertebra; D: each vertebra as a collection of two rigid bodies attached by two deformable beams; and E: reduced properties for vertebrae.

in degenerated discs, could play a role in the pathomechanics of spondylolysis [80-82]. The foregoing results also indicate the likely error involved in the extrapolation of results of *in vivo* measurements through external systems attached to the spine (usually by insertion of pins to bony spinous processes) directly to corresponding intervertebral motions [83 84].

1.6 Role of Nucleus Fluid Content

The nucleus pulposus portion of intervertebral discs is generally recognized as playing an important role in the mechanics of the lumbar spine. Previous studies have demonstrated the role of disc fluid content on the segmental response by either removing the entire nucleus material (i.e., total nucleotomy) or altering its volume or pressure [28, 33, 53, 85-89]. The nearly hydrostatic pressure in normal or slightly degenerated nuclei [90, 91] increases the disc stiffness directly by resisting the applied compression force and indirectly by prestressing the surrounding annulus layers. The confined nucleus fluid may be lost into surrounding tissues as a result of disc prolapse, end-plate fracture, or diffusion. It could also be resolved by injection of nucleolytic enzymes utilized to treat disc herniation. Moreover, it may be removed during surgery (i.e., partial or total nucleotomy) or could mechanically alter with age and degeneration to become semisolid and dry. Such changes are expected to alter not only the disc pressure and volume but also the global response as well as the state of stress and strain in the whole structure. The role of disc fluid content in lumbar degenerative processes has been indicated and discussed by a number of researchers [92-95].

Using a novel approach [96], the effect of arbitrary changes in the nucleus fluid content or pressure on the detailed response of lumbar motion segments has been investigated under various preloads [31]. That is, prescribed changes in fluid content or pressure have been considered to act as additional loading conditions even when external loads remain unchanged. A loss or gain in nucleus fluid content reaching incrementally to a maximum value of 12% of its initial volume (i.e., about 0.73 cc for the segmental model used for sagittally symmetric loads and 0.80 cc for the model with nonsymmetric loads) is considered in the presence of various preloads. The intradiscal pressure is directly related to the disc fluid content; the pressure rises as the fluid content increases and drops as it decreases, as shown in Fig. 1.15, for various loading cases. The absolute change in disc pressure is seen to be greater as fluid content is increased. In terms of segmental rigidities, gain in fluid content increases the stiffness substantially in axial compression alone and combined with axial torque, while it increases slightly in combined flexion and lateral loadings (Fig. 1.16). In extension loading, a reverse trend is observed in which the segmental stiffness decreases as the fluid content increases. Under all loads, contact forces transmitted through facet joints markedly decrease with fluid gain while fluid loss tends to noticeably increase facet loads. Reverse trends are computed for disc fiber forces, which increase with fluid gain and decrease with fluid loss, with

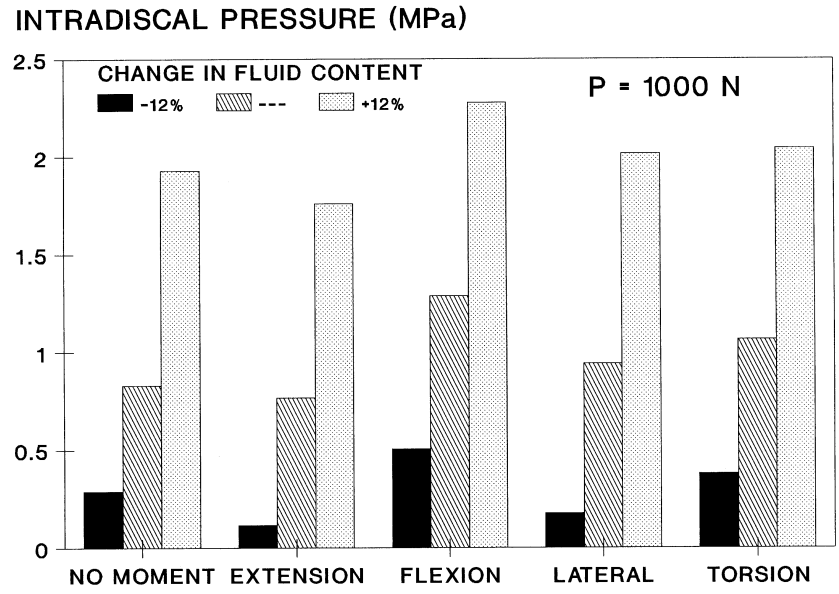

FIGURE 1.15 Variation of intradiscal pressure with percentage changes in the nucleus fluid content under a compression load of 1000 N with and without moments. Extension: 12 N-m; flexion: 12 N-m plus 200 N anterior shear force; lateral: 12 N-m; torsion: 15 N-m.

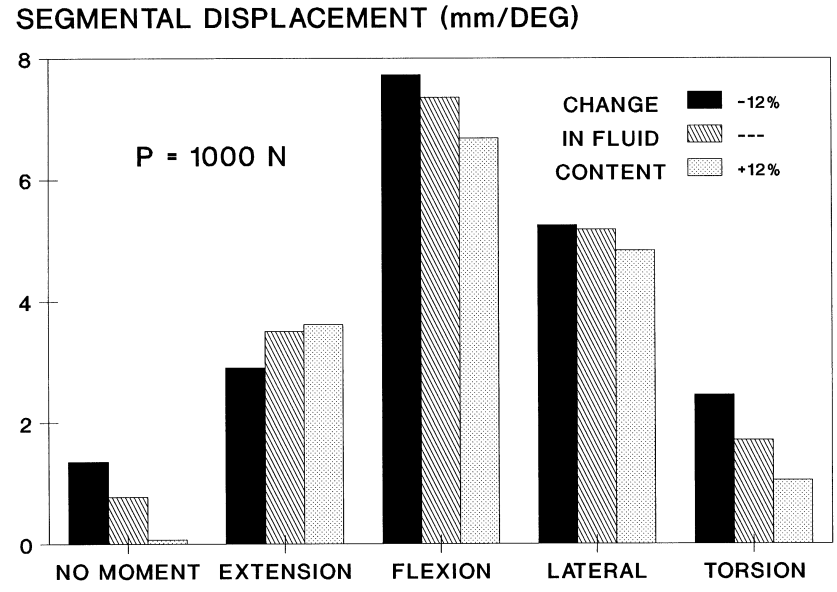

FIGURE 1.16 Effect of changes in the nucleus fluid content on the overall segmental displacement under 1000 N axial compression with and without moments. Extension: 12 N-m; flexion: 12 N-m plus 200 N anterior shear force; lateral: 12 N-m; torsion: 15 N-m.

changes more evident at inner fiber layers than at outer ones. A fluid gain, therefore, increases the load-carrying contribution of disc and ligaments in the segment, whereas it reduces the effectiveness of facets in supporting loads. Reverse trends are observed in the event of a fluid loss.

In the model of the entire lumbosacral spine, nucleus fluid loss at a segmental level is computed to significantly influence the response at that level only. For example, a loss of 0.26 cc at the L4-L5 disc (i.e.,

3% nucleus fluid loss) under 10 N-m right axial torque primarily affects the response at the altered level only. The segmental rotation and total force on compression facet increases from about 1.86° to 2.07° and from 78 N to 97 N, respectively, while the disc pressure decreases from 0.13 MPa to nearly nil. In another study on the entire ligamentous lumbosacral spine with constrained sagittal and lateral rotations under 800 N axial compression force, a fluid loss of 0.96 cc (i.e., 11% of initial volume) at the L4-L5 disc nucleus decreases the disc pressure from 0.68 MPa to 0.17 MPa while it increases forces on the left and right facets from 21 N and 12 N to 39 N and 20 N, respectively, and the segmental axial displacement from 0.79 mm to 1.58 mm. The response at remaining intact levels is not noticeably altered.

As the nucleus loses its content and becomes semisolid, it carries less and less load and at the same time its support for inner annulus layers diminishes. That is, loads on the disc annulus and facets increase while fiber layers carry smaller tensile force and may become lax. Consequently, inner annulus layers, under larger compression and smaller lateral support, become unstable and bulge inward into nucleus space [31]. Inward instability of inner annulus layers reduces the compressive strength of the disc and, in turn, causes further reduction in the disc height, a process that can be accelerated in the presence of circumferential clefts frequently observed in the disc annulus. Loss of nucleus fluid content, hence, tends to predispose disc layers to lateral instability and disintegration. With further disruption of annulus layers toward outer layers, the complete loss of disc mechanical function similar to that observed in advanced stages of disc degeneration might result.

In view of the mechanical functions of the disc nucleus discussed above, it becomes apparent that modest values of intradiscal pressure (not excessive values) under daily activities may be desirable. Since flexion moments increase the disc pressure more than extension moments [35], modest flexion postures might be recommended over extension postures. Moreover, foregoing results indicate that fluid loss markedly decreases the tensile strains in disc fibers and, hence, the risk of disc rupture in heavy lifting tasks. In contrast, it significantly increases the loads on facet joints under all loading conditions. It may then be concluded that loss of disc fluid (for example, following a creep long-term loading or, to some extent, the disc degeneration) appears to shift the risk of injury from disc annulus to facet joints.

1.7 Role of Annulus Modeling

The annulus region of intervertebral discs is comprised of a series of concentric laminated bands each containing relatively strong collagenous fibers embedded in a matrix of ground substance. Since the latter is a soft material, collagen fibers are expected to play an important role when the disc annulus undergoes tensile strains. The annulus fibrosus is, therefore, a nonhomogeneous material with direction-dependent properties. Realistic representation of this structure is necessary for reliable prediction of stresses in its constituent materials. In homogeneous models of the disc annulus, orthotropic or isotropic, there is no distinction between the matrix and fibers. That is, each layer is assumed to be macroscopically homogeneous. Alternatively, a nonhomogeneous fiber reinforced model represents an annulus layer as a composite of collagenous fibers embedded in a matrix of ground substance, each considered by distinct elements with different material properties.

Although both foregoing composite models of the disc annulus may accurately predict the gross response of the disc (i.e., overall displacements, horizontal bulge, and disc pressure), such cannot be expected in terms of computed stresses. In other words, no matter how the annulus fibrosus is modeled, the material properties may be adjusted so as to predict displacements and strains comparable with results of *in vitro* measurements carried out under similar loading and boundary conditions. However, such agreement in displacements or strains in no way guarantees similar agreement between the computed and measured stresses; i.e., for the same displacements different stress conditions are evaluated in these models. The authors have proposed and extensively used a nonhomogeneous material model for the disc annulus [28, 31-33, 45, 46, 53]. In this section, two equivalent models of the disc annulus are developed and used to compare the predicted displacements and stresses in a linear axisymmetric model of the disc-body-disc unit under axial compression (both short-term elastic and creep poroelastic conditions) and axial torque (short-term elastic analysis only).

Table 1.2 Distribution of Fiber Membrane Properties Among Eight Layers

Layer	Innermost	2	3	4	5	6	7	Outermost
Thickness (mm)	0.047	0.102	0.112	0.127	0.147	0.167	0.186	0.097
Modulus (MPa)	195	210	225	240	255	270	285	300

Table 1.3 Equivalent Material Properties for the Orthotropic Model of the Annulus

Modulus	E(ω)[a] Mpa	E(R) = E(Z) Mpa	G(ω) MPa	(Rω)	(RZ)
Innermost layer	25.90	4.83	1.38	0.084	0.750
Outermost layer	66.23	4.94	1.38	0.034	0.791

[a]Orthogonal axes (R-ω-Z) represent the material principal directions, with ω being in the direction of fibers.

In the nonhomogeneous model, the annulus fibrosus is modeled as a composite of collagen fiber layers reinforcing an isotropic matrix of ground substance as shown in Figs. 1.4 and 1.5. A collagen volume fraction of 16% is assumed. Based on our earlier studies [28, 33, 53], the linear modulus and thickness of eight fiber membranes (see Figs. 1.4 and 1.5) are chosen as given in Table 1.2. In each layer, the fibers are inclined in both + and – directions. For the matrix, in elastic studies, the isotropic elasticity modulus of E = 4 MPa and Poisson's ratio of $\nu = 0.45$ are assumed. In the creep poroelastic model, using the coupled diffusion-deformation analysis of the ABAQUS finite element program [97], the matrix is modeled by a drained modulus of E = 2.5 MPa, drained Poisson's ratio of $\nu = 0.1$, permeability of $\kappa = 0.3 \times 10^{-15}$ m4/N-s and voids ratio of e = 2.3 [51, 52].

In the homogeneous model of the annulus, assuming transverse isotropy in the plane normal to fibers, the five unknown moduli are evaluated on the basis of equivalence of the foregoing two models. That is, the properties are chosen so that samples of both models result in identical displacements under equal forces. Unknown material properties of this model are, therefore, uniquely calculated for each annulus layer being dependent on the fiber modulus, fiber volume fraction, and two moduli of the matrix. These properties are given in Table 1.3 for the innermost and outermost layers only. In creep poroelastic studies, the equivalent drained moduli are also calculated in a similar way based on the fiber volume fraction, fiber modulus, and matrix drained moduli. The permeability and voids ratio remain the same as those in the nonhomogeneous model.

For the analysis of the disc-body-disc unit in axial compression (elastic and poroelastic), the adjacent fibers in both $+\alpha$ and $-\alpha$ directions are combined in a single equivalent layer. In this manner, for both homogeneous and nonhomogeneous models, the coupling between shear stresses in the θR and θZ planes and strains in the remaining directions are neglected. Under the axial torque loading, fibers running opposite to the direction of the applied torque are compressed and, hence, should not play a load-bearing role. For this loading case, the finite element formulation is modified to incorporate a general non-restricted form of stress-strain relations. The membrane layers are, therefore, reinforced by fibers in the $+\alpha$ direction only. The equivalent material properties for the homogeneous orthotropic model are subsequently evaluated, accounting for the modified fiber volume fraction.

As expected, the gross response in terms of displacements, strains, and disc pressure are almost identical in both models under 0.5 mm downward elastic axial displacement, 5 N-m axial torque (Table 1.4), and 400 N creep compression (Table 1.5). Variation of the fiber angle from 0° to 90° in axial torque demonstrates that the disc stiffness and pressure are maximum at the fiber angle of $\alpha = 45°$ (Table 1.6). In axial compression, however, the axial and horizontal stiffnesses as well as disc pressure are highest at the fiber angle of $\alpha = 0°$.

Despite almost identical strains and displacements under various loads, different stress results are predicted depending on the annulus model utilized. For example, the stress results in annulus circumferential planes (θZ) along the radius at mid-height plane under 5 N-m axial torque are shown in Fig. 1.17 for both models. Had the fibers in the –30° direction been modeled as well, the normal hoop and axial stresses would

Table 1.4 Overall Response for Both Material Models in 5 N-m Axial Torque (α = +30°)

Anulus Model	Axial Rotation(°)	Disc Pressure (MPa)	Disc Bulge (mm)
Nonhomogeneous	2.50	0.105	-0.159
Homogeneous	2.52	0.106	-0.159

Table 1.5 Overall Response for Both Material Models in 400 N Compression (α =30°)

	Axial Displacement (mm)		Disc Bulge (mm)		Disc Central Pressure (MPa)	
Time (s)	25	3925	25	3925	25	3925
Nonhomogeneous	0.473	0.839	0.456	0.472	0.358	0.253
Homogeneous	0.478	0.846	0.470	0.488	0.360	0.254

Table 1.6 Overall Response in 5 N-m Axial Torque for Various Fiber Angles

Fiber angle α(deg)	0	20	30	45	90
Axial rotation (deg)	9.02/9.02[a]	3.88/2.13	2.50/1.33	2.04/1.04	9.02/9.02
Disc pressure (MPa)	0/0	0.074/0	0.105/0	0.158/0	0/0
Disc bulge (mm)	0/0	-0.26/0	-0.16/0	0.01/0	0/0

[a]Results with fibers in tension only/Results with the compressed fibers considered as well.

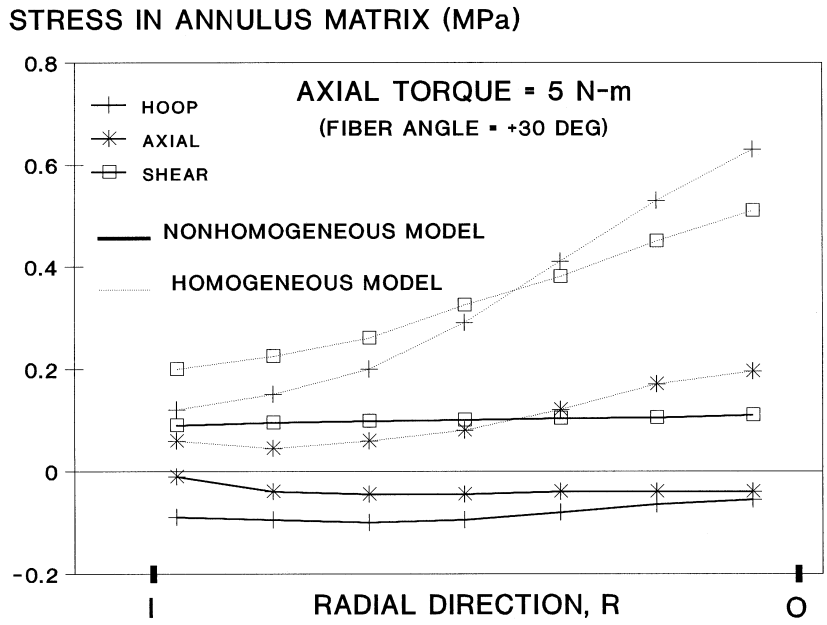

FIGURE 1.17 Predicted normal hoop, normal axial, and shear stresses in the Z plane (see Figs. 1.4 and 1.5) in annulus tissue of the disc-body unit along the radial direction at the mid-height for both homogeneous and non-homogeneous models under 5 N-m axial torque. The fibers in –30° orientation are in compression and, hence, are not active in the model. I: inner annulus boundary, O: outer annulus boundary.

have been computed to be null everywhere. Similar to the case in axial compression, the normal stresses are seen to be much smaller in nonhomogeneous models and remain compressive everywhere. In contrast, these stresses are tensile in the homogeneous model. The shear stresses in circumferential planes (θZ) are also smaller in the former model. The foregoing differences in bulk stresses are due to the tensile membrane stresses, which are shown in Fig. 1.18. Similar differences between annulus models are computed under creep loading of 400 N, as shown in Figs. 1.19 and 1.20. In comparison with stresses in the homogeneous

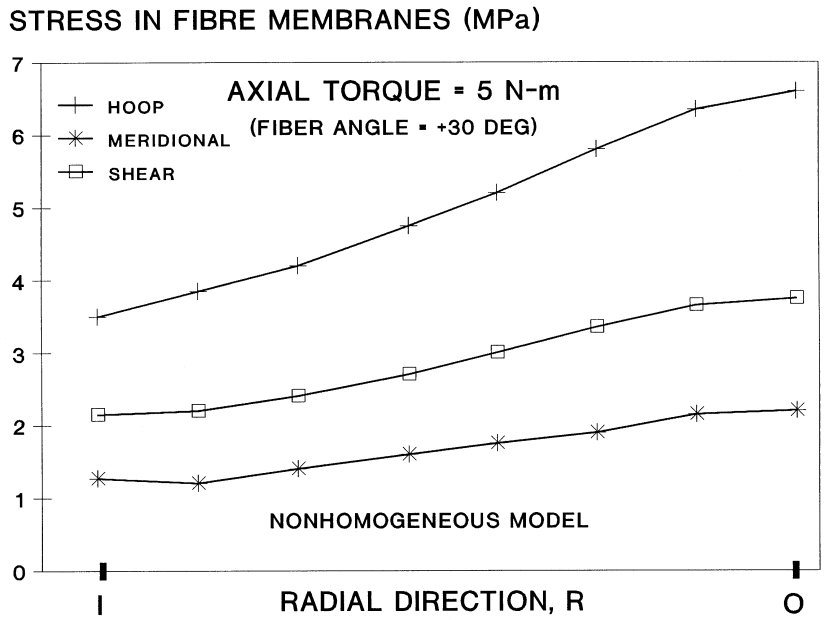

FIGURE 1.18 Normal and shear stresses in Z' plane (see Figs. 1.4 and 1.5) in annulus fiber membrane layers of the disc-body unit along the radial direction at the mid-height for the nonhomogeneous model under 5 N-m axial torque. The fiber layers in –30° orientation are in compression and, hence, are not active in the model. I: innermost layer; O: outermost layer.

model, effective hoop and axial stresses in the nonhomogeneous model are much smaller (i.e., more compressive) everywhere along the disc radius in the annulus. Unlike the matrix, the fiber membranes in the nonhomogeneous model are in tension as depicted in Fig. 1.20. The magnitude of stresses in the matrix and membrane elements of both models, nevertheless, diminishes with time.

The basic difference between the homogeneous orthotropic and nonhomogeneous composite models of the disc annulus is that there is a distinction between the matrix and fibers in the latter model while no such distinction exists in the former model. In the nonhomogeneous model, neglecting the interfacial slip, the matrix and fibers experience dissimilar stresses under identical strains, whereas no such difference in stresses exists in the homogeneous model. It is evident that the difference in stress predictions depends on the relative stiffness of the matrix and fibers that is expected to increase under greater loads and displacements. The fiber membranes while under tension, in turn, apply compression on the annulus matrix and, hence, increase compressive stresses in various directions. The distinct nature of these two annulus models, as well as their dissimilar predictions, raises the question as to which model better represents the disc annulus. The definitive answer to this question must await further reliable detailed studies on the microstructure of the annulus and on the measurement of stresses in this material. The annulus structure and relative mechanical role of its constituent elements, however, appears to support our view that the nonhomogeneous model is more realistic. The prediction of tensile stresses in annulus fibers and of compressive stresses in the matrix is also desirable, employing each component to carry stresses for which it is best suited. Such nonhomogeneous presentations have already been utilized in our biomechanical studies of similar soft tissues such as the knee meniscus [73,74] and cartilage [98].

1.8 Time-Dependent Response Analysis

While performing various tasks during routine daily, as well as athletic, activities, the human spine is subjected to loads and motions with different magnitudes, directions, and time characteristics. Because of the time-dependent nature of actions applied and the structure itself, consideration of the dynamic

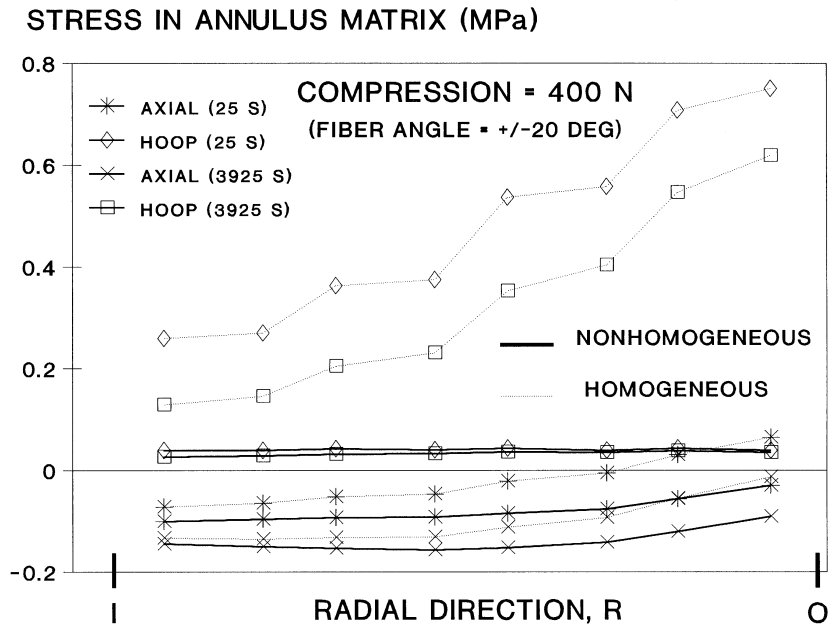

FIGURE 1.19 Effective normal stresses in the annulus of the disc-body unit (Figs. 1.4 and 1.5) along the radial direction at the disc mid-height for both homogeneous and nonhomogeneous models at different times under a creep compression loading of 400 N using a poroelastic analysis. The fiber angles are in both ±20° directions. I: inner annulus boundary; O: outer annulus boundary.

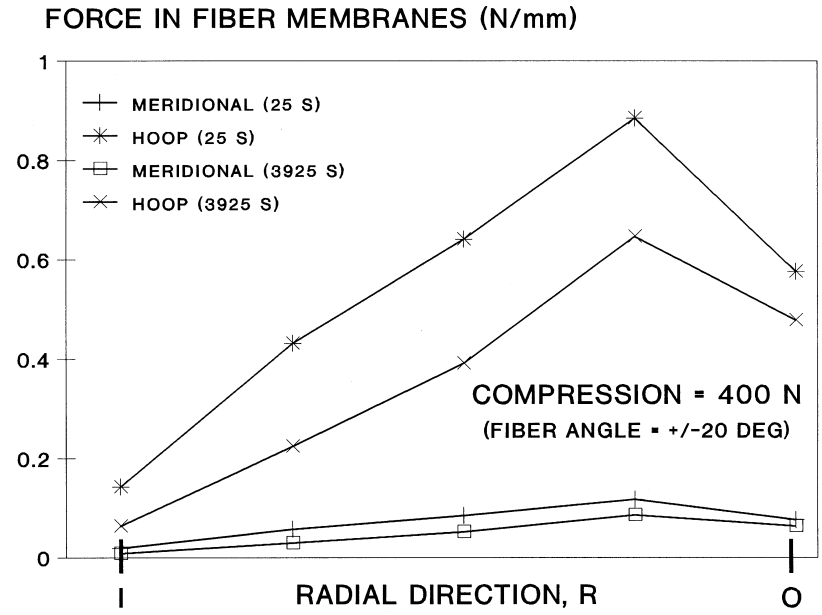

FIGURE 1.20 Variation of normal stresses in fiber membranes of the disc-body unit (Figs. 1.4 and 1.5) along the radial direction at the annulus mid-height for the nonhomogeneous model at different times under a creep compression loading of 400 N using a poroelastic analysis. The fiber angles are in both ±20° directions. I: innermost layer; O: outermost layer.

Table 1.7 Natural Frequencies for the Top Constrained Disc-Body Unit (Hz)

Mode	m = 0, P = 0[a]	m = 40 kg, P = 0	m = 40 kg, P = 680 N
1	1158	23.6	26
2	1256	1058	1330
3	1853	1353	1977

[a]m: upper-body mass, P: upper body compression preload.

Table 1.8 Natural Frequencies for the Unconstrained Disc-Body Unit with m = 40 kg (Hz)

Mode	K = 0[a]	K = 2.2 Mpa	K = 22 Mpa	K = 2200 MPa
1	5.1	5.2	5.3	6.1
2	15.8[b]	18.0[b]	21.4[b]	23.4[b]
3	25.3	25.6	26.0	30.9

[a]K: bulk modulus of the nucleus fluid.
[b]Axial mode of vibration comparable to resonant frequency in the unit with the top constrained.

nature of the response in spinal biomechanics is of prime importance. This is particularly important in various industrial settings where workers perform sedentary activities with static postures for prolonged periods of time, operate vehicles and equipment with exposure to various levels of impact and vibration, and perform frequent manual handling tasks often involving lifting at different rates with and without asymmetry. Epidemiological studies have suggested the frequent lifting, sudden forceful incidents, static postures, and vibration exposure are risk factors for low-back disorders [10, 99-101]. These indications have prompted a considerable interest in the measurement of human whole-body creep, impact, vibration, and fatigue responses under different postures and loading conditions [13, 88, 102-106]. The time-dependent response of the spinal motion segments has also been investigated by both experimental [30, 91, 107-114] and numerical [26, 30, 39, 40, 49, 51, 52, 116-119] studies. The fluid flow and inherent viscoelastic characteristics of tissues have been argued to influence the temporal response of spinal segments [39, 40, 107, 108, 119, 120]. In this section, some results of our numerical investigations on nonlinear temporal response of the motion segments are presented under various dynamic conditions using elastic (with inertial forces), poroelastic, or viscoelastic analyses.

Vibration Analysis

To compute natural frequencies of the disc-body unit, free vibration analyses of the segment without posterior elements have been carried out with and without additional upper body mass of 40 kg or compression preload of 680 N. The results for the case with the top of the model constrained to move in the axial direction only (i.e., neglecting lateral and rotational modes of vibration) are listed in Table 1.7. The important role of the upper-body mass in diminishing the fundamental frequency and of the presence of a compression preload in stiffening the response is evident. Repetition of analyses without the constraint on the top reveals that there is a smaller resonant frequency in each case, which relates to the rotational mode of vibration. To study the likely effect of the disc nucleus on the response, the bulk modulus (i.e., nucleus incompressibility) is varied and the natural frequencies are computed (see Table 1.8). A significant decrease in resonant frequency (i.e., segmental stiffness) is observed as the fluid compressibility increases (i.e., fluid content is lost). These results are in accordance with the earlier discussion on the role of disc fluid content and combined loading in joint mechanics.

Forced-vibration linear elastic analysis of the disc-body unit reveals an increase of about 2.5 times in disc pressure and of about twice in global response when a 400 N compression load is applied suddenly (i.e., step loading). Steady-state compliance response analyses with a damping ratio of 0.08 [30] indicate that the compression preload increases the resonant frequency but decreases the resonant amplitude. In contrast, nucleotomy (i.e., removal of disc nucleus) diminishes the resonant frequency and increases the resonant amplitude.

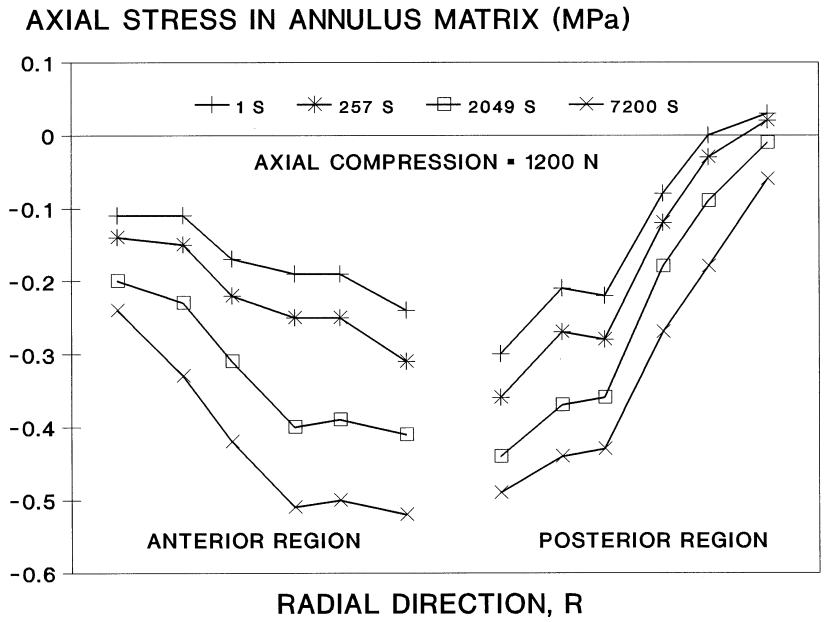

FIGURE 1.21 Variation of effective axial stress in the annulus matrix of the motion segment model (Fig. 1.6) along the anterior and posterior directions in the mid-height sagittal plane for the nonhomogeneous model at different times under a creep compression loading of 1200 N, using a nonlinear poroelastic analysis. Coupled sagittal rotation is allowed, nonlinear strain-dependent permeability is assumed, and pore boundary condition is taken as nil.

Poroelastic Analysis

Assuming the segmental tissues as fully saturated porous media made of voided solid skeleton matrix and interstitial pore fluid, the creep response of the motion segment including posterior elements is investigated utilizing nonlinear poroelastic analyses under various compression loads with duration of up to two hours. In this coupled deformation-diffusion problem, the temporal response in creep is due solely to the fluid flow while the inherent viscoelastic character of constituent tissues is neglected [40]. The relative influence of fluid movement and fluid-independent tissue viscoelasticity in the segmental temporal response is yet unknown and requires further studies. As the material skeleton takes up more stresses, the pore pressure in tissues decays and the structure consolidates. With time, a greater portion of the applied load is transmitted through the annulus and facet joints. The temporal variation of effective axial stresses in annulus matrix in the radial direction is shown in Fig. 1.21 at both anterior and posterior mid-height sagittal regions. Adoption of strain-dependent nonlinear permeability in the analysis is found to have substantial effect on the temporal response. As porous structure compacts under compression, due to increasing diffusive drag forces that resist fluid flow, it becomes increasingly harder for the pore fluid to permeate. Since consolidation diminishes the permeability, the time required to dissipate excess pore pressure increases. The nonlinear strain-dependent variable permeability markedly stiffens the creep response, reduces fluid loss, and decreases facet forces. A non-zero pore pressure of 0.1 MPa prescribed along the outer boundaries of the segment increases the pore pressure at equilibrium and decreases the fluid loss and overall flexibility. Pressures of similar magnitude have been measured at epidural and intramuscular regions during exercise [121, 122].

The creep response is primarily dictated by the fluid flow out of the nucleus region; that is why nearly no time variation in response is observed following total nucleotomy [40]. The preferential pathway of fluid diffusion from the nucleus region is through the central cartilaginous end-plates to adjacent vertebral bodies rather than through the annulus tissue which is due to the lower permeability of the latter. It is interesting to note that the foregoing computed trends in this poroelastic study are almost identical to

those predicted in elastic studies of the segment following disc fluid loss as presented earlier. This further confirms the important role of nucleus fluid content or nucleus fluid pressure in the segmental mechanics. The likely clinical implications of prolonged compression loading, therefore, would be the same as those discussed following loss of disc fluid content. The limitation in taking the fluid movement (i.e., poroelasticity) as the sole mechanism for the time-dependent response of the human discs has been argued previously [108]. The prediction of poroelastic finite element model studies [26, 51, 52] indicating, in contrast to the experimental observations, no creep response in closed top simulations (i.e., no fluid through the top and bottom of the model) also tends to support such arguments in favor of the presence of other mechanisms as well. The relative role of tissue-inherent viscoelasticity as compared to poroelasticity in temporal response needs further studies.

Viscoelastic Analysis

It is important to note that material properties and failure mechanisms are generally affected by strain rate [123, 124]. Neumann et al. [125] argued that the relative risk assessment should include the rate dependencies of the tissue tolerance. Osvalder et al. [126] compared two dynamic loading conditions simulating flexion-distraction injuries prevalent in car accidents and found that the specimens could withstand higher dynamic bending moment prior to the injury, while the deformation at injury was smaller than that in static loadings. This indicated a smaller margin of safety for deformations at faster loading rates. Adams and Green [127] and Green et al. [128] tried to establish the S-N curves to indicate the fatigue strength of the annulus fibers. During cyclic tensile loading, they found that the fatigue failure could occur in less than 10,000 cycles for a tensile force greater than 45% of the ultimate strength. The strength and fatigue life of both cortical and cancellous bone has also been studied extensively. Bowman et al. [129] showed that the strength of the trabecular bone could be reduced substantially if the relatively large stress (i.e., approximately half of its ultimate strength) is continuously applied for 5 hours. Schaffler et al. [130], in their study of the effects of strain rate on the fatigue of compact bone, indicated that within physiological ranges of strain, higher strain rates resulted in larger loss of stiffness (indicative of higher microdamage). The accumulation of microdamage may outpace the remodeling and repair processes.

Models that are most often used to describe the viscoelastic phenomena of biological tissues are the discrete lumped parameter models (i.e., the Kelvin, Maxwell, and various combinations of these two models) and the Quasi-Linear Viscoelastic (QLV) model [131, 132]. The shortcoming of lumped parameter models is that the estimated parameters are dependent on the tests used for their estimation, and there is no assurance that the same set of parameters will describe other cases. This lack of generalization has motivated more detailed modeling approaches that could predict the response not used in parameter estimation. In addition, finite element models will provide more detailed information that is not available in lumped parameter models [114]. Wang [39] has detailed the development of the viscoelastic FE model of the L2-L3 motion segment and subsequent analysis under diverse loading conditions [39, 133-136]. The viscoelastic elements in the model (see Fig. 1.6) consist of the annulus fibrosus (matrix and fibers) and nucleus pulposus. The viscoelastic behavior of the disc fibers is modeled by a nonlinear Zener model, while the Prony series is used for that of the remaining tissues. In this model, the bulk modulus of annulus and nucleus are defined to vary with time in order to simulate both the compressibility and viscoelasticity.

The parameter identification is first performed on the experimental data of the individual components such as the stiffness of isolated fibers, long-term stiffness modulus of the annulus, and shear modulus of the nucleus. Since the material properties are not available for all individual components, the global behavior of the motion segment (body-disc-body unit) is also used in this process. The simulations for constant strain rate loading are compared to the average behavior of eight motion segments as shown in Fig. 1.22 [113, 114]. In 1 hour of creep simulation with 600 N of compressive load, we have observed about a 9% decline in the disc pressure and a 4% volume loss which are in agreement with the results of Argoubi and Shirazi-Adl [40]. The predicted creep curve of the FE simulation is also located within one standard deviation of experimental results, as shown in Fig. 1.23, without the instantaneous strain

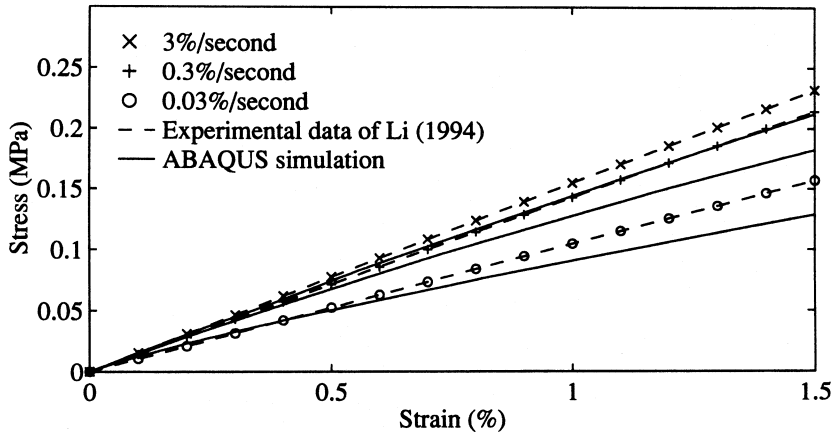

FIGURE 1.22 Comparison of short-term response of viscoelastic finite element model and the averaged experimental results of eight motion segments [113] for three different rates.

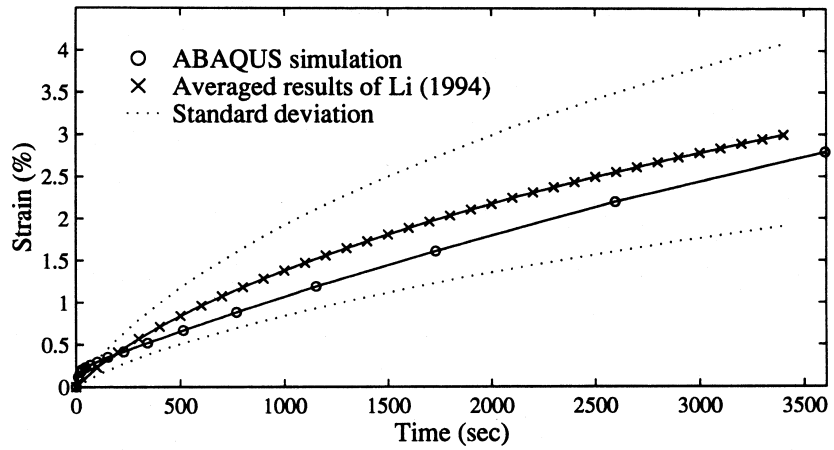

FIGURE 1.23 The experimental [113] and finite element model simulation of a disc under compressive creep. The axial load is 426 N and the instantaneous strain is subtracted to allow ensemble averaging over eight motion segments.

[113, 114]. The FE model of axial cyclic loading at 0.01 Hz provides an excellent match with experimental results of Li [113], pointing to the validity of both short- and long-time constants (Fig. 1.24).

The predictive power of the developed viscoelastic FE model of L2-L3 is shown by illustrating the effect of loading rate and 1 hour of creep on the detailed stress/strain response of the motion segment. The compression and anterior shear forces and the sagittal moment simulating a lifting task reach their maximum respective values of 2000 N, 400 N, and 20 N-m in three durations of 1 sec, 10 sec, and 100 sec. These analyses are repeated twice, before and after 1 hour of creep simulating upright standing (600 N of compression, 60 N anterior shear). At the end of movement for post-creep simulations, the faster loading condition generates significantly less sagittal flexion, total facet force, strain in the posterolateral fibers of the innermost annulus layer, and dissipated strain energy, while generating higher disc pressure and cancellous bone stress. Figure 1.25 summarizes the effect of creep on some of the key computed parameters that characterize the intensity and severity of response of the motion segment to the same loads under two movement times. At the end of the movement, creep has significantly increased the sagittal flexion, facet force, and fiber strains, while reducing the ligament force, disc pressure, and end-plate strain. Creep, as expected, affects the faster motion more because the slower motion has more chance for stress relaxation.

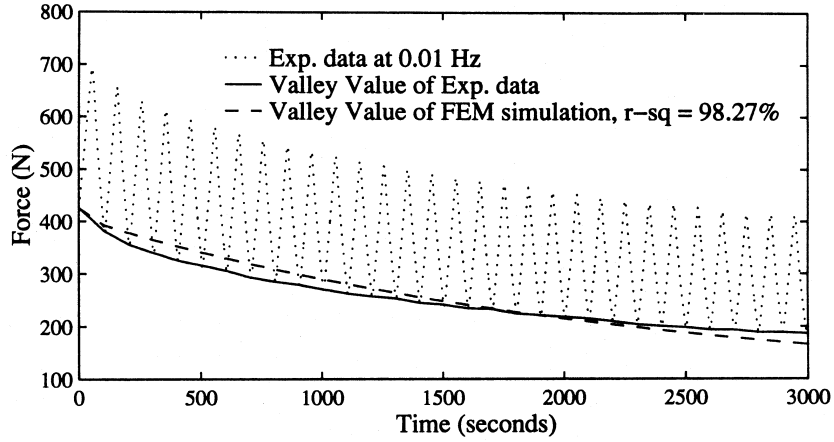

FIGURE 1.24 The stress relaxation during cyclic loading showing both the experimental data [113] and finite element model results of cyclic loading. The preload is 426 N of axial load and amplitude of displacement is 0.1 mm at 0.01 Hz.

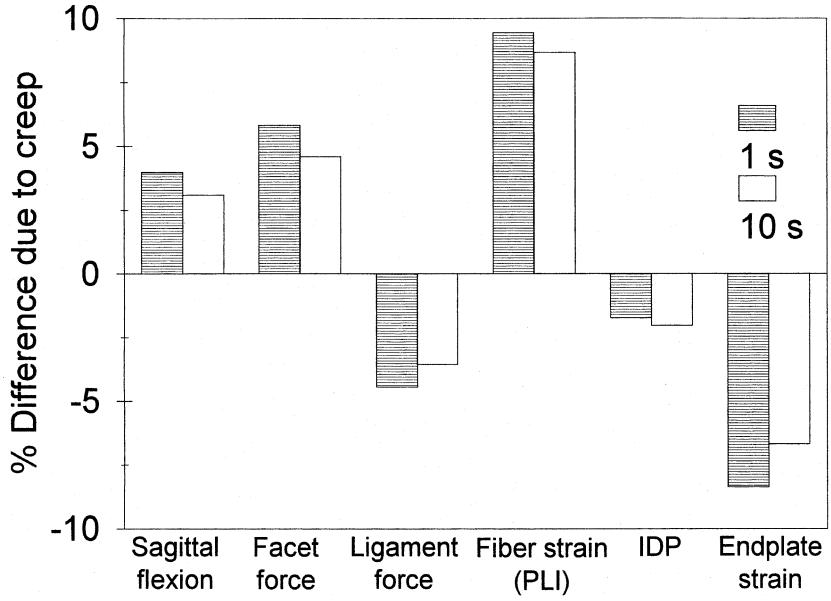

FIGURE 1.25 The effect of creep on the spinal mechanics at two loading rates. The loading conditions before and after 1 hour of creep consist of reaching 2000 N compression force, 400 N anterior shear force and 20 N-m of flexion moment in 1 and 10 seconds durations. IDP = Intradiscal pressure; PLI = Posterolateral inner (annulus fibers in this layer have the highest fiber strain in these loading conditions).

1.9 Stability and Response Analyses in Neutral Postures

The ligamentous lumbar spine, L1-S1, devoid of musculature has been reported to exhibit mechanical instability (i.e., hypermobility) under relatively small compression loads of less than 100 N [44, 137]. The question then arises as to how this structure may withstand much larger compression loads during daily activities. Using finite element models of the lumbosacral and thoracolumbar spines with and without muscles, we have identified a number of mechanisms that stabilize the passive system allowing it to carry large compression loads with minimal displacements [44, 47, 138, 139]. The neural controller

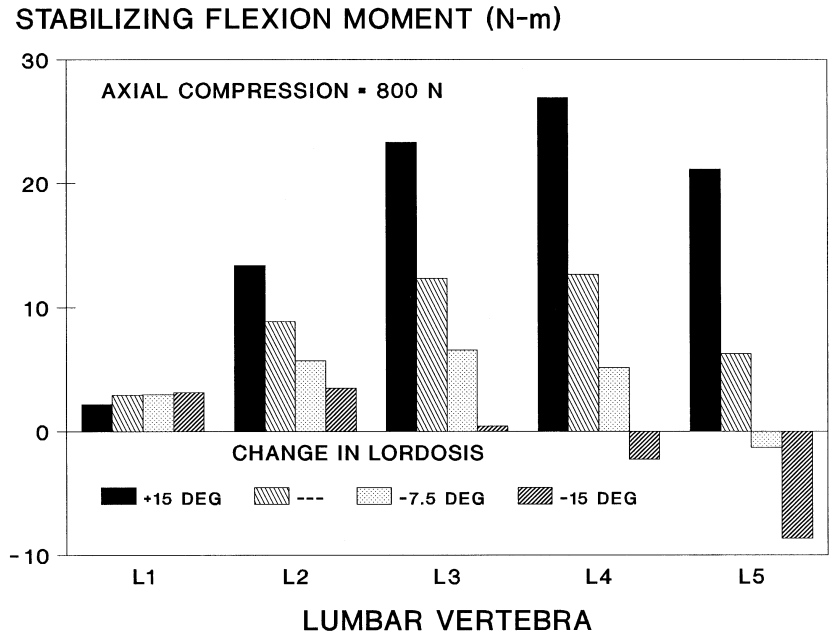

FIGURE 1.26 Stabilizing sagittal moments at different lumbar levels under 800 N axial compression for various postures. +15°: lodosis is increased by 15°; ---: no change in lordosis; –7.5°: lumbar is flattened by 7.5°; –15°: lumbar is flattened by 15°.

has been suggested to exploit the off-center placement of the line of gravity, pelvic tilt, and changes in lordosis in order to stabilize the passive system with minimal need for muscular exertions. In support of these predictions, in neutral standing and sitting postures, it has been found that the line of gravity lies anterior to the lumbar vertebrae resulting in moments in addition to axial compression force [140, 141]. The sagittal curvature of the lumbar spine and pelvic orientation are also known to change as external loads are added to subjects in erect postures [142-144]. Flattening of the lumbar spine has been observed in microgravity [145] and in low-back populations in standing postures as compared to normal subjects [146]. Minimal muscular activities have been recorded in standing subjects with and without loads in their hands [143].

Our model studies have demonstrated that the passive lumbar spine alone undergoes very large displacements (i.e., hypermobility) under compression loads as low as 100 N [44]. This characteristic makes it impossible to undertake studies on the response of the entire lumbar spine alone with no stabilizing mechanisms under physiological compression loads. In other words, biomechanics of the lumbar spine in physiological loads cannot and should not be investigated in isolation with no regard for the stability of the structure. In our earlier studies [44], the presence of a flexion moment at the L1 level noticeably stabilized the structure, allowing it to carry much larger loads with minimal displacements. This effect has further been confirmed by our more recent studies of the thoracolumbar stability in erect postures [138, 139].

The stabilizing sagittal and lateral moments at different lumbar levels allowing it to carry 800 N axial compression applied at L1 without exhibiting any sagittal and lateral rotations are shown in Figs. 1.26 and 1.27, respectively. Apart from some expected axial shortening, the other displacements are predicted to be negligible; see Fig. 1.28 for the deformed sagittal profile of the lumbar spine with and without prior alteration in lordosis under 800 N axial compression force. The effect of posture is investigated by altering the lordosis from its initial value of 46° by +15° to simulate an extended posture or by –7.5° and –15° to simulate a flattened lordosis. It is seen that the stabilizing moments vary with the lordotic posture adopted and the vertebral level along the lumbar spine. A more lordotic posture increases the stabilizing

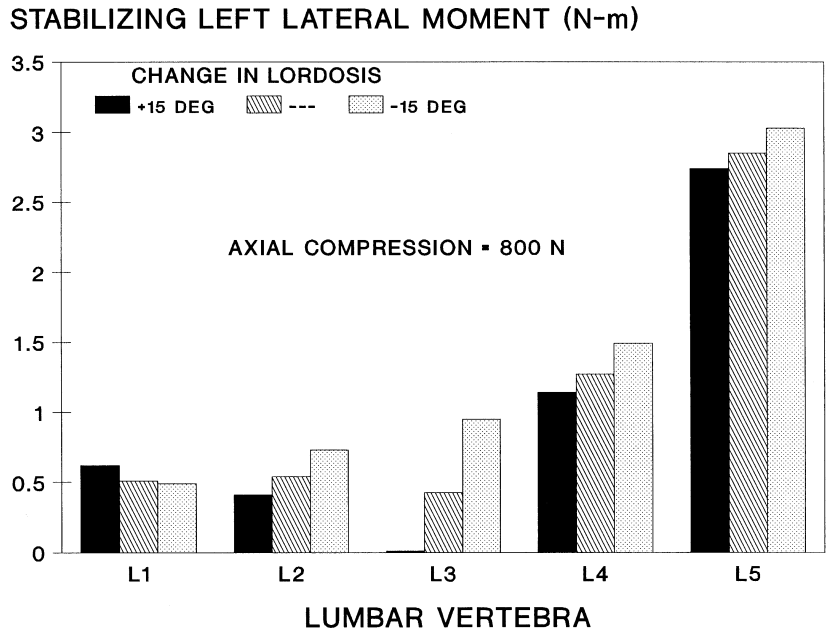

FIGURE 1.27 Stabilizing lateral moments at different lumbar levels under 800 N axial compression for various postures. +15°: lodosis is increased by 15°; ---: no change in lordosis; –15°: lumbar is flattened by 15°.

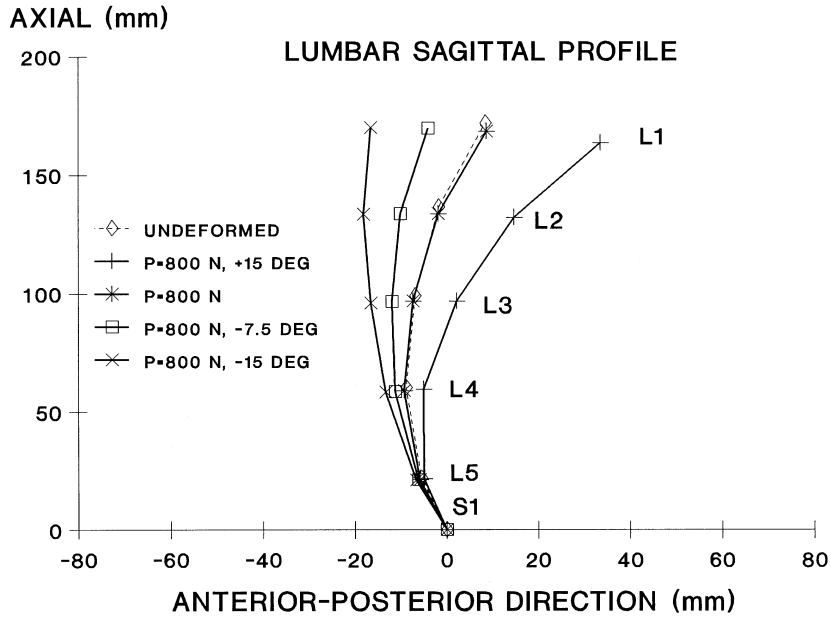

FIGURE 1.28 Sagittal profile of the lumbar spine before loading and subsequent to loading of 800 N axial compression for different lordotic postures. +15°: lumbar lordosis is increased by 15°; –7.5°: lumbar lordosis is flattened by 7.5°; –15°: lumbar lordosis is flattened by 15°.

flexion moments. In the lateral plane, the lumbar spine requires left lateral moments due primarily to the lateral deviation in the initial geometry. In contrast to the sagittal moments, the lateral moments are of smaller magnitude and are less affected by lordotic posture. The addition of 10 N-m right axial torque

to the 800 N compression is verified to have negligible effects on the stabilizing sagittal moments, while the lateral moments are substantially influenced and demonstrate dependence on the lumbar lordosis [47].

The entire ligamentous lumbar spine in various erect postures is found to carry 800 N axial compression while exhibiting relatively small displacements when sagittal and lateral moments given in Figs. 1.26 and 1.27 are also present. Larger axial compression loads can also be supported in the presence of sagittal and lateral moments of larger magnitude. It is interesting to note that even a fraction of these axial compression and moment loads, when applied alone separately, is sufficient to generate excessive displacements [44, 46]. Such a coupled response in which the detrimental effect of each loading disappears when they are combined together is attributable to the lumbar curvature, as a straight column cannot be expected to demonstrate the same behavior. The required computed sagittal and lateral moments are influenced by position of the applied load at the center of the L1 and its application at the L1 only and not among all levels. The former, however, plays a much more important role. The pelvic rotation and postural changes could also alter the magnitude of stabilizing moments. Once the proper position of the applied load and the spinal posture has been accounted for, the remaining moments should then be generated by muscle activations. The line of gravity and spinal posture are, therefore, hypothesized to be exploited to redistribute the applied loads in an optimal manner; i.e., to maximize the stability of the passive structure with minimal requirement on muscular exertions [47, 138, 139].

1.10 Kinetic Redundancy and Models of Spinal Loading

The kinetic redundancy present in the biomechanical models of complex joints, such as the spine, has presented an obstacle in estimating the joint reaction forces during simulation of the recreational or occupational physical activities. The lumbar spine is the most injury-prone region of the trunk during performance of manual material-handling tasks. Numerous biomechanical models for estimation of joint reaction forces in the spine have been developed. In the absence of any gold standard, one is unable to determine the accuracy and validity of these models. Earlier attempts to solve the problem simplified the role of muscles by grouping them into synergistic groups (i.e., flexor and extensor muscles) while carrying out the free-body analysis after passing an imaginary plane at a specificed level (i.e., L5/S1). This allowed the number of equations and unknowns to become identical so one could obtain the unique solution to the muscle forces and subsequently the net joint reaction forces. In these models the contribution of passive tissues in equilibrating moments of the external loads were ignored.

The second mathematical modeling approach reformulated the equilibrium conditions in terms of linear or nonlinear programming problems. The key motivation was that there may be a cost (objective) function that could be minimized while satisfying the equilibrium conditions (equality constraints) and keeping the muscle forces greater than zero and less than some maximum forces corresponding to the maximum allowable stress in the muscles (inequality constraints). Various linear and nonlinear cost functions have been used, such as compression, shear reaction forces, and sum of muscle stresses to different powers. Parnianpour et al. [147] investigated the effects of cost functions and the anatomical models utilized in equilibrium-based optimization models on the estimated joint reaction forces and maximum strength at upright posture. To test the effect of anatomical databases used in the prevalent biomechanical models, we selected the following six models from the literature: (1) Hughes et al. [148]; (2) Hughes and Chaffin [149]; (3) Marras and Granata [150]; (4) Thelen et al. [151]; (5) Schultz et al. [152]; and (6) Nussbaum et al. [153]. Although this list is by no means exhaustive, it should reveal the considerable variations among the models. In solving the constrained system satisfying the equilibrium conditions, the following cost (objective) functions have been minimized: (1) sum of muscle forces, (2) sum of muscle stresses; (3) sum of squared muscle stresses; (4) sum of cubed muscle stresses; (5) compressive component of the joint reaction force; and (6) modulus of the joint reaction force (its Euclidean norm). Twenty-four complex loading conditions were simulated, ranging from combinations of –30 Nm to +30 Nm of sagittal, lateral, and axial moments. The external loads were selected from the lower range of feasible values in order to minimize the chance of underestimating the joint reaction force,

due to the co-activity of muscles at higher exertion levels. Equilibrium-based optimization models that have been used in this study do not predict the experimentally observed co-activation at high exertion levels. A MATLAB optimization toolbox was used to solve the constrained (linear or nonlinear) optimization problems. A total of 864 models (24 external loads × 6 models × 6 cost functions) were solved numerically. The multivariate analysis of variance (MANOVA) was used to test the main and interaction effects of anatomical models and cost function on the predicted joint reaction forces.

The maximum allowable muscle stress was kept constant for all the models at 55 N/cm^2. The predicted maximum isometric strength at upright posture for different models ranged from 54 to 163 Nm for flexion, 104 to 351 Nm for extension, 109 to 240 Nm for right lateral bending, and 57 to 266 Nm for right axial rotation. The differences between models led to substantial variation in the predicted strength and joint reaction forces. For example, in a complex loading condition of 30 Nm of flexion, right lateral and axial moments, using the second cost function, the predicted compression forces ranged from 410 N to 1153 N, while the anterior-posterior shear forces ranged from –254 N to 76 N. The statistical analysis of the 24 loading conditions indicated that the effect of each model on joint reaction forces was statistically significant based on MANOVA ($p < 0.001$). While a technological breakthrough is needed to directly measure the internal muscle forces, the relative accuracy and consistency among these models deserve more attention.

The optimization algorithms provide mathematical solutions to the apparent redundancy. It has been recognized that, while based on the above analysis, the number of muscles spanning the joint at a given spinal level may outnumber the equilibrium conditions. The need to equilibrate the moments along the spinal column and satisfy the stability requirements may shed light on the presence of such apparent redundancy. By having these additional muscles, the central nervous system can stabilize the joint by an appropriate co-activation strategy while providing the net muscular moment needed to balance the external loads. Based on this principle, we have shown that by augmenting the equilibrium-based models with the stability constraints, the co-activation patterns of muscle recruitment could be predicted. This has significant implication in light of the criticism against the equilibrium-based optimization models that have failed to predict the presence of co-activation seen experimentally as measured by electromyography (EMG). In the course of formulating the stability conditions, one also realizes that muscles are not just simply force actuators to be represented by force vector, but their viscoelasticity (both the passive and active components) must be included in the models, especially those concerned with dynamic activities.

The third class of models has evolved to eliminate the need to use the optimization approach, which has been criticized for these three major shortcomings: (1) inability of the optimization-based approaches to predict the coactivation, (2) the lack of physiological basis for the assumption that the CNS uses an optimization approach to solve the distribution of loads among its actuators, and the arbitrary selection of the cost function, and (3) the deterministic nature of optimization-based recruitment predictions despite the presence of inter- and intra-individual variability in performance as observed by the EMG studies. In light of these criticisms, the use of processed EMG from trunk muscles has been advocated to drive the "biological-based models" of the trunk. Despite the controversy existing regarding the nature of linear or nonlinear relations between muscle force and EMG, and the difficulty in relating the force and EMG under dynamic conditions, a number of EMG-driven models have evolved.

Without covering much of the details, the following limitations in the assumptions of EMG-assisted models are identified. The concept of maximum allowable muscle stress has tremendous consequence in the algorithms for estimating the muscle forces based on normalized EMG. Strength or MVE assessment is a psychophysical phenomenon and not a material property independent of volitional influences. Extreme caution is warranted in relating the force generation during MVE to maximum allowable muscle force based on maximum allowable muscle stress. The maximum exertion solicited from subjects is often about joint axes in the cardinal planes of motion. However, lines of action of muscles are very complex and their functions are highly coupled. Therefore, instructing the subject to perform maximum exertion in the cardinal plane may not cause the maximum muscle force in all the muscles. The complex line of actions of muscle and dynamic constraints acting on the controller to safeguard the integrity of the

structure may preclude maximum observable activation of muscles during the MVE set used for calibration of the model. Should we treat all muscles the same by assigning them similar gains or should we have muscle-specific gains in our models? The answer to this question forces us to consider the nature of these models. The multicollinearity due to high correlations between some of the muscle activities precludes us from obtaining good estimates of muscle-specific gains. Recently, principal component regression and Ridge regression have been suggested to address this issue.

We have recently proposed a novel hybrid modeling approach using finite element analysis of the spine including muscles [139]. The unknown muscle forces are determined utilizing a number of kinematic constraints with or without an optimization approach. In this manner, the equilibrium of internal and external forces, structural stability, and input kinematic conditions are all respected simultaneously. It is our conjecture that this may be the most accurate method available to us short of the direct measurement of internal forces invasively. Complex finite element models of the lumbar and thoracolumbar spines including active and passive components are currently used to study the postural stability of the torso in short-term and prolonged neutral positions. An advantage of these models is in using the kinematic data as constraint equations in which we have reasonable confidence. The kinematic-based modeling approach is based on a hybrid formulation that provides the model with some input displacements that constrain the spinal deformation under external loading and muscle exertions. It seems that this latter approach has the most promising potential in providing realistic bounds on the internal stresses and strains in the constitutive elements. The next level of improvement in kinetic modeling is expected to combine the strength of each of the three methods (optimization-, EMG-driven-, and kinematic-based FE approaches) and to cross-validate the results across the paradigms.

1.11 Future Directions

The modeling approach taken by our group has been to develop a series of modular models that are step by step incorporated to construct more realistic models required for accurate analysis of the biomechanics of the neuromusculoskeletal spinal system. The understanding gained based on less sophisticated models is continuously used in subsequent steps when dealing with more improved and complex models. The preceding sections have covered some of these applications on the effect of combined loadings, bone compliance, annulus modeling, facet articulation, and nucleus fluid content on the spinal response. These models have been and are currently applied for the identification of influence of spinal posture, structural alterations, remodeling, progressive failure, and impairment or performance degradation of active and passive components of the system due to repetitive submaximal or prolonged loadings on the spinal behavior. The proper incorporation of active components and stabilizing mechanisms, dynamics of degenerative processes, remodeling, and progressive failure, time-dependent characteristics, material constitutive relations and failure mechanisms, appropriate boundary conditions, various couplings and nonlinearities, and individualization of geometry and material properties are some challenges facing the current and future finite element model studies of the human spine.

It is intended that the collective set of models could provide the analytical tools for identifying injury mechanisms of spine and hypothesis testing of relevant clinical, biomechanical, and industrial medicine theories. Our models have stressed both the analysis and synthesis of movement and loading conditions with the hope that these could aid a multidisciplinary team to design an environment with a reduced risk of injury and disability.

Acknowledgments

The authors would like to acknowledge M. Kasra, M. Argoubi, C. Breau, A. Kiefer, P. Sparto, and J.L. Wang for having contributed to some parts of our studies presented in this work. The financial support of the Natural Sciences and Engineering Research Council of Canada (NSERC-Canada) and NIDRR, REC (grant #H133E30009) is also gratefully acknowledged.

References

1. J. Frymoyer, The Lumbar Spine. W.B. Saunders (1996): 8-15.
2. A. Nachemson, W.O. Spitzer et al., Spine 12 (Suppl. 1) (1987): S1-S59.
3. B. Webster, and S.H. Snook, Spine 19 (1994): 1111-1116.
4. J. Frymoyer and W. Cats Baril, Orthop. Clin. North Am. 22 (1991): 263-271.
5. T.B. Leamon, Industrial Ergonomics 13 (1994): 259-265.
6. M. Parnianpour and A. Engin, J. Rheum. Med. Rehab. 3 (1994): 114-122.
7. M. Parnianpour, F.J. Beijani, and L. Pavlidis, Ergonomics 30 (1987): 331-334.
8. M. Battie, Doctoral Dissertation, Gothenburg (1989).
9. P. Bongers, C. de Winter, M. Kompier, and V. Hildebrandt, Scand. J. Work. Environ. Health 19 (1993): 297-312.
10. J. Frymoyer, M.H. Pope, J.H. Clements, D.G. Wilder et al., J. Bone Joint Surgery 65-A (1983): 213-218.
11. D.K. Damkot, M.H. Pope, J. Lord, and J. Frymoyer, Spine 9 (1984): 395-399.
12. J. Troup, J. Martin, and D. Lloyd, Spine 6 (1981): 61-69.
13. M. Parnianpour, M. Nordin, N. Kahanovitz, and V. Frankel, Spine 13 (1988): 982-992.
14. S.A. Goldstein, T.J. Armstrong, D.B. Chaffin, and L.S. Matthews, J. Biomech. 20 (1987): 1-6.
15. T. Videman, H. Rauhala, S. Asp et al., Spine 14 (1989): 148-156.
16. S.J. Bigos, D.M. Spengler, and N.A. Martin, Spine 11 (1986): 246-256.
17. A. Burdorf, Scand. J. Work Environ. Health 18 (1992): 1-9.
18. L. Punnet, L.J. Fine, W.M. Keyserling, G.D. Herrin et al., Scand. J. Work Environ. Health 17 (1991): 337-346.
19. W.S. Marras, S.A. Lavender, S.E. Leurgans, F.A. Fathallah et al., Ergonomics 38 (1995): 377-410.
20. F. Fathallah, Doctoral Dissertation, The Ohio State University, Columbus, Ohio (1995).
21. T. Hansson, Seminars in Spine Surgery 4 (1992): 12-15.
22. R. Huiskes and E.Y.S. Chao, J. Biomech. 16 (1983): 385-409.
23. T.B. Belytschko, R.F. Kulak, A.B. Schultz, and J.D. Galante, J. Biomech. 7 (1974): 277-285.
24. R.F. Kulak, T.B. Belytschko, A.B. Schultz, and J.O. Galante, J. Biomech. 9 (1976): 377-386.
25. H.S. Lin, Y.K. Liu, G. Ray, and P. Nikravesh, J. Biomech. 11 (1978): 1-14.
26. B.R. Simon, J.S.S. Wu, M.W. Carlton et al., Spine 10 (1985): 494-507.
27. R.L. Spilker, D.M. Daugirda, and A.B. Schultz, J. Biomech. 17 (1984): 103-112.
28. A. Shirazi-Adl, S.C. Shrivastava, and A.M. Ahmed, Spine 9 (1984):120-134.
29. A. Shirazi-Adl, J. Biomech. 22 (1988): 357-365.
30. M. Kasra, A. Shirazi-Adl, and G. Drouin, Spine 17 (1992): 93-102.
31. A. Shirazi-Adl, Spine 17 (1992):206-212.
32. A. Shirazi-Adl, Spine 16 (1991): 533-541.
33. A. Shirazi-Adl, A.M. Ahmed, and S.C. Shrivastava, J. Biomech. 19 (1986):331-350.
34. A. Shirazi-Adl and G. Drouin, J. Biomech. 20 (1987):601-613.
35. A. Shirazi-Adl and G. Drouin, J. Biomech. Eng. 110 (1988):216-222.
36. K.H. Yang and A.I. King, Spine 9 (1984): 557-565.
37. K. Ueno and Y.K. Liu, J. Biomech. Eng. 109 (1987): 200-209.
38. V.K. Goel, J.M. Winterbottom, J.N. Weinstein, and Y.E. Kim, J. Biomech. Eng. 109 (1987): 291-297.
39. J.L. Wang, Ph.D. Dissertation, The Ohio State University, Columbus, Ohio (1996).
40. M. Argoubi and A. Shirazi-Adl, J. Biomech. 29 (1996): 1331-1339.
41. V.K. Goel, Y.E. Kim, T.H. Lim, and J.N. Weinstein, Spine 13 (1988): 1003-1011.
42. Y.E. Kim, V.K. Goel, J.E. Weinstein, and T.H. Lim, Spine 16 (1991): 331-335.
43. C. Breau, A. Shirazi-Adl, and J. deGuise, Ann. Biomed. Eng. 19 (1991): 291-302.
44. A. Shirazi-Adl and M. Parnianpour, Spine 18 (1993): 147-158.
45. A. Shirazi-Adl, J. Biomech. 27 (1994): 289-299.
46. A. Shirazi-Adl, Spine 19 (1994): 2407-2414.

47. A. Shirazi-Adl and M. Parnianpour, J. Spinal Dis. 9 (1996): 277-286.
48. F. Lavaste, W. Skalli, S. Robin et al., J. Biomech. 25 (1992): 1153-1164.
49. V.K. Goel, H. Park, and W. Kong, J. Biomech. Eng. 116 (1994): 377-383.
50. A. Shirazi-Adl, Computational Methods in Bioengineering (American Society of Mechanical Engineers, New York, 1988), pp. 449-460.
51. A. Shirazi-Adl, Advances in Bioengineering (American Society of Mechanical Engineers, New York, 1990), pp. 257-260.
52. A. Shirazi-Adl, Transactions (Orthopaedic Research Society, Chicago, 1991) 16:241.
53. A. Shirazi-Adl, A.M. Ahmed, and S.C. Shrivastava, Spine 11 (1986): 914-927.
54. A. Shirazi-Adl, Spine 14 (1989): 96-103.
55. A. Shirazi-Adl, J. Biomech. Eng. 116 (1994): 408-412.
56. A.B. Schultz, D.N. Warwick, M.H. Berkson, and A.L. Nachemson, J. Biomech. Eng. 101 (1979): 46-52.
57. K.L. Markolf, J. Bone Joint Surg. 54A (1972): 511-533.
58. M.A. Adams and W.C. Hutton, Spine 6 (1981): 241-248.
59. H.F. Farfan, J.W. Cossette, G.H. Robertson et al., J. Bone Joint Surg. 52A (1970): 468-497.
60. R.B. Dunlop, M.A. Adama, and W.C. Hutton, J. Bone Joint Surg. 66B (1984): 706-710.
61. A.F. Tencer, A.M. Ahmed, and D.L. Burke, J. Biomech. Eng. 104 (1982): 193-201.
62. J.M. Cavanaugh, A.C. Ozaktay, H.T. Yamashita, and A.I. King, J. Biomech. 29 (1996): 1117-1129.
63. A.A. El-Bohy, K.H. Yang, and A.I. King, J. Biomech. 22 (1989): 931-941.
64. Y.E. Kim, V.K. Goel, J.E. Weinstein, and T.H. Lim, Spine 16 (1991): 331-335.
65. M. Lorenz, A. Patwardhan, and R. Vanderby, Spine 8 (1983): 122-130.
66. M. Sharma, N.A. Langrana, and J. Rodriguez, Spine 20 (1995): 887-900.
67. H. Farfan and J.D. Sullivan, Can. J. Surg. 10 (1967): 179-185.
68. A.M. Ahmed, N.A. Duncan, and D.L. Burke, Spine 15 (1990): 391-401.
69. F.R. Murtagh, R.D. Paulsen, and G.R. Rechtine, J. Spinal Dis. 4 (1991): 86-89.
70. T.P. Andriacchi, R.P. Mickosz, S.J. Hampton, and J.O. Galante, J. Biomech. 16 (1983): 23-29.
71. R. Crowinshield, M.H. Pope, and R.J. Johnson, J. Biomech. 9 (1976): 397-405.
72. M. Panjabi, J. Biomech. 6 (1973): 671-680.
73. M.Z. Bendjaballah, A. Shirazi-Adl, and D.J. Zukor, The Knee 2 (1995): 69-79.
74. M.Z. Bendjaballah, A. Shirazi-Adl, and D.J. Zukor, J. Clin. Biomech., submitted.
75. G.A. Dannucci, R.B. Martin, and C.E. Cann, Transactions (Orthopaedic Research Society, Chicago, 1988), 34:227.
76. S.P. Richardson, A. Winick, and J. Black, Transactions (Orthopaedic Research Society, Chicago, 1986), 32:462.
77. C.B. Ruff, H. Spurgeon, C.S. Lauderbaugh, and G.R. Smith, Transactions (Orthopaedic Research Society, Chicago, 1989), 35:120.
78. T.H. Hansson, T.S. Keller, and D.M. Spengler, J. Spinal Dis. 5 (1987): 479-487.
79. S.M. Bowman, T.M., Keaveny, L.J. Gibson et al., J. Biomech. 27 (1994): 301-310.
80. B.M. Cyron and W.L. Hutton, Spine 4 (1979): 163-167.
81. T. Morita, T. Ikata, S. Katoh, and R. Myake, J. Bone Joint Surg. 77-B (1995): 620-625.
82. M. Dietrich and P. Kurowski, Spine 10 (1985): 532-542.
83. M.H. Pope, M. Svensson, H. Broman, and G.B.J. Andersson, J. Biomech. 19 (1986): 675-677.
84. T. Steffen, R. Rubin, J. Antoniou et al., Transactions (Orthopaedic Research Society, Chicago, 1995), 41:656.
85. G.B.J. Andersson and A.B. Schultz, J. Biomech. 12 (1979): 453-458.
86. V.K. Goel, S. Goyal, C. Clark et al., Spine 10 (1985): 543-554.
87. M.M. Panjabi, M.H. Krag, and T.Q. Chung, Spine 9 (1984): 703-713.
88. R.E. Seroussi, M.H. Krag, D.L. Muller, and M.H. Pope, J. Orthop. Res. 7 (1989): 122-131.
89. D.L. Spencer, J.A.A. Miller, and A.B. Schultz, Spine 10 (1985): 555-561.
90. A. Nachemson, Spine 6 (1981): 93-97.

91. D.S. McNally and M.A. Adama, Spine 17 (1992): 66-73.
92. L.M. Jonck, J. Bone Joint Surg. 43-B (1961): 362-375.
93. S.J. Lipson and H. Muir, Spine 6 (1981): 194-210.
94. B. Vernon-Roberts and C.J. Pirie, Rheumatol. Rehab. 16 (1977): 13-21.
95. P.M. Waters and S.J. Lipson, J. Spinal Dis. 1 (1988): 81-85.
96. A. Shirazi-Adl and S.C. Shrivastava, Comput. Struct. 34 (1990): 225-230.
97. ABAQUS, Theory and User's Manual (Hibbit, Karlsson & Sorensen, Inc., 1989), Version.
98. J. Soulhat, Master's Thesis, in preparation, Ecole Polytechnique, Montreal, Quebec, Canada.
99. G.B.J. Andersson, Spine 6 (1981): 53-60.
100. J.L. Kelsey and A.A. White, Spine 5 (1980): 133-142.
101. J. Sandover, Spine 8 (1983): 652-658.
102. J.A.E. Eklund and E.N. Corlett, Spine 9 (1984): 189-194.
103. A. Sullivan and S.M. McGill, Spine 15 (1990): 1257-1260.
104. M. Mangusson, M. Almqvist, H. Broman et al., J. Spinal Dis. 5 (1992): 198-203.
105. M. Panjabi, G.B.J. Andersson, L. Jorneus et al., J. Bone Joint Surg. 68-A (1986): 695-702.
106. M.H. Pope, T. Broman, and T. Hansson, J. Spinal Dis. 3 (1990): 135-142.
107. M.A. Adams and W.C. Hutton, Spine 8 (1983): 665-671.
108. W. Koeller, F. Funke, and F. Hartmann, Biorheology 21 (1984): 675-686.
109. L.E. Kazarian, Orthop. Clin. North Am. 6 (1975): 3-18.
110. L.E. Kazarian, Acta Orthop. Scand. Suppl. 146 (1972).
111. K.L. Markolf, Proceedings of Workshop on Bioengineering Approaches to Problems of the Spine (1970): 87-143.
112. T.S. Keller, D.M. Spengler, and T.H. Hansson, J. Orthop. Res. 5 (1987): 467-478.
113. S. Li, Doctoral Dissertation, University of Illinois at Chicago (1994).
114. S. Li, A. Patwardhan, F. Amirouche et al., J. Biomech. 28 (1995): 779-790.
115. M.A. Adams and P. Dolan, Clin. Biomech. 11 (1996): 194-200.
116. A. Lamer, A. Shirazi-Adl, G. Drouin, and G. McIntyre, Transactions (Orthopaedic Research Society, Chicago, 1987), 12:430.
117. N.S. Hakim and A.I. King, J. Biomech. 12 (1979): 277-292.
118. A. Natali and E. Meroi, J. Biomech. Eng. 112 (1990): 358-363.
119. J.F. Laible, D. Pflaster, M.H. Krag et al., Spine 18 (1993): 659-670.
120. J. Urban and A. Maroudas, Instn. Mech. Eng. 2 (1980): 63-69.
121. J. Styf, Spine 12 (1987): 675-679.
122. K. Takahashi, T. Miyazaki, T. Takino et al., Spine 20 (1995): 650-663.
123. R.D. Crowinshield and M.H. Pope, J. Trauma 16 (1976): 99-105.
124. F.R. Noyes and E.S. Grood, J. Bone Joint Surg. 58-A (1976): 1074-1082.
125. P. Neumann, T.S. Keller, L. Ekstrom, and T. Hansson, Spine 19 (1994): 205-211.
126. A.L. Osvalder, P. Neumann, P. Lovsund, and A. Nordwall, J. Biomech. 26 (1993): 1227-1236.
127. M.A. Adams and T.P. Green, Eur. Spine J. 2 (1993): 203-208.
128. T.P. Green, M.A. Adams, and P. Dolan, Eur. Spine J. 2 (1993): 209-214.
129. S.M. Bowman, T.M. Keaveny, L.J. Gibson, W.C. Hayes et al., J. Biomech. 27(1994): 301-310.
130. M.B. Schaffler, E.L. Radin, and D.B. Burr, Bone 10 (1989): 207-214.
131. J.L. Wang, A. Shirazi-Adl, A.E. Engin, and M. Parnianpour, 2nd Biennial European Joint Conference on Engineering Systems Design & Analysis, London, England, ESDA 4 (1994): 177-182.
132. J.L. Wang, A. Shirazi-Adl, A.E. Engin, S. Li et al., Advances in Bioengineering ASME (1994): 49-50.
133. J.L. Wang, A. Shirazi-Adl, A.E. Engin, S. Li et al., Advances in Bioengineering ASME (1995): 19-20.
134. J.L. Wang, A. Shirazi-Adl, A.E. Engin, and M. Parnianpour, Advances in Bioengineering ASME (1995)19-22.
135. J.L. Wang, A. Shirazi-Adl, M. Parnianpour, and A.E. Engin, Annals of Biomed. Eng. 23(Supp.1) (1995): S-114.

136. J.L. Wang, A. Shirazi-Adl, M. Parnianpour, and A.E. Engin, 3rd Biennial European Joint Conference on Engineering Systems Design & Analysis, Montpellier, France, ESDA 5 (1996): 51-56.
137. J.J. Crisco and M. Panjabi, Spine 16 (1991): 793-808.
138. A. Shirazi-Adl and M. Parnianpour, J. Biomech. Eng. 118 (1996): 26-31.
139. A. Kiefer, A. Shirazi-Adl, and M. Parnianpour, Euro. J. Spine, in press (1996).
140. Y.K. Liu and J.K. Wickstrom, Perspectives in Biomedical Engineering (MacMillan, New York, 1973), pp. 203-213.
141. D.J. Pearsall, Doctoral Thesis, Queen's University, Kingston, Ontario, Canada (1994).
142. S. Gracovetsky, The Spinal Engine (Springer-Verlag, New York, 1988).
143. M. Parnianpour, A. Shirazi-Adl, H. Hemami, and P. Quesada, Proceedings (12th Triennial Congress of the International Ergonomics Association, 1994), pp. 119-121.
144. G. Vanneuville, J.M. Garcier, G. Poumarat et al., Surg. Radiol. Anat. 14 (1992): 29-33.
145. K. Kroemer, H. Kroemer, and K. Kroemer-Elbert, Ergonomics (Prentice-Hall, Englewood Cliffs, 1994), pp. 1291-299.
146. R.P. Jackson and A.C. McManus, Spine 19 (1994): 1611-1618.
147. M. Parnianpour, A. Shirazi-Adl, J.L. Wang, H.J. Wilke et al., 3rd Biennial European Joint Conference on Engineering Systems Design & Analysis, Montpellier, France, ESDA 5 (1996): 63-67.
148. R.E. Hughes, J.C. Bean, and D.B. Chaffin, J. Biomech. 28 (1995): 875-878.
149. R.E. Hughes and D.B. Chaffin, J. Biomech. 28 (1995): 527-533.
150. W.S. Marras and K.P. Granata, Spine 20 (1995): 1440-1451.
151. D.G. Thelen, A.B. Schultz, S.D. Fassois, and J.A. Ashton-Miller, J. Biomech. 27(1994): 907-919.
152. A.B. Schultz, G.B. Andersson, R. Ortengren, K. Haderspeck et al., J. Bone Joint Surg. 64-A (1982): 713-720.
153. M.A. Nussbaum, D.B. Chaffin, and C.J. Rechtien, J. Biomech. 28 (1995): 401-409.

2

Finite Element Modeling of Embryonic Tissue Morphogenesis

David A. Clausi
University of Waterloo

G. Wayne Brodland
University of Waterloo

The intriguing shape changes that occur as embryos develop have been studied extensively from a biological perspective. However, from a mechanical standpoint, many questions remain concerning the source, magnitude, and timing of the driving forces. These forces originate within individual cells and cause sheets of cells to deform to produce organs and other essential structures. Finite element-based computer simulations make it possible to investigate which of the various possible driving forces actually operates to produce specific shape changes. They make it possible to investigate questions about the magnitude and duration of the driving forces, how variations in driving forces or initial geometries affect the shapes of the resulting structures, and what control mechanisms are present.

Although computer simulations of a variety of morphogenetic processes will be surveyed, this contribution will focus on a process called neurulation. During neurulation a sheet of cells called the neural plate rolls up to form the neural tube, a sealed tube which is the precursor of the spinal cord and brain. Finite element simulations show that the *sequence* of specific shape changes characteristic of neurulation can be produced by contraction of structural components called microfilaments and by elongation of a structure called the notochord, which underlies the neural plate. As the plate changes shape, the microfilaments act on a structure that has a new geometry and produce a different incremental, global effect than they did in the original configuration. Thus, the sequence of shape changes characteristic of neurulation is produced by mechanical interaction or feedback between the current geometry and the internal force generators.

Current finite element simulations provide an important step toward the development of "virtual embryos" in which virtual experiments might be carried out. They also make an important contribution to the development of numerical methods that overcome the significant technical challenges inherent in the modeling of embryo morphogenesis.

2.1 Introduction

The development of a fetus from a single cell, a fertilized egg, requires the successful completion of a sequence of elegant and highly specific processes (Alberts et al., 1989). These processes include cell proliferation, a repeated and controlled series of cell divisions necessary to produce the trillions of cells found in a normal fetus. Each mitosis requires the self-assembly, operation, and self-disassembly of complex biomechanical structures which are governed by finely tuned control systems. Cell differentiation, an intriguing process whereby cells become functionally different from each other, also occurs repeatedly to produce an embryo that has several hundred kinds of cells. Another critical process in embryogenesis is the occurrence of a succession of highly specific shape changes. These critical shape changes give rise to organs and other critical structures. Morphogenesis, literally the "the genesis of form," includes all three of these essential behaviors and the control mechanisms that govern them.

From species to species, striking similarities exist in these processes. These have led some to postulate a common evolutionary ancestry and others a commonality of design. From a practical standpoint, these similarities allow scientists to make qualified inferences about morphogenetic and physiological processes in humans based on studies of parallel processes in vertebrates ranging from apes and axolotls, species in which various interventions can be carried out more easily and legitimately.

The advent of realistic computer simulations provides another important means to investigate aspects of human development, including the mechanisms of normal development and the causes of malformation-type defects. Such simulations also provide a new focus, as suggested by Koehl (1990):

> Therefore, as we try to unravel the mechanisms responsible for the genesis of form in developing embryos, it is crucial that we complement the popular molecular and biochemical approaches to the control of morphogenesis with nuts-and-bolts analyses of the physics of how morphogenetic processes occur.

The purpose of this work is to investigate ways in which computer simulations can be used to investigate the physics of morphogenesis, outline principles that must be followed in the formulation of simulations, review some recent simulations, and discuss reasons that simulations can be expected to become increasingly important to the field of morphogenesis.

2.2 Modeling of Morphogenesis

Perhaps the most important role of modeling at present is to test hypotheses about developmental processes. When the factors thought to be important to a certain process are incorporated into a soundly formulated computer model, the output of the model often shows whether or not the initial understanding is correct and complete. Initial simulations usually indicate that less is known about the physical problem than was originally thought. Computer modeling can also serve as a reliable adjudicator for distinguishing between what is a good idea and what is actually true. Simulations of neurulation, for example, have demonstrated clearly that not every plausible idea produces shape changes that match those that occur in real embryos. Fortunately, in simulation studies, the differences between the model behavior and the behavior of the real system often provide clues regarding the area of misunderstanding.

It is important to note that just because a simulation produces output that matches the corresponding real data does not guarantee that the model or input parameters are correct. This is especially true of phenomenological models, that is models that are not based exclusively on known physical properties and principles.

Computer models also allow sensitivity analyses to be carried out to investigate the effect of changing particular parameters or boundary conditions (Brodland and Clausi, 1994). Furthermore they provide an engine that can be used to solve so-called inverse problems. For example, in the neural plate, many structures that are known to generate forces in other contexts are present. To determine which structures actually act and produce the observed sequence of shape changes is a kind of inverse or, more specifically, parameter estimation problem (Beck, 1977).

Simulations provide a common point of focus for studies of embryo mechanics. They do this in part by forcing discoveries to be expressed in a quantitative fashion so they can be either incorporated into or used to test simulations. Koehl (1990) writes: "I stress the importance of formulating theories quantitatively, and of measuring the mechanical properties of embryonic tissues and the forces exerted during morphogenetic events." Simulations also require that relationships be established between commonly agreed-on quantities, so that one study might relate quantities A and B, another A and C, and another B, C, and D. Often, significant gaps in understanding are revealed simply by attempting to write the relationships (and interactions) between governing quantities in a form suitable for numerical modeling.

Computer simulations probably will soon be used to increase the confidence level of inferences between species. Consider, for example, a shape change such as neurulation, which occurs in both humans and axolotls. Although the subcellular structures that drive it appear to be common to both, the geometries of the two systems have significant differences. That differences in initial shape can profoundly affect subsequent shapes produced by a given set of forces and constraints is well known in mechanics (Brodland and Cohen, 1989). Suppose that computer simulations based on actual physical properties and known physical processes can be devised and verified in detail using axolotl embryos. Such verification might include comparisons over time between three-dimensional shapes produced in simulated and real embryos. It might also include similar comparisons with teratogen-treated and surgically altered embryos. Confidence can then be gained in the validity of the theoretical formulation, material properties, and other input parameters used, and in the software implementation. More confidence can then be realized when the same software is used to simulate similar aspects of normal or perturbed human embryogenesis, where the data is significantly more sparse.

It is reasonable to expect that subsequent generations of computer simulations will embrace a broader range of relevant phenomena. For example, mechanical, biochemical, and electrical behaviors and their interactions might be simulated. In addition, simulations will likely progress in terms of the smallest scale explicitly incorporated: from tissue to cell to subcellular to molecular and perhaps even to atomic level (Brodland, 1997). Although molecular level studies of entire embryos seem unlikely in the foreseeable future, molecular aspects of particular processes may be studied and subsequently embodied as constitutive-type equations that accurately describe in bulk or continuum terms the behaviors of large systems of molecules. Unlike present estimates of bulk behavior, these would be founded on and would accurately embody the molecular phenomena.

To date, most biomechanical modeling has focused on two morphogenetic processes: gastrulation and neurulation (Brodland, 1997). These have received attention because the shape changes associated with these processes could be observed and because they appeared to be reasonably straightforward mechanically. Both have turned out to be more intriguing and elegant than originally thought. Here, we will focus on the process of neurulation, since it is the process which to date has received the most attention and yielded the broadest insights.

2.3 The Process of Neurulation

The three-dimensional shape changes that are a critical part of the process of neurulation have intrigued researchers for millennia. Intensive research during the last 100 years (His, 1874; Roux, 1888; Lewis, 1947; Jacobson, 1978; Lee and Nagele, 1988; Schoenwolf and Smith, 1990; Clausi and Brodland, 1993; Brodland and Clausi, 1995) has identified the kinematics of the shape changes and revealed the morphology and mechanical properties of various structures in and around the neural plate which might

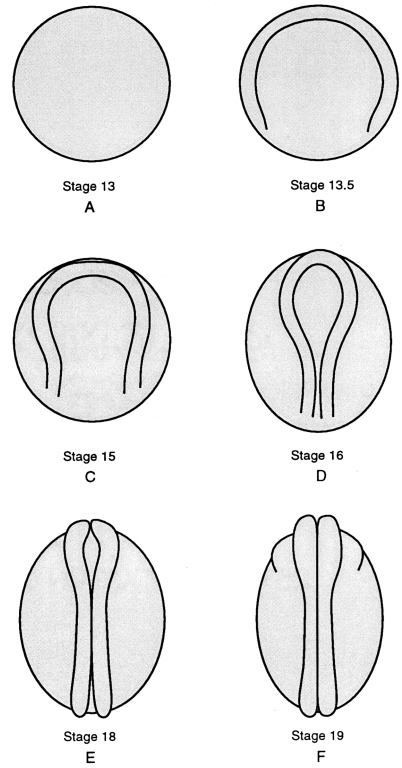

FIGURE 2.1 The process of neurulation. A: At the beginning of neurulation the embryo is a hollow ball. B: Neural ridges form. C: With time the ridges become more prominent and move toward the midline of the embryo. D-F: The ridges contact and fuse to form a sealed neural tube. After Brodland (1997).

drive these shape changes. Many theories have arisen to explain how various combinations of force generators, regulated by certain control mechanisms, might drive neurulation shape changes (Gordon, 1985). The advent of reliable computer simulations has made it possible to identify which of these theories makes mechanical sense and which does not (Clausi and Brodland, 1993; Brodland and Clausi, 1995).

Gross Shape Changes

During neurulation, a sheet of cells called the neural plate rolls up to form a sealed tube called the neural tube (Fig. 2.1). The cephalic end of this tube (the upper part of each figure) becomes the precursor of the brain, while the dorsal and caudal parts become the spinal cord. Figure 2.1 shows developmental Stages 13 through 19 of the axolotl (*Ambystoma mexicanum*). Neurulation in other vertebrates, especially amphibians, is very similar. Axolotl embryos are approximately 2.5 mm in diameter during neurulation.

At the onset of neurulation (Stage 13), the embryo is basically a hollow sphere with an outer layer comprised of a few thousand cells. The cells at the top of the embryo thicken and form a flat surface known as the neural plate. An indentation (neural groove) develops along the dorsal midline of the embryo. At the edge of the neural plate, ridges (neural folds or ridges) begin to appear (Stage 13.5). With time, the neural folds become more pronounced, rise, and bend toward each other. Meanwhile, in-plane motions cause the plate to change from a disk shape to a keyhole shape (Stages 13.5 to 16). The wide section of the keyhole occurs at the cephalic end of the embryo where the brain will subsequently form. The neural ridges along the narrow part of the keyhole shape meet and fuse along the midline of the embryo to form the neural tube (Stages 17 to 19). These shape changes are remarkably symmetrical.

If any part of the tube fails to close and fuse, a serious birth defect may result. Openings in the dorsal or caudal regions of the tube give rise to spina bifida, a potentially serious defect in which the spinal cord may not develop properly in the unfused area. Partial paralysis and other serious health problems may result. If the cephalic part of the tube fails to close, anencephaly results. Infants with this condition do not live. Neural tube defects are known to be caused by environmental, nutritional, and genetic factors (Mutchinick, 1990; Werler, 1993). However, it is not known whether these factors give rise to a mechanical defect through a common pathway, or whether they work through different mechanisms. Because the defect is first manifested as a mechanical abnormality, researchers have focused on the mechanics of the process, and especially the structures that drive it. A better understanding of the mechanics of neurulation is expected to provide a basis for steps directed toward its prevention.

Cellular Contributions to the Observed Shape Changes

The gross shape changes outlined above are caused by coordinated shape changes in the cells that make up the neural plate and by shape changes in underlying tissues, most notably the notochord. These shape changes have been measured in detail for the *Taricha torosa*, a newt whose patterns of neurulation are very similar to those of the axolotl. During the early stages of *Taricha torosa* neurulation (Stages 13 to 15), the neural plate cells change shape from cuboidal to columnar. They change from an approximate height of 58 μm and diameter of 18 μm to a height of 94 μm and diameter of 14 μm (Burnside, 1973). From Stages 15 to 19, the apical ends of the cells continue to constrict until the cells are approximately 145 μm tall and have a strongly tapered or "bottle" shape with a typical apical diameter of 6 μm.

When this shape change occurs in a coordinated way between adjacent cells, the plate they form is caused to bend more and more sharply. Cells in some regions become more strongly tapered than others, creating regions of high transverse curvature known as hinge points (Schoenwolf and Smith, 1990). Contraction of cell apices also produces the in-plane motions noted above.

2.4 Force-Generating Structures

A typical cell contains many different mechanical structures (Alberts et al., 1989). The primary structures that are known to play a mechanical role in neurulation and other morphogenetic shape changes are shown in Fig. 2.2. These include microfilaments, microtubules, intermediate filaments, the cytoplasm, the plasma membrane, the notochord, and cell adhesion.

Microfilaments

Microfilaments, with a diameter of 5 to 7 nm each, are a principal contractile component not only of neural plate cells, but of most embryonic cells. In the neural plate and many other epithelial cell sheets, microfilament bundles form a ring just inside the apical end of each cell (Fig. 2.2). As they contract, they have a purse-string effect, causing the apical end of the cell to narrow. Because the volume of the cell is constant, as the apical end narrows, the cell must become taller, wider at its basal end, or a combination of both.

Burnside (1971, 1973) correlated the degree of apical constriction of the cells to the cross-sectional diameter of the apical microfilaments. Her measurements also showed that the average bundle width increased from 0.17 μm (±0.005 μm) to 0.32 μm (±0.006 μm) between Stages 13 and 19. Calculations indicated that the total volume complement of microfilaments remains constant from Stage 13 to Stage 19. Thus, the individual microfilaments apparently intercalate as the bundle shortens. If the stress σ remains constant (based on current cross-sectional area), the force F_M produced by a microfilament bundle would be expected to follow a relationship of

$$F_M = \sigma A_0 L_0 / L, \tag{2.1}$$

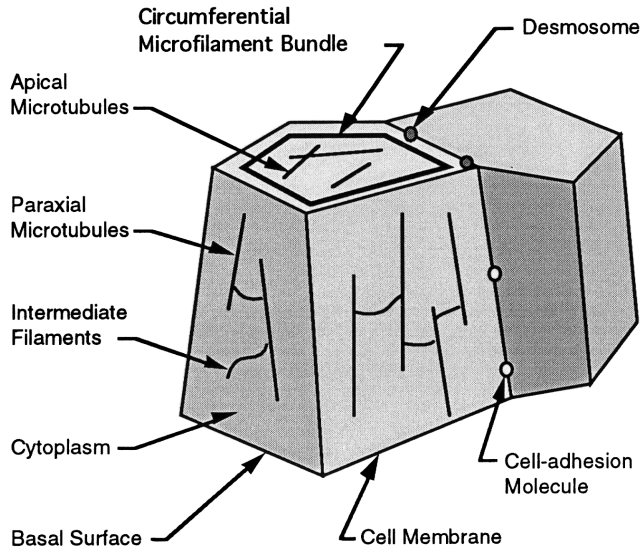

FIGURE 2.2 Structures known to be of mechanical importance to morphogenetic shape change. After Brodland (1997).

where A_0 is the initial cross-sectional area, L_0 is the initial length, and L is the current length.

What regulates microfilament contraction? Calcium ions are believed to activate microfilament contraction in a manner similar to smooth muscle (Alberts et al., 1989). Force in a microfilament bundle is assumed to be a function of its current cross-sectional area, which varies inversely with lengthening in order to maintain constant volume. Thus, as the microfilament bundle length decreases, its force magnitude increases. Microfilaments exist in adult epithelia and likely serve a variety of mechanical functions during the life of an animal (Ettensohn, 1985).

Microtubules

Microtubules (diameter of 24 nm and made of tubulin) are highly versatile organelles within the cell. At different times, they form the structures that produce chromosomal movements during mitosis, actively translocate particulate components of the cytoplasm, and maintain and change cell shape (Fawcett, 1981).

In neural plate cells, they occur as both apical mats and as paraxial elements that are oriented across the thickness of the neural plate (Fig. 2.2). The apical microtubules are randomly oriented in a plane parallel with and immediately below the apical cell surface (Burnside, 1971). These microtubules may affect cell shape by producing a constant outward force (Clausi and Brodland, 1993), thus opposing the action of microfilaments.

In contrast, paraxial microtubules may be partly responsible for cell elongation and for moving cytoplasm toward the basal end of cells to produce tapered or bottle-shaped cells. They might also push directly on the ends of the cell to produce elongation. In either case, it is apparent that intermediate filaments must provide lateral stability to the microtubules in order for them to buckle as they attempt to produce and carry these compressive loads (Brodland and Gordon, 1990).

Other Components in the Neural Plate

The material inside of the cell, exclusive of the nucleus, is called cytoplasm. The mechanical properties of cytoplasm in various biological systems have been measured by Hiramoto (1969a, b) and others. A meshwork of 10 nm diameter intermediate filaments runs through the cytoplasm. In addition to preventing the buckling of paraxial microtubules, they apparently give rise to the elastic component of cytoplasm.

Each cell is enclosed by a plasma membrane, which contains various channels that control entry of ions and other materials essential for regulating cytoskeletal components (Alberts et al., 1989). Structurally, this membrane is known to be weak. Thus, the plasma membrane is not considered an important mechanical component.

Cells have specialized structures for mechanically linking and communicating with adjacent cells. Desmosomes are button-like points of intercellular contact which provide strong connection sites for microfilaments (Burnside, 1971). Desmosomes act like rivets to transmit tensile and shearing forces within the neural plate.

Notochord

One of the key features of neurulation is elongation of the neural plate. This occurs in plates that have been excised from the rest of the embryo (Jacobson and Gordon, 1976). This elongation is driven largely by the notochord (Koehl, 1990). The notochord is a rod-like structure, approximately 80 μm in diameter, which is located immediately beneath the midline of the neural plate. Of the entire neural plate, the only cells that are attached at their basal ends are those above the notochord (Jacobson and Gordon, 1976). Notochord elongation also apparently causes the neural groove to form.

Cell–cell adhesions are important to certain kinds of morphogenetic movements (Nardi, 1981; Steinberg, 1996). However, their importance to neurulation is not clear.

Another mechanism that has been proposed as a driving force for neurulation is cortical tractoring (Jacobson et al., 1986). It postulates a flow of cytoplasm from the basal and lateral surfaces to the apical surface whereby membrane and adhesive structures would be carried and deposited where required. This phenomenon may also be referred to as cytoplasmic streaming. The authors argue that cortical tractoring explains thickening, invagination, and rolling of the neural plate. How such a process might be initiated at the right time and how it might be controlled is not clear. It may not be possible to evaluate the possible merits of this mechanism with certainty until computer simulations of the postulated subcellular cytoplasm movements are carried out.

Summary

A complete explanation for the shape changes that occur during neurulation has been elusive. Since neurulation occurs early in the development of an embryo with few cells and little if any cell specialization, it is likely that only a few mechanisms contribute to the shape changes. It seems unlikely that the behaviors of individual cells are somehow preprogrammed, although this was once a popular idea. Experiments have shown that neurulation and other morphogenetic processes are highly robust and synchronized and not easily perturbed by surgical and teratogenic interventions. The outcomes of these experiments strongly suggests that these morphogenetic movements are regulated by ongoing interactions between cells. In some cases, these interactions may be chemical or electrical. However, as we will show, mechanical interactions can be a powerful regulation device.

2.5 Simulations of Morphogenetic Processes

Computer simulations and other kinds of simulations play an important role in evaluating the mechanical validity of various theories about the forces that drive specific morphogenetic processes. Lewis (1947) constructed a physical model of the neural plate using brass plates hinged at their centers to a flexible spine, and tied to each of its neighbors by rubber bands. The lateral cell surfaces were represented by the plates, while the rubber bands acted as tension generators in the apical and basal ends. Different rubber band distributions produced different patterns of cell sheet folding. Practical considerations have limited the number of such physical simulation models. Fortunately, the rapid development of computers has made possible computer simulation models that are more accurate, realistic, and flexible than these early physical models.

Jacobson and Gordon (1976) constructed a mathematical model of "the formation of the neural plate based on different autonomous, preprogrammed schedules of shape changes for different regions of the neural ectoderm." In their model of in-plane motions, each cell had an autonomous program of shape change controlled by a cellular "clock" to synchronize the cell motion. Superposition showed that the coexistence of cell shrinkage and notochord extension produced normal in-plane shape changes. Using this model, they analyzed cell shrinkage without notochord extension and notochord extension without cell shrinkage (the latter test is not possible *in vivo*). That individual cells are preprogrammed to behave in such a manner is not a well-accepted notion. However, the model did illustrate that there are two separable aspects to the in-plane motions of the neurulation process. Jacobson (1980) subsequently addressed a number of related issues regarding computer simulations.

One of the first computer models, by Odell et al. (1981), presented "a mechanical model for the morphogenetic folding of embryonic epithelia based on hypothesized mechanical properties of the cellular cytoskeleton." Cells were modeled as two-dimensional quadrilaterals with hypothesized properties and contraction behaviors at the apex. These models demonstrated a possible two-dimensional folding process for the neural plate. In these models, the cell body is not modeled as a continuum, but by truss elements connected to opposite nodes of the quadrilateral. A limitation, acknowledged by Odell et al., is that their neural plate cells should not remain in the same vertical plane during neurulation, as assumed in this model, but should undergo a migration process. Another issue is the ratio of cell height to the radius of the embryo (3:1 instead of the actual 20:1). The model does, however, dramatically illustrate the possibility of modeling plate bending and rolling under the action of apical constrictions.

A few years later, Weliky and Oster (1990) simulated coordinated cell rearrangement by accounting for the balance of forces between adjacent cells. The net force at cell junctions is the difference between the passive elastic inward forces of the microfilament bundles and the osmotic plus hydrostatic pressure of the outward forces. Cell protrusion is produced when the net force is not zero. The finite difference method (a technique related to the finite element method) is used, and viscous behavior is included. The cells are treated as two-dimensional polygons; however, cell sliding may require understanding of the interactions along the entire length of the cell. No mention of absolute force magnitudes nor cell mechanical properties is included. The authors recognize that the "model is a simplification of the actual cellular machinery responsible for the generation of these forces, but we believe it captures the essential mechanical forces." The paper offers insight to relative cell motion caused by unbalanced forces at cell interfaces and to the node rearrangements required to simulate this behavior.

More recent computer simulations have made use of the finite element method (FEM). These include plausibility tests of aspects of neurulation (Jacobson et al., 1986) and studies of the mechanics of individual cells (Cheng, 1987a, b). The basis, formulation, and principal conclusions obtained using detailed FEM simulations of neurulation are extensive and are, therefore, discussed in separate sections below.

In 1995, Davidson et al. used the FEM to investigate the onset of gastrulation, a morphogenetic event occurring prior to neurulation. Relatively few of the relevant mechanical properties had been measured mechanically. Thus, these simulations had a different objective than those of neurulation, where much is known about the relevant mechanical properties. During the invagination phase of gastrulation, a localized, circular dimple is formed in a hollow ball of cells. Five different hypotheses including apical constriction and cortical tractoring were considered, and the unknown mechanical properties were given different values. They concluded that all five hypotheses could create the observed morphological shape changes, if the values of the unknown properties are suitable. Thus, the study provides an important basis for the design of future experiments to measure the unknown properties and ultimately to determine which hypothesis or hypotheses might be correct.

Unfortunately, in their model, the mechanical properties of the tissue are assumed to be elastic, although viscous or viscoelastic properties seem more plausible. Also, standard aspect ratios are violated without explanation and no explanation is provided as to what kind of elements are used to model the thin layers. To maintain incompressibility of the cytoplasm, Davidson et al. compress the cell apex and simultaneously stretch the base using a comparable force. It is not guaranteed that the finite element

volume will remain constant. Since no biological explanation is stated for generating a basal force, basal stretching should only be a passive consequence of the apical constriction and volume constancy. Cell incompressibility is, apparently, ignored in the simulations of the other four hypotheses.

A number of significant technical challenges arise in the modeling of morphogenetic shape changes. During morphogenesis, large strains, deformations, and rotations occur. In addition, the material properties may be highly nonlinear. To model these properly requires the use of a carefully and suitably formulated updated Lagrangian approach. In addition, during morphogenesis, cells and tissues are typically incompressible. Thus, a Poisson's ratio of $\nu = 0.5$ must be used. Unless the element integrations and equations are formulated properly, the elements will suffer from either locking or hourglassing behaviors (Belytschko and Ong, 1984). Few, if any, commercial packages are capable of satisfying these criteria. In the sections that follow, we present a FEM model that addresses all of these key biological issues and discuss principal findings made using it.

2.6 Formulation of a Finite Element Model

What is the Finite Element Method (FEM)?

The label "finite element method" was first used in 1960, although mathematically similar techniques had been used since 1943 (Huebner and Thornton, 1982). Over the past three decades, coupled with the advent of high-speed digital computers, the finite element method (FEM) has become a well-established technique in a diverse range of engineering applications, including structural analysis, solid mechanics, heat transfer, mass transport, fluid mechanics, electromagnetics, vibration analysis, soil mechanics, and even acoustics. This method is especially useful to obtain approximate solutions to analytically intractable systems such as those that describe embryo morphogenesis.

A finite element formulation typically follows a canonical approach that is independent of the problem type (Zienkiewicz and Taylor, 1989, 1991). First, the continuum is subdivided into subregions of appropriate shape (discrete elements) interconnected by nodes. By increasing the number of elements in a regular fashion, a more accurate solution is obtained. The variation of the field variable (for example, displacement in the case of a mechanics problem) within each element is represented by shape functions. Next, the behavior of each element is formulated into a matrix system of linear algebraic equations. A global system of simultaneous equations is then constructed by assembling the matrices that represent each element. Assembly is possible because the value of the field variable is assumed to be the same at all points that share a node. In its most basic form, the resulting equations have the following form:

$$\mathbf{K}\mathbf{u} = \mathbf{f} \tag{2.2}$$

where K is the generalized global stiffness matrix, u is the generalized global displacement vector, and f is the generalized global force vector.

The equations are solved using standard numerical routines. The solution is not exact since a piecewise approximation between nodes is assumed. In the case of a transient problem, the solution is also piecewise over time. For a complete explanation of the FEM approach, see Zienkiewicz and Taylor (1989, 1991). A description of the FEM as applied to biological systems is presented by Brodland (1994).

Basic Criteria

To model morphogenetic shape changes, a FEM simulation must take into account complex temporal shape changes, large strain, displacement and rotation, physical property changes, creation of new cells by mitosis, sliding of cells past each other, viscous or viscoelastic material properties, material incompressibility and internal force generation. To accommodate these characteristics, custom software was written in the C programming language (Clausi, 1991).

A properly formulated updated Lagrangian formulation can accommodate these requirements. The time steps and element sizes should be sufficiently small so that if either is further reduced, the solution does not change; i.e., the result is not dependent on the temporal or geometric discretizations used.

Eight-noded isoparametric volume elements are used to represent the bulk properties of the cell cytoplasm. These finite elements do not have to necessarily model single cells, but can be used to model suitable groups of cells (Brodland and Clausi, 1994). In fact, without any loss of validity, the finite element boundaries do not have to correspond to any cell boundaries since the elements are assigned the bulk physical properties of the cell sheet. To model neighbor changes between cells is more difficult, but possible (Chen and Brodland, 1997).

Derivation of the elastic stiffness matrix for an isotropic, eight-noded isoparametric volume element is available in standard finite element texts (Zienkiewicz and Taylor, 1989). A viscoelastic version of this formulation is presented in Clausi (1991) and summarized in Brodland and Clausi (1994), and the simplified derivation for a purely viscous system is described in Brodland and Clausi (1995).

Experiments have shown that during amphibian neurulation, tissue volume remains essentially constant, even when mitoses occur (Burnside and Jacobson, 1968; Keeton and Gould, 1986). To ensure incompressibility in the finite element formulation, Poisson's ratio (ν) should be set to 0.5. However, this causes some terms in the stiffness matrix to become singular. If ν is set to a value just below 0.5 and full integration is used, then all terms of the stiffness matrix can be determined. However, some terms are magnitudes larger than the other terms, and "locking" occurs. This is a spurious increase in stiffness caused by numerical difficulties. The problem can be overcome by reducing the order of the integration, but this leads to spurious zero-energy modes of deformation called "hourglass" modes. Proposed explanations and solutions for this phenomenon are presented in Belytschko and Ong (1984). In our formulation, reduced order integration is used and hourglassing is controlled using a technique devised by Liu et al. (1985). By using this approach, the incompressibility condition can be satisfied completely and without introducing other problems.

Internal force generation is another characteristic of morphogenetic systems. Truss elements are used to produce these forces. For example, the local net effect of the apical microfilaments and microtubules is determined using statistical mechanics, and truss elements that produce a mechanically equivalent effect are positioned around the apical perimeter of each volume element (whether it models a single cell or a group of cells).

Suitable formulations also allow individual cell behaviors and neighbor changes to be modeled (Chen and Brodland, 1997).

2.7 Simulations

The FEM formulation outlined above provides a methodology for studying a wide variety of morphological behavior. Simulations of neural plate shaping and fold formation, invagination, and pattern formation are presented here.

Neural Plate Shaping

To investigate the intriguing in-plane motions by which a circular neural plate is transformed into a keyhole shape, a flat plate model (Fig. 2.3) of one half of the neural plate (radius 1600 μm) is used. Patches of cells are modeled by volume finite elements, each initially 80 × 80 × 120 μm thick. Truss elements (identified with wider lines) are used to model the actions of constricting apical microfilaments. The region identified in Fig. 2.3C is elongated at a rate of 100 μm/h to model the elongation of the notochord. This agrees with the physical location of the notochord (Youn et al., 1980) and its rate and region of active elongation (Jacobson and Gordon, 1976).

Corresponding time-lapse photographs of the axolotl dorsal surface are shown in Figs. 2.3D through F. A regular grid was placed on the first figure and deformed manually to match observed cell motions. The deformation produced in the finite element simulation is quite similar to that observed in the time-

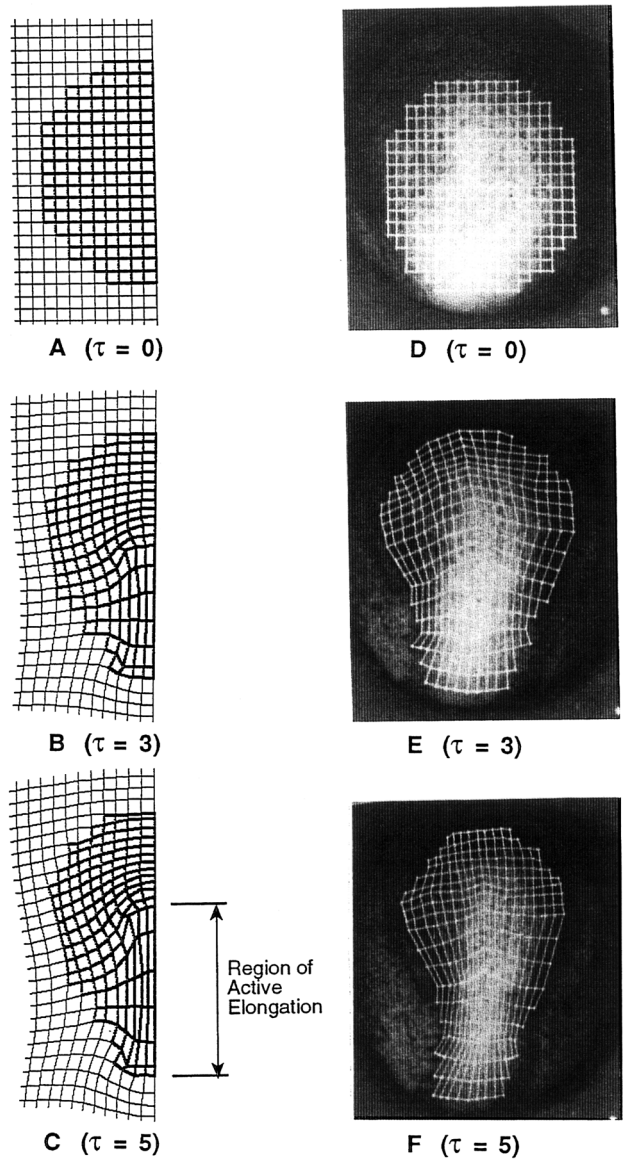

FIGURE 2.3 In-plane shape changes associated with neurulation. A-C: Finite element simulations driven by notochord elongation and microfilament contraction. D-F: Corresponding time-lapse photographs of axolotl embryo development. Cell motions were tracked manually and used to construct a tracking grid. After Clausi and Brodland (1993).

lapse sequence. Also, the patterns of thickness change parallel to those observed in *Taricha torosa* (Clausi and Brodland, 1993).

Neural Fold Formation and Tube Closure

To study the transverse or out-of-plane aspects of neural tube formation, a transverse strip from the left side of an embryo is modeled. By modifying the parameters, we can perform analyses that are not only impossible to perform *in vivo* but that allow precise investigation of the sensitivity of the process to variations in starting geometry or applied force.

For simulations of cross-sectional strips, the net apical constriction force is represented using the dimensionless parameter (Clausi and Brodland, 1993):

$$F_A = 2.3N_{MF}F_{MF} - N_{AMT}F_{MT}/\mu whθ \tag{2.3}$$

where N_{MF} and N_{AMT} represent, respectively, the total number of microfilaments and apical microtubules across the width of the strip, w and h are the initial cell sheet thickness and width, μ is the viscosity, and θ is an inverse time parameter given by

$$\theta = \tau/t. \tag{2.4}$$

The variable τ represents a dimensionless time and t the actual developmental time. If the microtubule force is assumed to be negligible, then the $N_{AMT}F_{MT}$ term can be assumed to be zero. For the simulations described in this section, $F_A = 0.10$.

In the reference case (Fig. 2.4), 20 finite elements, each 40 μm wide by 120 μm in the cephalocaudal direction by 120 μm tall, are connected side by side to model the transverse strip. Microfilaments are placed on the apical surface of the 10 elements closest to the midline of the embryo. To model the effects of the notochord, the cell sheet is stretched at a rate of 56 mm·θ. This rate is based on time-lapse images of axolotl neurulation taken in our laboratory.

A remarkable outcome of the simulation was that a *sequence* of shape changes was produced. In addition, both general reshaping and distinctive, detailed characteristics were produced that closely matched the shape changes that occur in real embryos.

The mechanisms by which this sequence of shape changes is produced can be understood in mechanical terms. In the starting configuration, the apical microfilament forces are balanced between adjacent elements everywhere except at the junction between the neural plate and the nonneural ectoderm. The unresisted microfilaments in the cells near this junction contract and cause the edge of the neural plate to curl upward (Fig. 2.4B). The attached nonneural ectoderm is forced to bend the opposite way to maintain continuity at the junction. As the microfilaments contract, their force increases according to Eq. (2.1), and the ogee shape at the edge becomes increasingly sharp until the microfilaments have contracted their maximum amount (Fig. 2.4C).

As the microfilaments across the whole width of the neural plate continue to contract, the neural plate narrows and, because the volume of its cells remain constant, it thickens (Fig. 2.4D). As it thickens, the microfilament forces move further away from the neutral plane of the sheet, and produce an ever-increasing moment about the middle surface. This causes the thickened plate to roll up (Fig. 2.4E). Regions of higher curvature, called "hinges" (Schoenwolf and Smith, 1990), are produced because of the bending instability produced by Eq. (2.1) (Brodland and Clausi, 1994). The neural plate continues to roll up until it eventually forms a closed tube (Fig. 2.4F).

This simulation demonstrates that using only apical constriction and cephalocaudal elongation, the salient features of neural tube formation — ridge formation, plate narrowing and thickening, cell skewing, creating of hinge points, closure, and rounding — can be produced in the proper sequence. Only established biological characteristics of the neural plate cells are used. No cell preprogramming, cortical tractoring, or forced basal stretching are used to invoke the observed shape changes. One set of applied forces (apical microfilaments plus notochord elongation) produces an entire sequence of intriguing shape changes because the instantaneous effect of these forces changes as the geometry changes. Thus, a kind of mechanical feedback is produced between the current geometry and the applied forces. The neural plate can thus be considered to have a self-regulating mechanical control system.

How sensitive are the shape changes to details of the applied force? To answer this question, the microfilament forces are changed from Eq. (2.1) to a constant value; i.e.,

$$F = \sigma A_0 \tag{2.5}$$

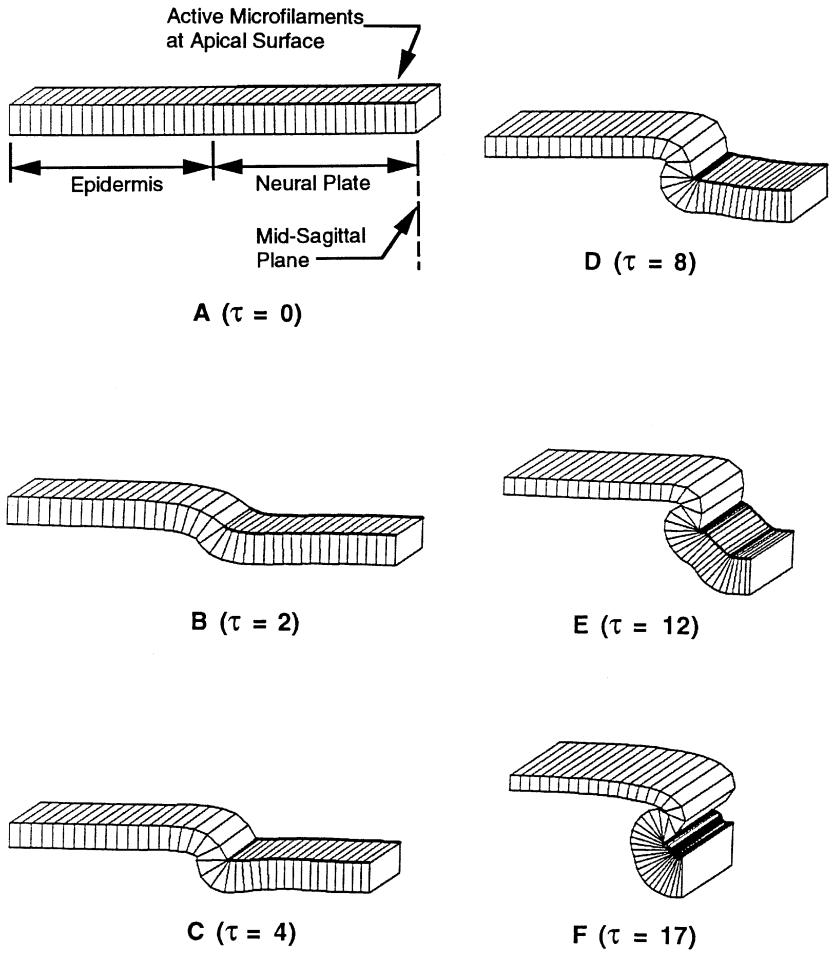

FIGURE 2.4 A "reference case" simulation of neurulation. The strip represents a symmetrical half of a transverse cross-section of an embryo. Microfilaments are placed on the neural plate part of the strip (the region adjacent to the midline). The shape changes in the strip are driven by axial elongation and microfilament contraction. After Clausi and Brodland (1993).

In this case (Fig. 2.5), no hinge points appear, and the plate curls in a more uniform way compared to the reference case (Fig. 2.4). The shape changes produced by this simulation do not match well with those that are typical of amphibian neurulation, and suggest that Eq. (2.1) provides a better description of microfilament forces during neurulation.

Is it possible that transverse forces produced by paraxial microtubules or cell-cell adhesions might cause an invagination or other neurulation-type movement to occur? These two driving mechanisms are mechanically equivalent (Brodland and Clausi, 1994). Figure 2.6 shows the results of a simulation in which transverse forces of dimensionless magnitude

$$F_T = \eta^d + N_{PMT}F_{MT}/\mu wh\theta = 0.04 \tag{2.6}$$

where η is the adhesion force per unit length are applied. Such forces thicken the neural plate, but do not produce an invagination or other neurulation-type shape change (Clausi and Brodland, 1993).

Another hypothesis that has been suggested is that forces external to the neural plate might cause the plate to buckle and collapse to form a closed tube (Schoenwolf and Smith, 1990). To investigate this

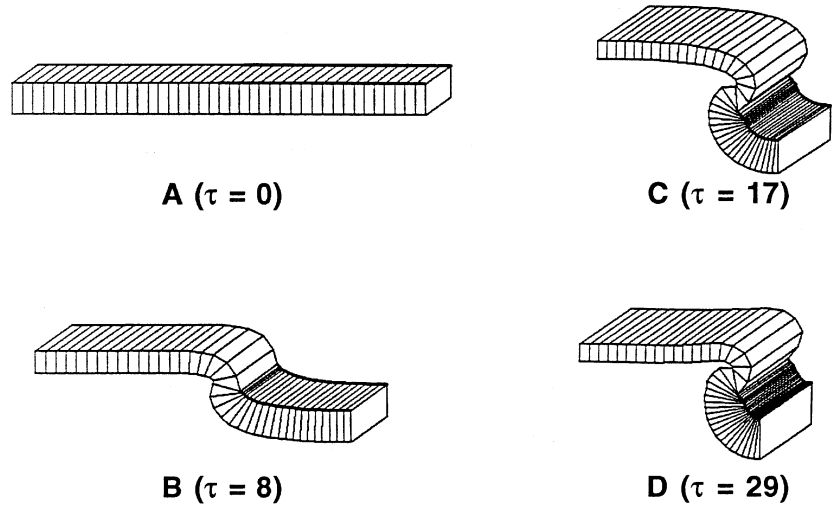

FIGURE 2.5 A simulation in which the microfilament force is constant. The driving forces and boundary conditions are identical to that shown in Fig. 4, except that the microfilament force is constant [Eq. (2.5)] rather than increasing as microfilament contraction [Eq. (2.1)]. After Brodland and Clausi (1995).

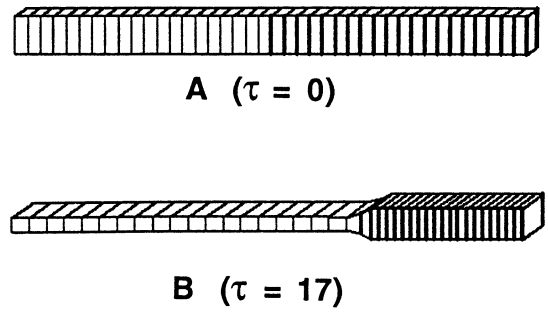

FIGURE 2.6 A simulation of the action of transverse forces from paraxial microtubule elongation or cell-cell adhesions. Microfilament forces are not acting. After Clausi and Brodland (1993).

hypothesis, the apical microfilament force from the reference case is removed, and a dimensionless, external force F_M of magnitude

$$F_M = F_{Medial}/\mu whe = 0.15 \tag{2.7}$$

is distributed uniformly between the nodes at the neural plate edge. The shape changes depicted in Fig. 2.7 are produced. This shape resembles the transverse section of a chick embryo treated to arrest microfilament contraction (Schoenwolf and Smith, 1990, Fig. 18). To date, a particular mechanism to generate such a force has not been identified.

The results of this simulation and the experiments of Schoenwolf and Smith (1990) do, however, suggest that there are redundant force systems at work. Thus, if the primary driving forces are weak or absent, a secondary system of forces may play a significant role. The presence of such redundant mechanisms may account, in part, for the robustness of the neurulation process.

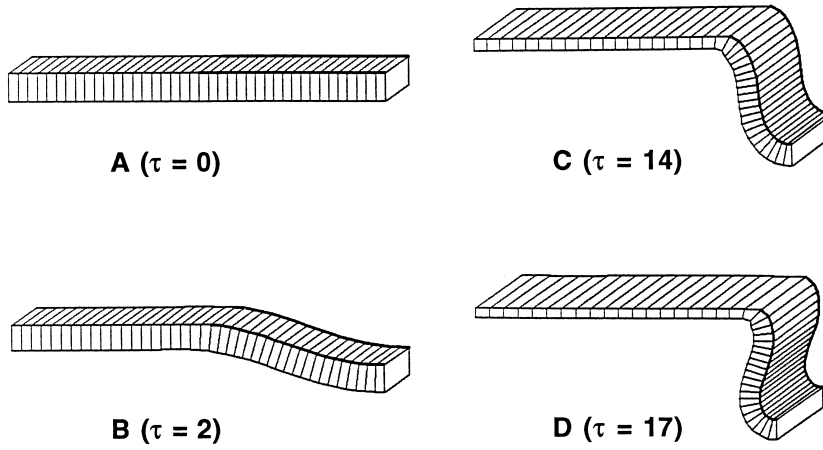

FIGURE 2.7 Extrinsic forces at the edge of the neural plate. The forces are directed toward the midline of the embryo, and there are no microfilament forces. After Brodland and Clausi (1995).

Invagination

Invagination is another fundamental morphogenetic process (Alberts et al., 1989). Here we model a symmetric invagination around a localized patch of cells (Brodland and Clausi, 1994). Due to the symmetry of the geometry and the loading, only one quarter of the plate needs to be modeled (Fig. 2.8). Each element in the top layer is initially $20 \times 20 \times 30$ μm. Microfilaments constrict the apical surface of the 5×5 patch of cells in the front right corner of the model.

Twenty time steps of $\Delta\tau = 0.2$ are used and steps $\tau = 0$, 2.0, and 4.0 are shown (Fig. 2.8). An invagination occurs by the same mechanism as the neural ridges are initially produced in neurulation. Additional simulations (not shown) have shown that any tissue below the epithelial cell sheet has little mechanical effect on formation of the invagination (Brodland and Clausi, 1994). Whereas Davidson et al. (1995) used basal expansion to generate an invagination, here we show that invaginations can be produced by apical constriction only, provided that the finite element engine is formulated appropriately so that cell volumes remain constant.

Pattern Formation

Pattern formation, "a process by which an initially homogeneous collection of cells develops heterogeneous features, is another critical embryonic process..." (Brodland and Clausi, 1994). It is known to be an important aspect of the creation of surface features, coloration, and internal structures. Both biochemical changes and mechanical events are involved in most pattern formation processes. For further examples and explanations for pattern formation, see Maini and Solursh (1991). Here, we demonstrate that pattern formation in epithelial sheets might be driven solely by microfilament contraction. In this case, the pattern results from the same basic mechanical instability as that which gives rise to hinges in the neural plate.

A simulation was created using a bilayer sheet of cells that are initially $20 \times 20 \times 60$ μm high (Fig. 2.9). Microfilaments described by Eq. (2.1) are applied to the top surface of the top layer. A perturbation (lateral displacement) of 1 μm is applied to the top left node. This causes the width of the top left cell to be increased slightly. According to Eq. (2.1), the force carried by the microfilament bundle along this top edge becomes slightly reduced and thus the cell continues to increase in width. This, in turn, allows adjacent cells to contract. As they contract, they exert an ever-increasing force. A propagating set of alternating imbalances thus arises and produces a sequence of alternating states (i.e., a pattern). This method of pattern formation is highly robust. Additional simulations (Brodland and Clausi, 1994) indicate that the pattern spacing is largely unaffected by cell size and the thickness and properties of the

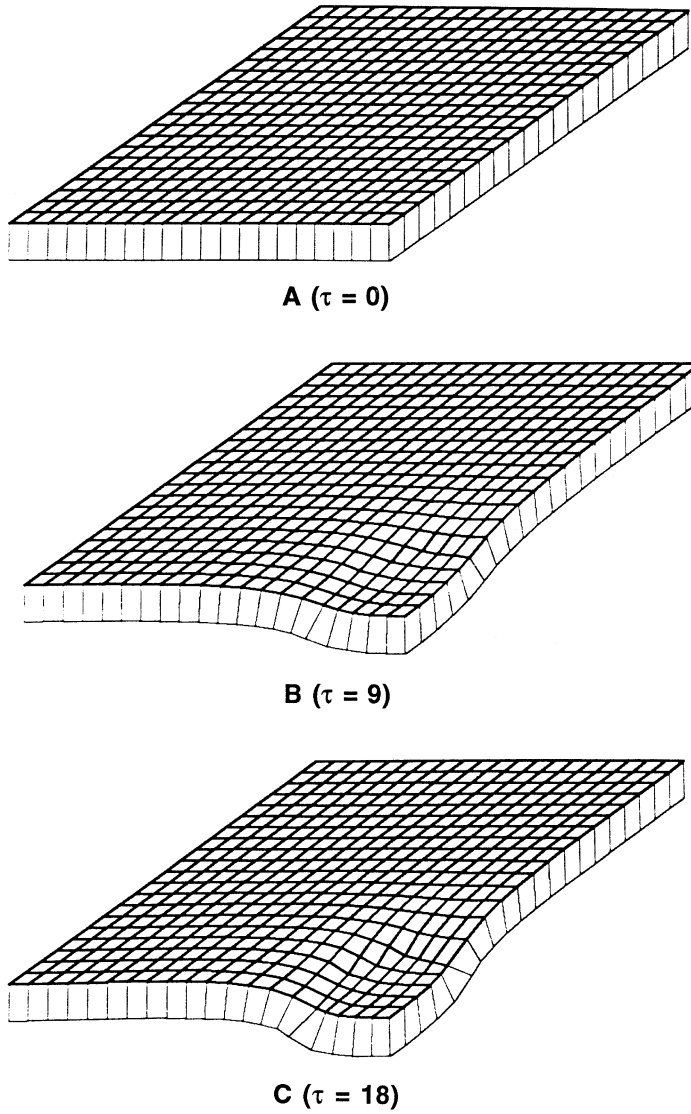

FIGURE 2.8 Simulation of an invagination. Due to bilateral symmetry, one quarter of the total tissue is shown. Microfilaments act only on the apical surface of the 5×5 cell region at the front right corner.

underlying layers. The primary outcome of this simulation is to show that purely mechanical systems can produce regular patterns.

2.8 Conclusions

A number of important principles for the modeling of biological systems have become apparent:

1. Models must be firmly anchored on established biological data. This means that properties must be derived from known morphologies and properties of cytoskeletal components and other force-generating structures. In addition, reference and progressive geometries predicted by simulations must be compared with similar data from live or fixed embryos.

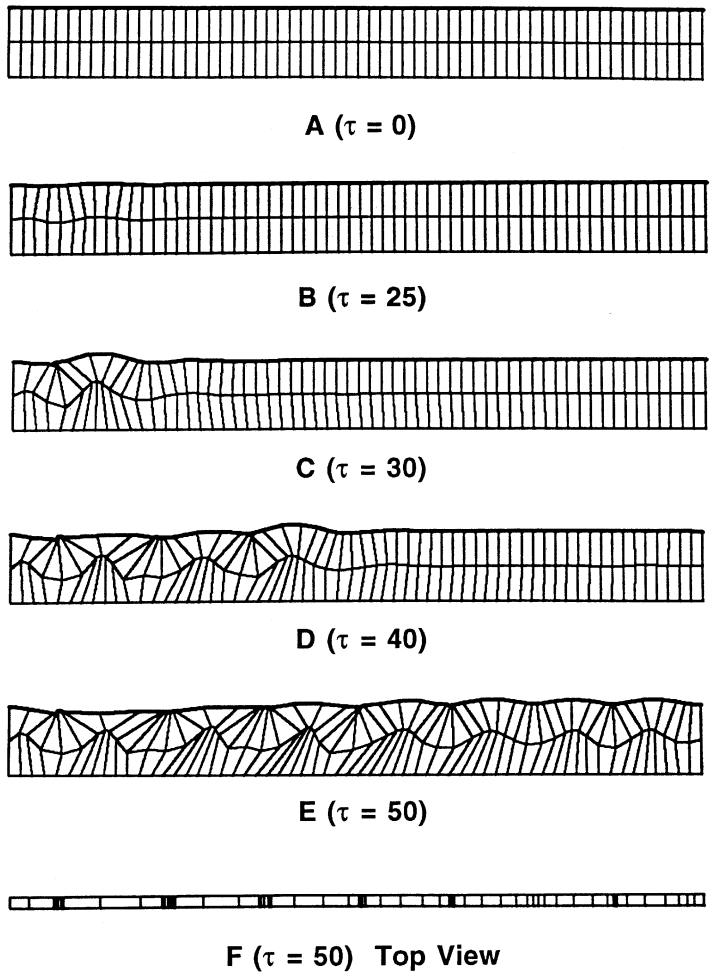

FIGURE 2.9 Pattern formation produced solely by microfilament contraction. A mechanical instability develops because the microfilaments are described by Eq. (2.1). The phenomenon is related to "hinge" formation during neurulation. After Brodland and Clausi (1994).

2. Models must have a sound mechanical basis. In studies of morphogenetic shape changes, this requires that numerical formulations must properly accommodate large strains, deflections and rotations, nonlinear material properties, and the various kinds of coupling that can occur between these.
3. Finite element models can be formulated to satisfy all of the mechanical criteria and are sufficiently general that all relevant biological data such as initial geometries and mechanical properties can be incorporated.

Much can be learned from suitably formulated finite element-based computer simulations. In particular, computer simulations provide a powerful means to evaluate hypotheses about the forces that produce specific morphogenetic shape changes such as neurulation. Because a large number of possible force-generating structures exist, it is not surprising that numerous theories have arisen. Although drug studies can provide some important information, they are often not conclusive. This is in part because standard teratogenic drugs are believed to have a variety of unknown side effects.

Simulations of neurulation have demonstrated that many popular and apparently plausible theories about neurulation are mechanically unsound. In some cases, the difficulties are apparent only after

boundary conditions and other physical constraints are applied. These simulations showed that the shapes that are produced are highly sensitive to the active forces and to the starting geometries. The presence of redundant sets of forces has also been supported by the simulations.

Computer simulations have also revealed the presence of elegant mechanical control systems. During neurulation, for example, the effect of microfilament contraction changes as the geometry of the plate changes. Since the shape changes are caused by these same microfilaments, a mechanical control system is seen to be at work. That mechanical control system causes a distinct sequence of shape changes to be produced. Mechanical control and feedback are also apparent during pattern formation.

Simulations of this kind form an important step toward the development of "virtual embryos" in which extensive virtual experiments might be carried out. It also makes an important contribution toward the development of numerical methods that overcome the technical challenges inherent in modeling embryos that are made of incompressible materials that undergo large strains, deformations, and rotations.

References

Alberts, B., Bray, D., Lewis, J., Raff, M., Roberts, K., and Watson, J. (1989) *Molecular Biology of The Cell*, 2nd ed., Garland Publishing, Inc., New York.

Beck, J.V. (1977) *Parameter Estimation in Engineering and Science*, Wiley, New York.

Belytschko, T. and Ong, J.S. (1984), Hourglass in linear and nonlinear problems, *Comp. Meth. in Appl. Mech. and Eng.*, **43**, pp. 251-276.

Brodland, G.W. (1994) Finite element methods for developmental biology. *In* The Cytoskeleton in Development Biology. *Int. Rev. Cytol.*, **150**, pp. 95-118.

Brodland, G.W. (1997) Computer modelling of morphogenesis: Recent advances and future prospects. Proceedings of the 16th Canadian Congress of Applied Mechanics CANCAM 97, June 1-5, Quebec, **2**, pp. 84-95.

Brodland, G.W. and Clausi, D.A. (1994) Embryonic cell sheet morphogenesis modelled by FEM. *ASME J. Biomech. Eng.*, **116**, pp. 146-155.

Brodland, G.W. and Clausi, D.A. (1995) Cytoskeletal mechanics of neurulation insights obtained from computer simulations, *Biochem. Cell Biol.*, **73**, pp. 545-553.

Brodland, G.W. and Cohen, H. (1989) Deflection and snapping of ring-loaded spherical caps, *ASME J. Appl. Mech*, **111**, pp. 127-132.

Brodland, G.W. and Gordon, R. (1990) Intermediate filaments may prevent buckling of compressively loaded microtubules. *J. Biomech Eng.*, **112**, pp. 319-321.

Burnside, B., (1971) Microtubules and microfilaments in newt neurulation. *Dev. Biol.*, **26**, pp. 416-441.

Burnside, B., (1973) Microtubules and microfilaments in amphibian neurulation. *Amer. Zool.*, **13**, , pp. 989-1006.

Burnside, M.B. and Jacobson, A.G. (1968) Analysis of morphogenetic movements in the neural plate of the newt *Taricha torosa*. *Dev. Biol.*, **18**, pp. 537-552.

Chen, H.H. and Brodland, G.W. (1997) Finite element simulation of differential adhesion-driven cell sorting and spreading. Proceedings of the 16th Canadian Congress of Applied Mechanics CANCAM 97, June 1-5, Quebec, **1**, pp. 597-598.

Cheng, L.Y. (1987a) Deformation analyses in cell and development biology. Part I — Formal methodology. *J. Biomech. Eng.*, **109**, pp. 10-17.

Cheng, L.Y. (1987b) Deformation analyses in cell and development biology. Part II — Mechanical experiments on cells. *J. Biomech. Eng.*, **109**, pp. 10-17.

Clausi, D.A. (1991) *Finite Element Simulation of Early Embryonic Development,* M.A.Sc. Thesis, University of Waterloo, Waterloo, Ontario.

Clausi, D.A. and Brodland, G.W. (1993) Mechanical evaluation of theories of neurulation using computer simulations. *Development*, **118**, 1013-1023.

Davidson, L.A., Koehl, M.A.R., Keller, R., and Oster, G.F. (1995) How do sea urchins invaginate? Using biomechanics to distinguish between mechanisms of primary induction. Development, **121**, pp. 2005-2018.

Ettensohn, C.A. (1985) Mechanisms of Epithelial Invagination, *The Quarterly Review of Biology*, **60**, No. 3, pp. 289-307.

Fawcett, Don, M.D. (1981) *The Cell*, 2nd ed., W.B. Saunders Company, Toronto, pp. 743-783.

Gordon, R. (1985) A review of the theories of vertebrate neurulation and their relationship to the mechanics of neural tube birth defects. *J. Embryol. exp. Morph.*, **89**, pp. 229-255.

Hiramoto, Y. (1969a) Mechanical properties of the protoplasm of the sea urchin egg: I. Unfertilized egg. *Exp. Cell Res.*, **56**, pp. 201-208.

Hiramoto, Y. (1969b) Mechanical properties of the protoplasm of the sea urchin egg: II. Fertilized egg. *Exp. Cell Res.*, **56**, pp. 209-218.

His, W. (1874) Unsere Körperform und das physiologische problem ihrer enstehung, briefe an einen befreundeten naturforscher. F.C.W. Vogel, Leipzig.

Huebner, K.H. and Thornton, E.A. (1982) *The Finite Element Method for Engineers*, 2nd ed., John Wiley & Sons, Toronto.

Jacobson, A.G. and Gordon, R. (1976) Changes in the shape of the developing vertebrate nervous system analyzed experimentally, mathematically and by computer simulation. *J. Exp. Zool*, **197**: 191-246.

Jacobson, A.G. (1978) Some forces that shape the nervous system. *Zoon* , **6**, pp. 13-21.

Jacobson, A.G., Oster, G.F., Odell, G,.M., and Cheng, L.Y. (1986) Neurulation and the cortical tractoring model for epithelial folding. *J. Embryol. exp. Morph.*, **96**, pp. 19-49.

Keeton, W.T. and Gould, J.L. (1986) *Biological Science*, 4th ed., W.W. Norton and Company, New York.

Koehl, M.A.R. (1990) Biomechanical approaches to morphogenesis. *Developmental Biology,* **1**, pp. 367-378.

Lee, H. and Nagele, R.G. (1988) Intrinsic forces alone are sufficient to cause closure of the neural tube in the chick. *Experientia*, 44, pp. 60-61.

Lewis, W.H. (1947) Mechanics of invagination. *Anat. Rec.*, **97**, pp. 139-156.

Liu, W. K., Ong, J.S., and Uras, R.A. (1985), Finite element stabilization matrices — a unification approach, *Comp. Meth. in Appl. Mech. and Eng.*, **53**, pp. 13-46.

Maini, P.K. and Solursh, M. (1991) Cellular mechanisms of pattern formation in the developing limb, *International Review of Cytology*, K.W. Jeon and M. Friedlander, eds., **129**, pp. 91-133.

Mutchinick, O., Orozco, E., Lisker, R. Babinsky, V., and Nunez, C. (1990) Factores de reisgo asociados a los defectos de cierre del tubo neural: Exposicion durante el primer trimestre de la gestacion. *Gaceta Medica de Mexico*, **126**, pp. 227-233.

Nardi, J.B. (1981) Epithelial invagination: Adhesive properties of cells can govern position and directionality of epithelial folding, *Differentiation*, **20**, 97-103.

Odell, G.M., Oster, G., Alberch, P., and Burnside, B. (1981) The mechanical basis of morphogenesis, I. Epithelial folding and invagination, *Developmental Biology*, **85**, pp. 446-62.

Roux, W. (1888) Beiträge zur entwickelungsmechanik des embryo. Über die künstliche hervorbringung halber embryonen durch zerstörung einer der beiden ersten furchungskugeln, sowie über die nachentwickelung (postgeneration) der fehlenden körperhälfte. *Virchows Arch. Path Anat. u. Physiol. u. Kl. Med.* **114**, pp. 113-153, pp. 289-291.

Schoenwolf, G.C. and Smith, J.L. (1990) Mechanics of neurulation: traditional viewpoint and recent advances, *Development*, **109**, 243-270.

Steinberg, M.S. (1996) Adhesion in Development — An Historical Overview, *Developmental Biology*, 180, pp. 377-388.

Weliky, M. and Oster, G. (1990) The mechanical basis of cell rearrangement I. Epithelial morphogenesis during Fundulus epiboly. *Development*, **109**, 373-386.

Werler, M.M., Shapiro, S., and Mitchell, A.A. (1993) Periconceptual folic acid exposure and risk of occurent neural tube defects. *J. Amer. Med. Assoc.*, **296**, pp. 1257-1261.

Youn, B.W., Keller, R.E., and Malacinski, G.M. (1980) An atlas of notochord and somite morphogenesis in several anuran and urodelean amphibians. *J. Embryol. Exp. Morph.*, **59**, 223-247.

Zienkiewicz, O.C. and Taylor, R.L. (1989) *The Finite Element Method, Basic Formulation and Linear Problems*. Volume 1, 4th ed., McGraw-Hill, London.

Zienkiewicz, O.C. and Taylor, R.L. (1991) *The Finite Element Method, Solid and Fluid Dynamics*. Volume 2, 4th ed., McGraw-Hill, London.

3

Techniques in the Determination of Uterine Activity by Means of Infrared Application in the Labor Process

Wen-Jei Yang
University of Michigan

Paul P.T. Yang
Southeast Permanente Medical Group

3.1 Introduction

The changes undergone by the uterus during pregnancy are not seen in any other muscles. The intrauterine volume of an unpregnant nulliparous woman is about 2 cm^3, but the volume at the end of pregnancy reaches 4 to 5 liters. Meanwhile, the weight of the uterus muscle, the myometrium, increases from 50 g to about 1 kg. The growth is mainly due to the growth and stretching of muscle cells five- to tenfold, while the number of cells increases as well. Due to stretching, the myometrium thins out from 2 to 3 cm during the first month of pregnancy to 1 to 2 cm at the end of pregnancy. See Yrjana.[1]

The myometrium consists of visceral smooth muscle tissue which lies in three layers: the outer layer is thinnest, consisting mainly of longitudinal fibers. The middle layer is thickest. It is well developed at the body of the uterus and less developed at the cervix. This layer contains a lot of blood vessels in its inner part where fibers have a flexible arrangement. The inner muscle layer is thinner than the middle one. This layer is also well developed at the uterine body but the fibers are aligned more irregularly at the cervix. The inner surface of the myometrium is covered with mucous membranes, endometrium, through which the conceived egg cell penetrates. During pregnancy the endometrium is referred to as decidua. The cervix consists mainly of connective tissue. During pregnancy, collagen concentration decreases to about one-half of the original concentration with its fibers changing their structure. This, and changes in other connective tissue components, result in the ripening, namely, softening and dilation, of the cervix at term.

In the myometrium, smooth muscle cells are dispersed throughout an extracellular material composed mainly of collagen fibers, which act as intramuscular tendons. Muscle cells are connected to each other with pathways of low electrical resistance, called gap junctions. The gap junctions facilitate not only the propagation of electrical activities but also the intercellular migration of specific metabolites. Without gap junctions, the spreading of contractions throughout the uterus would be impossible. During pregnancy, especially during the second half, hormones cause the number of gap junctions to increase so that effective contractions are produced during labor.

The uterus undergoes contractions throughout pregnancy which facilitate the return of venous blood. However, only in the late period of pregnancy do strongly noticeable contractions become regular. Local uterine prostaglandin synthesis, changes in placental hormone production, and mechanical stretching of the uterine wall are all involved in the events which culminate in contractions which cause parturition. Labor begins with the first regular, usually painful contractions that result in dilating the cervix. In the first stage of active labor, the cervix dilates from 3 cm to a total dilation of 10 cm in diameter. This stage usually lasts 8 to 24 hours for a nulliparous woman. The intensity (amplitude) and frequency of contractions increase as cervical dilation increases. During the second stage of labor, the fetus is forced through the birth canal by contractions and maternal expulsive efforts. This stage lasts about half an hour for a nulliparous woman. The frequency of contractions during labor increase from 2 to 5 contractions per 10 min. The intensity of contractions increases from 30 to 60 mmHg in intra-uterine pressure during the active first stage of labor to 150 mmHg in the second stage when contractions are coupled with maternal expulsive efforts. The duration of contractions during labor is about 0.5 to 1.5 minutes. The baseline pressure, i.e., the intrauterine pressure in the absence of contraction peak, is about 8 to 12 mmHg.

In general, the intensity of contractions varies with the total myometrial mass and the number of excited myometrial cells. Each contraction begins at the top of the uterine fundus spreading downward through the body of the uterus. It is most intense at the top and in the uterine body and diminishes toward the cervix. After each contraction, fibers slowly relax, but do not fully return to their original length, becoming slightly shorter and thicker. Aside from this retraction, muscle fibers in the uterus still retain their ability to contract upon relaxation. Each retraction results in both a shortening of the upper segment of the uterus and a reduction in the volume of the uterus.

Although many principles are similar in smooth and skeletal muscle contraction there are four major differences: (1) Autonomic function varies. Smooth muscle contractions develop only one quarter to one twentieth of skeletal muscle contractions with relaxation being prolonged. (2) Due to differences in cellular structures, the degree of shortening in the smooth muscle is about one order of magnitude greater than that in the striated, or skeletal, muscle. (3) Smooth muscle can contract in any direction whereas the contraction and force generated in skeletal muscles are aligned with the axis of the muscle fibers.

The measurement of uterine activity during labor is important for at least four reasons: (1) measuring contractions can assist in the timing of maternal expulsive efforts, (2) it can help diagnose the reasons for unsatisfactory progress in labor which may indicate a need for a Caesarean section, (3) it may help avoid uterine hyperstimulation, and (4) it may aid in determining the correct drug dosage being administered to modify uterine activity.

There are a variety of means to measure uterine activity, depending upon the objective. For example, (1) manual palpation is satisfactory for a quick evaluation of contractions, (2) belt-type cardiotocography, an external recording of contractions, is most convenient for normal, uncomplicated labor, (3) internal monitoring by means of intra-uterine pressure devices is irreplaceable in complicated labor which requires more accurate monitoring of uterine pressure. It can also be used in labors of obese mothers or with medication that influences the uterus.

During the last few months of pregnancy, the uterus undergoes periodic episodes of weak and slow rhythmic contractions. These become progressively stronger toward the end of pregnancy eventually changing rater suddenly — within hours — to become exceptionally strong contractions that start stretching (pull open) the cervix through the mechanism of brachystasis or retraction,[16] and alter force the baby through the birth canal, thereby causing parturition. This process is called labor. The strong

contractions that result in the final parturition are called labor contractions. It is still uncertain what suddenly changes the slow and weak rhythmicity of the uterus into the strong labor contractions. However, two phenomena are known: (1) Maternal temperature rises during labor and the strength of contractions is related to uterine wall temperature and therefore to abdominal wall temperature. Since heat and work are interconvertible, uterine activity during labor contractions can be determined by measuring timewise variations of the abdominal wall temperature; (2) the state of cervical dilation is related to the progress of labor in human parturition. Hence, the work expended by the uterus can be evaluated by understanding its significance with respect to various changes in the intrauterine pressure and cervical dilation wave forms, which can be charted on a labor graph.

Obstetrical textbooks in the nineteenth century indicated that the maternal temperature rose during labor.[2,3] Using both skin and tympanic membrane temperature sensors, Goodlin and Chapin[4] measured intrapartum maternal temperatures and the neonatal temperature immediately after birth. Goodlin and Brooks[5] used a hand-held infrared temperature sensor to measure the temperature of the abdominal wall in antenatal patients at least 35 weeks into gestation. The inguinal and periumbilical areas appeared to be relative hot spots in normal pregnancy. Marx and Loew[6] monitored tympanic temperature, by means of a thermocouple, during labor and delivery. Temperature increased temporarily with each contraction and progressively throughout the course of the labor. The increases were greater in the primiparae (1.46°C) than in the multiparae (0.51°C) and were attributed to the metabolic expenditures associated with contraction of uterine and skeletal muscles. Kapusta et al.[7] measured core and peripheral body temperatures in parturients in labor with and without analgesia. The effect of epidural analgesia was a temporary temperature drop in the periphery but no significant alteration of core temperature.

Yan et al.[8,9] monitored the temporal and spatial variation of temperature in the whole maternal abdominal wall during labor and delivery by means of an infrared thermovision system. The infrared thermovision method is non-invasive and the result is global, sensitive, and quantitative. Based on the measurement, the heat transfer rate through the abdominal and uterine walls can be evaluated by conduction heat transfer modeling. The heat generated in the uterine wall results from an energy conversion associated with muscular work of the uterine wall in the delivery of a fetus. Hence, uterine activity during labor can be quantitatively determined by means of infrared thermography with the aid of a heat conduction model. It is well known that an ultrasonic vision device provides vivid pictures of the activities of a fetus in the uterus but fails to yield quantitative information of these activities.

Friedman[10] demonstrated the importance of making frequent measurements of dilation with the augmentation of labor. His labor graph, Fig. 3.1, shows that in normal labor, dilation exhibits a reproducible pattern, while aberrations in this pattern suggest abnormal labor. note that the dilation wave form changes with each contraction and that this change diminishes with the augmentation of labor. Subsequently, Kriewall and Work[11] and Azdor et al.[12] developed instrumentation to measure continuously cervical dilation in human parturition, while Crawford,[13] and Van Praach and Hendricks[14] used intrauterine pressure only to evaluate uterine work by empirical means.

3.2 Theoretical Analysis of Uterine Work in Parturition

There are two approaches to the theoretical analysis of uterine work in parturition: mechanical[15] and thermal.[8,9]

Mechanical Approach

The contractions of labor pull open the cervix through the mechanism of brachystasis, or retraction.[16] The mechanism of the uterine contraction and subsequent fetal movement is explained by Kriewall[15] and follows: Physiologically, the cycle of the uterine system begins with the onset of a contraction and ends with the beginning of the successive contraction. As the contraction begins, the biochemically stored energy of the myometrium is transformed to shorten the muscle fibers which in turn causes brachystasis with the effect of moving the fetus down against the cervix. From the mechanical viewpoint, the contents

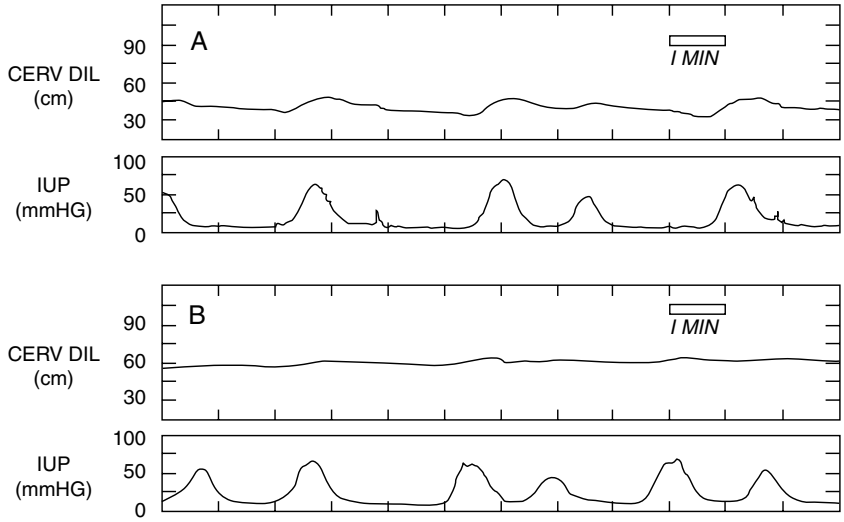

FIGURE 3.1 Two portions of the labor graph, time history of cervical dilatation (CD) and intrauterine pressure (IUP), A: from early labor; B: from late labor.

of the uterus are incompressible, the amount of work required to dilate the cervix can be determine by measuring the change of the uterine volume with each contraction. The energy of a contraction which does not dilate the cervix is lost as heat generated in the myometrium or used to change the structure of the myometrium.

In this approach, the work expended by the uterus is related to the synergistic relationship between intrauterine pressure (IUP) and cervical dilation (CD). By utilizing a geometrical model for the fetal presenting part which is assumed to be in contact with the cervix, the changes in internal volume of the uterus with each contraction are functionally related to cervical dilation. Thus, work can be determined using the integral of pressure times incremental volume. Intrauterine pressure and cervical dilatation are simulated with those wave forms generated by labor monitors. The alterations required in uterine work to dilate the cervix are calculated for various waveform aberrations which occur in clinical situations. the waveform aberrations are applied to an elastic cervical model as well as a viscoelastic model.

The purpose of the contractions is to dilate the cervix. Treating a contraction as a quasi-equilibrium process, the work of dilating the cervix can be expressed as

$$W = \int P dV \tag{3.1}$$

Here, P denotes the intrauterine pressure, which can be measured directly using standard labor room monitoring techniques. The change in volume dV refers to the change in cervical dilation which is determined as follows. The fetal head is modeled as a sphere with which the cervix (hatched) is in close contact, as in Fig. 3.2a. The presenting part is assumed to be a hemisphere, as illustrated in Fig. 3.2b. In other words, the part of the fetal skull that contacts the cervix in a normal vertex position is spheroidal and the cervix retracts around this hemisphere as it dilates. Thus, the internal volume change is equal to the external volume change, ΔV, of a slice of the hemisphere delineated by the beginning and ending values of dilation, $D_3 = 2R_a$ and $D_2 = 2R_2$, respectively. One may write

$$\Delta V = \pi \Delta S(3R_2^2 + 3R_3^2 + \Delta S^2)/6 \tag{3.2}$$

Here,

$$\Delta S = R_1[1-(R_3/R_1)^2]^{1/2} - R_1[1-(R_2/R_1)^2]^{1/2} \tag{3.3}$$

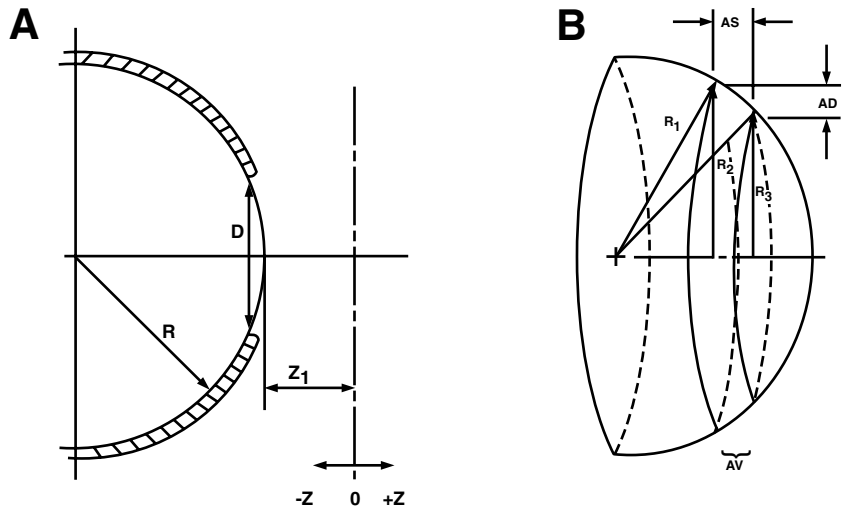

FIGURE 3.2 Physical and analytical models, A and B respectively, for the calculations of uterine work.

and R_1 is the radius of the hemisphere, taken as 5 cm.

The clinical wave forms of the pressure, P, and dilatation, D, are simulated to be half-sinusoidal (Fig. 3.3) as

$$P = P_a \sin \omega_1 t + P_t \qquad \tau_p \geq t \geq 0 \qquad (3.4a)$$

$$P = P_t \qquad \tau* \geq t \geq \tau_p \qquad (3.4b)$$

$$D = D_a \sin (\omega_2 t - \theta) + D_b \qquad \tau_d \geq t \geq \tau_D \qquad (3.5a)$$

$$D = D_b \qquad \tau^* + \tau_D \geq t \geq \tau_d. \qquad (3.5b)$$

Here, t denotes the time; P_a, IUP amplitude; $\omega_1 = 2\pi/\tau_p$, frequency if IUP oscillation; τ_p, IUP duration; τ^*, duration of an individual contraction; P_t, tonus; D_b, base (state of dilatation between contractions); D_a, CD amplitude; $\omega_2 = 2\pi/\tau_d$, frequency of CD oscillation; τ_d, CD duration; $\theta = \omega_2 T_D$, phase lag between the IUP and CD waveforms; and τ_d, time delay between the IUP and CD waveforms. The tonus is the residual pressure that exists within the uterus between contractions, while base refers to the state of dilatation between contractions. Since the tonus P_t is constant over the entire change in volume, Eq. (3.1) can be written as

$$W = P_t V_{total} + \int (P_a \sin \omega_1 t) dV. \qquad (3.6)$$

It shows that the work arises from two sources of pressure, thus separating the effects of the tonus pressure from the pressure due to an individual contraction.

A parameter α in cm/s is included to account for any permanent increase in dilatation with a contraction. It is defined as the slope of a dilating effect, i.e., an increase in the cervical dilatation divided by the CD duration in an individual contraction, as shown in Fig. 3.4. Note that there is no permanent dilatation (i.e., $\alpha = 0$) when the pressure peak, P_a, does not exceed 25 mm Hq.[17,18]

Table 3.1 presents standard waveforms of pressure and dilatation which closely represent those waveforms generated by labor monitors. The uterine work of the standard waveforms is used to compare with that of the actual parturition wave forms.

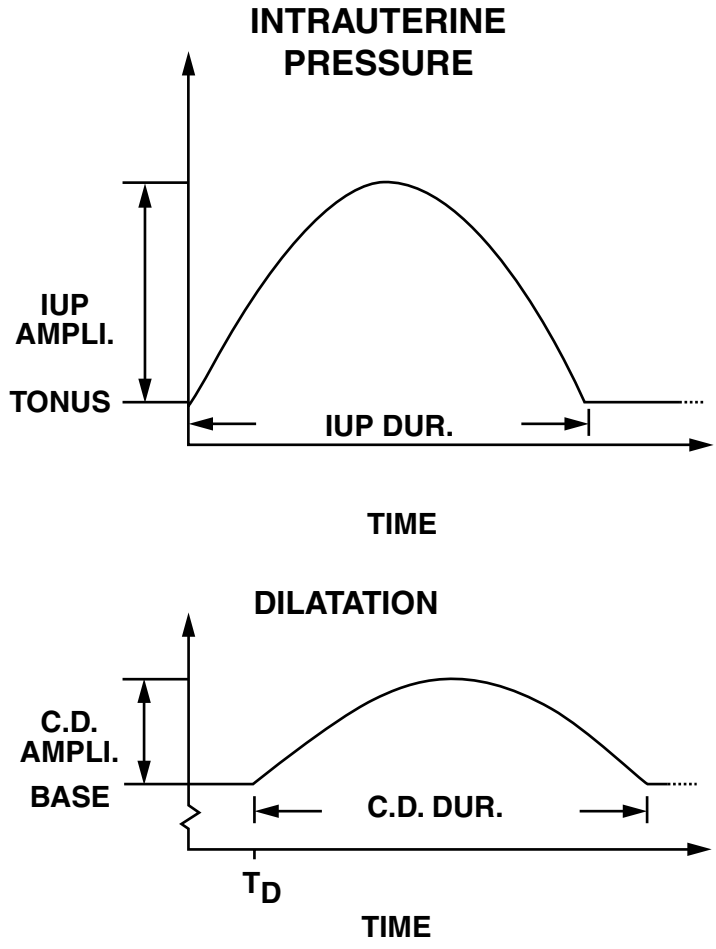

FIGURE 3.3 Half-sinusoidal wave forms simulating clinical wave forms.

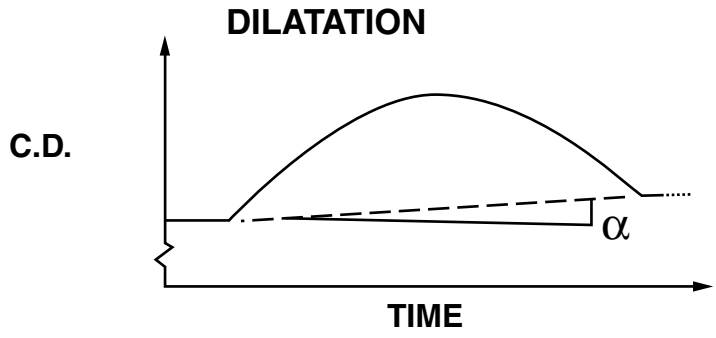

FIGURE 3.4 Permanent dilatation parameter α.

Results and Discussion

Equation (3.1) is integrated by evaluating the Riemann sum using a time increment of 2 sec and the standard waveforms. Results are illustrated as the solid line in Fig. 3.5, superimposed with that for a shorter contraction of 40 sec (with open squares). It is seen hat the work begins and ends at zero for both cases and reaches the same maximum amount of 0.7×10^{-2} ft-lb midway through a contraction.

TABLE 3.1 Standard Wave Forms of Pressure and Dilatation

Parameter	Symbol	Value
IUP duration	T_p	60 s
IUP tonus	P_t	10 mmHG
IUP amplitude	P_a	50 mmHG
CD duration	τ_d	60 s
CD baseline	D_b	3 cm
CD amplitude	D_a	ϕ cm
Time delay	τ_D	0 s
Dilatation slope	α	0 cm/s

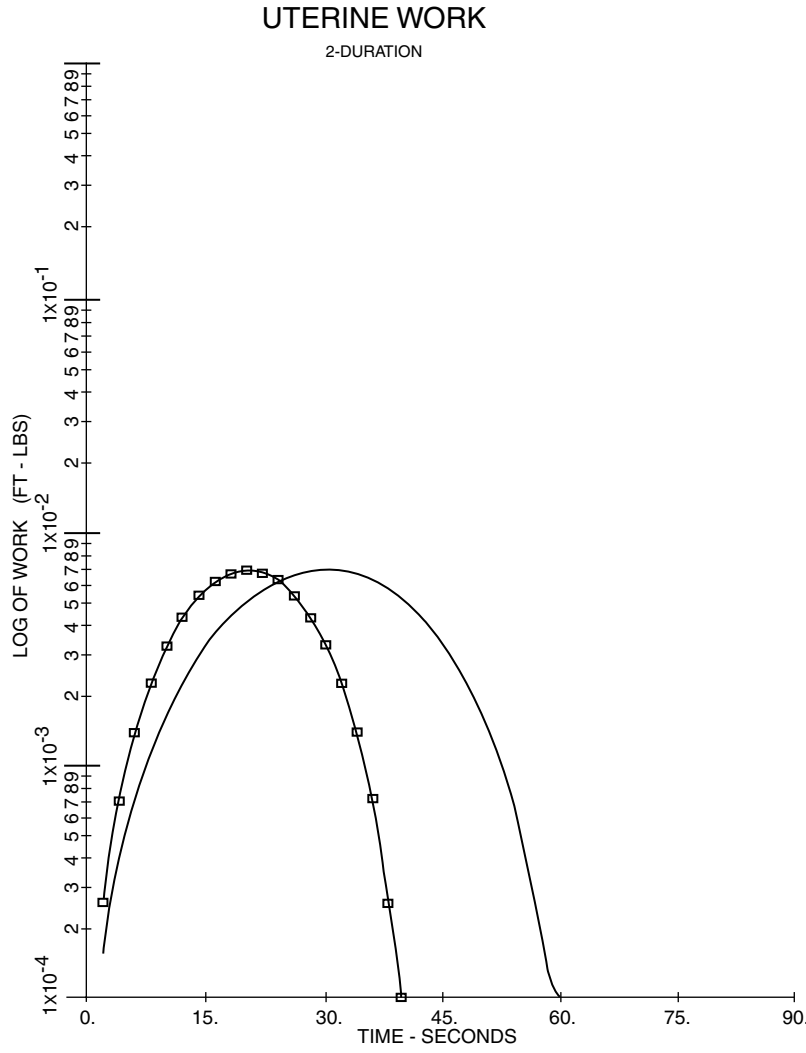

FIGURE 3.5 Time history of uterine work for the standard (60 sec) and a shorter (40 sec) durations of a contraction.

The effects of the tonus, base dilation, time delay, and permanent dilatation were also studied by Kriewall.[15] The efficiency of the contraction is defined and estimated to be on the order of 0.01%, due to a gross overestimation of heat loss to the uterine blood flow.[19] Note that this estimation was based on the misconception of the definition of the efficiency.

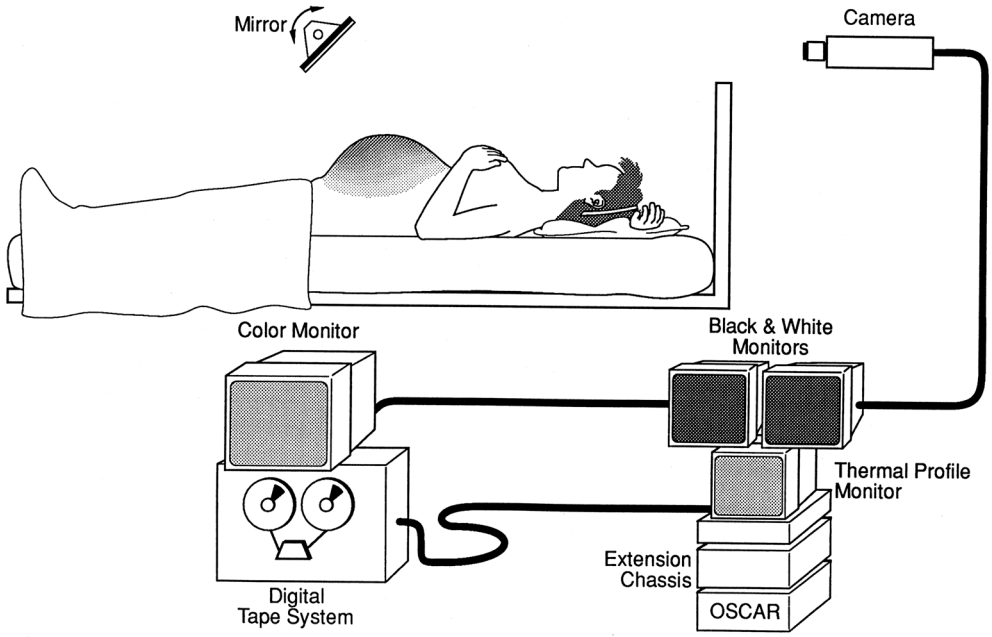

FIGURE 3.6 Clinical setup for infrared thermographing of abdominal wall during the entire parturition process using an AGA infrared thermovision 780 system.

The mechanical approach can predict (1) the work of each contraction and the cumulative sum of this work, (2) how much longer labor may last, and (3) the capability of a normal vaginal delivery or the eventuality of Cesarean sections.

Thermal Approach

In the thermal approach, infrared thermography is used to monitor the temporal and spatial variation of the temperature of whole abdominal wall during normal labor. Based on these measurements, a quasi-steady conduction model is developed to simulate heat transfer through the abdominal and uterine walls. This heat originates in the work of uterine contraction since heat and work are interconvertible, as it is known in thermodynamics.

Infrared Thermography Method

The principle and applications of infrared thermography are available in References 20 through 22 and are thus not repeated here.

The setup included the use of a high-speed infrared detection apparatus, the AGA Thermovision 780 System by the AGA Infrared System AB of Sweden. The clinical setup is illustrated in Fig. 3.6. A mirror with a 99.99% reflective rate was placed on an adjustable frame about 1 m above the patient, which would not obstruct the necessary operation of the obstetrician. The image of the patient's body could be received through the mirror by a signal scanner. The scanner was placed in another room and kept in a horizontal position because liquid nitrogen was used to cool its detector. The system combines real-time infrared scanning with thermal measurement capability. The infrared scanner unit converts electromagnetic thermal energy radiated from the abdominal skin into electronic video signals. These signals are amplified and transmitted via an interconnecting cable to a color display monitor where the signals are further amplified. The resultant signal is displayed on a black and white monitor. In the present study, both color and black and white monitors were employed for display. A digital tape recorder recorded the desired portion of the birth process. The recorder was played back on the color monitor for photographing.

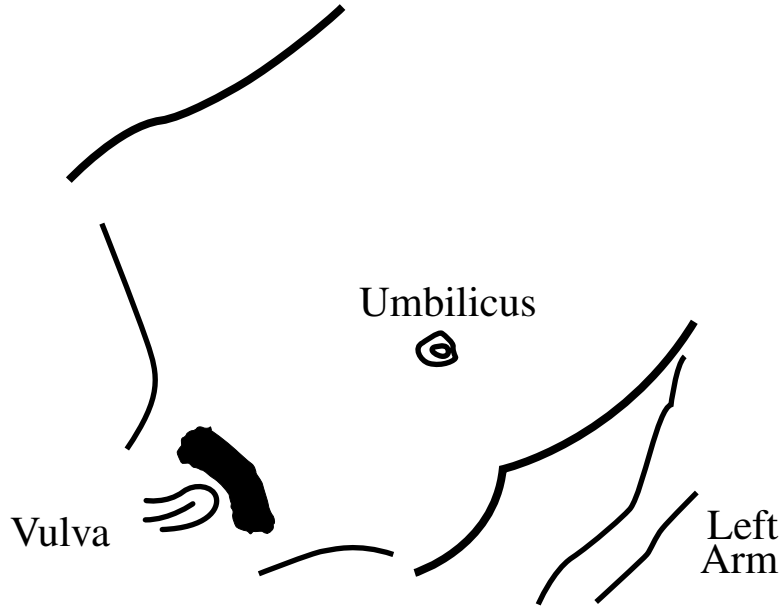

FIGURE 3.7 Orientation of the thermographs of the maternal abdomen (Figs. 3.8 through 3.11).

The detector produces an electronic signal output which varies in proportion to the radiation from the object. The scale of each photograph indicates the level of signal output. A controller can select different signal output levels to vary the color distribution in the photographic image. A proper temperature scale corresponding to a color distribution is thus selected. The color-to-temperature conversion is achieved by a simple calculation.

Three patients were studied whose gestational ages were 24, 26, and 27, respectively. The studies were performed in the same delivery room in July 1988. The patients gave an informed consent for the studies, but only the 27-year-old patient agreed to release the photographs of her labor. The patient went into spontaneous labor for her first baby at a room temperature of 28°C and an atmospheric pressure of 736 mmHG in Beijing, China. Since the infrared detection apparatus had to be installed in a special delivery room, the observations and recordings made through the apparatus could be started only several hours before the deliveries. The 27-year-old patient was sent to the delivery room at 6:15 AM on July 7. The record of her birth process started at 6:30 AM and lasted until the delivery at 8:40 AM.

Figure 3.7 shows the orientation of the photographs. The color bar chart ranges in color from shades of black at the minimum power level, through shades of several other colors, and to shades of purple at the maximum power level. Each color corresponds to certain temperature levels determined through calibration. The color–temperature relationship can be changed during the course of recording to best fit the varying temperature range of the abdominal wall. For example, the color bar chart in Figs. 3.8 and 3.9 has temperatures ranging from 29.5 (dark) to 34.5°C (purple), while that in Figs. 3.10 and 3.11 has the temperatures ranging from 30.5 to 35.5°C. White indicates a temperature exceeding the limit of the scale.

Results and Discussion

Color photographs of the entire birth process of the three patients were taken. A few representative photographs of the 27-year-old patient are depicted here (Figs. 3.8 through 3.11). Figure 3.8 was taken approximately 2 hours before delivery with the color bar chart ranging from 29.5 to 34.5°C. It is obvious that the temperature of the majority of the abdominal wall is between 32.0 and 33.0°C. A cold band at about 31°C appeared to the right of the umbilicus, extending downward from the thorax to the right inguinal area. During a contraction 1 hour and 50 min before delivery (Fig. 3.9), several hot spots at

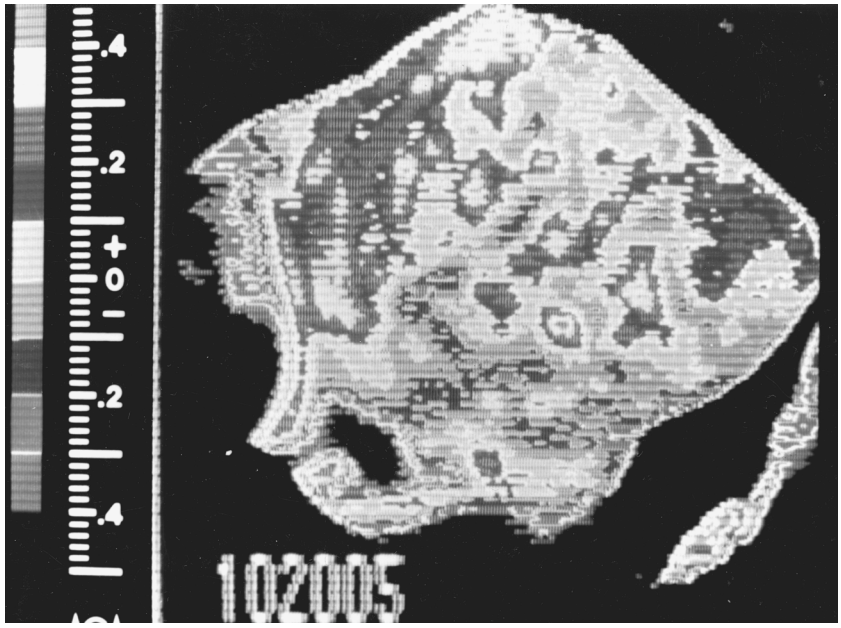

FIGURE 3.8 Thermograph of maternal abdomen 2 hours prior to birth. Temperature range is 29.5 to 34.5°C.

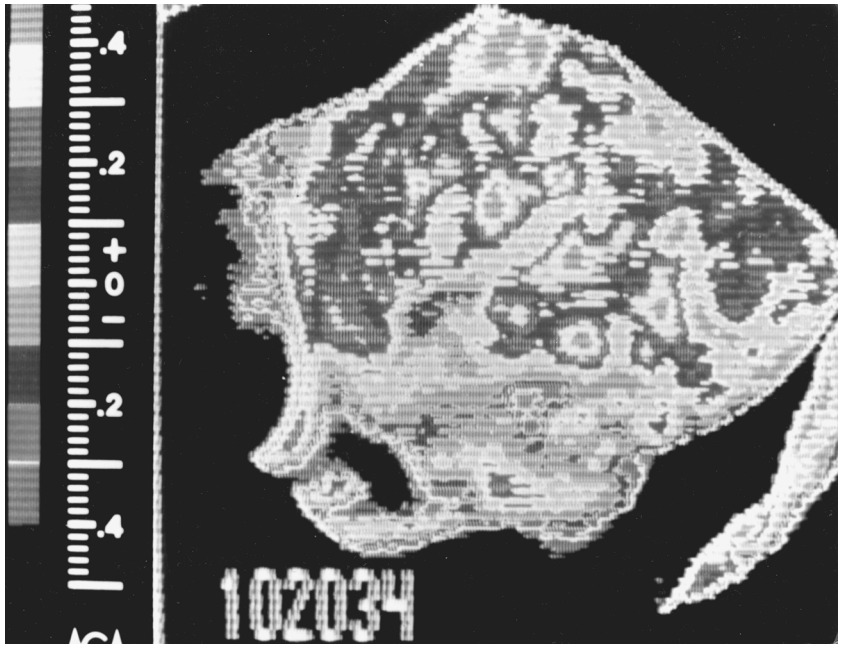

FIGURE 3.9 Thermograph of maternal abdomen 1 hour 50 min prior to birth, during a contraction. Temperature range is 29.5 to 34.5°C.

34°C appeared, scattering randomly on the abdominal wall. the cold band temperature rose to 32°C. As contractions became more frequent, the number of hot spots increased and a hot region spread from the upper right corner of the abdominal wall downward to the right inguinal area. When contractions became intense and continuous, starting approximately 10 min before delivery, the whole abdominal wall had a nearly uniform temperature of 35.5°C, with the cold band at 34.5°C, and several hot spots

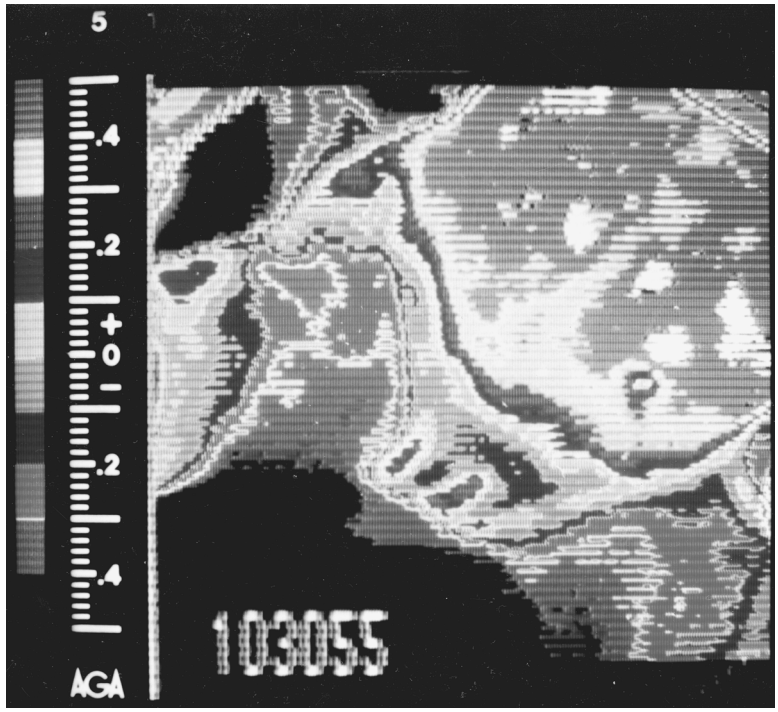

FIGURE 3.10 Thermograph of maternal abdomen 38 sec prior to birth. Temperature range is 30.5 to 35.5°C.

FIGURE 3.11 Thermograph of maternal abdomen immediately following delivery. Infant is seen at the lower left corner of the photograph, still attached by the umbilical cord. Temperature range is 30.5 to 35.5°C.

above 35.5°C. Since the temperature range of the abdominal wall changed the color–temperature relationship, the instrument was adjusted to a new scale (ranging from 30.5 to 35.5°C) in order to keep the same measurement accuracy. Figure 3.10 is a typical photograph which was recorded at 38 sec before

delivery. Figure 3.11 was taken immediately following delivery. The baby, at a temperature above 35.5°C, is shown at the lower left corner, still connected to the maternal body by the umbilical cord. The maternal abdominal wall temperature range following delivery suddenly fell to 31.5 to 33°C characterized by an apparently random temperature distribution which resulted from the rapid relaxation of the maternal abdominal muscles.

These results demonstrate the complexity of the temperature distribution patterns of the maternal abdomen during labor. The heat generated by muscular contractions of the uterus during labor is removed by two mechanisms: convection via uterine venous blood flow and radiation through the abdominal wall. Since uterine perfusion decreases during a contraction, the principal mechanism of heat loss during a contraction is probably radiation. A pattern of increasing abdominal wall temperature distribution is observed as well. A consistent cold spot was noted over the umbilicus. The relatively cool band extending vertically to the right of the umbilicus could be due to the rectum's muscle; however, we cannot explain the absence of a similar band on the left.

The results of this patient are in partial agreement with the findings made by Goodlin and Brooks.[5] We did not note the inguinal and umbilical hot spots which they found, however. The inguinal region tended to be relatively cool, and the suprapubic region was the coolest of all, at least during labor. These differences may be due to differences in instrumentation.

The merits of the present method include measurement sensitivity and global coverage of the abdominal wall. The infrared device is known to have an accuracy of 0.1°C, according to the manufacturer. Since heat results from the work performed during uterine contraction, this method has the potential to non-invasively determine whether significant contractions are occurring. We are undertaking further studies of the work of uterine contractions as measured by heat production.

Rate of Heat Generation in Uterine Wall

Figure 3.12 illustrates the cross-sectional views of (a) the uterus and (b) the abdominal and uterine walls. The uterine wall thickness varies from about 5 mm at the cervix to 15 mm at the middle of the base (or fundus). The uterus is covered by the peritoneum behind, above, and in front, except where it is attached to the base of the bladder. Between the peritoneum and the abdominal skin lie a facia of 1 to 2 mm thickness, a muscle layer of about 5 mm thickness and a fat layer whose thickness varies from 20 to 50 mm in normal cases, but may be 10 to 100 in thickness in extreme cases.

A theoretical model is developed which simulates the heat transfer phenomenon through the abdominal wall as quasi-steady and one-dimensional. The physical geometry consists of two flat plates representing the uterine and abdominal walls of thicknesses b and a, respectively, as depicted in Fig. 3.13. The interior surface of the uterine wall is considered either at the fetus temperature, T_f for models (a) and (b) or insulated for model (c). The exterior surface of the abdominal wall is in convection and radiative heat transfer with the ambient at a temperature of T_∞ and heat transfer coefficient h. The uterine wall undergoes uniform heat generation at a volumetric rate of q''', which results from an energy conversion associated with muscular work, dW/dt per unit volume of the uterine wall, w''' is proportional to the rate of shear in the uterine wall $d\tau/dt$. The problem is formulated in the following.

Let x be the distance measured from the uterine interior wall. Under a quasi-steady state, one-dimensional heat conduction equations in the uterine and abdominal walls read

$$\text{uterine wall:} \qquad d^2\theta/dx^2 + q'''/k_u = 0; \tag{3.7}$$

$$\text{abdominal wall:} \qquad d^2T/dx^2 = 0. \tag{3.8}$$

Here, θ and T denote the uterine and abdominal wall temperatures, respectively, and k_u is the thermal conductivity of the uterine wall. Two cases are considered:

Case 1. Interior surface temperature of the uterine wall = fetus temperature, T_f. The boundary conditions are:

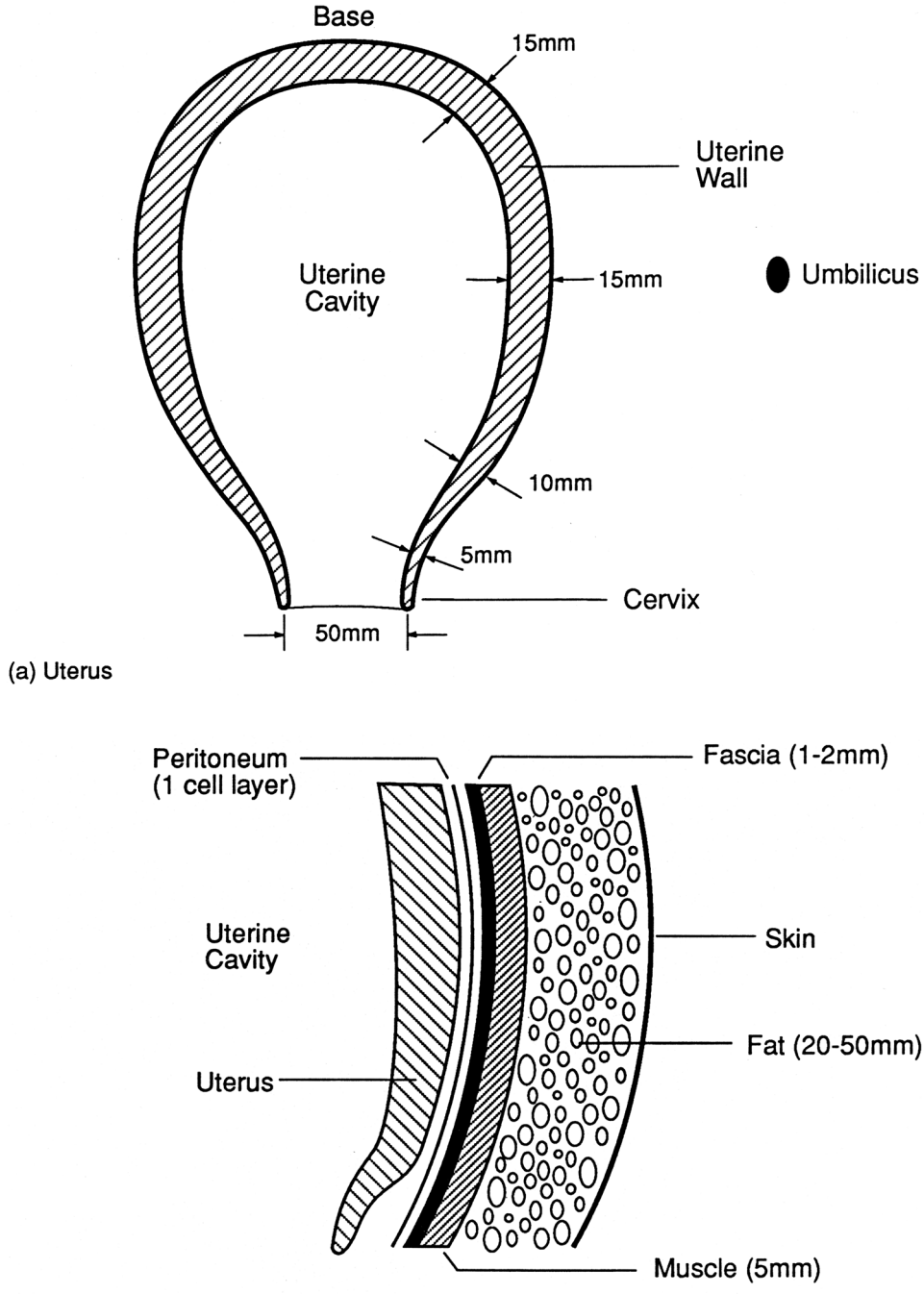

FIGURE 3.12 Median section of the uterus and abdominal wall.

$$\theta(0) = T_f; \tag{3.9a}$$

$$\theta(b) = T(b),\ k_u\, d\theta(b)/dx = k_a\, dT(b)/dx; \tag{3.10}$$

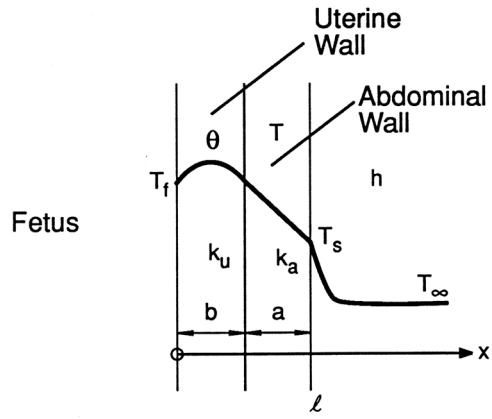

(a) Interior surface temperature of uterine wall equal to fetus temperature

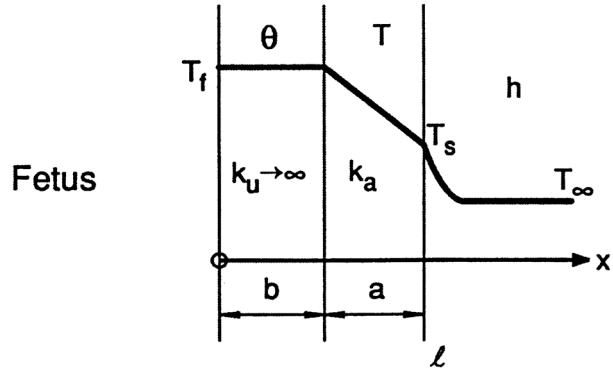

(b) Uniform uterine wall temperature

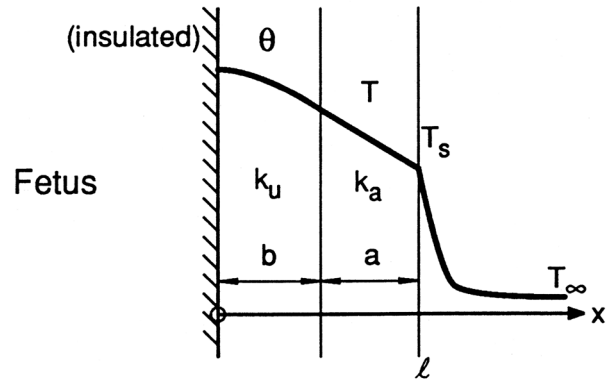

(c) Insulated interior surface of uterine wall

FIGURE 3.13 Quasi-steady, one-dimensional thermal model.

$$-k_a\, dT(\ell)/dx = h[T(\ell) - T_\infty], \tag{3.11}$$

where k_a is the thermal conductivity of the abdominal wall and ℓ is the location of the exterior surface of the abdominal wall, $\ell = a + b$. The solutions are obtained as: uterine wall temperature (for $X < 1$):

$$\theta = -Q_u X^2 + [[K(Q_u + T_f - T_\infty)/1 - K - L - K_a] + 2Q_u]X + T_f; \tag{3.12}$$

abdominal wall temperature (for $L \geq X \geq 1$):

$$T = (Q_u + T_f - T_\infty/1 - K - L - K_a)X + T_\infty - (L + K_a)(Q_u + T_f - T_\infty)/1 - K - L - K_a \tag{3.13}$$

Here,

$$Q_u = q'''b^2/2k_u,\ X = x/b,\ L = \ell/b = 1 + a/b,\ K = k_a/k_u,\ K_a = k_a/hb.$$

For a special case, model (b), in which k_u approaches infinity, Q_u and K become zero and Eqs. (3.12) and (3.13) are reduced to $\theta = T_f$ and

$$T - T_\infty/Q_a = -X + L + K_a \tag{3.14}$$

respectively, where $Q_a = q'''b^2/k_a$.

The heat generated in the uterine wall is transferred through the abdominal wall into the ambient. heat balance yields

$$q''' = h/b(T_s - T_\infty). \tag{3.15}$$

Here, T_s is the exterior surface temperature of the abdominal wall which is monitored by infrared thermography. Equations (3.14) and (3.15) are combined to yield

$$T_f = T_s + q'''ab/k_a. \tag{3.16}$$

Since $q''' = w''' = d\tau/dt$ and $T_f = \theta$, Eqs. (3.15) and (3.16) predict the uterine wall stress rate and the uterine wall temperature, respectively.

Case 2. Insulated fetus. The boundary conditions are identical with those of Case 1, except that Eq. (3.9a) is replaced by

$$d\theta(0)/dx = 0. \tag{3.9b}$$

The temperature distributions are obtained as:

uterine wall temperature (for $X \geq 1$):

$$(\theta - T_\infty)/Q_a = (K/2)X^2 + K/2 - 1 + K_a + L; \tag{3.17}$$

abdominal wall temperature (for $L > X \geq 1$) is identical with Eq. (3.14).

The assumption of uniform heat generation implies that uniform shear force is produced in the uterine wall to push the fetus during delivery. The effective component is applied on the fetus, while the remaining portion of the muscular force is converted into heat within the uterine wall. It is uncertain how much fraction of shear force is effective. The total efficiency of the human heat is estimated to be about 65%.[23] A uterus may have total efficiency in the same order as a heart.

For the limiting cases considered, namely specified interior surface temperature and insulated interior surface of the uterine wall, the latter is mathematically simpler and perhaps more realistic. In both cases, the temperature profiles in the uterine wall are parabolic with maximum temperature located on the

interior surface in Case 2 and inside the uterine wall in Case 1. There will be heat flow from the uterine wall to the fetus in Case 1. The flux of this heat flow is equal to $k_u\, d\theta\,(0)/dx$.

A computation is made on a patient whose entire delivery process was recorded by infrared thermography. The strong labor contractions continued for 10 min prior to delivery during which the entire abdominal surface temperature, T_s, was almost uniform at 35.5°C in the delivery room at a temperature, T_∞, of 28°C. The exterior surface of the abdominal wall of a patient in a supine position during delivery is considered a heated horizontal surface facing upward, since $T_s > T_\infty$. The combined convective and radiative heat transfer coefficient, h, can be determined by the empirical formula:[23]

$$h = A + Bv^n. \tag{3.18}$$

Here, v is the air velocity in m/s while A, B, and n are experimentally determined constants. For the case investigated here, A = 2.7, B = 6.8, n = 0.5, and v = 0 for natural convection in still air. Therefore, h = 2.7 Kcal/h-m^2 –°C = 3.14 W/m^2 –°C. Using the data

$$a = 35 \text{ mm},\ b = 12 \text{ mm},\ k_a = 0.586 \text{ W/M–°C (for biological tissues)},$$

one obtains

$$q''' = 1962.5 \text{ W/m}^3,\ T_f = 36.9°C.$$

Considering the fetus to be at the core temperature of 37°C, the predicted value of 36.9°C is very close. It is known that q''' results from energy conversion associated with uterine force during labor contractions.

3.3 Comparison Between Mechanical and Thermal Approaches

Since work and heat are interconvertible, the work expended by the uterus obtained from the synergistic relationship between intrauterine pressure (IUP) and cervical dilation (CD) should be equal to the heat generated in the uterine wall by contraction. In other words, results obtained should be equal provided that no loss in heat occurs during labor.

It is reported by Kriewall[15] that the work characteristics change with the waveform parameter alterations, with the peak work for a contraction ranging from 9.49×10^{-3} to 0.244 J. for a 60-sec duration contraction (and cervical dilatation). As contractions become shorter and shorter in late labor, the peak work remains unchanged and the cervical dilatation waveform becomes flattened. Finally near the moment of chile delivery, the contraction duration is reduced to zero and the amount of peak work in Joules becomes the work rate in J/sec or Watt. This implies that the work rate is in the order of 0.244 W according to the mechanical model.

In calculating heat generation in the uterine wall, the volume of the wall shown in Fig. 12a can be estimated as the inner surface area, $4\pi(0.05)^2$, m^2 times the wall thickness of 0.015 m, or $[(0.065)^3 - (0.05)^3]/^3$ m^3. Here, the inner radius of the uterus is assumed to be 5 cm. The rate of heat generation in the uterine wall at the moment of delivery is found to be 0.925 W or 1.230 W according to the thermal model. One, thus concludes that both the mechanical and thermal models predict the same order of magnitude, about 1 W for the rate of uterine work in parturition. However, it is important to note that the thermal model is more accurate than the mechanical model because there are no assumptions of waveforms for intrauterine pressure, cervical duration, or others.

3.4 Concluding Remarks

The quasi-steady, one-dimensional conduction model leads to the expression, Eqs. (3.15) and (3.16), for predicting the heat production rate in the uterine wall resulting from strong labor contractions and the

fetal temperature, respectively. The latter prediction appears very accurate. However, it is important to note a lack of precise, *in vivo* information on the thermal conductivity of the uterine wall, k_a, and the dimension of abdominal and uterine walls, a and b. The efficiency of a uterus from which the heat-work energy conversion can be determined is still unknown. more precise information on the temporal and spatial distributions of the abdominal temperature and heat generation rate in the uterine wall can be obtained by the application of inverse problems on the abdominal surface temperature monitored by infrared thermography.

References

1. S. Yrjana, Biophysical Aspects of Uterine Contractions, Department of Physical Sciences, Biophysics, University of Oulu, Oulu, Finland, 1995.
2. B.C. Hirst, *Obstetrics*, W.B. Saunders Co., Philadelphia, PA, 1988.
3. A.L. Galabin, *Manual of Midwifery*, Blakiston, Philadelphia, PA, 1986.
4. R.C. Goodlin and J.W. Chapin, *Am. J. Obstet. Gynecol.,* 143, 97–103, 1982.
5. R.C. Goodlin and P.G. Brooks, *J. Reprod. Med.,* 32, 177–180, 1987.
6. G.P. Marx and D.A.Y. Loew, *Br. J. Anaesth.,* 47, 600–602, 1975.
7. L. Kapusta et al., *Int. J. Gynecol. Obstet.,* 23, 185–189, 1985.
8. W-J. Yang, N. Zhang, and H.F. Andersen, Abdominal Wall Temperature Variations During Labor and Parturition by Infrared Thermography, Abstract, Vol. II, p. 341, First World Congress of Biomechanics, Aug. 30–Sept. 4, 1990, LaJolla, CA.
9. W-J. Yang et al., *J. Biomech. Eng.*
10. E.A. Friedman, *Obstet. Gynecol.,* 6, 567–589, 1955.
11. T.J. Kriewall and A. Work, *Med. Instrumentation.*
12. I. Zador et al., *27th Alliance Eng. Med. Biol..,* Arlington, VA, 1974.
13. J.W. Crawford, *Am. J. Obstet. Gynecol.,* 121, 342–350, 1975.
14. I. Van Praach and C.H. Hendricks, *Obstet. Gynecol.*, 24, 258–265, 1964.
15. T.J. Kriewell, *J. Appl. Physiol.,* 41, 316–322, 1976.
16. J.R. Wilson et al., *Obstetrics and Gynecology, 3rd ed.,* Mosby, St. Louis, MO, 1971, 340.
17. L. Lindgren, The influence of uterine motility upon cervical dilatation in labor, *Am. J. Obstet. Gynecol.*, 117, 530–536, 1973.
18. L. Lindgren and C.N. Smith, Measurement and interpretation of pressure upon the cervix during normal and abnormal labor, *J. Obstet. Gynecol. Br. Commonw.,* 68, 901–915, 1961.
19. J.N. Belchner, V.G. Stenger, and H. Prestowsky, Uterine blood flow in women at term, *Am. J. Obstet. Gynecol.,* 120, 633–640, 1974.
20. W-J. Yang, *Computer-Assisted Flow Visualization,* CRC Press, Boca Raton, FL, 1995, 95–106.
21. G.M. Carlomagno and L. deLuca, Infrared thermography in heat transfer, in *Handbook of Flow Visualization,* W.J. Yang, Ed., Hemisphere Publishing Corp., Washington, D.C., 1989, 531–553.
22. R. Monti, Thermography, in *Handbook of Flow Visualization,* W.J. Yang, Ed., Hemisphere Publishing Corp., Washington, D.C., 1989, 331–353.
23. W-J. Yang, *Biothermal-Fluid Sciences, Principles and Applications,* Hemisphere Publishing Corp., Washington, D.C., 1989, 238.

4

Biothermechanical Techniques in Thermal (Heat) Shock

Wen-Jei Yang
The Univeristy of Michigan

Paul P.T. Yang
University of Cincinnati

Thermal (or heat shock phenomena have been observed in all organisms at the cellular level. They cause an acceleration in the rate of expression of specific genes (heat shock genes), resulting in an increase and accumulation of heat shock proteins in cells. The purpose of this study is to investigate the mechanisms of thermal shock from two different viewpoints: biothermal and biothermomechanical. The former predicts more severe consequences on cells than the latter, whose thermal wave fronts are smoothed due to the coupling effects of thermoelasticity. In conclusion, it is the thermal wave propagation (the so-called "second sound" effect) which triggers a perturbation of normal gene expression. Thermotolerance is found to be inherited in the heat flux equation of the thermal wave model. The information obtained from this study can be useful to therapeutical hyperthermia, preservation of organs and tissues, and laser and cryogenic surgery.

4.1 Introduction

The terms heat (thermal) shock and stress response, interchangeably used in medicine and biology, refer to the response of cellular level living organisms to unfavorable thermal environmental conditions; for example, when a living cell is suddenly exposed to temperatures that exceed the normal growth range levels. Note that the response of living organisms to adverse conditions caused by other inducers (for example, ethanol or arsenite) has also been referred to as heat shock. The phenomenon, which occurs in all cells of organisms, leads to a perturbation of normal gene expression and other cellular events. Changes in the cell range from a temporary change in cell growth and function (due to increased speeds of reactions) to cell death (for example, References 1 and 2). Although the majority die when organisms are exposed to sufficiently severe heat shock or stress conditions, a mild heat treatment may, over a period of time, induce thermotolerance in cells following administration. This results since organisms have a memory and is essential to clinical applications of hyperthermia. As the temperature increases, reactions in the cell occur more rapidly and mismatch is likely to occur. This means that the cell cannot function

properly, i.e., gene production, protein synthesis, and many other cell functions do not take place at the proper pace for normal cell growth and function.

Heat shock, or stress response, has been a subject of great concern in biology and medicine for some time, due to its role in gene expression (for example, References 2 and 3). living organisms respond at the cellular level to adverse conditions such as heat shock or other stressful environments of many different origins, by rapid, vigorous, and transient acceleration in the rate of expression of a small number of specific genes, called heat shock genes. In other words, heat shock leads to a perturbation of normal gene expression (and other cellular events) which takes place in all cells of organisms. Consequently, the products of these genes, commonly referred to as heat shock protein or stress protein, increases and accumulate in cells to reach fairly large concentrations. The heat shock response has been observed in all organisms, and the heat shock proteins are among the most highly conserved proteins in nature.

When organisms are exposed to sufficiently sever heat shock environments, the majority die. However, if they undergo a mild heat treatment prior to this lethal heat shock, a considerable proportion of them survive. This finding has an important implication in the clinical application of hyperthermia for therapy.

The literature pertinent to the heat shock response from the biomedical viewpoint has been surveyed and reviewed in detail in Reference 2. Recently, theoretical molds have been proposed to explore the mechanism of heat shock.[4,5]

This chapter treats the mechanics of the heat shock response from the thermal and thermomechanical viewpoints separately, and discusses how the heat shock may damage cells in all organisms. The former treats the damage on cells to be solely due to heat conduction, while the latter coupled the effects of both temperature and stain. The classical theory of heat conduction (diffusion mechanisms) indicates the severity of the temporal and spatial variations of temperature to be the damage mechanism, while the wave theory in heat conduction suggests the generation of thermal shock wave caused by a rapid change in thermal conditions combined with memory effect in living organisms. The information obtained from the study can also be useful to the therapeutical application of hyperthermia, preservation of organs and tissues, and laser and cryogenic surgery.

4.2 Theory

Three theoretical models have been developed in the course of evolution of studies on the mechanisms of heat shock.

Thermal-Diffusion Aspect of Heat Shock

Cellular structures are modeled with spherical and finite-cylindrical geometries, as show in Fig. 4.1. The cell and its nucleus are in concentric positions. The cell membrane is subject to a sudden change in surrounding temperature, and solutions for the timewise variation in the interior temperatures are obtained. The criterion for inducing heat shock is the temperature gradient which exceeds a lethal value that the cell structure cannot tolerate. Below the heat shock inducing temperature gradient, the cell may restore itself to normal functions when returned to initial conditions/temperatures. Numerical results are obtained for various cases. A qualitative comparison is made between theory and some existing *in vivo* data.

Spherical and cylindrical coordinate systems are employed for the spherical and cylindrical cells with the origin being fixed at the sphere center, and cylinder axis. Let $T_1(rt)$ and $T_2(r,t)$ be the temperatures of the cell and its nucleus, respectively. r and t denote the radial distance and time. The governing heat equations reads

$$\partial T_1/\partial T = \alpha_1 \nabla^2 T_1 \text{ and } \partial T_2/\partial T = \alpha_2 \nabla^2 T_1 \tag{4.1}$$

where α represents the thermal diffussivity. The appropriate initial and boundary conditions are

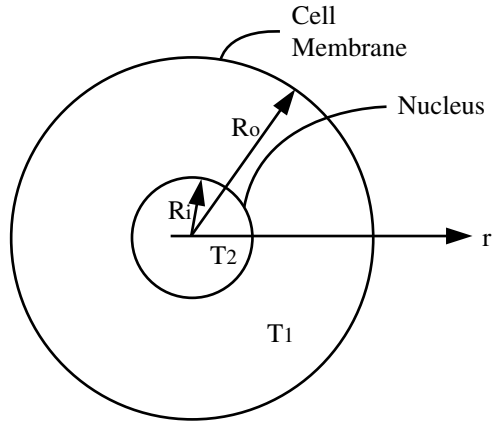

(a) Spherical cell

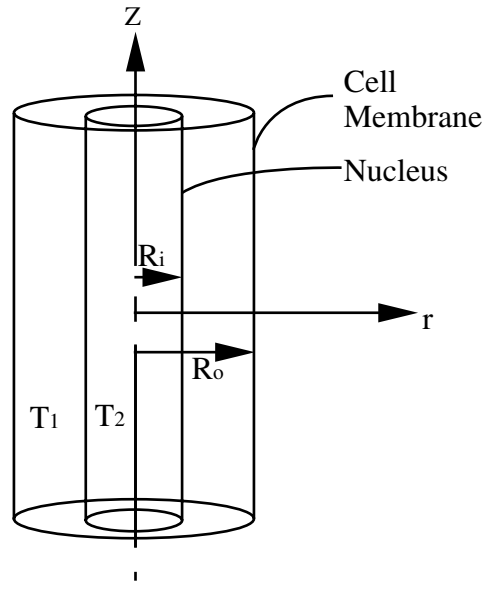

(b) Finite cylindrical cell

FIGURE 4.1 Cell structure.

$$T_1(r,0) = T_2(r,0) = T_0 - k[\partial T_1(R_0,t)/\partial r] = h[T_1(R_0,t) - T_\infty \tag{4.2}$$

$$k_1[\partial T_1(R_i,t)/\partial r] = k_2[\partial T_2(R_i,t)/\partial r] \tag{4.3}$$

$$[\partial T_2(0,t)/\partial r] = 0,\ T_1(R_i,t) = T_2(R_i,t)$$

The situation corresponds to a cell initially at a temperature of T_0 which is suddenly exposed to an environment (such as a culture) at T_∞. h denotes the heat transfer coefficient and k is the thermal conductivity. The solutions for $T_1(r,t)$ and $T_2(r,t)$ can be obtained by means of an intermediate transformation followed by the Laplace transformation technique where u(r,t) is an intermediate variable for the intermediate transformation. In turn taking the inverse Laplace transformation results in Eq. (4.4).

Equation (4.4) shows the temperature-time history in a cell with a very small nucleus for a spherical case where h takes a value of infinity, corresponding to a well-stirred fluid.[6]

$$T_1 - T_0 = (T_{XI} - T_0) + \frac{2R_0(T_{SI} - T_0)}{\pi r}\sum_{n=1}^{\infty}\frac{(-1)^n}{n}\sin\frac{n\pi r}{R_0}\exp\left(\frac{-\alpha_1 n^2\pi^t t}{R_0^2}\right) \tag{4.4}$$

where T_{SI} is the cell membrane temperature. The temporal gradient in dimensionless form is obtained as

$$\left(\frac{\partial T_{1/(\partial t)}}{(T_{SI} - T_0)\alpha_{1/R_0{}^2}}\right) = \frac{2\pi R_0}{r}\sum_{n=1}^{\infty}(-1)^n n^2\sin\frac{n\pi r}{R_0}\exp\left(\frac{-\alpha_1 n^2\pi^2 t}{R_0{}^2}\right) \tag{4.5}$$

which is the factor limiting the survival of a cell following heat shock. Its critical value varies with cell species, like the case for cell survival in freezing and thawing.

In the case of a long cylindrical cell, the results are obtained as

$$T_1 - T_0 = (T_{SI} - T_0) - \frac{2(T_{SI} - T_0)}{R_0}\sum_{n=1}^{\infty}\frac{J_0(r\beta_n)}{\beta_n J_1(R_0\beta_n)}\exp(-\alpha_1\beta^2{}_n t) \tag{4.6}$$

with the temporal gradient in dimensionless form

$$\left(\frac{\partial T_{1/(\partial t)}}{(T_{SI} - T_0)\alpha_{1/R_0{}^2}}\right) = 2\sum_{n=1}^{\infty}\frac{(\beta_n R_0)J_0(r\beta_n)}{J_1(R_0\beta_n)}\exp(-\alpha_1\beta_n{}^2 t) \tag{4.7}$$

Here, J_0 and J_1 represent the Bessel functions of the first kind, or orders 0 and 1, respectively. β_n, n = 1,2,…, are the roots of $J_0(R_0\beta) = 0$. Figure 4.2 illustrates the temperature-time history in a spherical cell of radius R_0 with a very small nucleus of $R_i = 0$ for h = infinite case.

This model treats heat shock as a transient heat transfer phenomenon which is induced by the timewise change in cell temperature. Hence, cell survival as a function of temperature-time variation is analogous to freezing and thawing of a cell. Both Eqs. (4.5) and (4.7) indicate that the local temporal gradients vary exponentially with time. Consequently, there is a certain instant when the gradient takes a maximum value beyond which damage is incurred in the cell.

Thermal Wave Aspect of Heat Shock

If heat shock has such an important consequence on cellular activities, a question naturally arises: what is the nature of heat shock? In other words, how is heat shock induced? Since the time of Fourier in 1822, diffusion theory of heat conduction has prevailed. That is, Fourier's law serves as the constitutive equation relating the heat flux vector a(r,t) to the temperature gradient $\nabla T(r,t)$ as

$$q(r, t) = -k\nabla T(r, t) \tag{4.8}$$

Here, the proportionality constant k is called the thermal conductivity; r is the position vector; and t is physical time. This law states that if a material is subjected to a thermal disturbance, the heating effect will be felt instantaneously in all parts of the conducting medium, although not homogeneously. This means that the speed of heat propagation is infinite, obviously incompatible with physical reality. The paradox of instantaneous propagation of heat was eliminated through the introduction of the thermal wave theory.

In 1867, Maxwell postulated another type of the constitutive equation, based on the dynamic theory of gases. The modified flux law introduces a time lag τ which is required for a heat flux vector to respond to the thermal disturbance, i.e., temperature gradient, being introduced at time t:

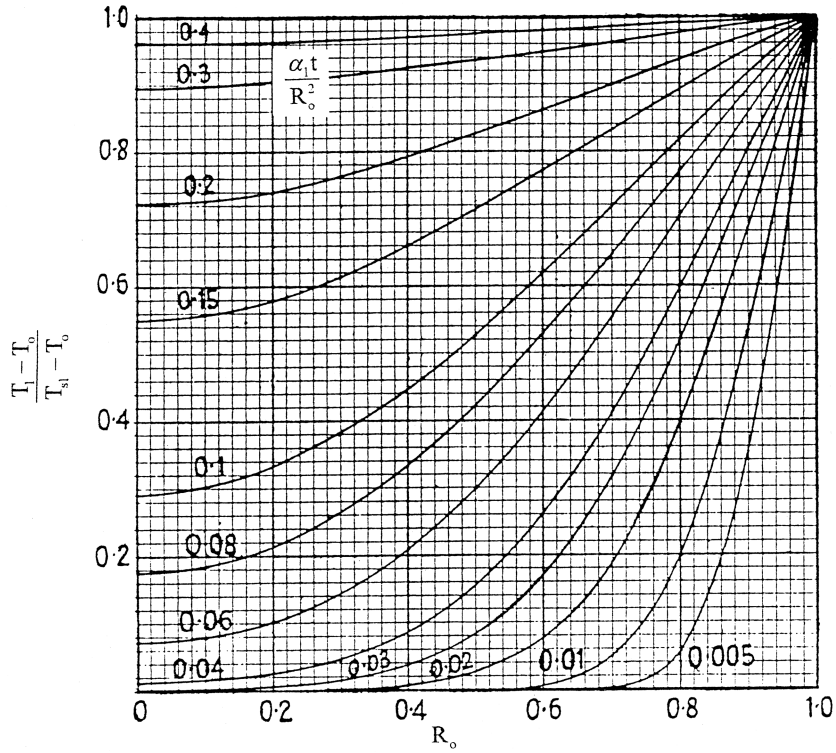

FIGURE 4.2 Temperature distribution at various times in a spherical cell of radius R_o with a very small nucleus for h = infinity case.

$$q(r, t + \tau) = -k\nabla T(r, t) \tag{4.9}$$

This expression is called the Maxwell–Cattaneo (or the Cattaneo–Vernotte) equation. The relaxation time is approximated as

$$\tau = \alpha / C_t^2 \tag{4.10}$$

Here, α is the thermal diffusivity, and C_t denotes the speed of the thermal wave in the medium, commonly referred to as "second sound". The magnitude of τ ranges from 10^{-10} sec for gases under standard conditions to 10^{-14} sec for metals, with values of t for liquids falling within this range. Our intuition is that the values for t for all cells of organisms should be less than 10^{-10} sec but larger than 10^{-14} sec.

With the application of the Taylor's series expansion to q, Eq. (4.9) can be expressed in the linearized form as

$$q(r, t) + \tau \partial q(r, t)/\partial t = -k\nabla T(r, t) \tag{4.11}$$

This is integrated to yield

$$q(r, t) = -\int_0^t (k/\tau_0) \exp[-(t - t')/\tau] \nabla T(r, t') dt' \tag{4.12}$$

A comparison of Eqs. (4.8) and (4.12) reveals the principle difference between the diffusion model and the thermal wave model: the heat flux q at time t is a point function of ∇T at time t in the diffusion model, but in the wave model is a path function (over the entire history) from t = 0 to t during which

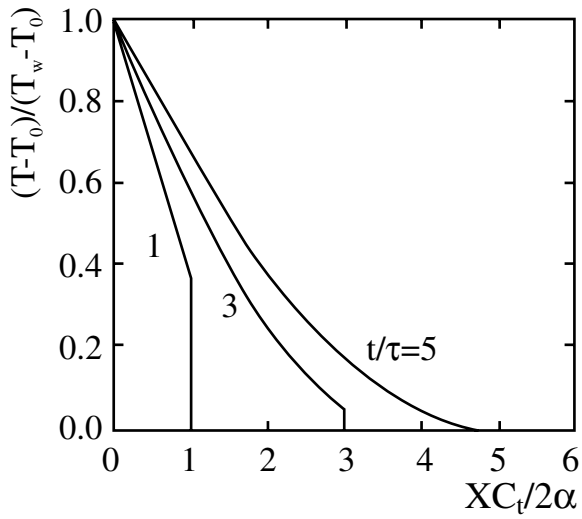

FIGURE 4.3 Temperature–time history in a semi-infinite, one-dimensional solid with a suddenly applied wall temperature T_w at X = 0.

∇T is established.[7,8] In other words, Eq. (4.12) implies heat conduction in a material with the time constant of fading memory.[9] Equation (4.10) and the energy equation

$$-\nabla \bullet q + S(r, t) = pC((\partial T)/(\partial T)) \tag{4.13}$$

are combined to yield: Eq. (4.8) the heat flux formulation as

$$\nabla[\nabla \bullet q] - \nabla S(r, t) = (1/\alpha)[\tau((\partial^2 q)/(\partial t^2)) + (\partial q)/(\partial t)] \tag{4.14}$$

by eliminating temperature T.[10] Equation (4.9) the temperature formulation is

$$\nabla \bullet k\nabla T(r, t) + [S(r, t) + \tau((\partial S(r, t))/(\partial t))] = pCp[(\partial T(r, t))/((\partial t) + \tau(\partial^2 T(r, t)))/(\partial t^2)] \tag{4.15}$$

through the elimination of heat flux q. Here, S represents the volumetric rate of heat generation such as heat generation due to metabolism, external heat sources, transformation from stressed, synthesis, etc. P, Cp, and α denote the density, specific heat, and thermal diffusivity of the medium, respectively. It is seen that both the temporal and spatial derivatives of the body heat function S(r,t) appear in the hyperbolic heat conduction equation, $\partial S/\partial t$ in Eq. (4.15) and $\partial S/\partial r$ in Eq. (4.14). A sudden increase in the localized temperature or that generation rate in a material can be represented by the Dirac delta function (i.e., a unit impulse). This delta function becomes a part of the solution to the heat conduction equation with time lag, and it mathematically creates the thermal shock wave that travels through the material. For example, consider a semi-infinite, one-dimensional solid subject to the disturbance of a suddenly applied temperature T_W at the surface at x = 0. The initial conditions are $T = T_0$ and $\partial T/\partial t = 0$ at t = 0. The temperature-time history is shown in Fig. 4.3. The difference between the conventional diffusion and thermal wave models is in a sharp wavefront in the thermal wave propagation. Across the wavefront, the temperature presents a finite jump while the temperature gradients present a singularity (not shown). It is the propagation of this wavefront that creates the phenomenon of thermal shock. The diffusion and wave models coincide at large times. The thermal shock wave conducts heat through the material at an exponential rate, much faster than typical heat diffusion. It soon becomes too weak to actually transmit much heat. Then, slow diffusion dissipates the rest of the heat until a steady state is reached. In most materials, the thermal shock effects are negligible because they dissipate with a very

short distance, perhaps within 100 or so mean free paths of a phonon. A phonon is the particle that transmits heat. However, the thermal shock effects are very important to heat conduction in all cells of organisms.

Since heat is transferred by phonons, quantum theory applies because these particles have wave-like properties, and thus can be used to justify the existence of thermal shock waves. Tzou[7] derived a general criterion for determining whether thermal shock waves or diffusion would be the principal heat conduction process:

$$(\partial T)/(\partial t) \gg ((T_0 C_t^2)/(2\alpha))\exp(C_t^2/\alpha)$$

Here, T_0 is the reference temperature. Three conditions for thermal shock waves to become the dominant form of heat conduction are revealed from Eq. (4.16)

1. The reference material temperature T_0 must be low.
2. The timewise temperature variation $\partial T/\partial t$, or consequently, the heat flux in a material, is very high. One way to get a sufficiently high heat flux is to use irradiation, for example by microwave or ultrasonic heating of cells. This is the situation observed in hyperthermia. Another way is to use high powered lasers. When lasers initially focus on a material, the heat flux between the exposed material and its adjacent medium becomes very high. The exposed material has almost instantly reached a high temperature, while heat has not yet diffused to the adjoining medium. Thermal shock waves are formed to rapidly conduct some of the heat away from the exposed material, thus rapidly heating its neighboring medium. This is the situation encountered in laser surgery. It should be noted that a rapid cooling may also induce a thermal shock, as in the cases of cryosurgery and cryotherapy. For example, that transmitted from the tip of a cryoprobe to the adjacent material would create a large heat flux because of the sharp difference in temperature.
3. Thermal shock waves are observed for a short time after the initiation of a transient. This might occur immediately following the application of microwave irradiation, a pulse laser, or a cryoprobe.

The three situations when thermal shock waves occur are closely coupled. The same situation that will have a low temperature will have a high rate of temperature change and a short time. This is obvious from the approximation that

$$(\partial T)/(\partial t) \cong (\Delta T)/(\Delta \tau) \tag{4.17}$$

However, the dirac delta function will rapidly dissipate the thermal shock waves which are, in turn, a very strong function of time.[11]

It is important to emphasize that of high heat flux, low temperature, and short time span, the common condition in biology and medicine is the short time span. This is because the distances involved in heat transfer in biology and medicine are cellular, even though organs and tissues are macro in size. The distances are cellular because damage to organs and tissues from heat transfer happens on the cellular level.

Two examples are presented to illustrate some features in thermal waves which may exert a strong influence on organisms. Figure 4.4 depicts thermal wave propagation in a one-dimensional solid subjected to the excitation of a suddenly applied temperature T_w at the wall at $x = 0$.[12] A sharp wave front advances in the material, separating the heat-affected region from the thermally undisturbed region. Across the wave front, the temperature presents a jump while the temperature gradient exhibits a singularity. It is believed that this sharp wave front and the singularity in the temperature gradient exert a strong stimulation on cells in an organism. Figure 4.5 displays the reflection and attenuation of the temperature wave, propagating back and forth between two boundaries, resulting from an energy pulse of width $\Delta\eta$.[13] The arrow indicates the direction of thermal wave propagation. Figure 4.6 shows the thermal wave emanating from a heat source moving at a thermal Mach number (M), defined as the ratio of the speed of the moving heat source to the thermal wave speed.[12]

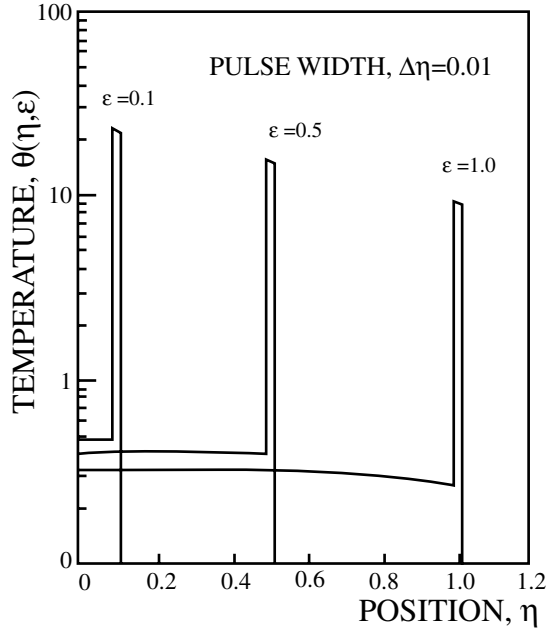

FIGURE 4.4 Temperature solutions to the hyperbolic heat equation with a pulsed heat source.

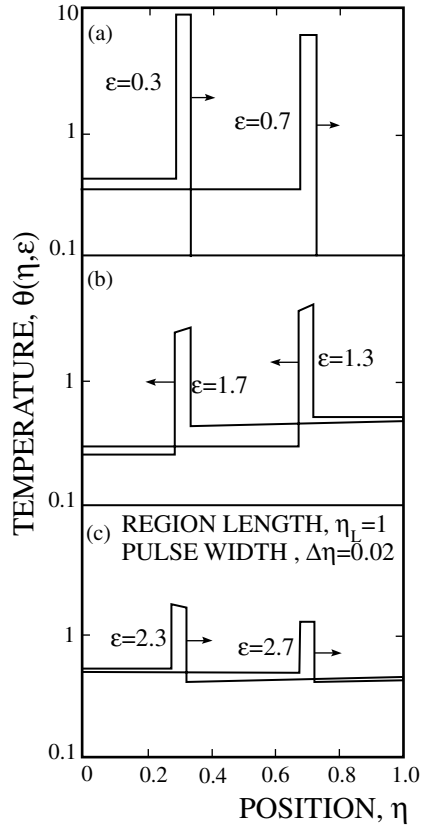

FIGURE 4.5 Temperature distributions for a sequence of times resulting from an energy pulse.

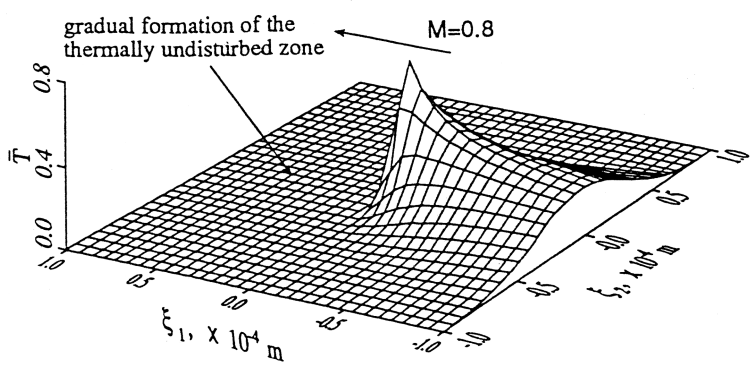

FIGURE 4.6 Temperature waves emanating from a heat source moving at M = 0.8. Gradual formation of the thermally undisturbed zone.

When organisms are exposed to sufficiently severe heat shock or stress conditions, the majority die. However, if they undergo a mild heat treatment preceding this lethal heat shock, a substantial portion of them survive. Take the experiment of Reference 15 as an example. Most or a third of all third-instar Drosophila larvae die being exposed to a temperature of about 40°C for 20 min. However, if the larvae are pretreated at 33 to 35°C for 30 min and then exposed to the lethal temperature, one half of them survive. (Note the ambiguity of their experimental procedure without an appropriate control or measurement of the initial heating rate of $\partial T/\partial t$ at t = 0.) The reason that a mild heat pretreatment protects the organisms from death caused by a more severe heat shock immediately thereafter is explained by the physical significance implied in Eq. (4.12). That is, the heat flux at the present instant depends on the past history during which the temperature gradient is established. This is the unique feature of the thermal wave theory which presents a strong path od dependency. The pretreatment of normal cells for survival has been used in clinical applications, for example, in cancer therapy by hyperthermia.

Thermomechanical Aspect of Heat Shock

If an external mechanical agency (namely a stress) produces variation of strain in a material, these variations of strain are, in general, accompanied by variations in temperature and consequently by a flow of heat. The whole process thus gives rise to an increase of entropy and therefore an increase in the energy stored in a mechanically irrecoverable manner. This phenomenon is known as thermoelastic dissipation, which has been observed in all organisms. The dissipative process is described by the term involving the coupling effect between temperature and stain rate. The thermoelastic coupling coefficient δ is defined as

$$\delta = (3\lambda + 2\mu)^2\beta^2T_0/(\lambda + 2\mu)\rho C_v \tag{4.18}$$

in which λ and μ are Lame's elastic constants and b is the thermal expansion coefficient. The coupling effect becomes negligible when $\delta << 1$.[16]

The inertia effect is another important factor in a transient thermoelasticity problem. Taking into account inertia effects but uncoupled, Danilovskaya[17] found the process of transmission of thermal stresses through the propagation of elastic waves at the speed of

$$C_s = [(\lambda + 2\mu)/\rho]^{1/2} \tag{4.19}$$

"Second sound" effects, which may well be small and short-lived in elastic solids, modify dynamic thermoelasticity theories. In 1967, Lord and Shulman[18] used the constitutive equation (4.11) to formulate a generalized dynamical theory of thermoelasticity. They obtained the coupled equations of motion and energy, both hyperbolic. Later Green and Lindsay[19] proposed a generalized theory of dynamic thermoelas-

ticity based on a vigorous treatment of thermodynamics. The new theory introduces the elastic-stress relaxation time τ_1 and entropy relaxation time τ_2 for thermoelastic processes.

The basic equations of linearized thermoelasticity are listed below, using Cartesian tensors.

Conservation equations:

(i) Mass:

$$\rho_o/\rho = 1 + U_{k,k} \tag{4.20}$$

(ii) Motion:

$$\sigma_{jij}\rho b_i = \rho\partial^2 U_i/\partial t^2 \tag{4.21}$$

$$\sigma_{ij} = \sigma_{ji}$$

(iii) Energy (heat conduction):

$$T(\partial\eta/\partial t) = -\nabla\cdot q + S \tag{4.22}$$

Here, the subscript o denotes the reference (stress-free) state; σ_{ij}, (Cauchy) stress tensor; U_i, displacement vector; b_i, body force vector; and h, entropy. A comma (,j) represents partial differentiation with respect to $x_j (j = 1, 2, 3)$.

Constitutive equations:

(i) Stress–strain (Duhamel-Neuman) relations:

$$\sigma_{ij} = C_{ijkl}U(k,l) - \beta_{ij}(T + \tau 1(\partial T/\partial t)) \tag{4.23}$$

(ii) Heat flux–temperature gradient relation:

identical to Eq. (4.11)

(iii) Entropy production inequality:

$$\eta = \eta_o + (\rho_c/T_o)T + (\rho_c T^2/T_o)\partial T/\partial t + (\rho/\rho_o)\beta_{ij}U_{(i,j)} \tag{4.24}$$

in which C_{ijkl} signifies the tensor of elastic moduli ($C_{ijkl} = C_{jikl} = C_{ijlk} = C_{klij}$); β_{ij}, tensor of thermal moduli ($\beta_{ij} = \beta_{ji}$); k_{ij}, thermal conductivity tensor ($k_{ij} = k_{ji}$) and $U_{(k,l)} = 1/2\ (U_{k,l} + U_{l,k})$, strain tensor.

For $\delta = 0$, Prevost and Tao[20] suggest computing the thermal wave speed as

$$C_t(\alpha/\tau_2)^{1/2} \tag{4.25}$$

in contrast to Eq. (4.10). However, experimental values for τ_1 and τ_2 are not available. Restricting the thermal wave speed to less than or equal to the speed of sound C_a, one can estimate τ_2 to be

$$\tau_2 = \alpha/C_a^2 \tag{4.26}$$

Based on thermodynamical arguments, τ_1 is restricted by

$$\tau_1 >= \tau_2 >= 0 \tag{4.27}$$

Using the property of water for cells, the value of τ_2 for cells is approximately 0.061 sec at a temperature of 20°C.

As an example, consider a one-dimensional solid subject to the disturbance of a suddenly applied temperature T_w at the wall at x = 0. this is the same problem as the first example in the previous section, except that effects of thermoelasticity will be included here. I has been solved analytically within the context of classical uncouple thermoelasticity (i.e., $\tau = \tau_1 = \tau_2 = 0$, $\delta = 0$) by Sternberg and Chakravorty.[21] Prevost and Tao[20] solved the problem for the case of the Green–Lindsay thermoelastic model (i.e., $\tau_1 = \tau_2 = \alpha/c_s^2$) using the finite element method. Figure 4.7 shows the timewise variations of the dimensionless temperature, axial displacement and axial stress recorded at a distance a from the wall, where $a = \alpha/C_s$. The effects of different thermal wave speeds are depicted in the figure, where $C_t = C_s$ and $C_t = 2C_s/3$. In addition, results for the classical thermoelastic model correspond to $C_t = \infty$. The following observations are noteworthy:

1. There is a drastic difference between the predictions of the Green–Lindsay model and those of the classical model due to the incorporation of τ_1 and τ_2 (especially τ_1).
2. Although restricted to very short time durations, the effect of finite thermal propagation speeds is important.
3. The time lag in the temperature, axial displacement, and the axial stress responses increases with a decrease in the thermal wave speed.
4. In comparison with the thermal wave theory in the previous section, the coupling of heat conduction and elasticity in a medium results in the smoothing of a sharp wave front (Fig. 4.3) that exists in the thermal wave propagation, as seen in Fig. 4.7a. This observation leads to an important conclusion, that heat shock based on heat conduction theory would exert more severe effects on organisms than heat shock treated by the thermoelastic mode.

4.3 Discussion

In homogeneous media, it has been estimated that the magnitude of τ is on the order of 10^{-8} to 10^{-10} sec for gases at standard conditions, 10^{-10} to 10^{-12} sec for liquids and dielectric solids, and 10^{-14} sec for metals. In nonhomogeneous media, Luikov[22] suggested that the magnitude of t can range from 10^{-3} to 10^{3} sec depending upon process intensity. Braznikov et al.[23] gave τ = 20 to 30 sec for meat products.

Kaminski[9] presented a detailed explanation of the physical meaning of τ and methods for the experimental determination of τ. For homogeneous media, the thermal interaction of structural elements is at the molecular or crystal lattice level. τ has a meaning and value of the relaxation time. Treating cells as a nonhomogeneous material, the thermal interaction of cellular structural elements is at a different level and τ may take a much higher value. The τ value for cells is not available and needs to be measured in the future. The temperature profile indued by a step change at the wall of a nonhomogeneous material is characterized by a sharp wave front[9] as observed in the case of a homogeneous medium, as depicted in Fig. 4.3. One may thus derive a conclusion that the thermal wave analysis for homogeneous media can also be applied to nonhomogeneous materials with the use of different values of τ.

In the thermal aspect, three conditions for thermal shock waves to become the dominant form (over diffusion mechanism) of heat conduction are: high heat-flux, low temperature, and short time span. Among them, the common condition in biology and medicine is the short time span. This is because the distances involved in that transfer in biology and medicine are cellular, even though organs and tissues are macro in size. The distances are cellular because damage to organs and tissues from that transfer happens on the cellular level. Two examples are presented to illustrate some features in thermal waves which may exert strong influence on organisms.

When organisms are exposed to sufficiently severe heat shock or stress conditions, the majority die. However, if they undergo a mild heat treatment preceding this lethal heat shock, a substantial portion of them survive. The reason is that the heat flux at the present instant depends on the past history during which the temperature gradient is established. This is the unique feature o the thermal wave theory which presents a strong path of dependency. The pretreatment of normal cells for survival has been used in clinical applications, for example, in cancer therapy by hyperthermia.

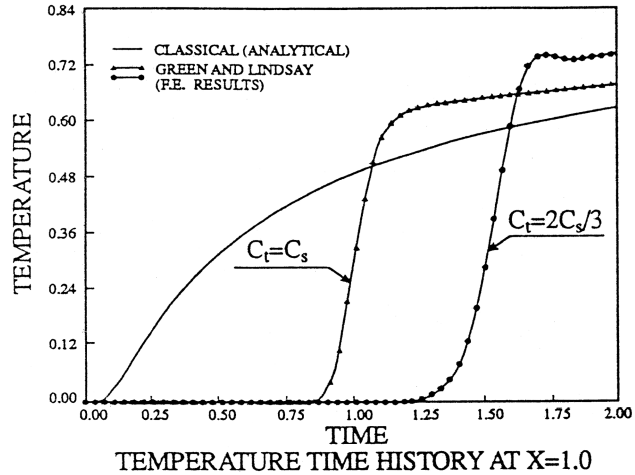

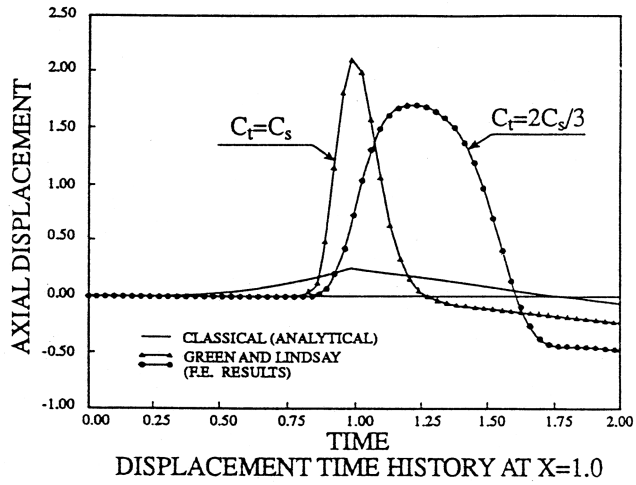

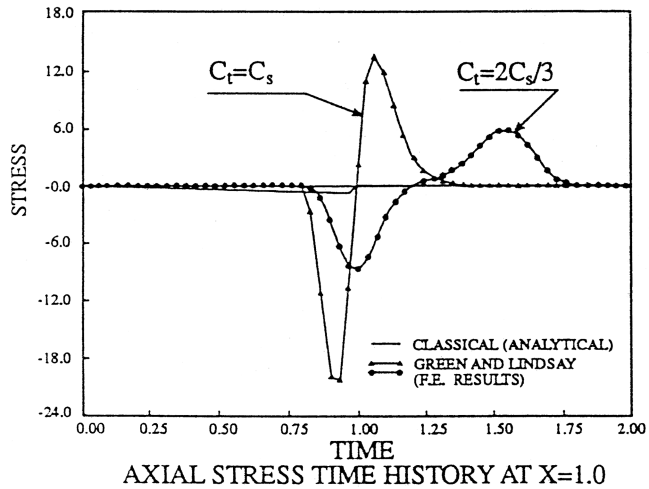

FIGURE 4.7 Components time histories at X = 1.0/ Green and Lindsay's thermoelastic model. (a) Temperature time history. (b) Axial displacement time history. (c) Axial stress time history.

From the thermomechanical viewpoint, the coupling of heat conduction and elasticity in a medium results in the smoothing of a sharp wave form that exists in the thermal wave propagation. This observation leads to an important conclusion, that heat shock based on heat conduction theory would exert more severe effects on organisms than heat shock treated by the thermoelastic model.

In short, it is identified that "second sound" effects, a propagation of thermal waves with sharp wave fronts, trigger the rapid, vigorous, and transient acceleration in the rate of expression of heat shock genes. these effects which are more severe according to the thermal wave model, are moderated by the coupling of the thermal and mechanical disturbances. the thermal wave theory is applicable to both homogeneous and nonhomogeneous materials, provided that an appropriate value of the thermal relaxation time is employed. Thermotolerance in organisms is found to be inherited in the heat flux equation of the thermal wave model. A quantitative treatment of thermal shock phenomena in organisms requires information on the magnitude of thermal, elastic stress, and entropy relaxation times.

4.4 Conclusions

Thermal shock phenomena in organisms have been treated within the contexts of both heat conduction and thermoelasticity in materials with an intermediate duration of memory. It is identified that "second sound" effects, a propagation of thermal waves with sharp wave fronts, trigger the rapid, vigorous, and transient acceleration in the rate of expression of heat shock genes. These effects, which are more severe according to the thermal wave model, are moderated by the coupling of the thermal and mechanical disturbances. The thermal wave theory is applicable to both homogeneous and nonhomogeneous materials, provided that an appropriate value of the thermal relaxation time is employed. Thermotolerance in organisms is found to be inherited in the heat flux equation of the thermal wave model. A quantitative treatment of thermal shock phenomena in organisms requires information on the magnitude of thermal, elastic stress, and entropy relaxation times.

References

1. M.J. Schlesinger, M.G. Santoroand, and E. Garaci (Eds.), *Stress Proteins—Induction and Function*, Springer-Verlag, Berlin, 1990.
2. R.I. Morimoto, A. Tissieres, and C. Gerogopoulos (Eds.), *Stress Proteins in Biology and Medicine*, Cold Spring Harbor Laboratory Press, New York, 1990.
3. M.-J. Gething and J. Sambrook, *Nature,* 355, 33, 1992.
4. W-J. Yang and T.L. Danks, *Analytical Models for the Mechanism of Heat Shock, 1992 Advances in Bioengineering*, M.W. Bidez, Ed., BED-Vol. 22, ASME, New York, 455, 1992.
5. W-J. Yang, *J. Biomech.,* 115, 617, 1993.
6. H.S. Carslaw and J.C. Jaeger, *Conduction of Heat in Solids*, Oxford University Press, Oxford, England, 1959, 233, 327–328.
7. D.Y. Tzou, Thermal shock phenomena under high-rate response in solids, *Ann. Rev. Heat Trans.,* C.L. Tien, Ed., Hemisphere, Washington, D.C., 1992, 111–185.
8. M.N. Oziski and D.Y. Tzou, On the wave theory in heat conduction, *ASME HTD-Vol. 227, Fundamental Issues in Small Scale Heat Transfer*, New York, 1992, 13–27.
9. W. Kaminski, *J. Heat Transfer,* 112, 555, 1990.
10. J.I. Frankel, B. Vick, and M.N. Ozisik, *J. Appl. Phys.,* 58, 3340, 1985.
11. B. Vick and M.N. Ozisik, *J. Heat Transfer,* 105, 902, 1983.
12. K.J. Baumeister and T.D. Hamill, *J. Heat Transfer,* 91, 543, 1969.
13. M.N. Ozisik and B. Vick, *Intl. J. Heat Mass Transfer,* 27, 1845, 1984.
14. D.Y. Tzou, *J. Heat Transfer,* 111, 232, 1989.
15. H.K. Mitchell, G. Moller, N.S. Petersen, and Lipps–Sarmiento, *Dev. Genet.,* 1, 181, 1979.
16. B.A. Boley and J.H. Weiner, *Theory of Thermal Stresses*, John Wiley & Sons, New York, 1969, 43.
17. V.I. Danilovskaya, *Priklanaya Matematika I Mekhanika*, 14, 316, 1950.

18. H.W. Lord and Y. Shulman, *J. Mech. Phy. Solids*, 15, 299, 1967.
19. A.E. Green and K.A. Lindsey, *J. Elast.,* 2, 1, 1972.
20. J.H. Prevost and D. Tao, *J. Appl. Mech.,* 50, 817, 1983.
21. E. Stemberg and J.G. Chakravorty, *J. Appl. Mech.,* 26, 503, 1959.
22. A.V. Luikova, *Intl. J. Heat Mass Transfer,* 9, 139, 1966.
23. A.M. Branzhikov, V.A. Karpychev, and A.V. Luikova, *Inzhenerno Fizicheskij Zhurnal,* 28, 677, 1975.

5

Contributions of Mathematical Models in the Understanding and Prevention of the Effects of Whole-Body Vibration on the Human Spine

Vijay K. Goel
University of Iowa

Joseph M. Schimmels
Marquette University

Fred Chang

Yi Wan
Marquette University

5.1 Introduction

Vibration is most simply defined as oscillating motion. It could be periodic or nonperiodic. Repeated loading of the lumbar spine occurs in activities of daily living like lifting and driving. Epidemiological studies point to repeated loading of the spine as one possible cause of low-back problems. The chronic exposure results in mechanical and chemical changes in the spinal components leading to spinal degeneration. These disorders in a person may lead to discomfort, loss in productivity, and an enormous increase in health care cost to society. In a chronic vibration environment, the prevalence of low-back problems is dependent on a host of factors including subject age, subject posture, magnitude of input vibration, and exposure time. It is imperative that efforts be made to understand the effects of whole-body vibration on the spine and how these can be prevented.

A number of approaches have been used to address these issues. This chapter focuses on the contributions of the mathematical models in this area. The next section provides a review of the epidemiological and other related studies delineating the effects of whole-body vibration on the human spine. Following this, lumped parameter models of the human body and finite element models of the lumbar spine are described. These models help us understand the likely basis for these effects and help us identify ways in which the effects may be prevented or reduced.

5.2 Epidemiology

The frequency of low-back pain (LBP) and associated disabilities appears to be increasing. Bremner et al. [1] suggest that the interface of people with rotational and oscillating machinery in industrialized societies may be the cause of the escalation of low-back problems. In a vehicle, the primary source of vibration is the interaction of the vehicle and the ground surface, but any component of the vehicle — engines, wheels, or drive shaft, for example — may be a source as well. Similar conclusions have been reported by other authors [2-13]. Cremona [7] reported a 70% prevalence of low-back pain in heavy equipment users. In the coal mining industry, 29% of workers attribute their LBP to traveling in vehicles. A review of published literature by Seidel et al. [13] revealed that people who sit in a vibrating environment that exceeds the exposure limit determined by the ISO place their musculoskeletal system at risk.

Frymoyer et al. [3] studied exposure to vibration associated with truck driving, tractor driving, and heavy equipment operation. The vibration environments had frequencies from 3.5 to 8.9 Hz with vertical accelerations of up to 2.6 g. Wilder et al. [4] found that vertebral bodies in the lumbar area underwent degenerative and geometric changes due to chronic occupational whole-body vibration exposure, based on studies of the truck drivers. Schmidt [8] compared drivers of heavy trucks and bank employees. Of the truck drivers, 75% had pathological changes of the spine compared to 61.1% of the bank employees. Both Heliövaara et al. [9] and Kelsey et al. [10] found an increased incidence of herniated discs with long-term exposure to driving automobiles and trucks. Kelsey et al. [10] also found that the relative risk was 2.75 for car drivers and 4.67 for truck drivers. Beevis and Forshaw [11] argued that back injury was due to intense vibration acceleration levels in conjunction with the poor posture of the spine. The data of Seidel et al. [13] suggested an increased health risk of the peripheral nervous system after intense, long-term, whole-body vibration. Pathological findings depend on subject age, subject posture, magnitude of input vibration, and exposure time.

In vivo biomechanical studies have helped us understand the effects of whole-body vibration on the spine in seating, standing, and supine postures in terms of its resonant frequency, transmissibility, impedance, and activity of the muscles spanning the spine.

Resonant frequencies of the spine occur between 4 and 6 Hz, attributed to upper torso vibration in the vertical direction with respect to the pelvis, and between 10 and 14 Hz, representing a bending vibration of the upper torso with respect to the lumbar spine.

The resonant frequencies also change with posture [4, 14]. Dieckmann [15] found that, in the standing posture, the first vertical natural frequency was about 5 Hz and the second was 12 Hz. Under horizontal excitation, 1 to 3 Hz was found to be particularly severe. Panjabi et al. [16] and Pope et al. [17, 18] showed that the resonant frequency in the lumbar region of the vertically vibrated, seated operator was 4.5 Hz. Zagorski et al. [19], using accelerometers taped to the backs of human subjects, found greater acceleration at L3 than at the sacrum, in the 2- to 5-Hz frequency range. For the relaxed seated posture, a transmissibility peak was recorded at L3 at 5 Hz coupled with an attenuation peak between 7 and 8.5 Hz [20]. For the erect seated posture, the response curve had the same general form but lower transmissibility peak. Pope et al. [21] also studied the effect of using cushions under the buttocks while sitting in a vibratory environment. Three different types of cushions were analyzed: two made of foam of different stiffness and one of a viscoelastic material. Response curves were measured for each cushion and compared to the curve with no cushion. The least stiff material moved the transmissibility peak to below 4 Hz and, at the same time, increased its amplitude. The high-frequency response was also markedly changed. The stiffer material tended to increase the frequency of the transmissibility peak and caused a rotational response of the system at higher frequencies. The viscoelastic material had little effect except at frequencies above 8 Hz. Backrest inclination had only a minor effect on vibration attenuation in the 4 to 6 Hz range [22]. In the standing erect posture, there was a single transmissibility peak at 5.5 Hz. A pelvic tilt and Valsalva caused the peak to move to 6.5 Hz and 7 Hz, respectively, while the adoption of a tiptoe stance moved the peak to 3 Hz. Standing on foam materials caused the peak to move to lower frequencies, while the wearing of different shoes did not significantly change the response. Magnusson

et al. [22] noted a decrease in spine height during vibration, whereas Althoff et al. [23] did not find any decrease in stature.

Electromyographic (EMG) related characteristics of the back muscles also exhibit changes in the vibratory environment. Dupuis [24] first reported that, under cyclic loading, the dorsal muscles also respond cyclically with bursts of activity synchronous with the cyclic excitation. Seroussi et al. [25], on the other hand, found that the time lag between the input displacement and the peak torque varied from 30 to 100 ms at 3 Hz and 70 to 100 ms at 10 Hz. At 10 Hz the muscle contraction tended to coincide with the input signal. At all other frequencies, it was out of phase. Seidel and Heide [13] found that the muscles were not able to protect the spine from adverse loads. At the natural frequency, Pope et al. [26] found significantly greater erector spinae muscle activity without any foot support than with foot support. Pelvis rocking, reduced with the aid of a foot support, was shown to be an important factor in the production of the first natural frequency response of the seated individuals. Although the back muscles are capable of responding to vibration loading while an individual sits in a flexed posture, they are not as responsive when the person sits upright or in extended postures [27].

The body's hard and soft tissues will respond to vibration temporarily and permanently. Bony structures may go through crack initiation and crack propagation processes as the loads exceed the critical value. Since the repair mechanisms can compensate partially or completely for the damage process, the long-term effects of the fatigue process are complex in nature. Muscles are capable of bracing the spine against the vibration exposure. As mentioned before, however, the timing of the back muscles may be so far out of phase that the muscular forces are effectively added to those of the stimulus [13, 25]. In addition, back muscles also exhibit fatigue in the vibrated environment. A frequency shift toward lower frequencies has been shown as a sign of muscles' fatiguing contractions [28-33]. Motor unit recruitment, synchronization, and changes in conduction velocity are proposed to be the cause of increased amplitude and the shifted frequency of the EMG signal observed during a sustained, constant force, and isometric contraction. Magnusson et al. [34] investigated the fatigue of the dorsal muscles under 5-Hz sinusoidal vibration. Among subjects vibrated over the 30-min time interval, a shift in the median frequency (EMG signal) of erector spinae muscles was recorded in response to the vibratory input, suggesting muscle fatigue.

Several studies have shown that oxygen consumption is affected by vibration exposure. Bennett et al. [35] showed that oxygen consumption increases with vibration, but found no increase as a function of frequency. Cole and Withey [36] and Webb et al. [37] reported an increase in oxygen uptake with increase in acceleration level. Magnusson et al. [38] reported a 14.3% increase in oxygen uptake in both the twisted erect posture and the erect posture under vibration.

The above studies clearly show that the human spine responds to the chronic exposure to whole-body vibration in several different ways. For example, the shape and size of the spinal components change, and the muscle function becomes erratic. The bases of these effects, however, are not clearly understood. Our hypothesis is that the human spine, like any other living tissue, exhibits remodeling of the structures in response to changes in the loads and displacements that occur during vibration, especially at the resonant frequency of the spine. The remodeling stimulus, from a mechanical perspective at least, is the chronic change in stresses and strains, intradiscal pressure and loads in various components of the spine. Thus, to understand the effects of vibration on the spine, it is essential to determine the changes in these parameters as a function of cyclic loads as compared to quasi-static loads. In the absence of a human model, this can be best achieved through *in vivo* animal studies and analytical models.

In the realm of animal studies, porcine-based models have been used most extensively. These studies have encompassed disc nutritional changes under vibration [39], disc pressure [40], and creep and vibration [41]. Holm and Nachemson [39] demonstrated a loss of nutrition to the intervertebral disc at the first natural frequency, suggesting a mechanism by which discs could degenerate with prolonged exposure. Hansson et al. [40] used a pressure needle technique to demonstrate high pressures in the disc nucleus at the first natural frequency. Keller et al. [41] used a pedicle screw fixation system to apply vibration directly to the porcine motion segment *in vivo*, and demonstrated accentuated creep. Witt and Fischer [42] exposed guinea pigs daily to vibration of 6 Hz in the direction of the vertebral column. After

exposure for 200 h, histological examination of the spinal tissues revealed lesions in the vertebral joints, the paravertebral musculature, and blood-filled spaces of the spongiosa. Homogenized muscle cells with loss of transverse striation were found in the muscle specimens. Fassbender [43] conducted vibration experiments using rats. Procreation of the mitochondria and growth of giant cells took place in the musculature after exposure to vibration stress for 4 weeks. After 8 weeks of vibration stress, the mitochondria showed discrete degenerative stages and cartilage cell degeneration. Weinstein et al. [44] vibrated rabbits at their natural frequency. Radioimmunoassay studies showed a significant change of neuropeptides important in pain response. McLain and Weinstein [45], using a rabbit model, also found that neurons of the dorsal root ganglion showed an increase in the number of mitochondria and lysosomes following exposure to whole body vibration. *In vivo* experimental studies suggest that long-time exposure to vibration decreases the proteoglycan content and eventually results in disruption of matrix integrity [46].

To better understand the source of these epidemiological effects, mechanical models of the human are used. The following sections describe various type of models (lumped parameter and finite element) used to describe human biodynamic characteristics.

5.3 Lumped Parameter Modeling of Human Dynamics

Although the human body is a unified and complex active dynamic system, lumped parameter models are often used to capture and evaluate human dynamic properties. Lumped parameter models consisting of multiple lumped masses interconnected by ideal springs and ideal dampers have proven to be effective in many applications, including those involving human exposure to whole-body vibration. Figure 5.1 illustrates an example of a lumped parameter human model useful in the simulation of human response to vertical (longitudinal) vibration. The head, upper, center, and lower torsos, right and left arms, and right and left legs are modeled as lumped masses. The masses are connected together in the vertical direction by massless springs and dampers that capture human viscoelastic properties.

A chronological review of the lumped parameter models that have been developed to assess vibration exposure is presented below. The models are classified based on: (1) the directions of motion considered in model development (vertical axis only or multi-axis), and (2) the characteristics (linear or nonlinear) of the model spring and damper constitutive equations. Four model categories are obtained using these criteria: vertical nonlinear models, multi-axis nonlinear models, vertical linear models, and multi-axis linear models. Below, for each model in each category, we provide: (1) a description of the interconnection of the model elements, (2) a description of the methods used to derive parameter values for each model element, and (3) an evaluation of model performance (wherever possible). We also provide a graphical model description and more detailed model simulation results for the most recently published model within each model category.

Vertical Nonlinear Models

In 1960, Coermann et al. [47] presented a 6-degree-of-freedom (DOF) model of a human (for standing and sitting postures) used to simulate human dynamic response to longitudinal vibration of very low frequencies. This model included masses for the head, the upper torso, the arm-shoulder, a simplified thorax-abdomen subsystem, the hips, and the legs. A nonlinear spring was connected between the upper torso and the hips in parallel with the thorax-abdomen subsystem to represent the elasticity of the spinal column. Model parameters for each element were estimated from measurements of the mechanical impedance. The performance of the whole-body model was not published and is therefore difficult to assess. The characteristics of the spine and the thorax-abdomen subsystem, however, were evaluated in detail. Each was modeled with 1 DOF in the whole-body model. Damping was not included in the spine and the performance of the thorax-abdomen subsystem did not match the experimental data particularly well.

In 1971, Hopkins [48] developed a 3-DOF model of a seated human consisting of the upper torso, viscera, and lower torso connected in series. Bilinear springs were used to connect the upper torso with the viscera and to connect the viscera with the lower torso. The vertebral column was represented by a

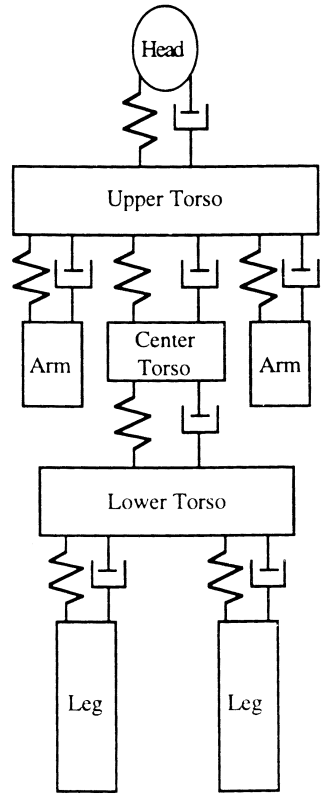

FIGURE 5.1 General lumped parameter human model.

linear spring connecting the upper and lower torsos. The model performance was compared with experimental impedance and transmission data. The model displayed the same number of resonant peaks as the experimental impedance data but had significantly different peak values. The model did not match the experimental transmissibility data, either in shape or in peak values. The model was used exclusively in the analysis of low-frequency vibration.

In 1974, Muksian and Nash [49] presented a 7-DOF nonlinear model dedicated to the analysis of vibration imposed on a seated human. The model included masses associated with the head, back, torso, thorax, diaphragm, abdomen, and pelvis. Linear springs and dampers were used between the head and the back, and between the back and the pelvis. Forces associated with the relative motion of the torso with respect to the back and muscle forces were included in the model as forces acting directly on the masses. The value of each lumped mass was obtained from previous studies by Hertzberg and Clauser [50], Colella [51], and Roberts et al. [52]. The source of the stiffness values was not provided, but the values were similar to the experimental data obtained by Vogt et al. [53]. The damping coefficients were obtained from Coermann et al. [47] and Vogt et al. [53] (except that of abdomen-thorax viscera was an assumed value). The model performance was compared with the experimental data for acceleration ratio (for each mass relative to the input acceleration) given by Goldman and von Gierke [54] and Pradko et al. [55, 56]. At lower frequencies (1 to 10 Hz), the model matched the experimental data by Goldman and von Gierke [54] and Pradko et al. [56] well, but did not compare well with experimental data by Pradko et al. [55]. At higher frequencies, the model performance was significantly different than that observed experimentally.

In 1976, Muksian and Nash [57] presented a 3-DOF model of the human body in the sitting position that contained a parallel connection between the pelvis and the head. Figure 5.2 shows the model arrangement. It included masses associated with the head (m_1), body (m_2), and pelvis (m_3) connected

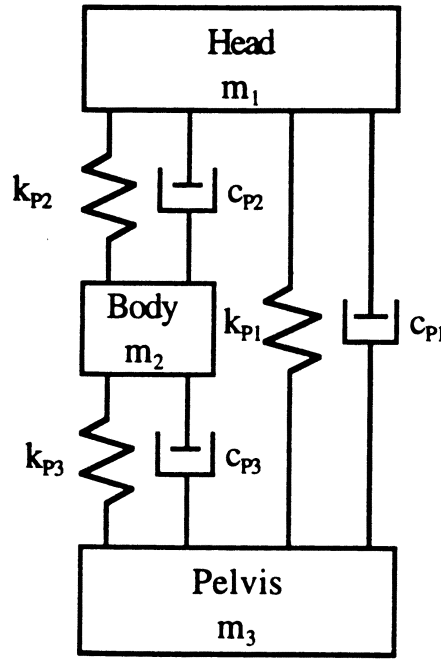

FIGURE 5.2 Vertical nonlinear model presented by Muksian and Nash [49] with permission from Elsevier Science.

in series, very similar to the model given by Coermann et al. [47]. It neglected the arms and legs, and combined the mass of the upper torso and thorax-abdomen into that of the body. The model was based on the assumption that: (1) all springs (k_{P1}, k_{P2}, and k_{P3}) were linear in the frequency range between 1 and 30 Hz, (2) the damping between the head and body (c_{P2}) was zero, and (3) all other dampers (c_{p1} and c_{P3}) were linear between 1 and 6 Hz but nonlinear between 6 and 30 Hz. The values of the masses were obtained from Hertzberg and Clauser [50]. The spring stiffness and damping coefficients were determined by matching existing experimental data at corresponding input frequencies by Magid et al. [58] and Goldman and von Gierke [54] (See Figs. 5.3 and 5.4). The parameter values of the model are listed in Table 5.1. Since two kinds of damper were used for different frequency ranges, the model performed well when compared with experimental data for single-frequency input. However, since the damping values depend on the input frequencies, analysis of the model performance is difficult to assess for conditions involving multiple-frequency input (i.e., random vibration).

Multi-Axis Nonlinear Models

In 1964, von Gierke [59] described a two-axis, 7-mass model of a human in standing and sitting positions for longitudinal force application and pressures derived from the model presented by Coermann et al. [47]. The thorax-abdomen subsystem was extended to include one additional degree of freedom, the mass of the chest wall. A damper was added between the upper torso and the hips in parallel with the spine spring. Neither the values of the model parameters nor the model simulation performance were provided. This model was applied to the evaluation of motion of the abdominal wall, the diaphragm, and the lung and thorax.

In 1996, Broman et al. [60] described a 2-mass, 3-DOF model of a seated human (as shown in Fig. 5.5). It included a linear horizontal subsystem (k_1 and c_1), a vertical subsystem (k_2 and c_2), and a rotational subsystem (k_3 and c_3). The horizontal and vertical subsystems were used to represent the coupling between the human and the seat. The rotational subsystem was used to represent the rotation of the upper body relative to the lower body. The model parameters were varied to match the experimental data from Pope

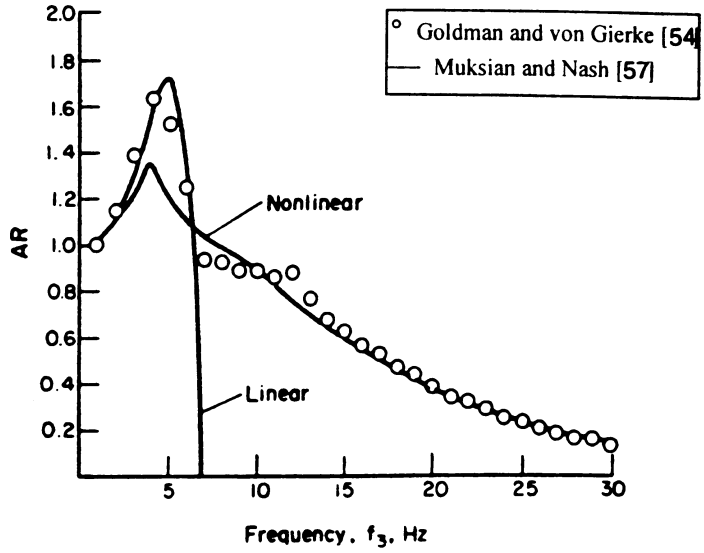

FIGURE 5.3 Body to seat acceleration ratio from Muksian and Nash [49] with permission from Elsevier Science.

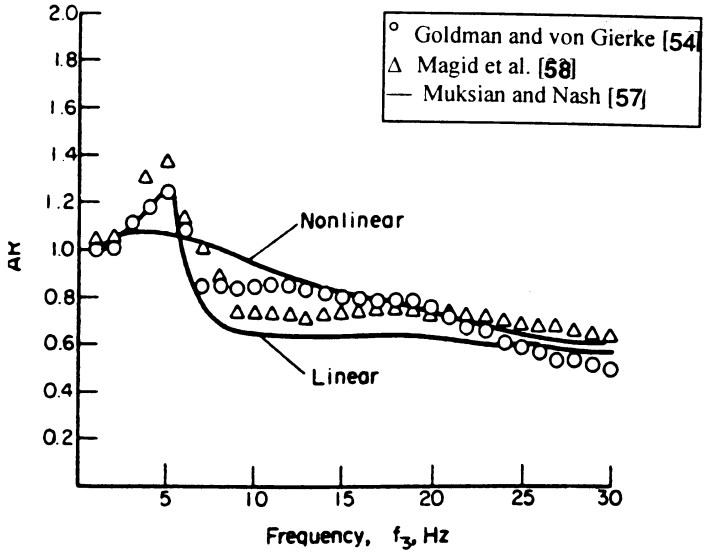

FIGURE 5.4 Head to seat acceleration ratio from Muksian and Nash [49] with permission from Elsevier Science.

et al. [20, 21, 61]. The parameter values are shown in Table 5.2. In Figs. 5.6 and 5.7, the model simulation yields results similar to that of a purely vertical subsystem (the horizontal subsystem spring (k_1) was assumed to have infinite stiffness in the simulation results). In the comparison, the model matched the experimental data very well; however, different values of the model parameters were used when matching the different experimental data, i.e., a single "average human" model was not developed.

Vertical Low-Amplitude Linear Models

Prior to the 1970s, most published models had nonlinear stiffness and damping characteristics to account for the nonlinear behavior observed in the relatively large deformation human tissue studies (necessary

TABLE 1 Parameter Values of the Model Presented by Muksian and Nash [57]

No. (j)	Mass m_j (kg)	Stiffness k_{Pj} (N/m)(Ns/m)	Linear Damping c_{Pj}
1	5.44	27158	1780
2	47.17	0	686
3	27.22	63318	467

f (Hz)	Nonlinear Linear Damping c_{31} (N(s/m)^3)	c_{33} (N(s/m)^3)
6	25462	15403
7	33949	157173
10	11316	2027689
15	5815	4346462
20	1044571	7036478
25	2358	10248780
30	51533	15088608

With permission from Elsevier Science.

TABLE 2 Parameter Values of the Model Presented by Broman et al.

Case	m_1 (kg)	m_2 (kg)	I(Nms^2/rad)	d_2 (m)	c_2 (Ns/m)	c_3 (Nms/rad)	k_2 (N/m)	k_3 (Nm/rad)
1	20	45	3.0	0.34	1500	50	60,000	10,000
2	9	56	3.0	0.39	2000	150	80,000	17,000

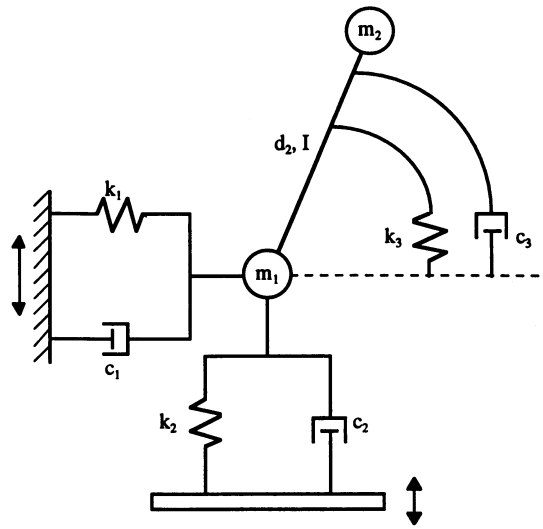

FIGURE 5.5 Multi-axis nonlinear model presented by Broman et al.

in an impact analysis). In 1978, Sandover [62] experimentally investigated the linearity of the human body response to vibration. Results from his investigation indicated that the human body could be modeled as linear when using a 2 m/s^2 rms broadband random vibration stimulus — typical of many transport situations.

In 1981, the International Organization for Standardization (ISO) published a parallel 2-DOF model for both sitting and standing positions [63]. The model was developed to match a composite average driving-point impedance vs. frequency profile (magnitude and phase for the frequency range of 0.5 to

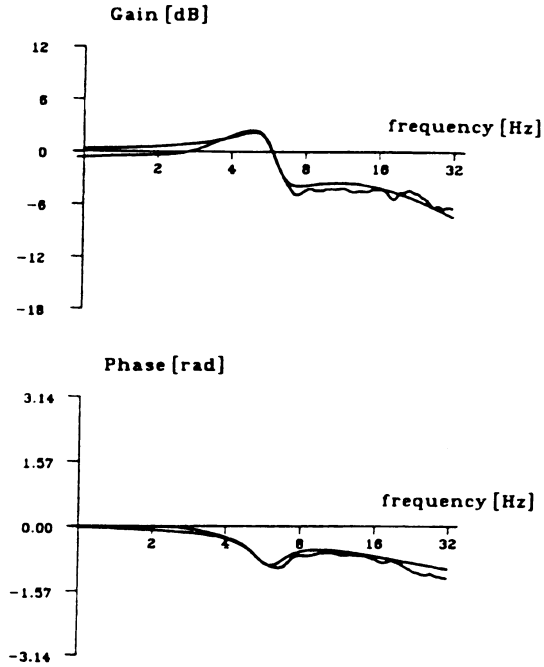

FIGURE 5.6 Comparison between an experimentally observed transfer function and the modeled transfer function of a vertical and rotational subsystem for the case of: $m_1 = 20$ kg, $m_2 = 45$ kg, $I = 3.0$ Nms^2/rad, $d_2 = 0.34$ m, $k_2 = 60{,}000$ N/m, $c_2 = 1500$ Ns/m, $k_3 = 10{,}000$ Nm/rad, $c_3 = 50$ Nms/rad from Broman et al. [60] with permission from Elsevier Science.

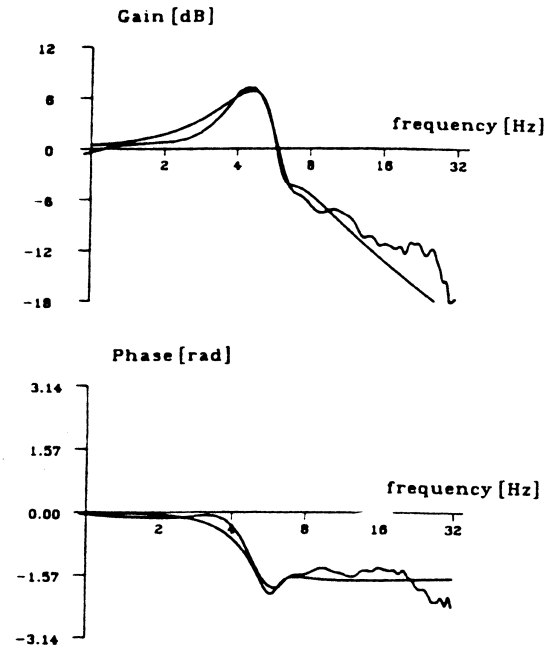

FIGURE 5.7 Comparison between an experimentally observed transfer function and the modeled transfer function of a vertical and rotational subsystem for the case of: $m_1 = 9$ kg, $m_2 = 56$ kg, $I = 3.0$ Nms^2/rad, $d_2 = 0.39$ m, $k_2 = 80{,}000$ N/m, $c_2 = 2000$ Ns/m, $k_3 = 17{,}000$ Nm/rad, $c_3 = 150$ Nms/rad from Broman et al. [60] with permission from Elsevier Science.

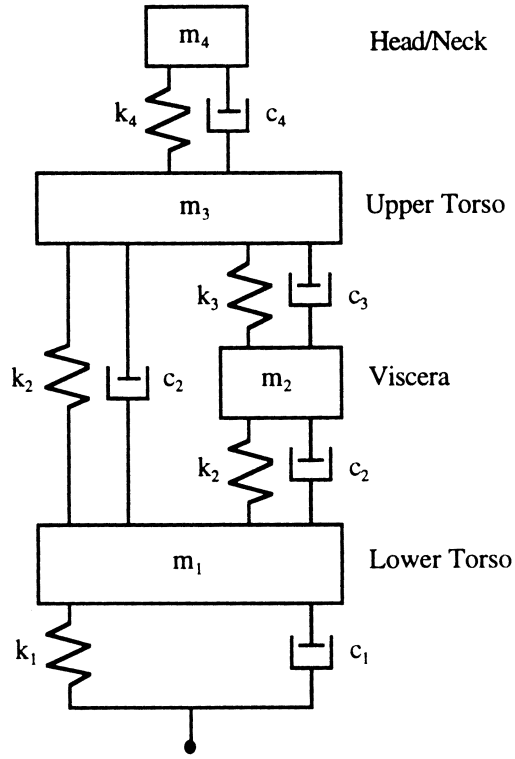

FIGURE 5.8 Vertical low-amplitude linear model developed by Wan and Schimmels.

31.5 Hz) derived from existing experimental studies. Since the model had only two suspended masses, it was unable to match the phase response observed in existing experimental seat-to-head acceleration transmissibility studies at moderate to high frequencies [64] (phase angle of approximately 270°).

In 1987, ISO [64] published a 4-mass, 8-DOF model of a human for both sitting and standing positions. No correlation between the elements of the model and anatomical segments was established. Each spring-damper set connecting masses included two springs and one damper (one spring parallel to the damper and the other in series). The model was developed to match a composite average seat-to-head acceleration transmissibility vs. frequency profile (amplitude and phase for the frequency range of 0.5 to 31.5 Hz) derived from existing experimental studies. The model matched the experimental data very well except for the transmissibility amplitude in the high-frequency range.

In 1987, Nigam and Malik [65] developed a 15-DOF undamped model for which only a standing posture was considered. It included masses for the head, neck, upper, central, and lower torso, upper and lower arms, upper and lower legs, and feet. The mass of each element was obtained from a previous anthropomorphic body segment study by Bartz and Gianotti [66]. The stiffness was obtained by combining the stiffness of adjacent segments. The model performance was compared with some experimental data such as resonance peaks from Goldman and von Gierke [54], and resonant frequencies for two modes from Greene and McMahon [67]. The natural frequencies of the model were in the range of the experimental resonant data but were relatively high. The leg stiffness was compared with the experimental values from Greene and McMahon [67, 68]. The approximate value of the single leg was 15% larger than the experimental data. As damping was ignored in this study, the model is less realistic and general.

In 1995, Wan and Schimmels [69] developed a series/parallel 4-DOF human dynamic model designed to match the response of seated humans exposed to vertical vibration. Since the model was constructed for subsequent use in optimal seat-suspension design, model simplicity was highly desired. The topology of the 4-DOF model is illustrated in Fig. 5.8. The model consisted of head/neck (m_4), upper torso (m_3),

TABLE 5.3 Parameter Values of the Model Presented by Wan and Schimmels

m_1(kg)	m_2 (kg)	m_3 (kg)	m_4 (kg)	c_1 (Ns/m)	c_2 (Ns/m)	c_2' (Ns/m)
36	5.5	15	4.17	2475	330	909.09
c_3 (Ns/m)	c_4 (Ns/m)	k_1 (N/m)	k_2 (N/m)	k_2' (N/m)	k_3 (N/m)	k_4 (N/m)
200	250	49341.6	20000	192000	10000	134400

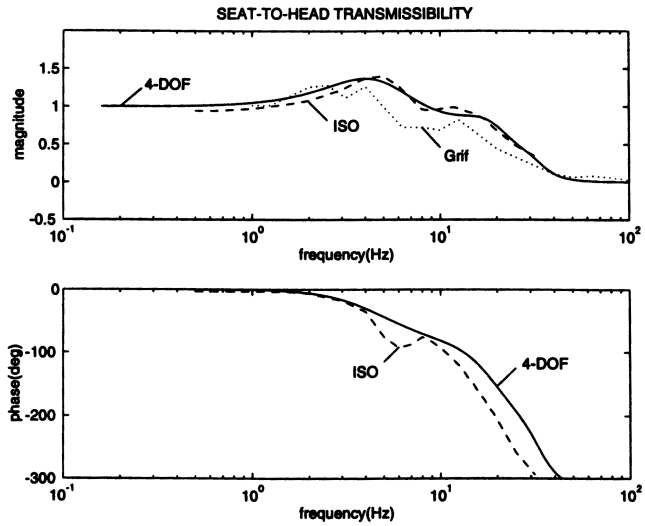

FIGURE 5.9 Comparison of model and experimental acceleration transmissibility variation with frequency from Wan and Schimmels [69] with permission from ASME.

viscera (m_2), and lower torso (m_1). The model parameters were obtained by comparing simulation results with the results of experimental tests on human subjects to determine: (1) the variation of seat-to-head acceleration transmissibility with frequency, (2) the variation of driving-point impedance with frequency, (3) acceleration ratio from Goldman and von Gierke [54], and (4) the published properties of the human body from Patil and Palanichamy [70].

The parameter values of the 4-DOF model are listed in Table 5.3. A comparison of simulation results (using the final refined model) with experimental data is presented below.

Figure 5.9 shows a plot of seat-to-head transmissibility magnitude vs. frequency and a plot of transmissibility phase vs. frequency for the 4-DOF model and for the experimentally obtained data. The curve identified as "ISO" is from experimental data presented in ISO 7962 [64]; the curve identified as "Grif" is from experimental data obtained by Griffin et al. [71]; and the curve identified as "4-DOF" is from the 4-DOF model. For the transmissibility magnitude, the "4-DOF" curve is virtually coincident with the "ISO" curve. For the transmissibility phase, the "4-DOF" curve is similar in shape to the "ISO" curve but has a smaller phase lag, especially at higher frequencies. Results show that variation between experimental studies is larger than the variation of the simulated model results from either experimental study. The variation of experimental results illustrates the variability of human dynamic behavior by subject and measurement method. The "ISO" curve represents a composite average of 11 experimental studies. The publishers of ISO 7962 believe that this data best represents average human dynamic behavior. The "Grif" curve is included here because it was published after the "ISO" curve was published and illustrates the variation between experimental studies. Because the "ISO" curve represents a larger number of experimental studies, the error in matching the "ISO" curve was weighted more heavily in the model matching procedure.

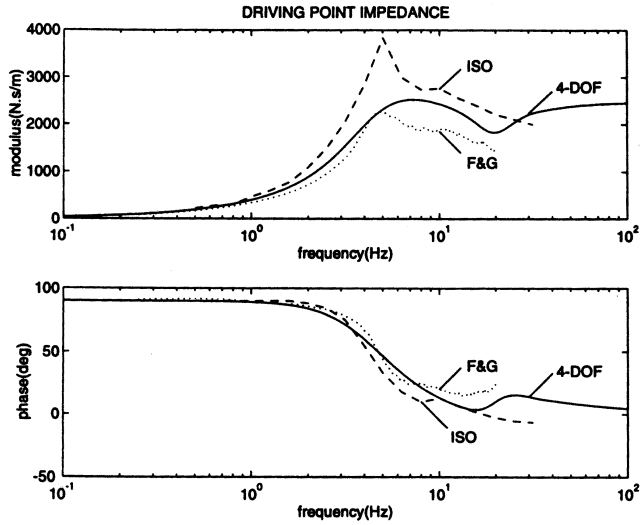

FIGURE 5.10 Comparison of model and experimental driving-point impedance variation with frequency from Wan and Schimmels [69] with permission from ASME.

Figure 5.10 presents a plot of driving-point impedance magnitude vs. frequency and a plot of impedance phase vs. frequency for the 4-DOF model and the experimental data. The curve identified as "ISO" is from experimental data presented in ISO 5982 [63]; the curve identified as "F&G" is from experimental data obtained by Fairley and Griffin [72]; and the curve identified as "4-DOF" is from the 4-DOF model. The impedance magnitude of the 4-DOF model lies between the experimental "ISO" curve and "F&G" curve except at higher frequencies. The impedance phase of the 4-DOF model compares well with the experimental data at all frequencies. Once again the data show that variation between experimental studies is larger than the variation of the simulated model results from either study. The "ISO" curve was obtained by averaging the responses of 39 subjects in at least 7 different experimental studies in which the entire body was exposed to the vibration input. The "F&G" curve was obtained in a study of 60 subjects for which the feet of the subjects were supported by a stationary surface (for which case, the mass of the human appears to be reduced). In addition to illustrating the variation in results among experimental studies, the "F&G" curve is included (and weighted more heavily) because of the increased number of subjects and because the experimental procedure is believed to be more representative of an operator seated on a seat suspension.

The 4-DOF model developed by Wan and Schimmels is judged to accurately capture the essential dynamics of a seated human exposed to vertical whole-body vibration. The 4-DOF model simulation results compare well with experimental data for transmissibility, impedance, and acceleration ratio. Also, its parameter values are close to the published properties of the human body. Relative to the results obtained using the previously developed models [63, 64, 68, 73], the 4-DOF model provides a better match with experimental results for longitudinal vibration, despite its simplicity.

Multi-Axis Low-Amplitude Linear Models

In 1971, Kaleps et al. [74] developed a two-axis, 5-mass model. The masses corresponded to the torso, lung and trachea, chest wall, abdomen, and buttocks. A thoracic cavity was formed by the torso, lungs and trachea, chest wall, and abdomen. The model was used to obtain the body deformation (spinal compression, pressure in the lungs, etc.) under external vertical forces (whole-body vibration and impact used as input) and pressure loads (blast, acoustic pressure, decompression loads as input). The parameters of the model were derived by best approximating the experimental data available. This model combined the mechanical response characteristics of the corresponding body segments. The model performance

was compared with the impact impedance measurements from Coermann [75] and the experimental data of the resonance from Clark et al. [76]. The model behavior was similar to the experimental data for each. This model is suitable for obtaining responses of the lung, chest, and abdomen.

In 1978, Jex and Magdaleno [77] developed a 6-mass biomechanical model of a human sitting on a semisupine seat. The model included an active neuromuscular subsystem. It consisted of masses for the head, neck, torso, lower body, upper arm, and forearm. The mass and inertia were obtained from human properties by Braune et al. [78]. The stiffness and damping values were obtained by matching the experimental results from Magdaleno and Jex [79, 80]. The model was then validated by comparing model results with the experimental data such as shoulder and head motions under sine and quasi-random vibration obtained by the authors. The model match was quite good except that the phase of the head response of the model was much different from that of the experimental data. This model was used to simulate an aircraft pilot when in a flying (partially reclined) position.

In 1988, Amirouche and Ider [73] developed a 13-mass, multi-axis model of a human used for both seated and standing postures. It included masses for the head, neck, upper, center, and lower torso, upper and lower arms, and upper and lower legs. The masses were obtained from the Part 572 dummy. The stiffness and damping coefficients in both vertical and rotary directions were obtained by matching the experimental results from Panjabi et al. [16]. For the vertical transfer function of the middle torso, the model simulation was very similar to the experimental data in the 5- to 7-Hz range, but was larger in the 2- to 5-Hz range and smaller in the 7- to 15-Hz range. The model phase angle of the vertical acceleration of the middle torso had similar values as the experimental data in the frequency range from 2 to 5 Hz, but had smaller values in the 5- to 13-Hz range. For the rotary transfer function of the middle torso, the model did not match the experimental data in either shape or peak value. The transmission of vibration from the seat to the head was compared with experimental data obtained by Pradko et al. [81], Sandover [62], Donati and Bonthoux [82], Coermann [75], and Griffin et al. [83]. In general, the model did not match the experimental data particularly well. The model compared fairly well with only the shape of the experimental data for relaxed posture by Coermann [75]. Compared with other experimental data, the model had larger transmissibility values in the lower frequencies and had smaller values in the higher frequencies.

In 1994, Qassem et al. [84] presented an 11-mass, two-axis model of a seated human subjected to input forces at the hand and the seat along vertical and horizontal axes. This model was obtained by modifying the model presented by Muksian and Nash [49]. Figure 5.11 shows this model. It included masses for the head, neck (cervical spine), thoracic spine, lumbar spine, torso, upper and lower arms, hand, thorax, diaphragm, abdomen, and pelvis. The mass of each part was obtained from Muksian and Nash [49], and Nigam and Malik [65]. The spring and damper values were obtained from previous studies by Mizrahi and Susak [85], Nigam and Malik [65], and Patil et al. [86]. These parameter values are listed in Table 5.4. The seat-to-head, seat-to-torso, and hand-to-lower arm force transmissibility of the model were compared with those of the experimental measurements in the frequency range between 4 and 500 Hz obtained in their study. Figures 5.12, 5.13, and 5.14 show the seat-to-head, seat-to-torso, and hand-to-lower arm transmissibility comparison of the model with the experimental data, respectively. For the seat-to-torso and hand-to-lower arm force transmissibility, the model matched the experimental data well. For the seat-to-head force transmissibility, the model did not match the experimental data very well, especially in the frequency range from 4 to 40 Hz for which the error was 40 to 100%.

Summary

An effective lumped parameter model is the simplest model that captures the dynamic response of interest. The purpose of developing a human model is to accurately assess human response to a variety of inputs without subjecting human subjects to hostile environmental conditions. Human lumped parameter models are particularly appropriate in optimizing suspension isolation for which human dynamic response is readily simulated and evaluated. However, if the model is overly complicated, simulation run time is excessive and it is difficult to develop a true appreciation of the human dynamic behavior.

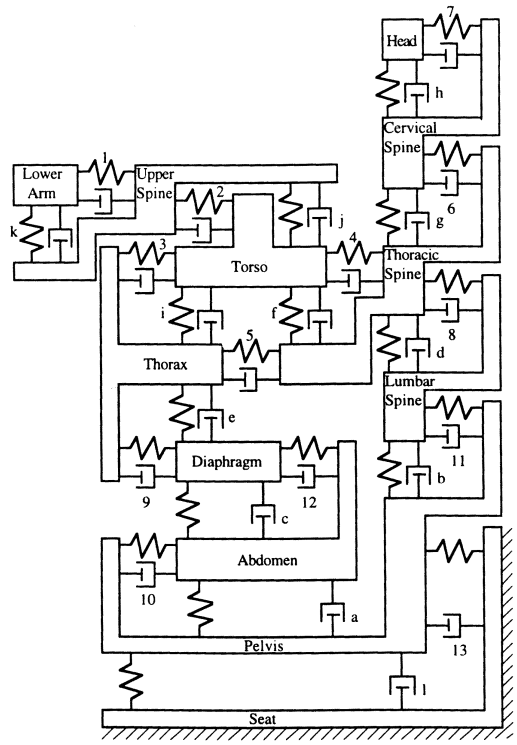

FIGURE 5.11 Multi-axis low-amplitude linear model presented by Qassem et al.

TABLE 5.4 Parameter Values of the Model Presented by Qassem et al.

Body Segment	Mass (kg)	Item No.	Stiffness (kgf/m)	Damping (kgf/ms)	Item No.	Stiffness (kgf/m)	Damping (kgf/ms)
Upper arm	5.47	1	6885	365.1	a	89.41	29.8
Lower arm	5.297	2	6885	365.1	b	5364	365.1
Torso	32.697	3	5364	365.1	c	89.41	29.8
Thoracic spine	4.806	4	5364	365.1	d	5364	365.1
Thorax	13.626	5	5364	365.1	e	89.41	29.8
Neck	1.084	6	5364	365.1	f	5364	365.1
Head	5.445	7	5364	365.1	g	5364	365.1
Lumber spine	2.002	8	5364	365.1	h	5364	365.1
Diaphragm	0.454	9	89.41	29.8	i	5364	365.1
Abdomen	5.906	10	89.41	29.8	j	6885	365.1
Pelvis	27.174	11	5364	365.1	k	6885	365.1
		12	89.41	29.8	l	2550	37.8
		13	2550	37.8			

An effective human lumped parameter model is the model properly chosen for its application based on the magnitude, direction, and location of the input, i.e., the particular dynamic environment to which a human is exposed. Due to the complexity of human dynamics, there currently does not exist a human model that can be used for all input conditions. Existing vertical models are better than the existing multi-axis models at matching vertical vibration input; however, vertical models are not suitable for use in the multi-axis vibration analysis. Linear models are appropriate for low-amplitude vibration but inappropriate for large-amplitude input (inputs that result in large deformation of human tissue).

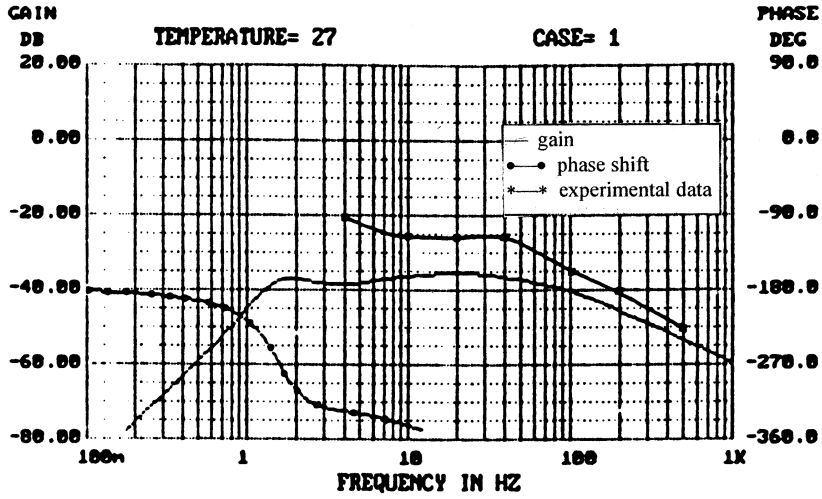

FIGURE 5.12 Transfer function of the force transmitted to the head for a 100-kg human body subjected to vertical vibration from seat from Qassem et al. [84] with permission from Elsevier Science.

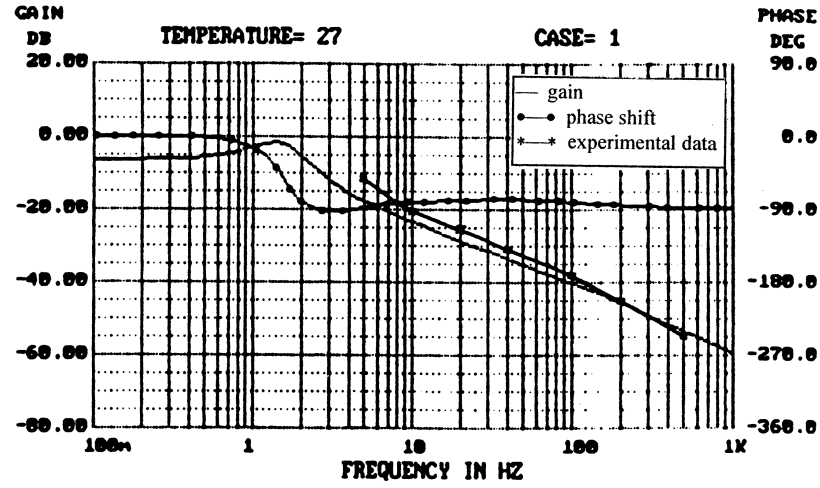

FIGURE 5.13 Transfer function of the force transmitted to the torso for a 100-kg human body subjected to vertical vibration from seat from Qassem et al. [84] with permission from Elsevier Science.

An effective human lumped parameter model is the model that "best" matches the experimental results. The quality of the match is determined by the level of confidence in experimental data. The level of confidence in the experimental data is determined, in part, by: (1) the number of the subjects included in experiments, (2) subject selection (e.g., subject age, weight, etc.), (3) subject posture (e.g., sitting erect, sitting relaxed, etc.), and (4) the proximity of the location of experimentally measured response relative to a degree of freedom in the model.

Due to variation in test results in previous studies, it is impossible for a model to match all the experimental data. Each of the human models discussed above matched some, but not all, experimental data.

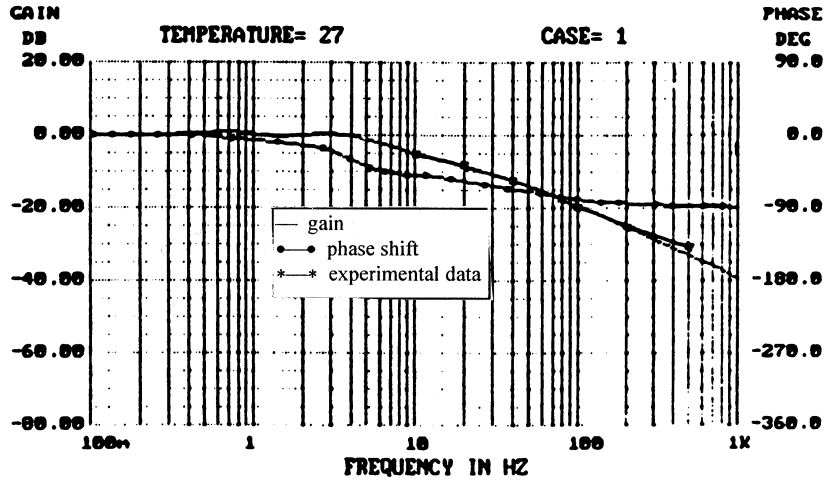

FIGURE 5.14 Transfer function of the force transmitted to the lower arm for a 100 kg human body subjected to horizontal vibration from hand from Qassem et al. [84] with permission from Elsevier Science.

5.4 Finite Element Models of the Spine

Ligamentous one and two motion segment finite element models of the lumbar region have been proposed to look into the effects of vibration on biomechanical parameters [87, 88].

Kasra et al. [87] identified a resonant frequency of 26 Hz of the ligamentous spine based on one motion segment model finite element analysis. Appropriate experimental studies were undertaken to validate the analytical results. The model results also indicated that the system resonant frequency decreased as the compression preload increased. The compliance decreased with increasing compression preload. Under preloads of not more than 680 N, removal of the facet joints tended to decrease slightly the segmental resonant frequencies irrespective of the magnitude of compression preload. The stresses and strains throughout the segment increased approximately twofold in comparison with equivalent static values. Partial or complete removal of the disc nucleus considerably decreased the resonant frequency and increased the corresponding segmental response amplitude (i.e., compliance). The results indicated that the most vulnerable element under axial vibration loads was the cancellous bone adjacent to the nucleus space. Fatigue fracture of bone as a cumulative trauma and the subsequent loss of nucleus content are likely to initiate or accelerate the segmental degenerative processes. The annulus fibers did not appear to be vulnerable to rupture when the segment was subjected to pure axial vibration.

Goel et al. [88] developed a nonlinear, three-dimensional, finite element model of the ligamentous L4-S1 segment (two motion segments) to analyze the dynamic response of the spine in the absence of damping. The effects of the upper body were simulated by including a mass of 40 kg on the L4 vertebral body. The model predicted a resonant frequency of 17.5 Hz in axial mode and 3.8 Hz in flexion-extension mode. Accordingly, the predicted responses for the cyclic load of –400 ± 40 N applied at four different frequencies (5, 11, 16.5, and 25 Hz) were compared with the corresponding results for axial compressive static loads (–360 and –440 N). As compared to the static load cases, the predicted responses were higher for the cyclic loading. For example, the effect of cyclic load at 11 Hz was to produce significant changes (9.7 to 19.0%) in stresses, loads transmitted through the facets, intradiscal pressure (IDP), disc bulge, as compared to the static load predictions. These responses were found to be frequency dependent as well, supporting the *in vivo* observations of other investigators that the human spine has a resonant frequency.

Although the above two studies provided useful information, data obtained were not in agreement with the experimental observations. For example, Kasra et al. [87] identified a resonant frequency of 26 Hz based on one motion segment lumbar spine study, both experimentally and analytically. Goel et al.

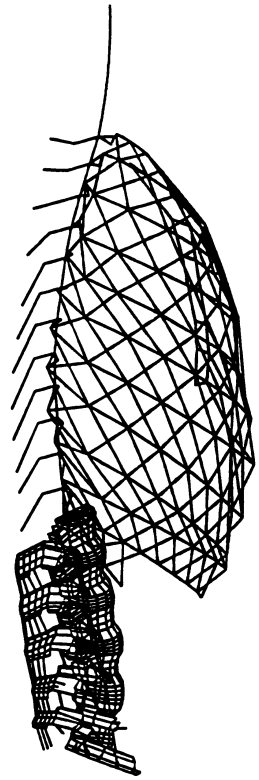

FIGURE 5.15 The head-to-sacrum (H-S1) finite element model of the ligamentous spine including the lumbar, thorax, and cervical regions. The head was simulated as a mass attached to the cervical spine.

[88] reported a resonant frequency of 17.8 Hz based on a finite element model of the L4-S1 segment (two motion segments model). The *in vivo* resonant frequency estimates of the human body, however, range from 4 to 8 Hz [4, 14, 16-18, 20, 89-91]. Hence, segmental models (at least up to two motion segments) cannot be used to predict biomechanical parameters including deformations, intradiscal pressure, strains, and stress in response to vibration. It becomes necessary to generate a finite element model, if feasible, whose dynamic features including the resonant frequency and transmissibility will match the experimental measurements. Once this is achieved, it would then be possible to quantify the effects of vibration on the spine. This was the impetus for the study undertaken by Kong et al. [92], and the hypothesis was that the finite element model of the entire spine would predict biomechanical parameters in agreement with the experimental data.

A finite element model of the upper body, including the entire spinal column, and the rib cage was generated to extract the resonant frequency and transmissibility during vertical vibration (head-to-sacrum model H-S1, Fig. 5.15). The model consisted of a detailed representation of the lumbosacral spine and a simpler beam-type model of the thorax and cervical spine regions. The element type and material properties are listed in Table 5.5 [93-97]. The costovertebral, costotransverse, and sternochondral articulations were modeled as 6-DOF joints and their stiffness values, listed in Table 5.6, were adapted from Closkey et al. [98]. The costal ligaments were modeled as tension-only truss elements and their cross-sectional areas and material properties were from Stokes and Laible [99].

The head and the internal organs of the thorax and abdomen were represented by mass elements. Mass values and their offsets to vertebral body centers at various levels were adapted from Takashima et al. [100]. Mass elements were rigidly connected to the centers of corresponding vertebral bodies. A damping ratio of 0.3 at the system level was assigned to the finite element model. The damping ratio

TABLE 5.5 Element Types and Material Properties of Various Structures Used for the Finite Element Model of the Head to Sacrum (H-S1)

Structure	Element Type	Elasticity (MPa)	Poisson's Ratio	Density (g/cm^3)
Cervical spine and thorax				
Motion segment	Beam	120	0.20	1.40
Rib	Beam	12000	0.20	1.40
Costal cartilage	Truss	300	0.10	1.10
Sternum	Shell	12000	0.20	1.40
Costal ligament	Truss	5.0	0.30	1.0
Lumbar spine				
Cortical bone	Brick	12,000	0.30	1.70
Cancellous bone	Brick	100	0.20	1.10
Posterior bone	Brick	3500	0.25	1.40
Nucleus pulposus	Brick	1.326	0.4999	1.02
Annulus fibrosis	Composite			
Ground substance		4.20	0.45	1.05
Outest layer		450	0.30	1.0
Ligaments	Truss			
Ant. longitudinal		7.80	0.30	1.0
Post. longitudinal		10.0	0.30	1.0
Transverse ligament		10.0	0.30	1.0
Ligamentum flavum		15.0	0.30	1.0
Interspinous		10.0	0.30	1.0
Supraspinous		8.00	0.30	1.0
Capsular		7.50	0.30	1.0
Iliolumbar		20.0	0.30	1.0
Muscles	Truss	1.0	0.30	1.0

TABLE 5.6 Stiffness Values Used for Various Thorax Joints and Cervical Spine in the Finite Element Model of the Upper Body (adapted from [94] and [98])

Joint	Axial (N/mm)	Lat. Shear (N/mm)	Torsional (Nmm/rad)	Lat. Bending (Nmm/rad)
Cervical motion segment	1120	52.5	7250	9575
Thoracic motion segment	1240	105	14500	19150
Costovertebral	25	500	1750	3750
Costotransverse	25	500	1750	3750
Sternochondral				
Rib1-Sternum	50	100	10000	7000
Rib2-Sternum	50	100	10000	7000
Rib3-Sternum	50	8	10000	2500
Rib4-Sternum	50	8	10000	2500
Rib5-Sternum	50	8	10000	2500
Rib6-Sternum	50	0	10000	1500
Rib7-Sternum	50	0	10000	1500

The values for the A-P shear and flexion-extension are the same as those for the lateral shear and lateral bending.

was determined from the experimental transmissibility–frequency relationships [64, 75]. Since the motions in the sagittal plane only were studied in the present study, a half-model (the right side) was used and no out-of-plane translational or rotational displacements were allowed for all nodes in the sagittal plane. The sacrum was fixed in all directions.

The trunk muscles were added to the ligamentous H-S1 model to study the effects of muscles on the resonant frequency. The extensor muscle fascicles were modeled in detail; the abdominal muscles were

TABLE 5.7 Effects of the Muscle and Weight of the Body on the First Four Natural Frequencies and Participation Factors of the Upper Body of the Head to Sacrum (H-S1) Model

Model Frequency (Hz)	Participation Factor	
	A-P	Vertical
Ligamentous model		
0.43	1.45	0.02
2.79	0.65	0.35
5.34	0.30	0.50
8.32	-0.32	0.95
Muscular model		
0.85	1.46	0.03
3.23	-0.59	-0.24
5.89	0.44	0.51
8.91	-0.31	1.02
Muscular and preload model		
0.29	1.44	0.04
2.37	0.71	0.45
4.94	0.24	0.33
6.82	0.41	-1.08

simply represented by 4 spar elements at this stage due to their geometrical complexity. Muscles were modeled as tension-only truss elements with the elastic modulus of 1.0 MPa [101, 102].

Modal analyses were performed to extract resonant frequencies. Damping was not considered in the frequency extraction. The H-S1 model was also used to investigate the dynamic response of the upper body to the vertical sinusoidal vibration. So as to simulate the vibration transmitted through a seat, the 0.1g (0.98 m/s^2) vibration was imposed on the sacrum. Transmissibility was obtained as the ratio of the predicted root-mean-square (rms) accelerations of points of interest within the model to the imposed rms acceleration. The magnitude and phase angle of the transmissibility were quantified. The sweep frequency range was from 0.01 to 30 Hz.

The predicted first resonant frequency in the vertical direction for the complete ligamentous head to sacrum (H-S1) model was 8.32 Hz (Table 5.7). Inclusion of muscles increased it to 8.91 Hz, while the self-weight decreased it to 6.82 Hz. These values are very close to the *in vivo* experimental data [103]. Further fine-tuning is possible if one includes the pelvis-buttocks system not simulated in the current model. Pope and Hansson [104] stated that the vibration response of the human is attributable to a combination of a vertical subsystem and a rotational subsystem characterized by rocking of the pelvis.

The predicted curves of the transmissibility magnitude-frequency and phase angle-frequency of the C1 center are very close to the reported measurements (see Figs. 5.16 and 5.17 [64, 75]).

The magnitude of transmissibility increased rastrally in the vertical direction at the resonant frequency. While the coupled A-P acceleration at the L3 vertebra was the largest, its flexion-rotation acceleration was much lower than those of the L1 and L5 vertebrae (see Figs. 5.18 and 5.19). This is most probably due to the lordotic shape of the lumbar spine. While the vertical vibration at the sacrum causes significant A-P motion and rotation in the lumbar region, the motions in the cervical spine and head are primarily in the vertical direction. The magnitude of the A-P acceleration of the head was only about 23% of that in the vertical direction under G_z simulation. As expected, damping played an important role in attenuating vibration. The higher the damping ratio, the lower the motion transmitted to the head (see Fig. 5.20). Amirouche and Ider [73] also found that the transmissibility decreased with an increase in damping. Inclusion of muscles increased the vibration transmitted to the head. This is in agreement to the findings of Pope et al. [61].

The current study presents a numerical method to investigate the response of the spine to vibration. It showed that the finite element technique can be used to predict the natural frequency and transmissibility.

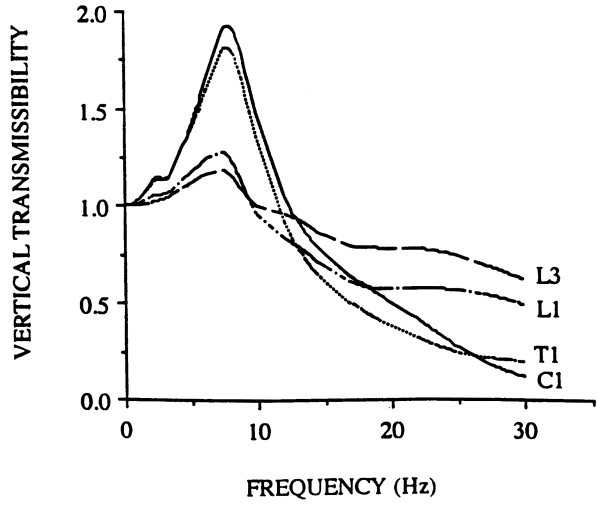

FIGURE 5.16 The magnitude of transmissibility at different vertebral centers with respect to the sinusoidal vertical vibration imposed on the sacrum.

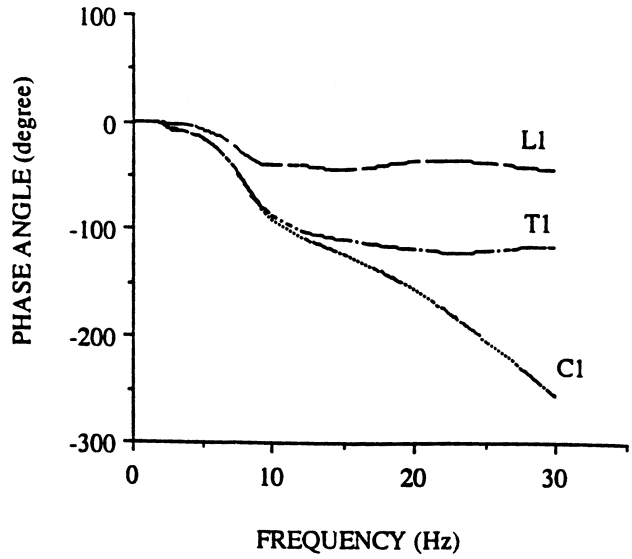

FIGURE 5.17 The phase angle of transmissibility at different vertebral centers with respect to the sinusoidal vertical vibration imposed on the sacrum.

The present head-to-sacrum model can be used to predict "clinically" relevant biomechanical parameters in the lumbar spine under vibration and impact loads, like the predictions made using one and two motion segment finite element models.

5.5 Conclusions

Lumped parameter models emphasize larger scale information about human dynamic response, such as the general motion of the head or torso. The performance of the lumped parameter human models is determined by the degrees of freedom of the model and the parameter values of the model. Although nonlinear models better approximate real human properties for large deformation, it has been shown

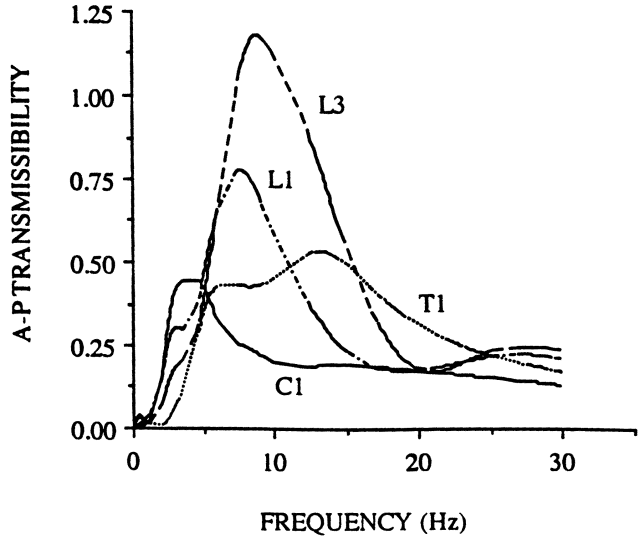

FIGURE 5.18 The A-P accelerations (rms) at different vertebral centers normalized to the imposed acceleration.

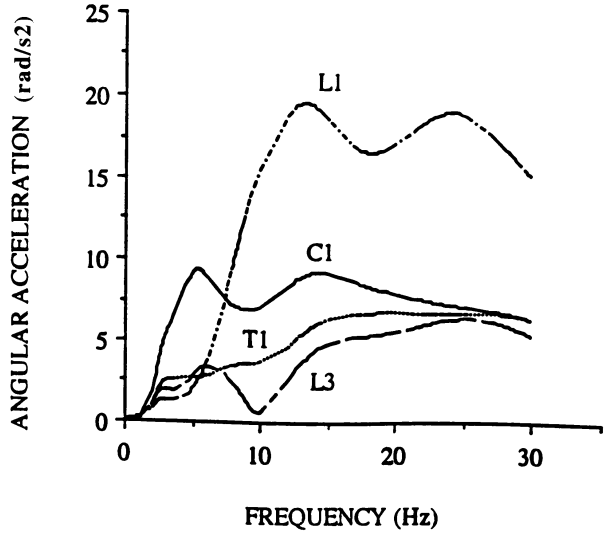

FIGURE 5.19 Angular accelerations (rms) of different vertebrae due to vertical accelerations imposed on the sacrum.

that linear models yield satisfactory results for low-amplitude vibration. In general, when compared with finite element models, the number of parameters and computation time is far less.

Finite element models emphasize smaller scale information about human dynamic response, such as the forces occurring at a particular point in bone or tissue. They can be used to simulate the internal structure of the body portion and analyze the internal stress and strain. As a consequence, model results (for a model with correct input) have the potential for high accuracy and good spatial resolution.

A hybrid form of model can be obtained by combining the finite element model and lumped parameter model (effectively using the lumped parameter model results as input to the finite element model. Combination of finite element models and lumped parameter models has the potential to not only increase the analysis accuracy and spatial resolution but also decrease the computation time required.

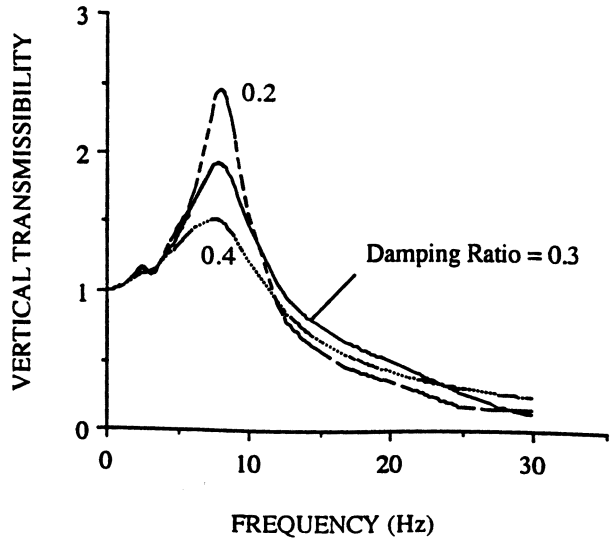

FIGURE 5.20 Effects of the damping ratio on the magnitude of transmissibility to the head.

References

1. Bremner, JM, Lawrence, JS and Miall, WE. Degenerative joint disease in a Jamaican rural population. *Ann Rheum Dis*, 27: 326-32, 1968.
2. Christ, W. Aufbaustörungen der wirbelsäule bei den in der Landwirtschaft tätigen jugendlichen im Hinblick auf das Schlepperfahren. *Grundl Landt*: 13-5, 1963.
3. Frymoyer, JW, Pope, MH, Clements, JH et al. Epidemiologic studies of low back pain. *Spine*, 5: 419-23, 1980.
4. Wilder, DG, Woodworth, BB, Frymoyer, JW et al. Vibration and the human spine. *Spine*, 7(3): 243-54, 1982.
5. Rosegger, R and Rosegger, S. Health effects of tractor driving. *Ann Agric Eng Res*, 5(3): 241-76, 1960.
6. Schultz, KF and Polster, B, Jr. Wirbelsäulenschäden bei Traktoristen und Landwirten. *Beitr Orthop Traum*, 26: 356-62, 1979.
7. Cremona, E. Die Wirbelsäule bei den Schwerarbeiten der Eisen- und Stahlindustrie sowie des Bergbaus. *Kommiss. Europ. Gem. Generaldir. Soz. Angelegenheitern*, Dok: 1911-72, 1972.
8. Schmidt, U. Vergleichende Untersuchungen an Schwerlastwagenfahrern und Büroangestellten Zur Frage der berufsbedingten Verschleibschäden an der Wirbelsäule und den Gelenken der oberen Extremitäten. Unpublished Dissertation, Humboldt-University, Berlin, GDR, 1969.
9. Heliövaara, M. Occupation and risk of herniated lumbar intervertebral disk of sciatica leading to hospitalization. *J Chron Dis*, 40: 259-64, 1987.
10. Kelsey, JL and Hardy, RJ. Driving of motor vehicles as a risk factor for acute herniated lumbar intervertebral disc. *Am J Epidem*, 102(1): 63-73, 1975.
11. Beevis, D and Forshaw, SE. *Back pain and discomfort resulting from exposure to vibration in tracked armoured vehicles.* Paper presented at the AGARD Specialists' Meeting, October, 1985.
12. Magnusson, M, Wilder, DG, Pope, MH et al. Investigation of the long-term exposure to whole-body vibration: A 2-country study. Winner of the Vienna Award for Physical Medicine. *Eur J Phys Med Rehabil*, 3(1): 28-34, 1993.
13. Seidel, H and Heide, R. Long-term effects of whole-body vibration: A critical survey of the literature. *Int Arch Occup Environ Health*, 58: 1-26, 1986.
14. Wilder, DG, Frymoyer, JW and Pope, MH. The effect of vibration on the spine of the seated individual. *Automedica*, 6: 5-35, 1985.

15. Dieckmann, D. A study of the influence of vibration on man. *Ergonomics*, 1: 347-55, 1958.
16. Panjabi, MM, Andersson, GBJ, Jorneus, L et al. *In vivo* measurement of spinal column vibrations. *J Bone Joint Surg*, 68A(5): 695-702, 1986.
17. Pope, MH, Kaigle, AM, Magnusson, M et al. Intervertebral motion during vibration. *J Eng Med*, 205: 39-44, 1991.
18. Pope, MH, Svensson, M, Broman, H et al. Mounting of the transducer in measurements of segmental motion of the spine. *J Biomech*, 19(8): 675-7, 1986.
19. Zagorski, J, Jakubowski, R, Solecki, L et al. Studies on the transmissions of vibrations in human organism exposed to low-frequency whole-body vibration. *Acta Physiol Pol*, 27: 347-54, 1976.
20. Pope, MH, Wilder, DG, Jorneus, L et al. The response of the seated human to sinusoidal vibration and impact. *J Biomech Eng*, 109: 279-84, 1987.
21. Pope, MH, Broman, H and Hansson, T. The dynamic response of a subject seated on cushions. *Ergonomics*, 32(10): 1155-66, 1989.
22. Magnusson, M, Pope, M, Rostedt, M et al. The effect of backrest inclination on the transmission of vertical vibrations through the lumbar spine. *Clin Biomech*, 8: 5-12, 1993.
23. Althoff, I, Brinckmann, P, Frobin, W et al. An improved method of stature measurement for quantitative determination of spinal loading: Application to sitting postures and whole body vibration. *Spine*, 17(6): 682-93, 1992.
24. Dupuis, H. Belastung durch mechanische Schwingungen und mögliche Gesundheitsschädigungen im Bereich der Wirbelsäule (Impact through mechanical vibrations and possible damage to health in the area of the spine). *Fortschr Med*, 92: 618-20, 1974.
25. Seroussi, RE, Wilder, DG and Pope, MH. Trunk muscle electromyography and whole body vibration. *J Biomech*, 22(3): 219-29, 1989.
26. Pope, MH, Wilder, DG and Seroussi, RE. Trunk muscle response to foot support and corset wearing during seated, whole-body vibration. *Trans Orthop Res Soc*, 13: 374, 1988.
27. Zimmerman, CL, Cook, TM and Goel, VK. Effects of seated posture on erector spinae EMG activity during whole body vibration. *Ergonomics*, 36: 667-75, 1993.
28. Chaffin, DB. Localized muscle fatigue - definition and measurement. *J Occup Med*, 15: 346-54, 1973.
29. DeVries, HA. Method for evaluating muscle fatigue and endurance from electromyographic fatigue curves. *Am J Phys Med*, 47: 125-35, 1968.
30. Hagberg, M. Electromyographic signs of shoulder muscular fatigue in two elevated arm positions. *Am J Phys Med*, 60: 111-21, 1981a.
31. Hagberg, M. Muscular endurance and surface electromyogram in iosmetric and dynamic exercise. *Am Physiol Soc*, 61: 1-7, 1981b.
32. Kadefors, R, Kaiser, E and Petersen, I. Dynamic spectrum analysis of myo-potentials with special reference to muscle fatigue. *Electromyography*, 8: 39-74, 1968.
33. Komi, PV and Tesch, P. EMG frequency spectrum, muscle structure, and fatigue during dynamic contractions in man. *Eur J Appl Physiol Occup Physiol*, 42: 41-50, 1979.
34. Magnusson, M, Hansson, T and Broman, H. Back muscle fatigue and whole body vibrations. *Ortho Trans*, 12(3): 598, 1988.
35. Bennett, MD, Webb, R and Withey, WR. Personality, performance, and physiological cost during vibration. *Proc Phys Soc*: 75-6, 1977.
36. Cole, SH and Withey, WR. Human response to whole body vibration of different wave forms. *Proc Phys Soc*: 76-7, 1977.
37. Webb, RD, Bennett, MD, Farmilo, B et al. Personality and intersubject differences in performance and physiological cost during whole-body vibration. *Ergonomics*, 24(4): 245-55, 1981.
38. Magnusson, M, Pope, M, Lindell, V et al. The metabolic cost of various occupational exposures. *Ergonomics*, 30(1): 55-60, 1987.
39. Holm, S and Nachemson, A. Nutrition of the intervertebral disc: Effects induced by vibration. *Orthop Trans*, 9(3): 525, 1985.

40. Hansson, TH, Keller, TS and Holm, S. The load on the porcine lumbar spine during seated whole body vibrations. *Orthop Trans*, 12(1): 85, 1988.
41. Keller, TS, Hansson, T, Holm, S et al. *In vivo* creep behavior of the normal and degenerated porcine intervertebral disc: A preliminary report. *J Spinal Disord*, 1(4): 267-78, 1988.
42. Witt, AN and Fischer, V. *Vibrationsbedigte Wirbelsäulenschäden bei Hubschrauberpiloten*: Research report Wehrmed, BMVg-FBWM 80-2, 1-118, 1980.
43. Fassbender, HG. *Tierexperimentelle liche- und elektronenoptische Untersuchungen über die Entstehung und den Charakter von Vibrationsschäden.* Unpublished research report, Mainz, 1979.
44. Weinstein, J, Pope, M, Schmidt, R et al. Neuropharmacologic effects of vibration on the dorsal root ganglion. *Spine*, 13(5): 521-5, 1988.
45. McLain, RF and Weinstein, JN. Effects of whole body vibration on dorsal root ganglion neurons: Changes in neuronal nuclei. *Spine*, 19(13): 1455-61, 1994.
46. Ishihara, H, Tsuji, H, Hirano, N et al. Effects of continuous quantitative vibration on rheologic and biological behaviors of the intervertebral disc. *Spine*, 17: S7-S12, 1992.
47. Coermann, RR, Ziegenruecker, GH, Wittwer, AL et al. The passive dynamic mechanical properties of the human thorax-abdomen system and of the whole body system. *Aerospace Medicine*, 31(6): 443-56, 1960.
48. Hopkins, GR. *Nonlinear lumped parameter mathematical model of dynamic response of the human body.* Paper presented at the Wright-Patterson AFB, Ohio, 26-28 Oct. 1970, 1971.
49. Muksian, R and Nash, CD. A model for the response of seated humans to sinusoidal displacements of the seat. *J Biomech*, 7: 209-15, 1974.
50. Hertzberg, HTE and Clauser, C. Size and motion. NASA, Washington, 1964.
51. Colella, A. Correspondence regarding autopsy fingings and procedures. Fogarty Memorial Hospital, Woonsocket, 1969.
52. Roberts, VL, Stech, EL and Terry, CT. Review of mathematical models which describe human response to acceleration. *No. 66-WA/BHF-13,* , 1966.
53. Vogt, HL, Coermann, RR and Fust, HD. Mechanical impedance of the sitting human under sustained aceleration. *J Aero Med*, 39: 675-9, 1968.
54. Goldman, DE and von Gierke, HE. Effects of shock and vibration on man. In C. M. Harris and C. E. Crede (Eds.), *Shock and Vibration Handbook*, (Vol. 3, pp. Chapter 44). McGraw-Hill, 1961.
55. Pradko, F, Lee, R and Greene, JD. Human vibration response Theory. *205-222,* ASME, 1967.
56. Pradko, F, Lee, R and Greene, JD. Theory of human vibration response. *66-WA/BHF-15,* ASME, 1966.
57. Muksian, R and Nash, CD. On frequency-dependent damping coefficients in lumped-parameter models of human beings. *J Biomech*, 9: 339-42, 1976.
58. Magid, EB, Coermann, RR, Lowry, RD et al. Physiological and mechanical response of the human to longitudinal whole-body vibration as determined by subjective response. *MRL-TDR-62-66,* Wright-Patterson AFB, 1962.
59. von Gierke, HE. Biodynamic response of the human body. *Appl Mech Rev*, 17: 951-8, 1964.
60. Broman, H, Pope, MH and Hansson, TH. A mathematical model of the impact response of the seated subject. *Med Eng Phys*, 18(5): 410-9, 1996.
61. Pope, MH, Broman, H and Hansson, T. Factors affecting the dynamic response of the seated subject. *J Spinal Disorder*, 3: 135-42, 1990.
62. Sandover, J. Modeling human responses to vibration. *Aviation, Space, and Environmental Medicine*, 49(1): 335-9, 1978.
63. Vibration and shock - mechanical driving point impedance of the human body. *5982,* ISO, 1981.
64. Mechanical vibration and shock - mechanical transmissibility of the human body in the z direction. *7962,* ISO, 1987.
65. Nigam, SP and Malik, MA. A study on a vibratory model of a human body. *J Biomech Eng*, 109(5): 148-53, 1987.

66. Bartz, JA and Gianotti, CR. Computer program to generate dimensional and inertial properties of human body. *ASME Journal of Engineering for Industry*, 97: 49-57, 1975.
67. Greene, PR and McMahon, TA. Reflex stiffness of man's antigravity muscles during kneebends while carrying extra weighs. *J Biomech*, 12: 881-91, 1979.
68. McMahon, TA and Greene, PR. The influence of track compliance on running. *J Biomech*, 12: 893-904, 1979.
69. Wan, Y and Schimmels, JM. Optimal seat suspension design based on minimum simulated subjective response, *J Biomechan Eng*, 119: Nov. 1997.
70. Patil, MK and Palanichamy, MS. A mathematical model of tractor-occupant system with a new seat suspension for minimization of vibration response. *Appl Math Modeling*, 12(2): 63-71, 1988.
71. Griffin, MJ, Whitham, EM and Parsons, K. Vibration and comfort I, II, III, IV. *Ergonomics*, 25(8), 1982.
72. Fairley, TE and Griffin, MJ. The apparent mass of the seated human body: vertical vibration. *J Biomech*, 22(2), 1989.
73. Amirouche, FML and Ider, SK. Simulation and analysis of a biodynamic human model subjected to low accelerations - a correlation study. *J Sound and Vibration*, 123(2): 281-92, 1988.
74. Kaleps, I, von Gierke, HE and Weis, EB. A five degree of freedom mathematical model of the body. *AMRL-TR-71-29-8,* Wright-Patterson AFB, Ohio, 1971.
75. Coermann, RR. The mechanical impedence of the human body in sitting and standing positions at low frequencies. *Human Factors*, 4: 227-53, 1962.
76. Clark, WS, Lange, KO and Coermann, RR. Deformation of the human body due to uni-directional forced sinusoidal vibration. *Human Factor*: 255-74, Oct. 1961.
77. Jex, HR and Magdaleno, RE. Biomechanical models for vibration feedthrough to hands and head for a semisupine pilot. *Aviation, Space, and Environmental Medicine*, 49(1): 304-16, 1978.
78. Braune, W, Fischer, O, Amar, J et al. Human Mechanics. *AMRL-TDR-63-123,* Four Monographs Abridged, 1963.
79. Magdaleno, RE and Jex, HR. Modeling of biodynamic effects of vibration. *1037-2,* Systems Technology, Inc., 1975.
80. Jex, HR and Magdaleno, RE. Modeling biodynamic effects of vibration. *1037-3,* Systems Technology, Inc., 1976.
81. Pradko, F, Orr, TR and Lee, RA. Human vibration analysis. *650426,* SAE, Chicago, Ill., 1965.
82. Donati, PM and Bonthous, C. Biodynamic response of the human body in the sitting position when subjected to vertical vibration. *J Sound and Vibration*, 90(3): 423-42, 1983.
83. Griffin, MJ, Lewis, CH, Parsons, KC et al. *The biodynamic response of the human body and its application to standards.* Paper presented at the NATO Advisory Group for Aerospace Research & Development (AGARD), 1979.
84. Qassem, W, Othman, MO and Abdul-Majeed, S. The effects of vertical and horizontal vibrations on the human body. *Med Eng Phys*, 16(3): 151-61, 1994.
85. Mizrahi, J and Susak, Z. *In vivo* elastic and damping response of the human leg to impact force. *J Biomech Eng*, 104: 63-6, 1982.
86. Patil, MK, Palanichamy, MS and Ghista, DN. Man-tractor system dynamics: towards a better suspension system for human ride comfort. *J Biomech*, II: 397-406, 1978.
87. Kasra, M, Shirazi-Adl, A and Drouin, G. Dynamics of human lumbar intervertebral joints - experimental and finite-element investigations. *Spine*, 17: 93-102, 1992.
88. Goel, VK, Park, HS and Kong, WZ. Investigation of vibration characteristics of the ligamentous lumbar spine using the finite element approach. *J Biomech Eng*, 116: 377-83, 1994.
89. Sandover, J. Behavior of the spine under shock and vibration: A review. *Clin Biomech*, 3: 249-56, 1988.
90. Pope, MH, Wilder, DG and Frymoyer, JW. *Vibration as an etiologic factor in low back pain.* Paper presented at the Proc Inst Mech Engs conf on Low Back Pain, 1980.

91. Seidel, H, Bastek, R, Brauer, D et al. On human response to prolonged repeated whole-body vibration. *Ergonomics*, 23(3): 191-211, 1980.
92. Kong, WZ, Goel, VK, Wilder, DG et al. Response of the human body to sinusoidal vertical vibration. *Unpublished*.
93. McGill, SM, Jones, K, Bennett, G et al. Passive stiffness of the human neck in flexion, extension, and lateral bending. *Clin Biomech*, 9: 193-8, 1994.
94. Panjabi, MM, Brand, RA and White, AA. Three-dimensional flexibility and stiffness properties of the human thoracic spine. *J Biomech*, 9: 185-92, 1976.
95. Moroney, SP, Schultz, AB, Miller, JA et al. Load-displacement properties of the lower cervical spine motion segments. *J Biomech*, 21: 276-9, 1988.
96. Roberts, SB and Chen, PH. Elastostatic analysis of the human thoracic skeleton. *J Biomech*, 3: 527-45, 1970.
97. Armenakas, AE. *Modern structural analysis - the matrix method approach*. McGraw-Hill, Inc., New York, 1991.
98. Closkey, RF, Schultz, AB and Luchies, CW. A model for studies of the deformable rib cage. *J Biomech*, 25: 529-39, 1992.
99. Stokes, IA and Laible, JP. Three-dimensional osseo-ligamentous model of the thorax representing initiation of scoliosis by asymmetric growth. *J Biomech*, 23(6): 589-95, 1990.
100. Takashima, ST, Singh, SP, Haderspeck, KA et al. A model for semi-quantitative studies of muscle actions. *J Biomech*, 12: 929-39, 1979.
101. William, JL and Belytschko, TB. A three-dimensional model of the human cervical spine for impact simulation. *J Biomech Eng*, 105: 321-31, 1983.
102. Dietrich, M, Kedzior, K and Zagrajek, T. Modeling of muscle action and stability of the human spine. In Multiple muscle systems: Biomechanics and movement organization. In J. M. Winters and S. L.-Y. Woo (Eds.), (pp. 451-60). Springer-Verlag, New York, 1990.
103. Hagena, FW, Wirth, CJ and Piehler, J. *In-vivo experiments on the response of the human spine to sinusoidal Gz - vibration.* Paper presented at the NATO AGARD, 1985.
104. Pope, MH and Hansson, TH. Vibration of the spine and low back pain. *Clin Orthopaedics and Related Res*, 279: 49-59, 1992.

6

Biodynamic Response of the Human Body in Vehicular Frontal Impact

Narayan Yoganandan
Medical College of Wisconsin

Frank A. Pintar
Department of Veterans Affairs Medical Center

6.1 Introduction

Enhanced seatbelt usage in the U.S., secondary to legislation, has reduced trauma in frontal impact environments. Recent introduction of air bags has further contributed to the reduction of injuries, particularly to the driver of the automobile. Despite the enhancements in vehicle design and public awareness, vehicular crashes are a predominant source of injury in the U.S. for adults under 44 years of age (Committee on Trauma Research et al., 1985; Rice and MacKenzie, 1989; USDHHS, 1989). A report to the U.S. Congress published by the National Academy of Sciences emphasizes the economic impact of injury in our society. For example, the number of years of life lost due to injury (4.1 million years) exceeds those due to heart disease/stroke (2.1 million years) and cancer (1.7 million years) combined. This is primarily because injury affects a younger age group compared to the other three leading causes of death (heart disease, stroke, and cancer).

Injuries are often classified as intentional and unintentional. Vehicular crashes fall under the classification of unintentional injuries. It is important to understand the biodynamic response of the human body in relation to its interaction with vehicular surfaces to mitigate these injuries. As can be expected, any region of the human body could be injured if the limits of tolerance of the tissues are exceeded. The objective of this chapter is to discuss the characteristics of the human body secondary to force applications under vehicular frontal impact conditions. Because of the voluminous, diversified, and multidisciplinary

nature of the topic, it is not possible to cover all aspects of the biodynamic response. However, an attempt is made to provide recent information on the subject matter. This chapter, therefore, focuses on the experimental biodynamic studies with specific relevance to the human body/tissues under frontal impact. Static or quasi-static type responses are not addressed. Furthermore, although mathematical analyses tools such as the finite element and occupant kinematics simulations have also contributed to our knowledge, this topic is considered to be outside the scope of the presentation (Dimasi et al., 1991; Dimasi et al., 1995; Hardy and Marcal, 1973; Kleinberger, 1993; Kumaresan and Radhakrishnan, 1996; Kumaresan et al., 1995; Prasad and Chou, 1993; Ruan et al., 1993; 1994; Voo et al., 1997; Yoganandan et al., 1996b,c; 1997c; 1987; 1995c). The cited list is not all inclusive. The reader is referred to literature and other chapters in this book for details.

Biodynamic Response Analyses

The effect of the external mechanical forces applied to the human body can be assessed using several methodologies: clinical evaluation including follow-up, epidemiological evaluation, and experimental evaluation. For the sake of brevity, the first two aspects are not the topics of presentation in this chapter. In addition, exhaustive analysis of all information cannot be provided on all the experimental studies because of practical constraints. An attempt is made to provide fundamental and recent research data.

6.2 Terminology

The following terminology is frequently used in impact biomechanics to understand and relate the external input mechanical variables to the response of the human tissues. Biomechanics can be defined as the application of the principles of mechanics, physics, engineering, and computer science to solve biological problems with specific reference to the human body in the current context. Biodynamics refers to the characteristics of the biological tissue under consideration secondary to external mechanical input applied at high loading rates wherein the effects of time or inertia cannot be ignored. Biofidelity can be defined as the capacity to mimic the human response under external mechanical loading. It must be emphasized that biofidelity, a term routinely used in impact biomechanics literature, is currently not in the common English dictionary. Crashworthiness, a frequent terminology used in safety engineering with particular reference to vehicular impact, refers to the protective ability of the vehicle to minimize or eliminate injuries to the human body secondary to a crash. Frankfort plane is the horizontal plane represented by a line between the lowest point on the orbit margin and the highest point on the margin of the auditory meatus. Human tolerance can be defined as the capability of biological tissues to resist (and absorb) externally applied mechanical forces without exhibiting damage. Consequently, no injury is anticipated below this tolerance level; injury is expected above this limit. Human surrogate is an experimental, physical, biological, or a mathematical model. It is used to understand the biomechanical response of the human tissue under consideration. Anthropomorphic manikins, frequently called dummies, are examples of human surrogates. Injury criterion/criteria can be defined as a mechanical index or a group of mechanical indices which is/are based on human tolerance. When this threshold is exceeded, injury is assumed to occur to the biological tissue under consideration. This may include probabilistic analysis for the injury quantification. Kinematics deals with the method of describing the motion of the structure without regard to the role of forces acting on the system. Kinetics relates the forces to the kinematic or the motion variables of the system.

Reference System

The right-handed Cartesian system is commonly used in biomechanics. The system consists of three mutually orthogonal axes, x, y, and z. Rotational and translational movements can occur on these axes. Translational movements are considered positive if they occur along the positive direction of the axis, and are considered negative if the movements are in the negative direction of the axis. Likewise, a clockwise

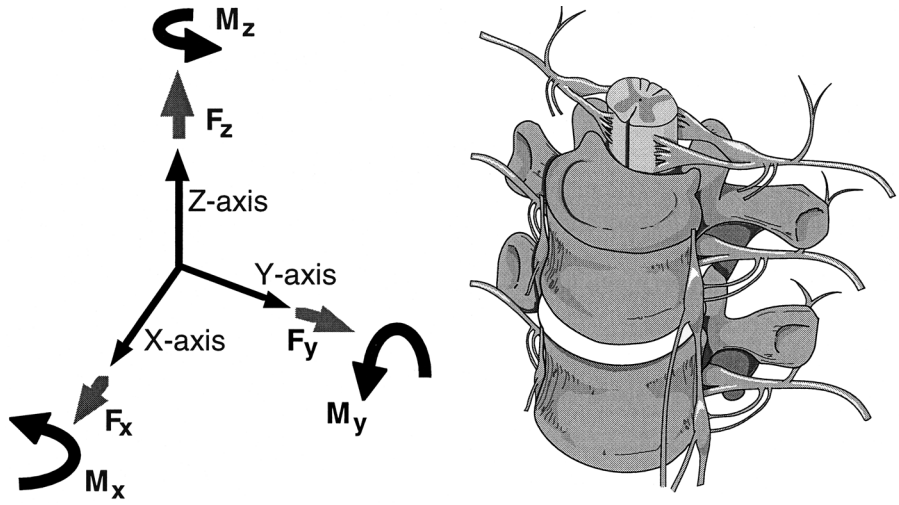

FIGURE 6.1 Cartesian coordinate system of reference.

rotation around an axis looking from the origin of the coordinate system toward the positive direction of the axis is termed positive rotation; counterclockwise rotation is negative. Figure 6.1 illustrates the right-handed Cartesian coordinate system of reference with the positive z-axis along the inferior to superior direction, the positive x-axis along the posterior to anterior direction, and the positive y-axis along the right to left direction. This results in a positive flexion moment (M_y), positive left to right lateral bending moment (M_x), and positive right axial twisting moment (M_z). In contrast, extension moment, right to left lateral bending moment, and left axial rotation are negative moments. This system of reference has also been adopted by the American Standards for Testing Materials. Anatomical position is an erect position with the eyes forward and the palms of the hand to the front (Fig. 6.2). This position of the hand is called supination. Pronation refers to the palms down or backward. Sagittal plane is the anteroposterior vertical plane through the body. The plane perpendicular to the midsagittal plane is called the coronal plane. The plane orthogonal to the vertical plane is the horizontal, transverse, or axial plane. Ventral and dorsal refers to the front and back, and cranial and caudal refers to the head and tail regions of the trunk. In the erect position, ventral and dorsal corresponds to the anterior and posterior, and superior and inferior refers to the cranial and caudal directions, respectively. Adduction is motion toward the midline and abduction is motion away from the midline.

6.3 Head

In vehicular frontal impact, the head can be injured by impacting with the vehicle interior surfaces such as the header and the pillar. A review of head injury has been given (Sances and Yoganandan, 1986). This review includes initial studies for the determination of the acceleration time tolerance curve, human volunteer studies, the Gadd severity index, the head injury criteria (known as HIC), the Vienna Institute Index, the Effective Displacement Index, the revised brain model, the development of the mean strain criterion, the Japanese Automotive Research Institute, and vertex impact human vertical drop studies from the Medical College of Wisconsin, Milwaukee. In addition, tolerance for lateral impacts, rotational head injury levels, and finite element head injury models were discussed (Sances and Yoganandan, 1986). Head injuries are classified as open and closed. Open head injuries are associated with skull fractures; soft tissue injuries to the intracranial contents can also occur in the presence of a skull fracture. However, in closed head injuries, skull fractures are absent and head trauma is limited to the internal contents of the skull. Skull fractures include linear, depressed, comminuted, and basilar varieties. Brain injuries are often categorized into focal and diffused types. Focal injuries are associated with lesions large enough to

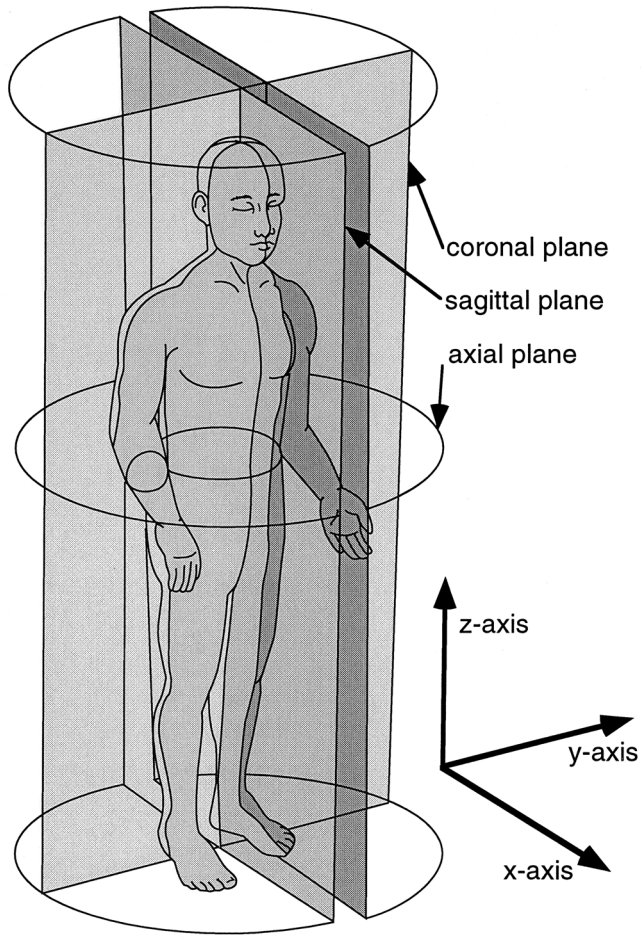

FIGURE 6.2 Anatomical position.

be visualized and include subdural hematoma, epidural hematoma, and intracerebral hematoma. They can produce shifts of the cerebral tissue within the cranium, herniation, and brain stem compressions. Diffused brain injuries occur with widespread destruction of neurologic function attendant with macroscopically visible brain lesions (Gennarelli, 1981). Brain injury secondary to blunt impact includes changes in the intracranial pressure resulting in shear strains. Causes of brain tissue contusion secondary to intracranial compression include the inward bending of the calvarium and the propagation of an internal compressive pressure wave. In contrast, at the contrecoup site (location opposite to the loading location), the build-up of a negative pressure as a reactive response can also cause brain injury.

Initial studies to determine the tolerance of the human head were conducted using human cadaver material. Other studies were reported by Evans et al. and Lissner et al., in the *Surgery Gynecology and Obstetrics Journal* in the late 1950s (Evans et al., 1958; Lissner et al., 1960). Four Caucasian male embalmed cadavers ranging in age from 64 to 76 were used to determine the relationship between the acceleration and intracranial pressure produced with the forehead striking an automobile instrument panel, large block of steel, or a tin-steel plate. The cadavers underwent a free-fall from a distance of approximately 1.7 m. Multiple tests were conducted on each specimen. The first drop was generally onto an automobile instrument panel, the second drop onto a steel flat plate, and the third onto a solid steel block. Accelerations were measured at the occiput with forehead impact. Intracranial pressure changes were measured in bilateral temporal regions with the transducers. Portions of the brain were removed and filled with fluid gelatin to provide access to ventricles. In some studies, a 75-mm polyurethane pad was placed over

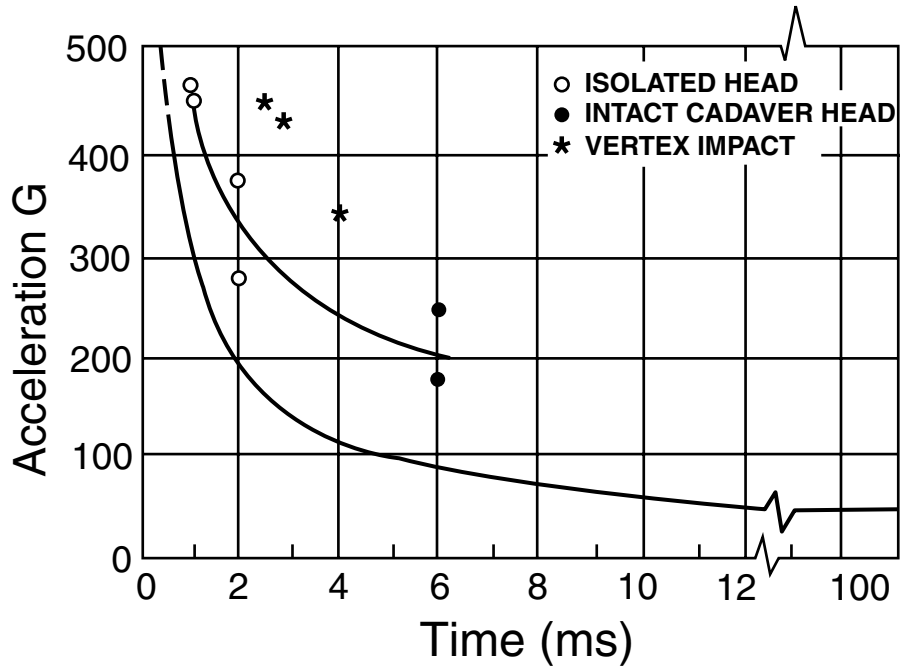

FIGURE 6.3 Acceleration time curves from experimental studies. Upper curve is the original acceleration versus time for the initial studies conducted by Lissner et al. The lower curve is the original average acceleration time tolerance curve for head impact of hard flat surface with an asymptote of 42 G. Data points for the head without the body, and head with the body, produced skull fractures for forehead impacts, and data points for vertex impact from our group produced skull fractures using unembalmed human cadavers.

the steel plate for comparison. Twenty-three drops were conducted on the four embalmed cadavers with impact velocities ranging from 4.9 to 6.7 m/s. For impact on the steel block in the intact cadaver drops, the maximum time duration ranged from 5 to 8 msec and the peak head accelerations ranged from 43 to 237 G. In addition, three isolated head specimens underwent free-fall testing at impact velocities ranging from 5.2 to 6.0 m/s. These specimens sustained fractures secondary to impact on the steel block with peak accelerations from 372 to 557 G and acceleration duration ranging from 1 to 2 msec. More recently, free-fall impact tests with isolated human cadaver head specimens impacting on the vertex were conducted by our group (Sances and Yoganandan, 1986). The specimens were dropped onto a force plate covered with 0, 12.5, 25.4, and 38 mm of padding with drop heights ranging from 0.3 to 1.2 m. Accelerations ranged from 325 to 450 G with pulse durations ranging from 2.2 to 4 msec. Both the force and the accelerations decreased with increasing pad thickness. The peak acceleration for skull fracture vs. pulse duration from the studies cited above is illustrated in Fig. 6.3. Because of the difficulties in dealing with peak accelerations, average values for the acceleration time tolerance curve were used.

Subsequent investigations were conducted to extend the curve beyond the 6-msec duration, and to determine the effect of forehead impact on laminated and tempered safety glass used in automobiles (Gurdjian et al., 1962a). The heads of the embalmed cadavers were filled with gelatin as previously described and 95 tests were conducted using 10 cadavers. Some of the cadavers had below-knee amputation and the remaining cadavers had their legs doubled back and tied down. The head struck the glass at impact velocities ranging from 1.3 to 15.6 m/s. The laminated glass demonstrated damage at impact velocities of 1.8 to 2.7 m/s, and the tempered glass at approximately 5.8 m/s. Peak head accelerations as high as 230 G were recorded for impact to the tempered glass with velocities of approximately 11.2 m/s. Generally, the intracranial pressures produced by impact to the laminated glass were lower compared to the pressures produced by impact to the tempered glass material. The maximum average accelerations ranged from 90 to 125 G measured at the occiput for impact to the midline of the forehead with side

window tempered or laminated windshield-type glass. The time durations ranged from 6 to 12 msec. The average pressures reached 0.15 MPa, which lasted from 6 to 12 msec (Gurdjian et al., 1961). These data were used to extend the previously described acceleration time tolerance curve from 6 to approximately 12 msec. The initial acceleration time tolerance curve had a 42-G asymptote for longer times. To extended the data beyond 12 msec, the data of Eiband and Stapp were used; the data was obtained from full-body human volunteer exposures who did not receive a direct blow to the head (Eiband and Stapp, 1955; Stapp, 1961). Patrick, however, reasoned that when an impact occurs to the head, a reasonable asymptote would be 80 G instead of the 40 G (Patrick et al., 1963). The acceleration time tolerance curve is commonly referred to as the Wayne State Tolerance Curve.

Based on these observations, in the early 1970s, various criteria were proposed which included the head injury criterion, the Vienna Institute Index, the Effective Displacement Index, the revised brain model, and the mean strain criterion. The head injury criterion (HIC), advanced by Versace in 1971, is given by the following equation (Versace, 1971).

$$(t_2 - t_1)\left[\frac{1}{(t_2 - t_1)}\int_{t_1}^{t_2} a(t)dt\right]^{2.5} < 1{,}000$$

where a in the equation is the resultant acceleration, and t_1 and t_2 are any two points in the acceleration curve that maximize the equation. Expressed in terms of energy, this equation relates the rate of changes of specific kinetic energy and acceleration over the interval $t_2 - t_1$. In 1985, probabilities were attached to HIC (Prasad and Mertz, 1985). A HIC value of 1000 was reported to correspond to 60% of the population sustaining a severe to fatal injury. It should be noted that HIC is an integration of the acceleration-time pulse, whereas the acceleration-time tolerance curve is based on average acceleration. Hodgson and co-workers in the 1970s determined the impact response of the head against a flat rigid surface by conducting drop tests with human cadavers (Hodgson and Thomas, 1971). Tests were conducted on the frontal, lateral, and occipital sides, and the biodynamic response was determined in terms of forces and accelerations. A large scatter in the data secondary to biological variations as well as regional variations in the calvarium was observed. Peak forces and accelerations for nonfracture at a drop height of 130 ± 19 mm were 4.24 ± 58 kN and 159 ± 42 G, respectively (Fig. 6.4). In contrast, peak forces and accelerations for fracture at a 330-mm drop height were 6.4 ± .6 kN and 230 ± 42 G, respectively. At a 1060-mm drop height, the peak force was 10.9 ± 1.1 kN and the peak acceleration was 293 ± 42 G (Prasad and Mertz, 1985).

Previous skull fracture studies conducted by Gurdjian indicated that static loading causes a skull to deflect with less force compared to dynamic loading (Gurdjian, 1975). An empty human skull fractured at an energy of 2.8 J; intact head with scalp required approximately 45 to 48 J for fracture (Gurdjian et al., 1962b). In human head drop tests (with the scalp intact) onto a heavy steel slab, Gurdjian reported that fractures occur at energies of approximately 70 J (Gurdjian, 1975). An acceleration-time tolerance curve for human linear skull fracture based on a drop test demonstrated approximately 70 G to be a threshold for a 5-ms duration acceleration pulse, and approximately 50 G for a duration greater than or equal to 30 ms (Gurdjian, 1975). More recently, Nahum et al. demonstrated depressed or comminuted fractures at the temporal parietal area at force levels of 2000 N, at the frontal area at force levels of 4000 N, and at the zygoma at force levels of 890 N, with a 645-mm^2 impactor (Nahum et al., 1968). Other studies indicate forces ranging from 980 to 1334 N to produce penetration of the parietal skull using an impactor of a 200- to 297-mm^2 area (Melvin and Evans, 1971; Melvin et al., 1969). Fracture of the frontal region under static loading was produced at a force of 4727 N using a 10 mm × 100 mm × 10 mm plate (Ehler et al., 1976a; Ehler et al., 1976b). Hodgson and Thomas in 1971 indicated that plates produced linear fractures and the small impactors caused penetration fractures (Hodgson and Thomas, 1971). Melvin and Evans data indicated that large impactors produced comminuted depressed fractures (Melvin and Evans, 1971). Assuming that the modulus of elasticity of the skull is 1579 kg/mm^2, and a minimum strain energy is 0.22 kg/mm^2, Shell theory predicts the fracture force at 3941 N for a 645-mm^2 impactor. Schneider and Nahum recorded a force of 2113 N associated with the kinetic energy of 29 J at velocities

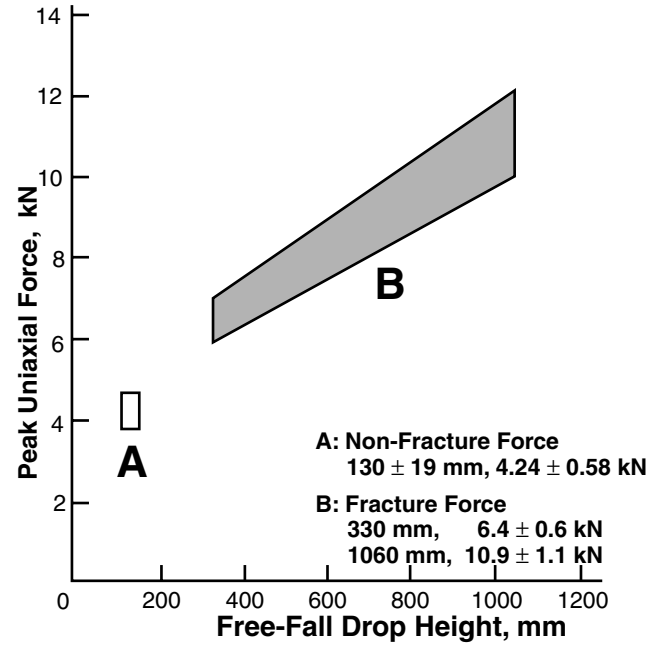

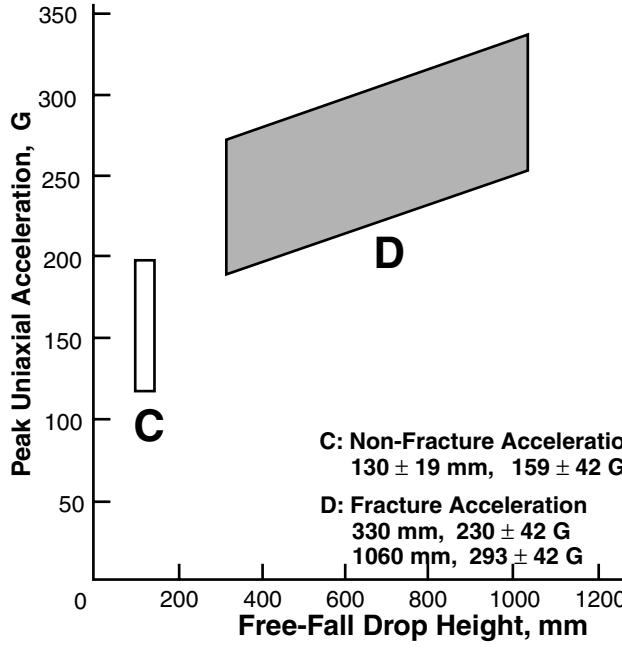

FIGURE 6.4 Head impact response obtained using embalmed human cadaver specimen experiments.

of 5.2 m/s for temporoparietal fracture (Schneider and Nahum, 1972). McElhaney et al. provided static force-deflection properties from tests on the human head at the frontal and lateral sites (McElhaney et al., 1972). Clinical follow-up of skull fracture studies have been reported (Braakman, 1972; Jamieson, 1974;

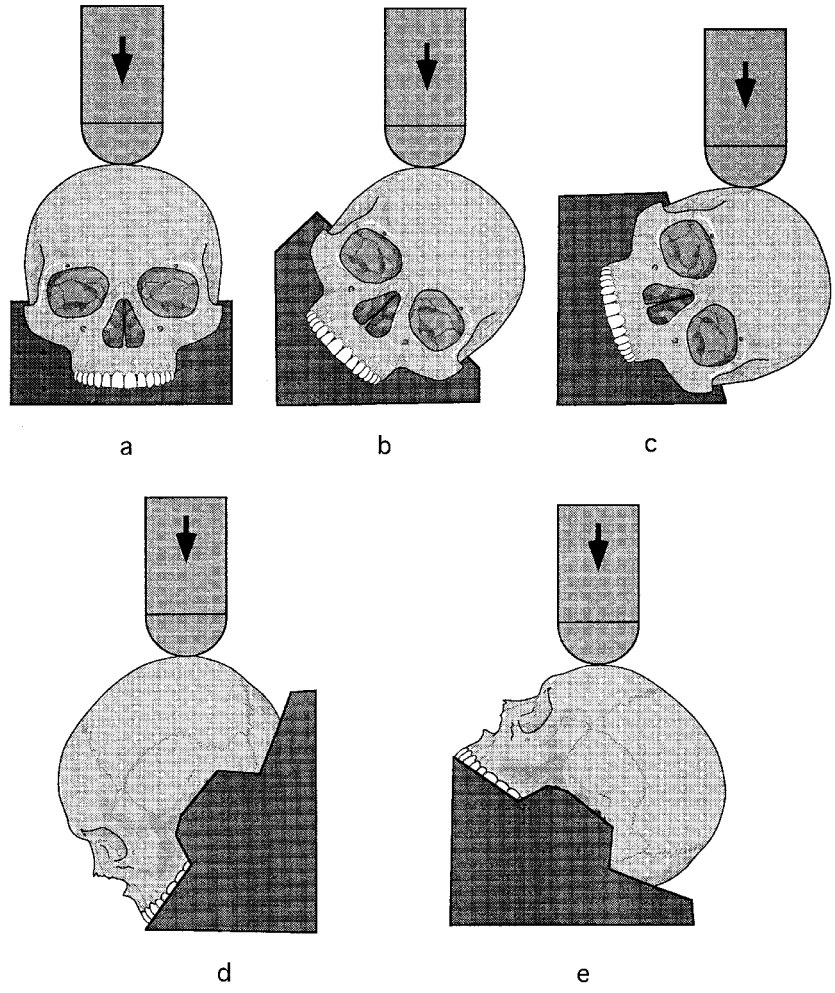

FIGURE 6.5 Schematic illustration depicting the various anatomical sides used to conduct impact loading experiments. In clockwise order, the sites shown correspond to the vertex, parietal, temporal, occiput, and forehead regions of the head.

Jamieson and Kelly, 1974; Jamieson and Yelland, 1972; Stover and Zeigler, 1976; Unterharnscheidt and Higgins, 1969; Walker et al., 1969).

More recently, additional studies were conducted by Yoganandan et al. to determine the static and dynamic response of the intact human cadaver head by applying controlled loading using a preprogrammed electrohydraulic material testing apparatus (Yoganandan et al., 1995b). The local force-deflection characteristics of the human occipital, lateral, parietal, and frontal areas of the intact head under known boundary conditions were determined. These experiments, described below, provided the force-deflection information required for finite element modeling. Using a total of 20 unembalmed human cadavers with age, height, and weight ranging from 50 to 85 years, 157 to 185 cm, and 56 to 102 kg, respectively, nondestructive quasi-static, failure quasi-static, and dynamic failure tests were conducted (Yoganandan et al., 1995b). Occipital, vertex, lateral, temporal, and frontal regions of the head were considered in the study (Fig. 6.5). For the nondestructive testing, the specimen was fixed in an adjustable device designed to locate both auditory meatuses and support the skull under the palate and the skull base. Polymethyl-methacrylate was molded into the skull to provide additional strength at the supported

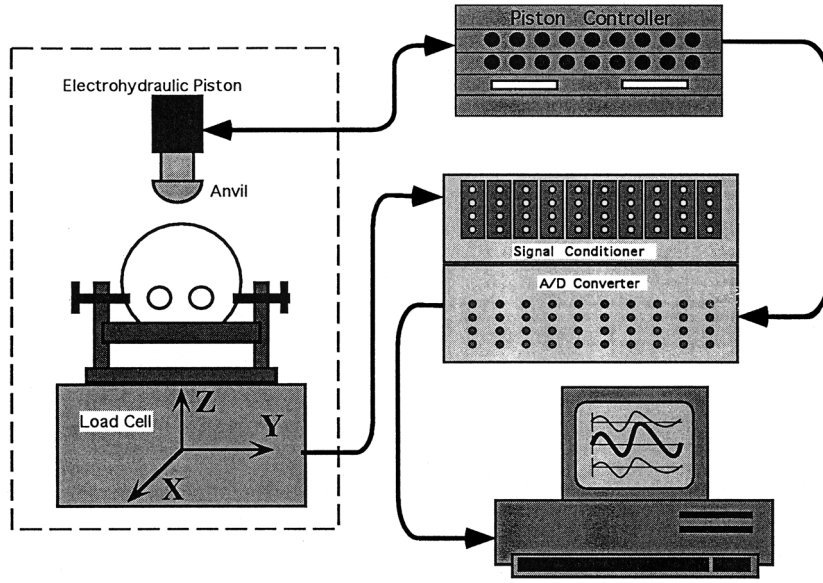

FIGURE 6.6 Illustration demonstrating the experimental test setup including the electrohydraulic piston and the associated data acquisition equipment.

regions. The fixture was mounted on a six-axis load cell fixed to the cross-frame of an electrohydraulic testing device (MTS Systems Corp., Minneapolis, Minn.).

For the destructive quasi-static and dynamic tests, the specimens were prepared in a similar manner as described above. Because of the destructive nature of the test, only one loading site was possible for each specimen. Following initial radiography, the specimens were aligned appropriately with the longitudinal axis of the electrohydraulic piston. They were loaded to failure at a loading rate of 0.002 m/sec in quasi-static tests and at 7.1 to 8.0 m/sec in dynamic experiments. After the test, the specimen was palpated, radiographs were taken, CT images were obtained, and the skulls were defleshed. A Snell-type hemispherical anvil with a radius of 48 mm was used as the impactor. The anvil was rigidly attached to the electrohydraulic actuator. A schematic of the experimental test setup is shown (Fig. 6.6). Specimen failure was identified when an increase in the piston excursion resulted in a concomitant decrease of the external force. The applied external force and the actuator displacement data, along with the six-axis load cell information placed at the distal end of the preparation, were recorded with a uniaxial force gauge, a linear variable differential transformer attached in series to the electrohydraulic piston, and a six-axis load cell placed underneath the specimen, respectively. All data were sampled according to the Society of Automotive Engineers SAE J221b specifications at appropriate sampling rates, using a modular digital data acquisition system. Processing of the raw signals included a transformation of the force-time and displacement-time responses into a force-deflection behavior. Stiffness and energy absorbed by the specimen were obtained according to accepted techniques (Yoganandan et al., 1988a; Yoganandan et al., 1988b; Yoganandan et al., 1989).

For the nondestructive quasi-static series, the forces ranged from 1639 to 1702 N with deformations ranging from 1.9 to 7.2 mm. The specimen returned to the initial position suggesting the absence of pathological alterations. This was additionally confirmed by radiography, computed tomography, and gross dissection followed by defleshing of the skull. For the destructive quasi-static failure tests, forces ranged from 4.5 to 11.9 kN (mean: 6.4 kN). The corresponding deflections at failure ranged from 7.8 to 16.6 mm (mean: 12.0 mm). The stiffness and energy absorption capacities ranged from 0.5 to 1.3 kN/mm (mean: 0.8), and 14.1 to 68.5 J (mean: 33.5 J), respectively. For the dynamic failure tests, the forces ranged from 4.5 to 15.4 kN (mean: 10.5 kN), the deflections ranged from 3.4 to 11.5 mm (mean: 6.7 mm), stiffness ranged from 1.0 to 6.1 kN/mm (mean: 3.1 kN/mm), and energy ranged from 13.0 to 55.8 J

(mean: 28.6 J). The forces, deflections, and stiffness were different between the quasi-static and dynamic loadings. Pathology included linear and circular, propagated unilateral and bilateral, and multiple fractures due to external loading. Fractures identified on CT were documented by the defleshed skull. These series of tests revealed the fracture pattern to be complex and dependent upon the anatomical location of the external loading. Retrospective evaluations of the radiographs and CT images, without a prior knowledge of the external loading vector, produced no definite indications regarding the loading site during the experimentation. In fact, fracture widths were narrower at the loading site compared to the other regions where the specimen demonstrated wider separations of the fracture lines. Fractures generally continued to penetrate into the inner table with the loading applied superior to the outer table. It must be emphasized that, despite significant research in terms of cadaver and animal experiments, and physical modeling studies coupled with computational simulation efforts in the past 25 years, the head injury criterion is the only accepted biomechanical index for assessing head trauma in vehicular environments.

6.4 Face

Facial bone fractures are often associated with dynamic contact with the vehicular interior including the steering wheel or external surfaces. Yoganandan et al. provided a brief summary of the previous work dating back to 1901 on the topic of facial injuries (Yoganandan et al., 1993; Yoganandan et al., 1991a; Yoganandan et al., 1991d). The relationship between the area of the impactor used to apply the external loading onto the facial bone and the resulting biomechanical parameters such as the peak force were discussed. Because these earlier studies were not conducted with the actual steering wheel of the vehicle to be the impacting object onto the human facial skeleton, Yoganandan et al. conducted a series of experiments to determine the biodynamics of the human facial skeleton subjected to steering wheel impact. In particular, the zygomatic region of the face was selected as the impacting structure of the human body (Yoganandan et al., 1993; Yoganandan et al., 1991a; Yoganandan et al., 1991d). Using a specially devised vertical drop test apparatus, which was validated with free-fall and rigid head form drops, tolerance values were reported using unembalmed human cadaver tests (Harris et al., 1993). Biomechanical variables such as peak force, area of contact/pressure, head injury criteria, and steering wheel deflection at the site of impact were investigated for facial trauma assessment. The pressure criteria that forms the basis for the honeycomb structure design, the conventional head injury criteria, and the steering wheel deflections were found to be weak correlates. The authors indicated that the weak correlation between the pressure criteria and the likelihood of facial injury is only applicable to the zygomatic impact (Yoganandan et al., 1996a). However, it may be useful for other regions of the face wherein factors such as larger area of contact may occur due to steering wheel contact. Proven biomechanical data are currently not available to provide confidence in the general applicability of the honeycomb test device for facial trauma assessment. Consequently, although the honeycomb appears to be appealing from a testing point of view, caution should be exercised to adopt this technique for all structures of the human face. There remains a need for suitable tolerance criteria for facial injury assessment and mitigation. Using the maximum likelihood approach and Weibull functions, Yoganandan et al. presented a fracture probability curve associated with the peak interface force to describe facial injury due to steering wheel loading at the spoke-rim junction. The probability curve indicates a force of 1525 N to correspond to a 50% probability of facial injury (Fig. 6.7). Significant amelioration of trauma can be attained if the injury assessment is made using this output (Yoganandan et al., 1996a; Yoganandan et al., 1993).

A complete assessment of steering wheel injury-induced facial trauma and the development of appropriate criteria and test devices for injury production require additional research. These topics are important because low-level vehicular crashes without the deployment of an air bag may have significant consequences. Since steering wheels with integrated air bags generally require a stiffer structure to handle the air bag deployment forces, this research may have significant implications in vehicular safety from a frontal impact perspective, particularly at low levels of energy dissipation.

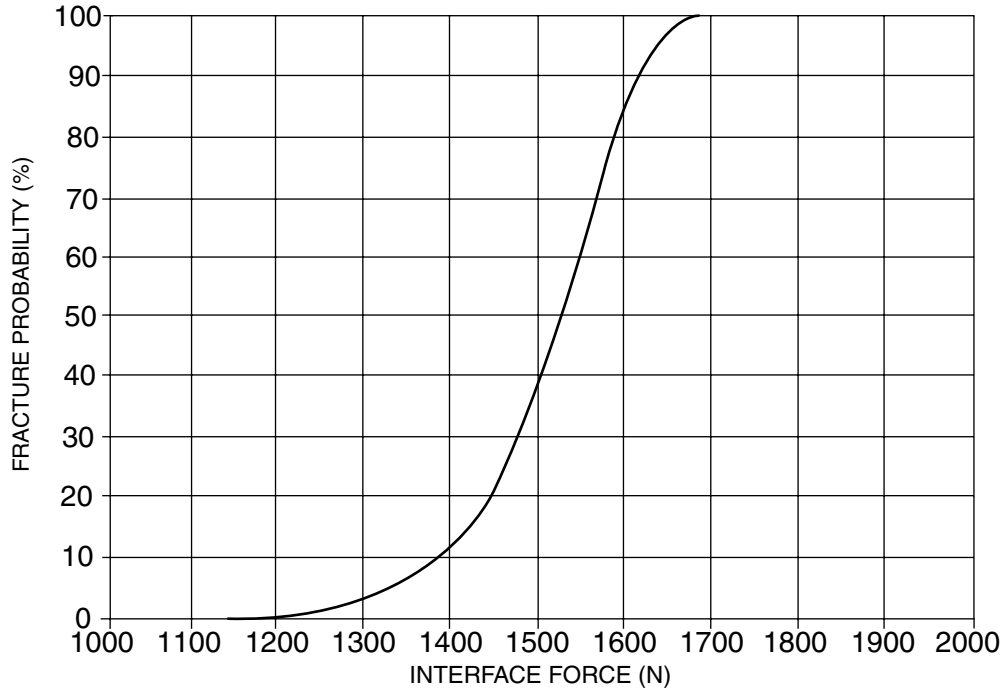

FIGURE 6.7 Probability distribution for facial fracture secondary to steering wheel impact.

6.5 Neck

The human neck connects the first thoracic vertebra (T1) and the torso with the head. The neck is composed of soft and hard tissue structures including trachea, esophagus, arteries, and spinal cord. The hard tissue structures are connected through a system of joints spanning across the entire length of the neck. While the bottom of the neck is connected to the first thoracic vertebra structurally, the top of the neck is connected to the base of the skull. The principal medium of external load transfer takes place through the vertebrae and the adjacent structures. The interrelationships among the seven cervical vertebrae are closely maintained by the surrounding soft tissue anatomy to protect the spinal cord under normal physiologic and traumatic conditions. Any external mechanical load vector that attempts to compromise the integrity of the cervical vertebrae through fracture or dislocation and/or the integrity of the spinal cord can have serious consequences to the individual. The anatomy and fundamental biomechanical aspects are covered elsewhere (Maiman and Yoganandan, 1991; Pintar et al., 1996a; Yoganandan et al., 1997b). Because of the complex articulated and segmented nature of the cervical spinal column, many mechanisms of injury are possible in vehicular frontal impact.

In earlier studies, Yoganandan et al. classified the mechanisms of cervical spine injury according to compression-flexion, hyperflexion, compression-extension, hyperextension, axial loading associated with vertical compression and vertical distraction, lateral bending, rotation, and shear (Yoganandan et al., 1990). A literature review has been conducted on the biomechanical aspects of cervical trauma (McElhaney and Myers, 1993). Since many of the previous experimental studies indicated the prealignment of the cervical column with respect to the head to be an important factor in spinal injury, Pintar et al. conducted a series of static and dynamic experiments using human cadaver head-neck complexes to determine neck injury tolerance (Pintar et al., 1990a,b; Pintar et al., 1995a-c). Based on these tests and on the theoretical beam-column analyses, it was surmised that the stiffest axis of the cervical spine results when the cervical lordosis is removed and the spinal vertebrae are aligned vertically (Liu and Dai, 1989; Pintar et al., 1995b). Cervical alignment along this axis prior to compressive loading produced

compression-related injuries to the mid- to lower-cervical vertebrae. Intact human cadaver head-neck complexes were used because traditional one- or two-level functional spinal models were inappropriate to study the injury mechanisms of the cervical spine secondary to impact loading (Pintar et al., 1990a,b). The cadaver head-neck complexes were mounted in a fixative at T1-T2 and the cranium was unconstrained. The inferior end was mounted to a six-axis load cell and fixed to the electrohydraulic testing device. The cervical spine was prealigned to remove the lordosis. The external compressive load, the deformation, and the output generalized (six-axis) force and moment histories at the inferior end of the preparation together with the information from the retroreflective targets placed along the cervical spinal column described the kinetics of the structure (Pintar et al., 1990a; Yoganandan et al., 1994a,b; Yoganandan et al., 1991b,c). Principles of continuous motion analysis techniques revealed the temporal sequelae of pathologic and nonpathologic motions occurring to the cervical spinal column secondary to impact loading to the cranium (Cusick et al., 1996; Yoganandan et al., 1994a). Data analysis revealed that burst fractures occur very early in the loading phase (within the first 10 msec) and soft tissue ligament injuries occur later.

Pintar et al. classified the injuries to be minor, moderate, and severe depending on the involvement of the bony and soft tissue structures (Pintar, 1986; Pintar et al., 1995b). The failure mechanism of the cervical spine was dependent on the initial spinal curvature and the point of application of the external load, i.e., anterior or posterior to the stiffest axis. Extension failures occurred with slight initial lordosis and flexion injuries occurred with slight kyphosis of the cervical spinal column. Compression injuries occurred consistently in the midcervical spine resulting in vertebral body damage with burst, wedge, and vertical fracture mechanisms. Flexion injuries were more ligamentous with the involvement of posterior structures. In contrast, cervical spines failing under an extension mechanism all had anterior ligament involvement. Generally, compression failure mechanisms had higher failure forces (mean 3.3 kN) and stiffness (mean 585 N/ mm) than extension or flexion modalities. Neck displacement at failure was generally consistent with no particular patterns with regard to mechanism of injury, severity of injury, or age (overall mean 18 mm ± 3). Based on these comprehensive analyses, Pintar et al. derived the human neck dynamic force deformation corridors which were of the bilinear type (Fig. 6.8). Specimen alignment on or close to the stiffest axis within 0.5 cm produced axial compression injuries of the midcervical column. In contrast, specimens aligned at greater than 1.5 cm anterior to the stiffest axis resulted in flexion injuries to the lower column. Consequently, Pintar et al. concluded that there is a window of alignment to produce midcolumn compression injuries and outside the window distinctly different injuries could occur. Furthermore, they concluded that midcolumn bony compression injuries occur only when the prealignment was within 1 cm of the stiffest axis. The authors of this chapter further analyzed these data to obtain the age-dependent tolerance curve for human cervical spine compression injury.

There have been a number of studies that have attempted to reproduce the common cervical spine injuries that are the most catastrophic. Few, however, have examined the acute effects to the spinal cord during impact loading. To understand what happens to the spinal cord during traumatic impact loading to the head-neck complex, a transducer was developed to measure the transient spinal cord changes during loading. We have developed and validated an instrumented artificial spinal cord for use in the human cadaver cervical column to understand the response of the spinal cord due to catastrophic cervical spine injuries such as burst and compression fractures (Pintar et al., 1996b). It was demonstrated that extremely high pressure recordings were found for areas in which burst fracture occurred with canal encroachment by bony fragments. These transient spinal cord pressures often exceeded 200 N/cm^2 (Fig. 6.9). The magnitude of the spinal cord pressure changes correlated with the severity of injury to the vertebral elements. Tests that produced fractures to the mid- to lower-column cervical levels were often above 50 N/cm^2. Ligamentous injuries under flexion and extension loading vectors produced relatively low spinal cord pressures below 30 N/cm^2. The instrumented artificial spinal cord is a new tool to understand the nature of spinal cord injury related to biomechanical parameters.

A series of axial compressive loading tests was conducted on a total of 30 human cadaver head-neck complexes ranging in age from 29 to 95 years, with 12 female and 18 male specimens. These tests were

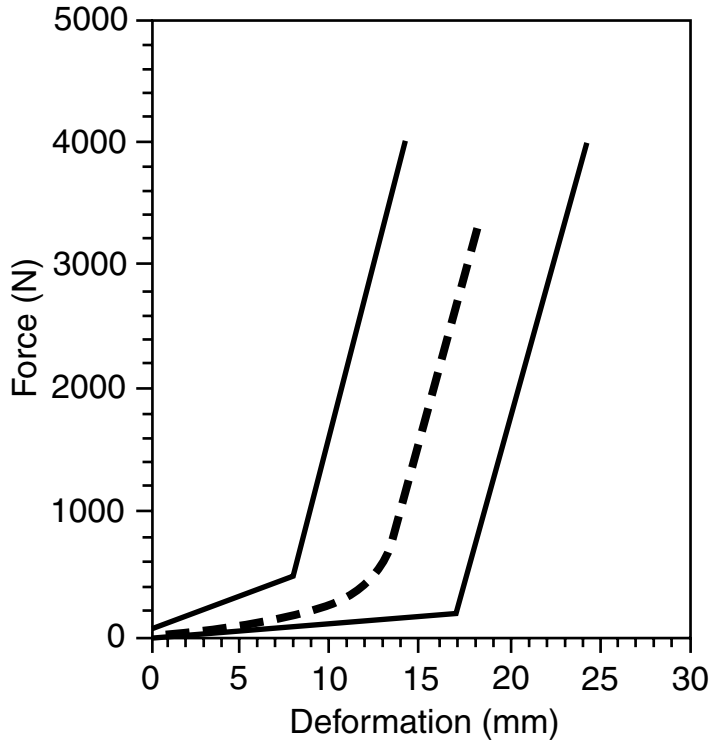

FIGURE 6.8 Dynamic force deformation corridors of the human neck. The dashed curve indicates the mean response.

evaluated for biomechanical tolerance of the human neck complex for different variables. Both force and deformation parameters were examined. When examining the deformation to failure parameter, it was found that for variations in gender, age, and loading rate, this parameter was consistent. The mean deformation to failure across all of these factors was 19 mm ± 4 mm. This indicates that the deformation to failure parameter was a good indicator of tolerance despite other biologic and anthropomorphic factors. For the axial load to failure parameter, the effects of age, gender, and loading rate were all significant factors. Using the least-square estimation process, each independent variable and all possible combinations were tested for their effect on the force at failure parameter. A linear regression equation including the interactive affects of age, gender, and loading rate proved to generate the best model for these factors. The correlation coefficient was 0.87. This statistical model indicated an interactive effect between age and loading rate such that loading rate had a greater effect at lower age groups than for higher age groups. At approximately 82 years of age, the model demonstrated convergence such that there was no effect of loading rate. The male population consistently displayed about 600 N greater failure force than the female population for all age groups and at every loading rate. A second statistical model was developed to analyze the probability of failure for different factors. A Cox proportional hazards survival analysis was done for the force to failure parameter. The Chi-square statistic for each parameter except age indicated statistically significant ($p < 0.05$) discrepancies between variables. Again, age was seen to be significantly linked to loading rate (Fig. 6.10). The effect of age was demonstrated as lower force values for higher ages at the same failure probability; 50% probability of failure for a 50-year-old male at 2.2 m/s loading rate was 3.1 kN, whereas for a 30-year-old male, the same parameter was 3.7 kN. Thus, the effects of age, gender, and loading rate must be considered when evaluating a force to failure parameter for dynamic human injury tolerance of the cervical spine.

Neck injury tolerance under other modes has been reported. For example, under flexion and extension, limits of 190 and 57 Nm were suggested by Mertz and Patrick (Mertz, 1967; Mertz and Patrick, 1967;

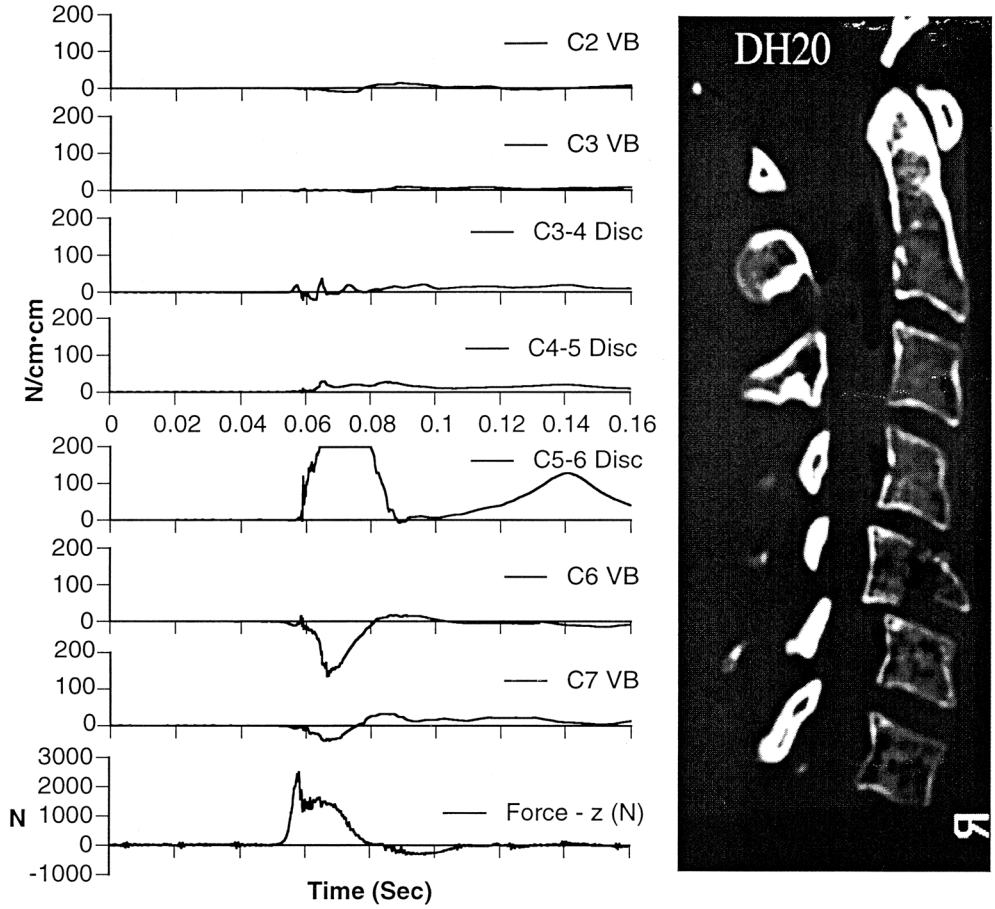

FIGURE 6.9 Pressure trace recordings from the instrumented artificial spinal cord at various spinal locations. The bottom trace is the vertical force from the distal six-axis load cell. On the right is a posttest sagittal CT.

Mertz and Patrick, 1971). Axial torque of 17.2 Nm (±5.1) produced upper cervical injury in cadaver cervical spinal columns; a torsional tolerance at 28 Nm was suggested (McElhaney and Myers, 1993). It was also suggested that 114¡ of axial rotation from the neutral position is required to produce upper cervical injury in whole cervical spine segments to mitigate the role of small axial rotations as a mediator of lower cervical injuries. Nightingale et al. (1996) reported biomechanical parameters of the cervical spine secondary to inverted head-cervical spine (plotted at T1 and carrying a fixed torso mass) drop without removing the natural lordosis, a condition that was deemed necessary to produce mid-lower cervical spine injuries typically seen in survivors of cervical spine injuries in motor vehicle accidents by Pintar et al. (1995b). Injuries occurred 2 to 19 msec following impact prior to significant head motion. Average compressive load to failure was 1.7 kN. Decoupling was observed between head and T1. In addition, dynamic buckling was observed including first and transient higher order modes which changed the structure from a primarily compressive mode of deformation to other bending modalities (Nightingale et al., 1996).

Another area of neck injury receiving more attention because of the advent and usage of air bags is the tension-extension mechanism. Pintar et al. and Yoganandan et al. described the biomechanics of the human head/neck under axial tension (Pintar et al., 1986; Yoganandan et al., 1996g). Using a part-to-whole approach (Fig. 6.11), the biomechanical response of the isolated spinal cord, intervertebral disc, functional spinal unit, base of skull to T3, head to T3, and intact human cadaver models (Fig. 6.12) under varying loading rates was determined. The force, distraction, stiffness, and energies were reported.

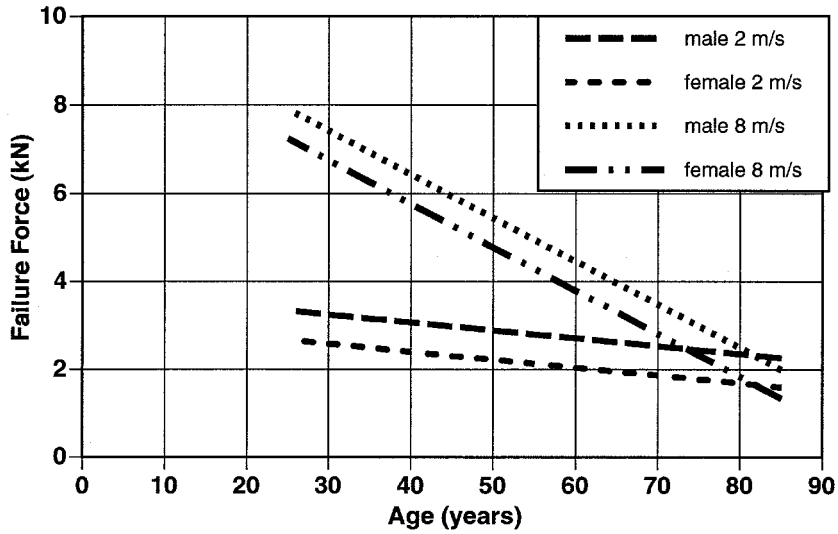

FIGURE 6.10 Biomechanical tolerance of human cervical spine as a function of age under compressive loading for both genders at 2 and 8 m/s rate of loading.

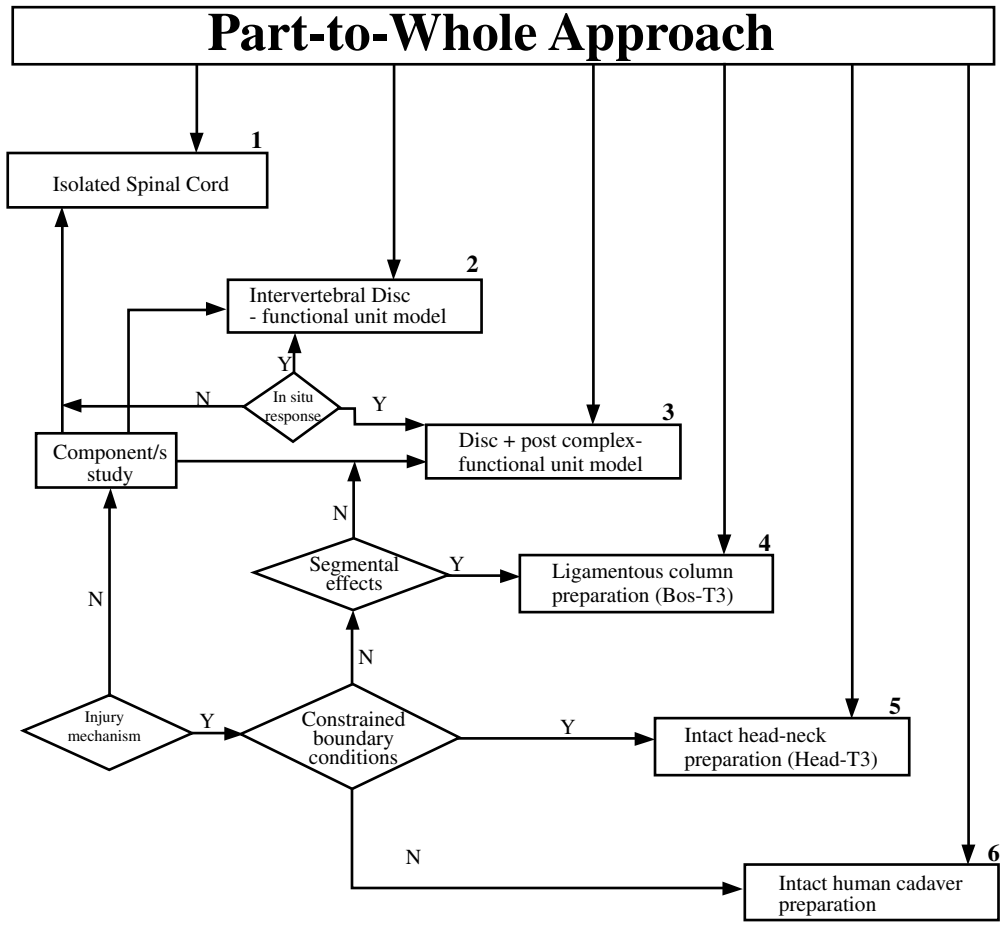

FIGURE 6.11 Part-to-whole approach to delineate the spinal biomechanical behavior due to tensile loading.

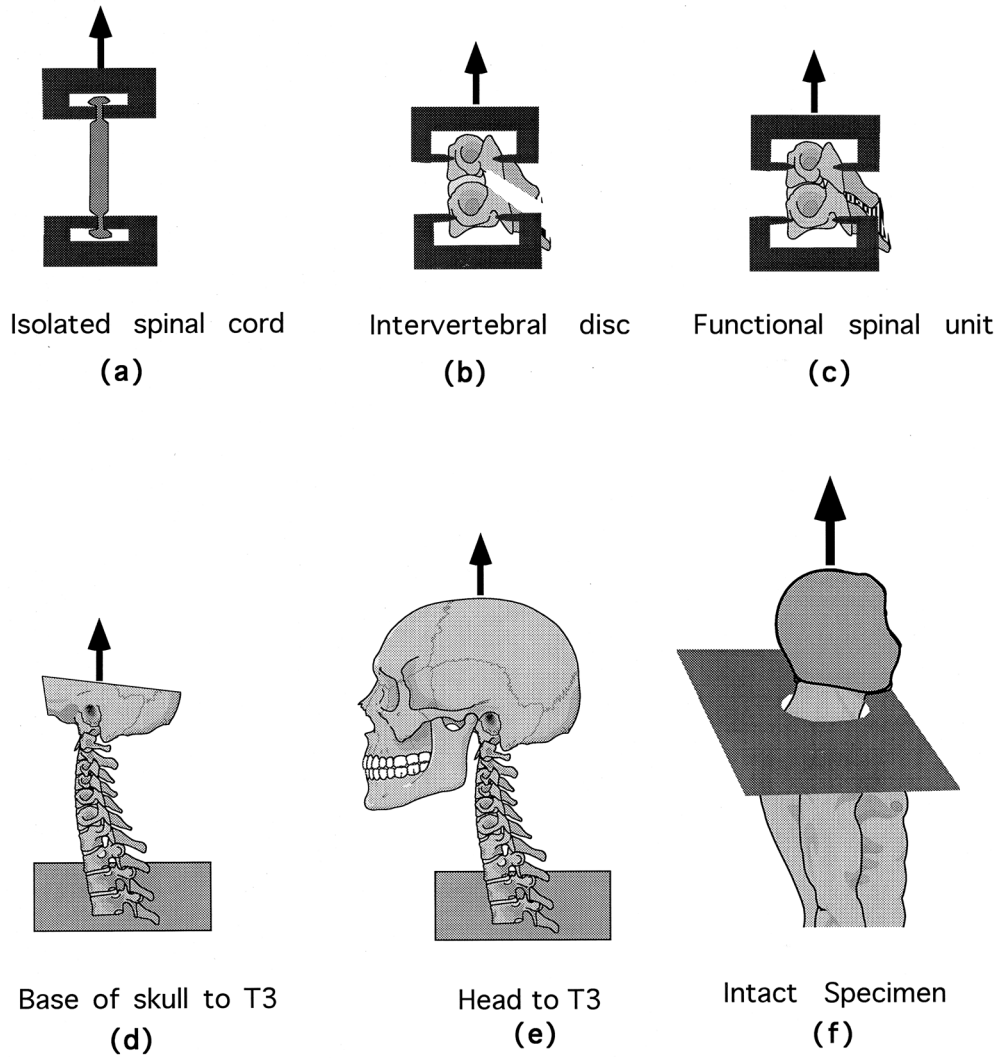

FIGURE 6.12 Schematic representations of the various specimens used to determine the biomechanics of the human head/neck structures under tensile loading.

Maximum forces for the spinal cord preparations were the lowest (278 N ± 90). The forces increased for the intervertebral disc (569 N ± 54), skull to T3 (1555 N ± 459), and intact cadaver (3373 N ± 464) preparations indicating the load-carrying capabilities when additional components are included to the experimental model (Fig. 6.13). In other studies, Shea et al. reported the tensile load to failure of 500 N ± 150 in quasi-static human cadaver spine experiments with an initial pre-extension of 30¡ and a mean extension moment of 3.9 ± 3.1 Nm (Shea et al., 1991).

6.6 Thorax

Evaluation of the impact biodynamic response of the human thorax is another important area of research because of its significant impact on injury assessment and prevention. The human thorax is a composite entity comprising a relatively rigid rib cage, which houses the internal vital organs such as the heart, liver, and lungs. The biodynamic response of this structure is complex, regionally dependent, and, furthermore, being a biological tissue, demonstrates rate dependency (Lau and Viano, 1986; Yoganandan

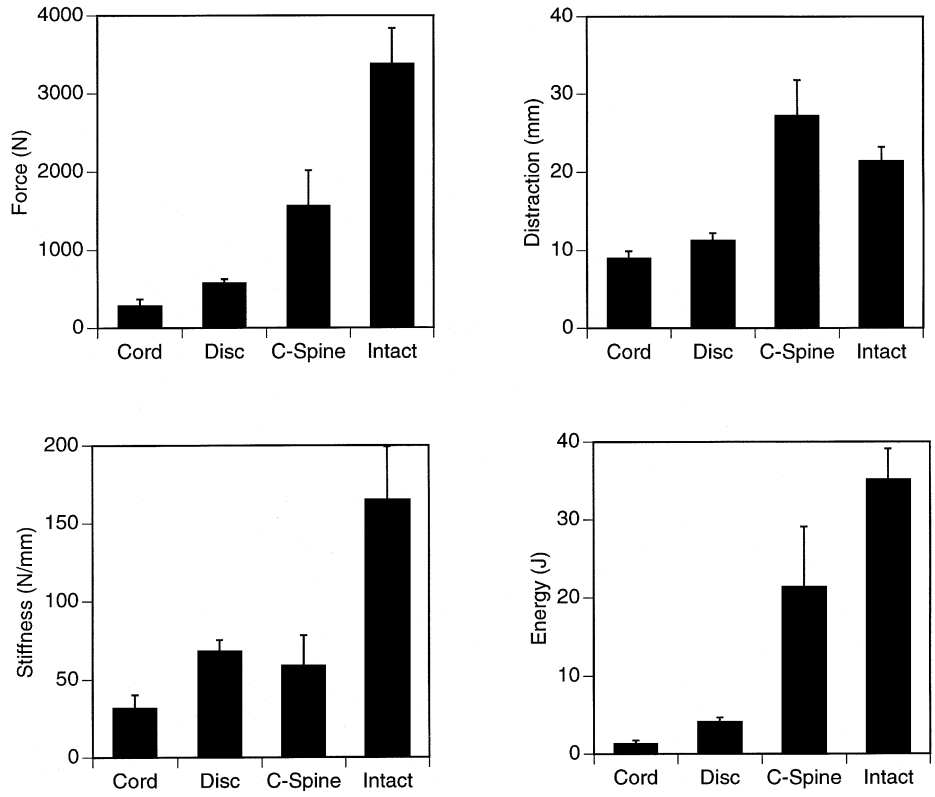

FIGURE 6.13 Bar chart representation of the biomechanical data of the human head/neck structures under tensile loading.

et al., 1994c; Yoganandan et al., 1991e). Depending upon the physical environment and the boundary conditions at the time of impact, thoracic injuries of varying severity routinely occur in motor vehicle crashes. Biomechanical studies have included experimental animals, human volunteers, and human and animal cadavers, and a review of these was given (Melvin, 1985). Earlier biomechanical research to evaluate the response of the thorax in frontal impact was based on few experimental data recordings. For example, dynamic forces from the impactor (inertially compensated) and deflections were measured, providing the force deformation characteristics of the human cadaver thorax placed in a seated configuration with midsternum impact (Kroell et al., 1971; 1974). Impact force and peak spinal accelerations were determined to be weakly correlated with injury compared to maximum chest compressions occurring along the line of anteroposterior impact direction.

Because of the advances in instrumentation technology and recent developments, experiments were designed to determine the thoracic dynamic responses on a regional and temporal basis by Yoganandan et al. These studies used a new electronic device developed by Eppinger, called the External Peripheral Instrument for Deformation Measurement, more commonly known as the chest band (Eppinger, 1989). This noninvasive device has the ability to track the deformations at various locations and levels of the human thorax during impact. From the curvature time responses, the thoracic cross-sectional contours as a function of time can be derived. Placing the chest band at different locations produces temporal deformation contours of the human thorax delineating the regional characteristics of the human body. This device obviates the measurement of biomechanical variables at one or two predetermined anatomical locations (accelerations at T1), which may not completely characterize the structural response. Furthermore, the regional and temporal definition of the thoracic contour data can be processed to determine the secondary variables, such as the velocity of compression at different locations, thus providing a

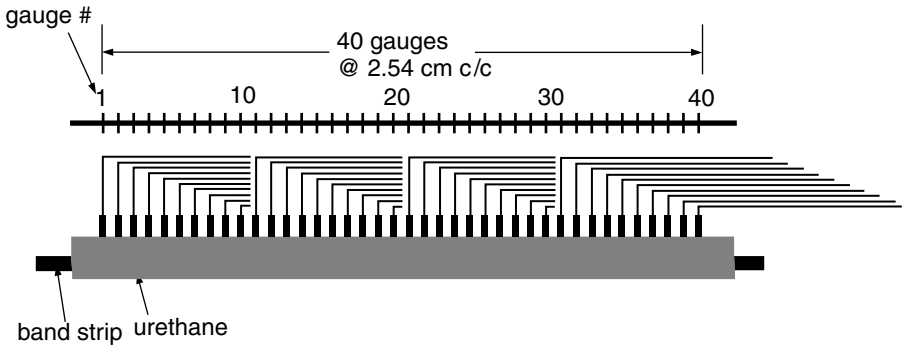

FIGURE 6.14 Schematic representation of the chest band with 40 channels.

comprehensive evaluation of the biodynamic response. A brief description of the chest band is given below.

The chest band is a high-carbon steel alloy, 140 cm × 2.5 cm × 0.025 cm, with strain gauges bonded at discrete locations. The steel strip with all the gauges is fixated with Flexane 80 liquid, which is a two-component urethane rubber for the fastening of durable, resilient, medium to hard devices. Each set of gauges in a four-arm Wheatstone bridge configuration constitutes one data channel (routinely referred to as a gauge). The bridge is configured such that it is sensitive to the longitudinal bending axis across the thickness. Each channel or gauge provides a curvature reading at that discrete location of the chest band. The locations of the gauges are nonuniformly spaced over the length of the chest band (Fig. 6.14).

A total of 30 unembalmed human cadavers (ages from 29 to 81 years) were instrumented with two chest bands (Yoganandan et al., 1996d; Yoganandan et al., 1995a; Yoganandan et al., 1994c; Yoganandan et al., 1991e). The first, the upper level chest band, covered the midsternum region approximately at the anterior level of the fourth rib. The second, the lower chest band, covered the xyphoid process approximately at the sixth rib anteriorly. The restraint system included three-point belts with and without air bag, air bag and lap belt combination, air bag and knee bolster combination, and air bag three-point belt restraint systems. Frontal impact velocities ranged from 24 to 50 kph. Belt loads, head accelerations, sled accelerations, and accelerations at the first thoracic vertebra were obtained. High-speed photography documented the kinematics. Pathological evaluations were done using palpation, radiography, and detailed autopsy. In the initial studies, using the three-point belt (alone) restraint system at velocities approximately 14 m/sec, the maximum accelerations ranged from 43 to 111 G. Lap belt forces ranged from 3.5 to 5.1 kN and shoulder belt forces ranged from 6.1 to 8.8 kN. The maximum lap belt force always preceded the peak tension on the shoulder belt. The chest deformation contours were found to be regionally dependent and temporally variant. The maximum deflections at the upper chest level ranged from 2.7 to 9.1 cm (mean 6.24). At the lower chest level, the maximum deflections ranged from 2.5 to 12.3 cm (mean 7.68). The overall mean maximum deflection computed by using the individual peak deflections at the upper and lower thoracic levels was 7.03 cm. The maximum deflections at the upper thoracic level were, in general, concentrated around the anterior portion of the upper lobe of the right lung and at the lower level over the region covering the liver. A typical thoracic deformation contour pattern at the upper and lower chest levels for a specimen tested at a velocity of 50 kph (Fig. 6.15).

Using these thoracic deformation contour histories obtained from the chest band, Yoganandan et al. computed the normalized chest deformation, the rate of deformation, and the viscous criterion at the upper and lower thoracic levels using data from four specimens tested at 50 kph velocities (Yoganandan et al., 1995a). The schematic diagram illustrating the computation of the above-described secondary variables and injury predictors is shown in Fig. 6.16. A typical output illustrating the variations of compression (C), velocity (V), and viscous (VC) criteria with respect to time at the upper and lower levels of the thorax is shown in Figs. 6.17 and 6.18, respectively. While the time of occurrence of the peak varied among the variables, their location with respect to the thorax remained approximately the same.

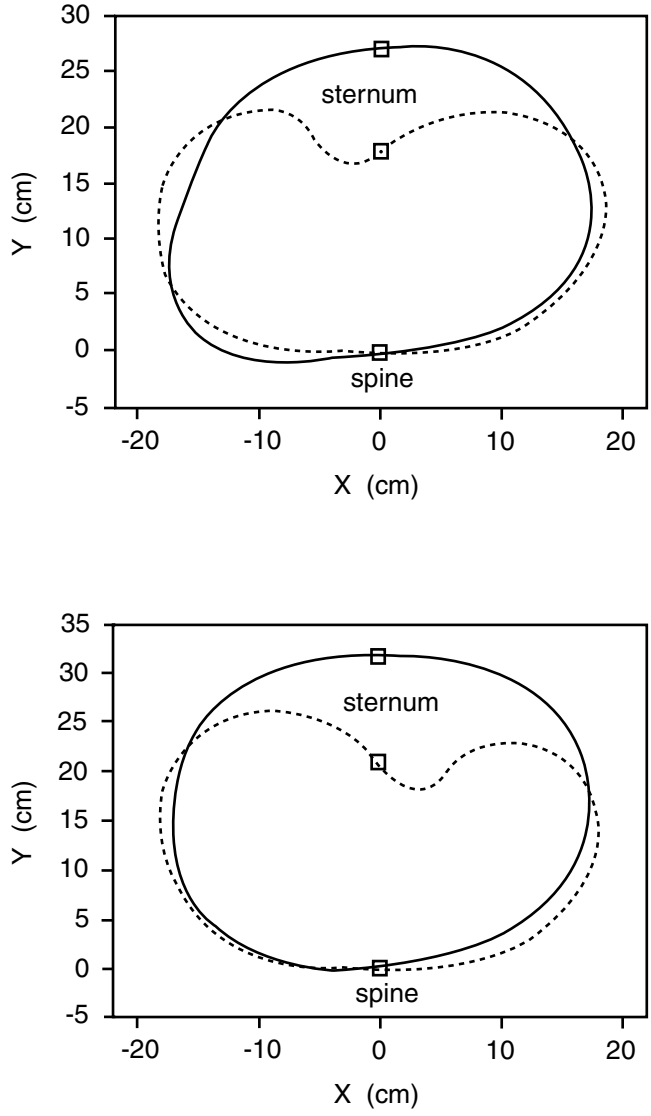

FIGURE 6.15 The deformation contours shown for the upper (top) and lower (bottom) thoracic levels were computed at the time of maximum chest deflection for a specimen restrained by a three-point belt undergoing a simulated frontal impact. Solid lines indicate the pretest shape of the chest (contour), and dotted lines refer to the contour at the time of maximum chest compression.

However, for a particular specimen, compression data at the upper thoracic level often varied considerably from the lower thoracic level, demonstrating regional differences in the biodynamic response of the chest. The peak compressive velocity for two specimens was above 3 m/s. In two specimens, C_{max} as well as $(VC)_{max}$ were above the suggested threshold at the upper and lower thoracic levels. However, three out of four specimens had injuries with a severity of AIS > 3. In the two specimens wherein C_{max} and $(VC)_{max}$ were at or below the threshold, serious thoracic injuries (AIS = 4) occurred. Peak V_{max} always preceded the occurrence of peak $(VC)_{max}$, followed temporarily by C_{max}. The velocity of chest compression was included in the viscous response analyses to predict injury. The following criterion corresponds to a 25% probability of serious (Abbreviated Injury Scale rating, AIS > 3) injury (Viano and Lau, 1988); (a) when the velocity of compression is below a threshold of 3.0 m/s, the compression criterion (C_{max} of 0.35), i.e.,

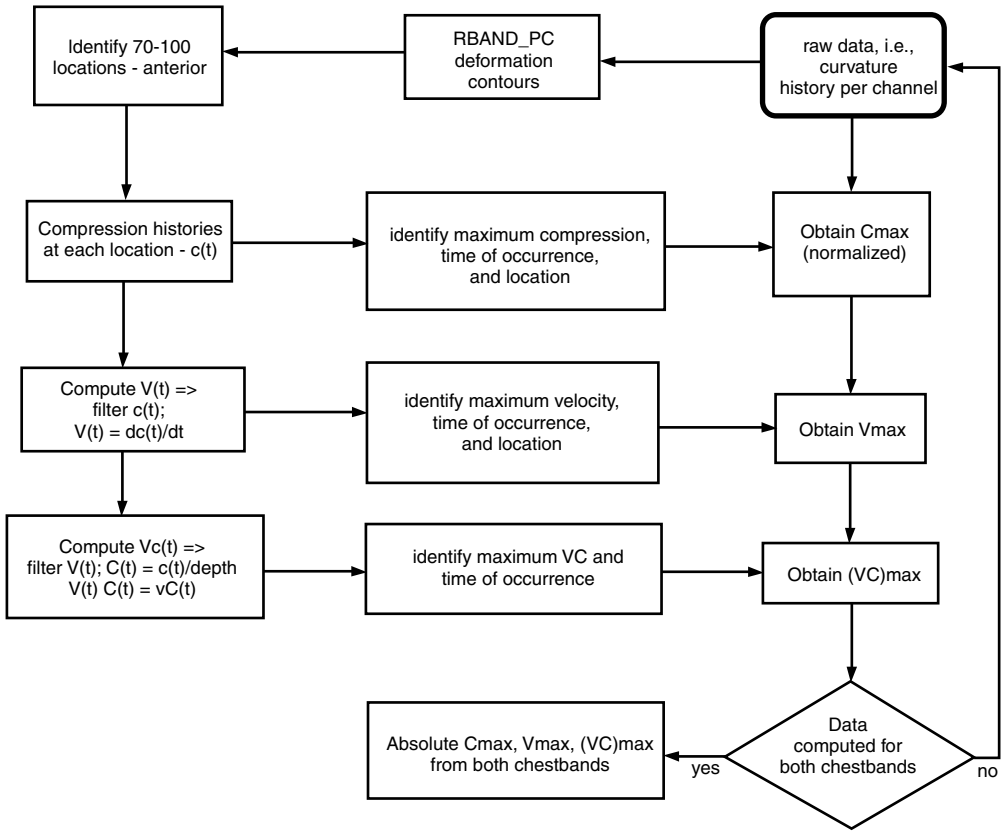

FIGURE 6.16 Computation of secondary variables under injury predictors such as the compression and viscous response from the chest band for specimens subjected to frontal impact.

anteroposterior chest deflection normalized with respect to the initial chest depth, most reliably describes the thoracic response, and (b) when the velocity of compression is above 3 m/s, the viscous criterion, i.e., a $(VC)_{max}$ of 1.0 m/s, governs the injury mechanism (Viano and Lau, 1988). A previous study reported that the viscous criterion applies in the following situations: an unrestrained occupant in a frontal impact; a restrained or an unrestrained occupant in a side impact; and impact by inflatable restraint deployment against an occupant directly against it (Lau and Viano, 1986). This leads to a suggestion, based on the criteria delineated in the foregoing, that the viscous response may not be appropriate under frontal collisions with belt-restrained occupants. Since data on the temporal compression response of the human thorax under three-point, belt-restrained frontal collisions were not available, this assumption may have been made in the previous study (Lau and Viano, 1986). The chest band instrument offers a method to quantify the biomechanical data required to test the validity of this assumption. Similar conclusions regarding the applicability of the viscous criteria in other frontal impact situations were advanced recently (Zhou et al., 1996).

In another investigation, Yoganandan et al. determined the biodynamics of the human thorax secondary to frontal impact under air bag-knee bolster restraint systems with or without three-point belts or lap belts using unembalmed human cadavers at velocities of 9 and 13 m/s (Yoganandan et al., 1994c). Fourteen subjects were used, with age ranging from 29 to 81 years, height 150 to 182 cm, and weight 41 to 85 kg. The kinematics of the air bag-knee bolster alone, the air bag-lap belt, and air bag three-point belt-restraint systems demonstrated significant differences. In the air bag-knee bolster restraint system (Fig. 6.19), the specimen kinematics indicated a forward motion and the contact of the knee with the knee bolster approximately at the time of full deployment of the air bag. With the knees further loading

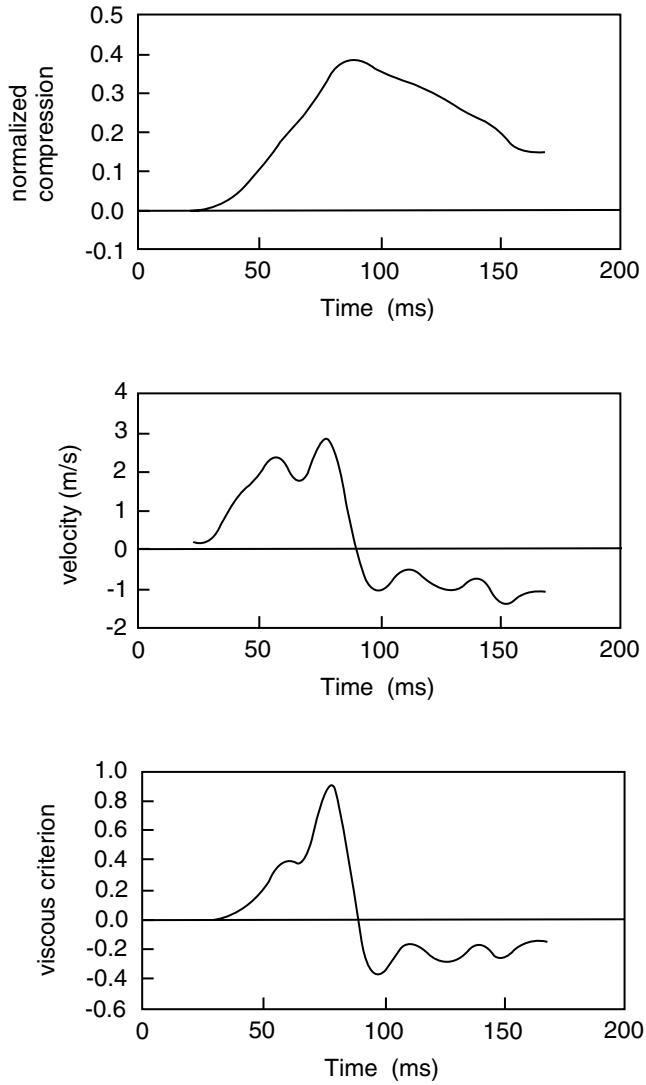

FIGURE 6.17 Variation of normalized chest compression (top), velocity (middle), and viscous response (bottom), with respect to time for a specimen subjected to simulated frontal impact. These data were derived from the upper chest band output.

the knee bolster, the lower torso initially contacted the air bag in the region of the lower rim of the steering wheel. The upper torso loaded the air bag and the lower regions of the thorax continued to load the air bag and the lower wheel rim up to approximately 100 ms for high-velocity tests, and 70 ms for the low-velocity sled experiments. The rebounding of the specimen initiated following these kinematics with continuing deflation of the air bag and unloading of the steering wheel and the column. Residual deformations occurred to the steering wheel in these tests.

In the air bag-lap belt tests (Fig. 6.19), the pelvis was restrained by the lap belt during the period of full deployment of the air bag. The upper torso pivoted around the restraint and contacted the air bag following full deployment. Loading of the steering wheel and column occurred, producing permanent deformations. The upper thoracic region contacted the air bag due to the pivoting action by the lap belt restraint. With the air bag three-point, belt-restraint system (Fig. 6.19), the belt loaded the specimen prior to air bag contact. The maximum shoulder belt force occurred at approximately 60 to 70 ms and

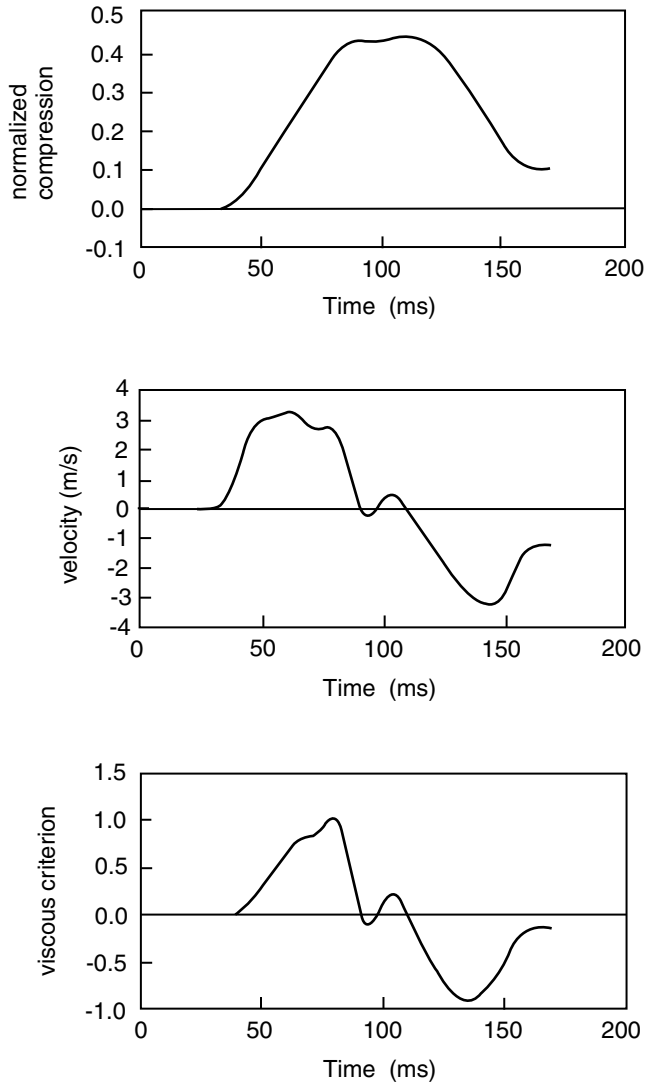

FIGURE 6.18 Variation of normalized chest compression (top), velocity (middle), and viscous response (bottom), with respect to time for a specimen subjected to simulated frontal impact. These data were derived from the lower chest band output.

during this period, the specimen was in contact with the air bag for approximately 20 ms. Little or no steering wheel and column deformations occurred in these experiments. The specimen began to rebound after approximately 100 ms for the high-velocity and 80 ms for the low-velocity tests without permanently deforming the wheel and column. For all three restraint combinations, increasing velocity resulted in increasing upper and lower thoracic deflections ($p < .05$). The type of restraint system had a significant effect on lower thoracic deflections ($p < .05$). In addition, deflections at the lower thoracic level were less with belt restraint combinations, i.e., lap or three-point belt, compared to the air bag-knee bolster system. At the upper thoracic level, however, peak chest compressions were greater with the air bag three-point belt combination. While no differences were observable in the time of occurrence of the upper and lower peak chest deflections between the knee bolster and lap belt systems, the introduction of the three-point belt restraint system produced significantly different ($p < 0.01$) early peaks (Fig. 6.20).

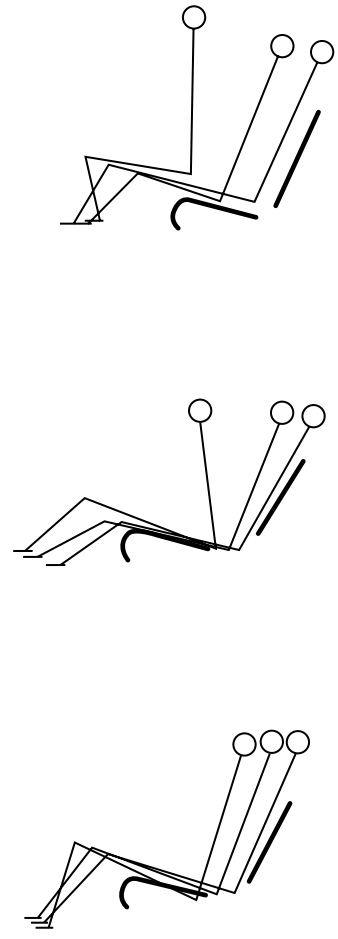

FIGURE 6.19 Stick figure representation of the kinematics of the human body secondary to simulated frontal impact with different restraint combinations. The top figure illustrates the kinematics in the air bag–knee bolster, the middle figure illustrates the kinematics in the air bag–lap belt, and the bottom figure illustrates the kinematics in the air bag three-point belt tests. The three positions in each of the three stick figure illustrations from right to left indicate zero time, time of air bag inflation, and time of maximum body excursion.

The thoracic deformation contours of the upper and lower levels were similar in the air bag–knee bolster (Fig. 6.21) and air bag-lap belt (Fig. 6.22) tests indicating a nearly uniform compression of the torso in the anterior region with air bag contact. Figure 6.23 illustrates a schematic of the injury pattern in these tests. In contrast, the pattern of thoracic deformation contours for the air bag three-point, belt-restraint indicated considerable local compressions of the thorax due to asymmetrical loading by the shoulder belt (Fig. 6.24). The shape of the deformation contours was similar to that of the three-point belt (no air bag restraint) cases (described earlier). From these studies it can be concluded that thoracic loading, the resultant deformation patterns, and the ensuing pathology in three-point belt restraint of human cadavers with and without the activation of the air bag primarily stems from the asymmetrical loading of the shoulder belt with lesser contribution from the air bag or column loading. This hypothesis was further reinforced by the fact that the peak upper and lower chest deflections that occurred earlier ($p < 0.01$) in the air bag three-point belt case compared to the other two restraint combinations.

Although the chest bands revealed uniform compressions at a given thoracic level in both air bag–knee bolster and air bag–lap belt series, the differences in the rib fractures may be explained by the direct impact of the torso onto the steering wheel in the air bag-knee bolster series. In contrast, in the air bag three-point belt series, initial shoulder belt loading may account for the multiple rib fractures. The pivoting action in the air bag–lap belt tests and the initial restraining action in the air bag three-point belt tests manifest as greater deflections at the upper chest level than the lower counterpart. However, in the air bag-knee bolster series, the lower chest deflections were greater compared to the upper chest deflections presumably because of direct contact of the lower torso with the steering wheel and lack of pivoting due to the absence of a belt restraint. The orientation of the specimen and the wheel-bag attitude

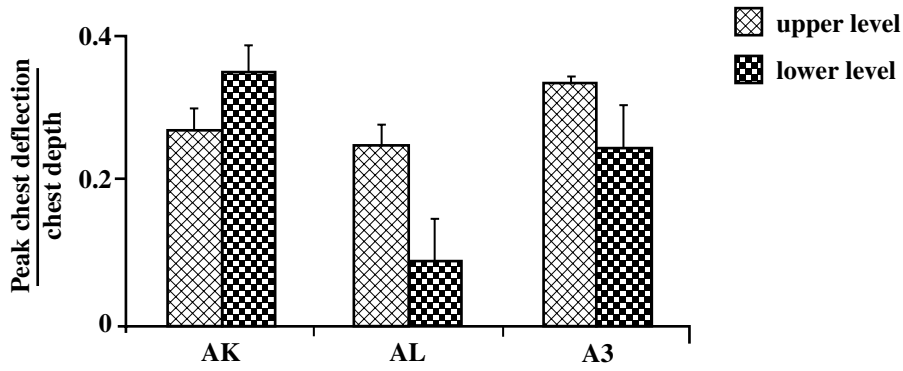

FIGURE 6.20 Bar chart representation of the mean normalized chest deflections at the upper and lower thoracic levels as a function of the restraint system. AK: air bag–knee bolster; AL: air bag–lap belt; A3: air bag three-point belt.

results in the primary contact at the lower torso level. The specimens in the three-point belt (alone), air bag three-point belt, air bag-knee bolster, and air bag-lap belt series of tests demonstrated multiple rib fractures at autopsy. However, plain radiography did not reveal all injuries because of the complex anatomy of the rib cage and the difficulty in identifying rib fractures using radiography (Yoganandan et al., 1996d). These findings indicate that there may be an overrating of the thoracic trauma based on injuries identified at autopsy in contrast to routine clinical radiography. The mechanisms of injury (Fig. 6.25) were asymmetrical compression and/or bending related to the air bag three-point belt system and uniform compression directed along the anteroposterior axis of the human torso for the air bag-knee bolster combination (Yoganandan et al., 1996d).

Earlier experimental studies found that the risk of thoracic trauma due to frontal impact at the midsternal level was associated with various formulations of the maximum normalized chest deflection, age, and the maximum time rate of change of deflection (Backaitis and Mertz, 1994). More recent investigations have focused on the extrapolation of this information on blunt impact subjects at the midsternal level to an environment where the subject is restrained by an air bag or a belt system. The above-cited studies using human cadavers and other research using human volunteers, manikins, and human cadavers as experimental models have demonstrated that the human body responds differently to air bag restraints and belt restraint systems (Backaitis, 1995; Backaitis and St. Laurent, 1986; Cesari and Boquet, 1990, 1994; Katz et al., 1987). Using these data as a basis, with recent experimental results of Yoganandan et al. (discussed above) and tests conducted by the University of Virginia and the University of Heidelberg as experimental data points, Morgan et al. statistically analyzed the data from 66 specimens from the three laboratories (Morgan et al., 1994). Risk functions were developed using the probit, log-logistic, log-normal, and logistic methods. Because of the similarity in the output, a two-parameter Weibull distribution was selected to present the data. Parameters such as chest deflection, chest velocity, viscous criteria, and anthropometric data were used in the discriminant analysis. The chest deflection or the chest acceleration alone was a poor predictor of thoracic trauma. However, a linear combination of the maximum normalized chest deflection (X), the 3-ms clip value of the spinal resultant acceleration (A_c), and the age of the human subject at the time of death (years) expressed by the following equation separated the trauma into AIS < 3 and AIS $\prod 3$ (AIS, 1990). The linear combination determined from the discriminate analysis is given below:

$$9.9\ X + 0.04\ A_c + 0.03\ (\text{age})$$

The probability of injury vs. this combination for all types of restraints shown in Fig. 6.26 indicated three regions: an initial region of no trauma corresponding to lower values of the linear combination; the transition region, i.e., where both injury and noninjury occurs; and the final region corresponding to trauma only. The probability of injury vs. the above linear combinations when separated for belt

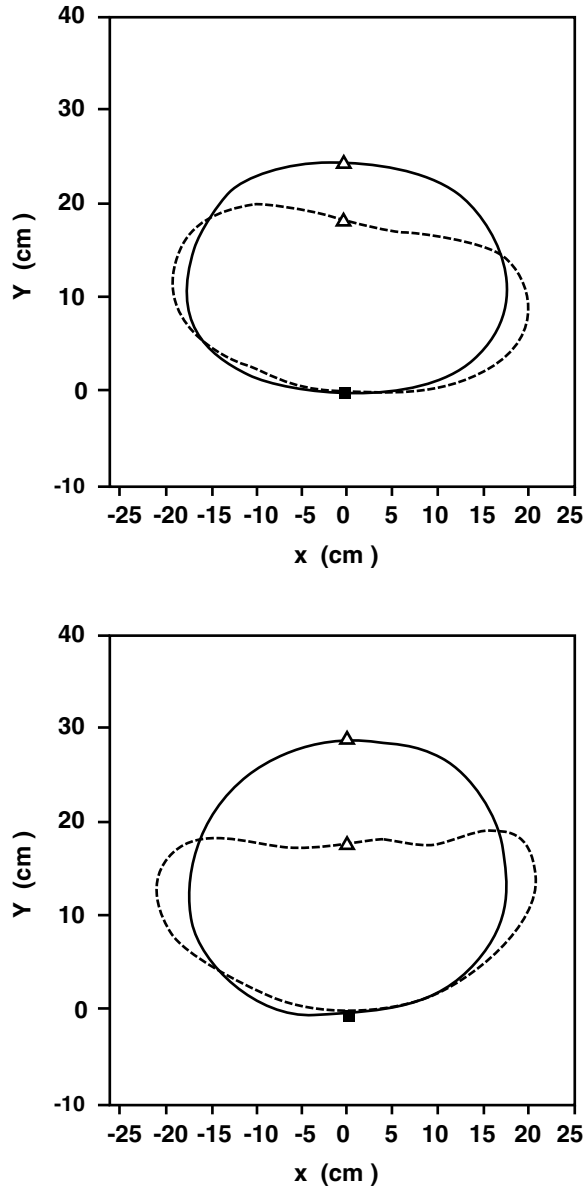

FIGURE 6.21 Thoracic deformation contours at the upper (top) and the lower (bottom) chest levels as viewed from head to toe. Solid lines represent the initial unloaded state and the dotted lines represent the deformed state. These data were obtained from a specimen restrained by air bag–knee bolster combination. Sternum is shown by a triangle, and spine is shown by a solid square.

restraint and air bag restraint data (Fig. 6.27), suggested a higher probability of injury with belt restraint than with air bag restraint using chest deflection, 3 msec clip value of the spinal resultant acceleration and age. Morgan et al., using an analytical sorter, presented a methodology for the restraint designer to evaluate the safety performance of an air bag only, a belt only, or a combination of belt-bag restraint systems. Newer improvements to the manikin thorax design have included (instead of the single potentiometer at the center of the Hybrid III manikin) multiple deformation sensing devices for better injury prediction under the current restraint systems (Haffner, 1987; Schneider et al., 1992).

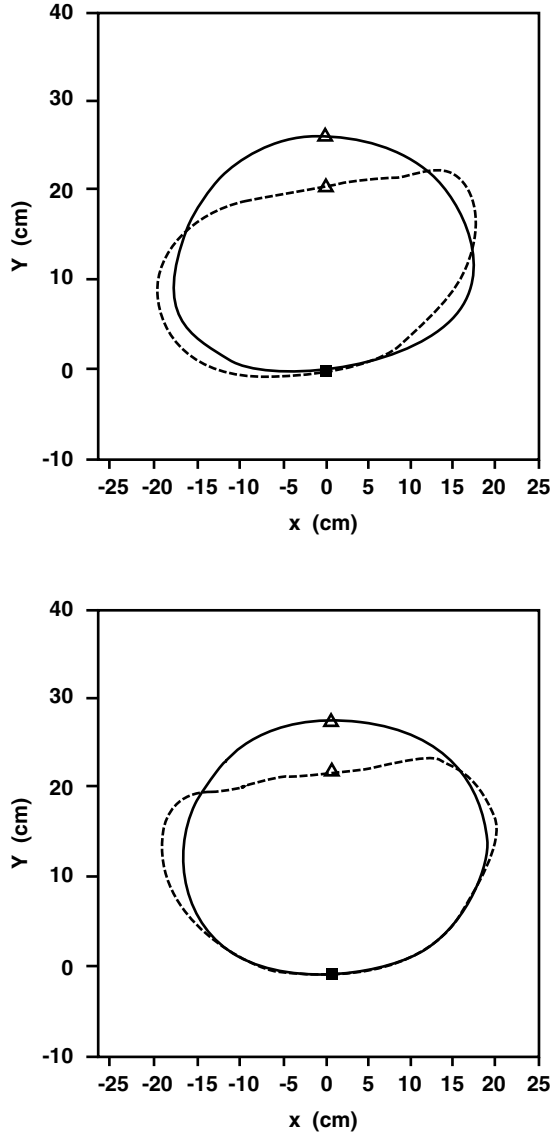

FIGURE 6.22 Thoracic deformation contours at the upper (top) and the lower (bottom) chest levels as viewed from head to toe. Solid lines represent the initial unloaded state and the dotted lines represent the deformed state. These data were obtained for a specimen restrained by air bag–lap belt combination. Sternum is shown by a triangle, and spine is shown by a solid square.

6.7 Abdomen

Epidemiological studies conducted in the 1990s indicated the occurrence of injuries to the lower thorax-abdomen region of the human body secondary to frontal impact (Augenstein et al., 1995; Crandall et al., 1994a,b). For example, liver injuries were reported in these investigations. The injuries were attributed to restraint systems such as automatic two-point belts. The widely used anthropomorphic Hybrid III manikin does not possess proven biofidelity in this region (Backaitis, 1995; Backaitis and Mertz, 1994; Yoganandan et al., 1996f). Since limited biodynamic data were available to describe the dynamic biomechanics of this region, Yoganandan et al. conducted a series of experiments using intact human cadavers (Yoganandan et al., 1996f). The specimens were instrumented with a 40-channel chest band and were

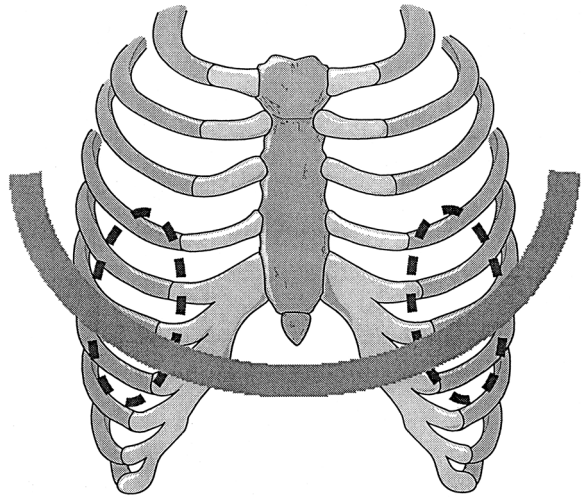

FIGURE 6.23 Schematic showing the rib cage and the contact of the lower torso with the steering wheel–air bag in a frontal impact. Dotted lines indicate the general region where rib fractures were identified on the air bag–knee bolster tests.

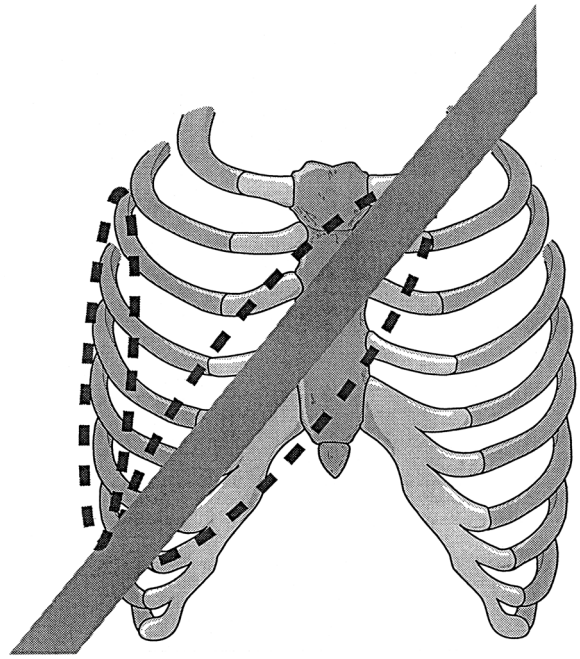

FIGURE 6.24 Diagram illustrating the position of the shoulder belt (shown in the diagonal shaded region) across the rib cage. The dotted line around the shoulder harness indicates the general area where the rib damage was observed for the air bag three-point belt tests. The other dotted region shown laterally in the rib cage demonstrates the area where additional rib damage was found.

impacted at the region of the eighth rib in the anterior region on the right side using a pendulum impactor at a velocity of 4.3 m/s. This velocity was based on occupant simulation models and analysis of high-speed data from human cadaver experiments with belt restraints (reported above), which indicated the velocity of chest compression to range from 1 to 5 m/s (Schneider, 1989; Yoganandan et al., 1995a). In addition, this velocity also facilitated a comparison with the previous blunt midsternum impact tests

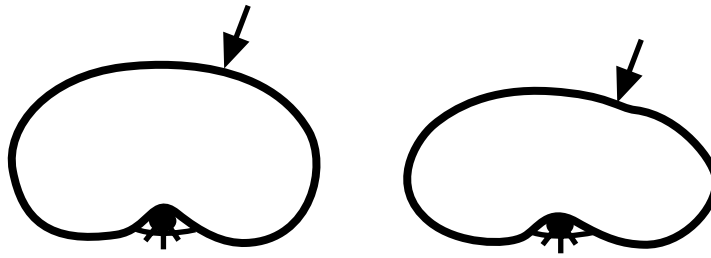

FIGURE 6.25 Mechanism of rib injury in the air bag three-point belt systems. The sketch on the left represents the initial state and on the right represents the deformed state. The focal loading applied by the shoulder belt is indicated by a solid arrow and the fracture is shown by two small discontinuities at the region of the load application and at the lateral region of the rib cage.

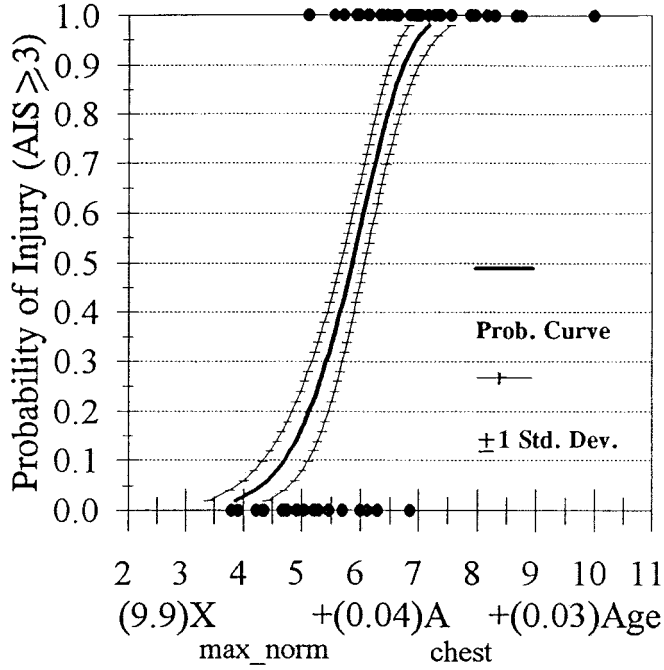

FIGURE 6.26 Probability of thoracic trauma versus linear combination for all restraint combinations.

(Kroell et al., 1971, 1974). Other instrumentation consisted of documenting the impactor load through a uniaxial load cell and a uniaxial accelerometer placed on the pendulum. These devices were used to compute the interface forces (inertially compensated load histories). The dynamic deformation at the region of impact and along the line of travel of the pendulum impactor was obtained by the deformation contours from the chest band signals. Posttest evaluations included palpation, radiography, and detailed autopsy to identify soft tissue and bony damage to the specimen. Peak deformations ranged from 34 to 110 mm with peak forces ranging from 1.9 to 2.9 kN. Normalized abdomen region compressions ranged from 0.16 to 0.39. Using these raw force deflection curves from each specimen (Fig. 6.28) and following an accepted transformation methodology, Yoganandan et al. presented scaled force-deformation curves assuming a body weight of 75 kg, i.e., the weight equivalent to that of a 50th percentile male (Eppinger, 1976; Yoganandan et al., 1997d). Details of this scaled human biodynamic response characteristics along with the average force-deformation plot is illustrated in Fig. 6.29.

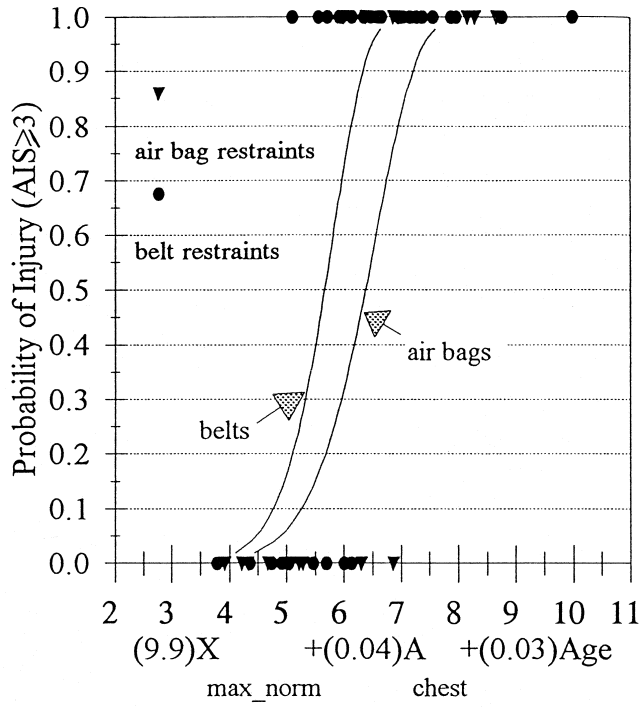

FIGURE 6.27 Probability of thoracic trauma vs. linear combination for belt and air bag restraints.

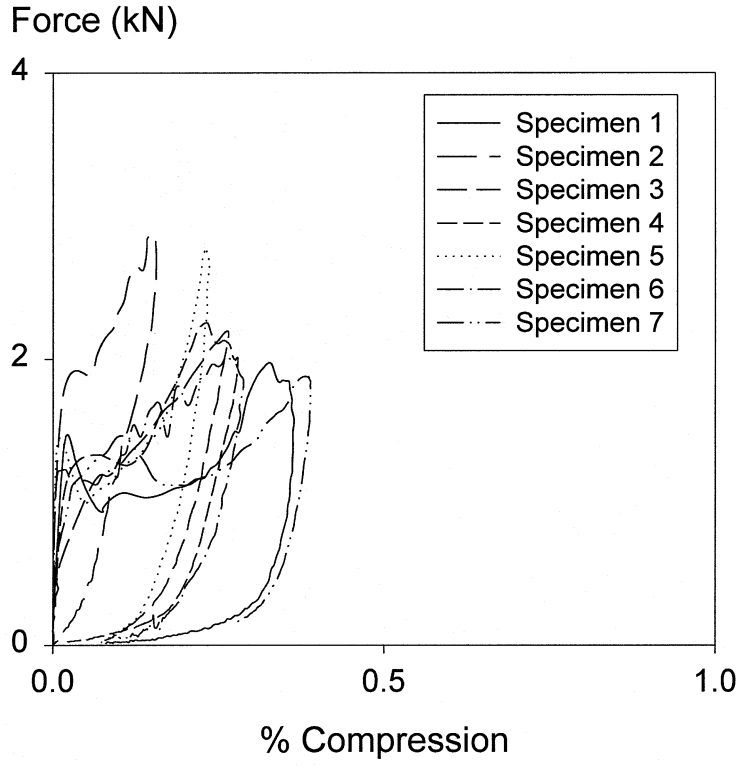

FIGURE 6.28 Force deformation characteristics (deformation expressed as a normalized compression) of the intact human thoracoabdominal complex secondary to impact loading.

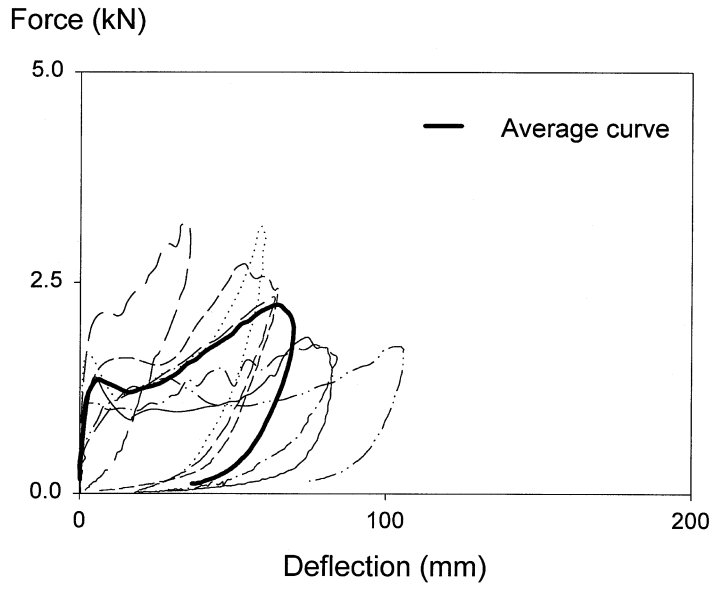

FIGURE 6.29 Scaled force deflection data for the curve shown in Fig. 6.28.

6.8 Extremities

Upper Extremities

The deploying air bag could be the cause of some upper extremity injury (Huelke et al., 1994; Kuppa et al., 1997). The severity of injury may be due to factors including arm position, velocity of impact, occupant anthropometry, and type of air bag (Kuppa et al., 1997). While attempts are underway to quantify these effects using physical arm devices, data on the human tolerance of the forearm is limited to static or quasi-static literature (Kuppa et al., 1997; Messerer, 1880; Saul et al., 1996; Yamada, 1970). Recognizing the need for defining the tolerance of the human forearm, which may offer design parameters for potential injury-mitigating devices, studies were reported by Pintar and Yoganandan in the 1996 Workshop on Human Subjects for Biomechanics Research held in Albuquerque, New Mexico. This work is summarized below.

Fresh intact human cadaver forearm specimens (elbow through fingers) were evaluated in dynamic three-point bending failure tests. Pretest X-rays and bone density measurements of the distal radius were taken prior to test. The supports were instrumented with a six-axis load cell to determine the transmitted loads. The arm was struck on its volar surface by a 2.5-cm diameter cylinder attached to the piston of an electrohydraulic test device across the entire midsection. In a total of six pairs of arms, one half of the specimens were tested at 3.3 m/s, and the other half were tested at 7.6 m/s velocities. The mean bending moment to failure for the entire data set was 124 Nm (± 42). Other data are given in Table 6.1. There were more comminuted and distal fractures in the high-velocity group. In contrast, the lower-velocity group produced more butterfly-type fractures of the ulna. This difference in fracture pattern may have implications in the definition of human tolerance. Since a higher percentage of distal fractures occur secondary to air bag deployment, results from these higher velocity studies may be more applicable.

Lower Extremities

With the introduction of passive restraint systems (such as air bags), evidence exists demonstrating an increase in injuries to the human foot-ankle complex. Lower-limb injuries are a frequent cause of permanent disability and impairment secondary to frontal impact in a motor vehicle environment

Table 6.1 Biomechanical Data

Parameter/(sample size)	3.3 m/s (n = 6)	7.6 m/s (n = 6)	Combined (n = 6)
Input force (N)	2407	2793	2600 ± 881
Elbow force (N)	1095	1159*	1127 ± 425
Wrist force (N)	1190	1520*	1356 ± 419
Force Sum (N)	2286	2679	2483 ± 812
Bend mom (Nm)	115	133	124 ± 42

*$p < 0.05$

(Burgess et al., 1995; Holub et al., 1995; States et al., 1987). In 1987, Backaitis and Roberts, from two occupant injuries in air bag-equipped vehicles, concluded that ankle trauma was due to a contact loading from the foot control of the automobile. Morgan et al. (1991) examined the 1979 through 1986 NASS files for frontal impact and found that lower extremity injuries were about 26% of the total moderate or greater injuries (AIS ≥ 2); contact with foot controls was the cause of 45% of foot-ankle injuries, and contact with the floor pan accounted for 24% of foot-ankle trauma. Studies conducted in Australia, the U.K., and Germany have also emphasized the occurrence of foot-ankle trauma secondary to vehicular frontal impact (Fildes et al., 1995; Kallina, 1995; Thomas et al., 1995). The external axial compressive impact load applied through a vehicular interior component is a predominant mechanism of injury to the foot-ankle complex. Since lower extremity injuries occur frequently, are disabling, and contribute to a large portion of the cost of injury in the U.S., vehicular modifications to create a more crashworthy environment for the lower extremities would be an effective means to reduce the incidence and severity of these injuries. With this objective in mind, Yoganandan et al. conducted studies to determine the biodynamics of the human foot-ankle complex under axial loading (Yoganandan et al., 1997a; 1996e). Using a minisled pendulum device and an unembalmed human cadaver knee-to-foot model, fundamental data such as the impact force at the plantar surface of the foot, proximal tibia forces, and dynamic deformations due to axial impact were obtained. The 26 specimens used in the study ranged in age from 27 to 67 years. Fracture forces measured by the tibia load cell ranged from 4.3 to 11.4 kN. The pathology included extra- and intra-articular fractures of the distal tibia/calcaneous with and without extensions into the anatomic joints.

Using parallel studies of Begeman and Aekbote, which indicated fracture forces in the 6.9- to 8.7-kN range for 17 specimens, and the study of Roberts et al., which indicated fractures forces to range from 7.8 to 13.0 kN for nine specimens, Yoganandan et al. combined their data on 26 specimens to derive the foot-ankle fracture probability distribution (Begeman and Aekbote, 1996; Roberts et al., 1993; Yoganandan et al., 1996e). This methodology, despite variations in the testing from individual laboratories, resulted in a total of 52 samples that included 25 fracture and 27 nonfracture data points. A Weibull probability curve based on age and fracture force vs. injury was derived (Fig. 6.30). If one is interested in a more simplified risk function with axial forces as the only discriminant variable without regard to age, the Weibull curve indicated a force of 6.8 kN to represent a 50% probability of injury (Fig. 6.31). The generalized two-parameter risk function was further used to describe the probability of injury with respect to axial force for specific age groups (Fig. 6.32). A 50% injury risk occurred for a 65-year-old specimen at a dynamic axial force of 6.2 kN. The force value rose to approximately 8.0 kN for a 45-year-old specimen. Experiments have also been conducted to describe the biomechanics of the human foot-ankle complex in dorsiflexion and plantar flexion, and eversion and inversion modalities (Begeman et al., 1993; 1994; Begeman and Prasad, 1990).

6.9 Crashworthiness

Vehicular crashworthiness, as defined earlier, is a phrase used to assess the protection of an occupant during a crash. Federal Motor Vehicle Safety Standard FMVSS 208 specifies the performance requirements for the protection of the occupant of a vehicle during crashes. The purpose is to reduce the number of

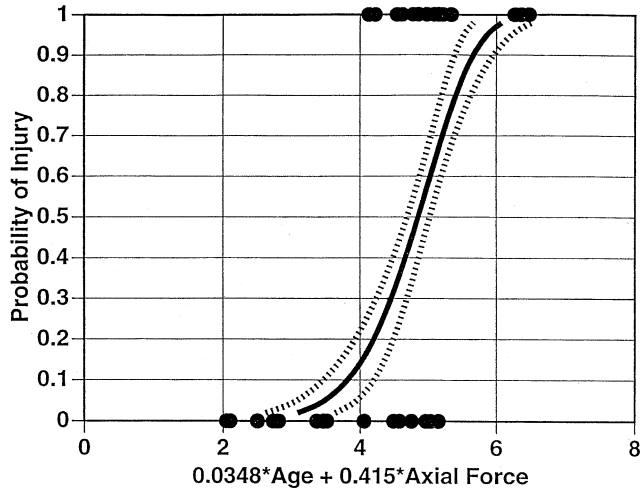

FIGURE 6.30 Probability distribution for human foot/ankle injury as a function of age and dynamic axial force.

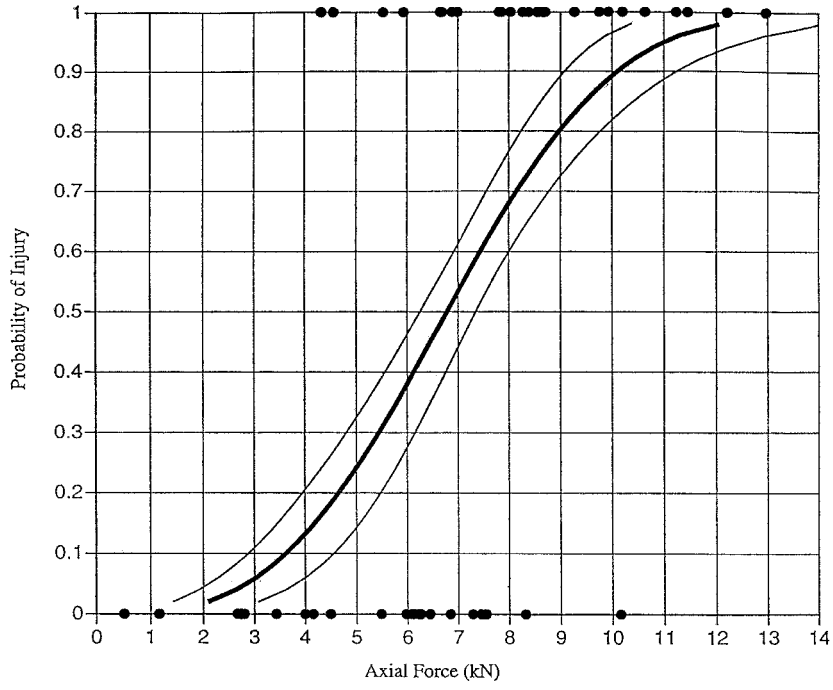

FIGURE 6.31 Probability distribution for human foot/ankle injury under dynamic loading. Solid circles represent the actual nonfracture (along the abscissa) and fracture data points from which the probability curve was developed.

injuries of the occupants by specifying vehicle crashworthiness requirements in terms of biomechanical parameters such as forces and accelerations measured using anthropomorphic manikins in simulated crash events, and by specifying vehicle equipment requirements for active and passive systems. The FMVSS 208 standard applies to passenger cars, multipurpose passenger vehicles, trucks, and buses. Frontal crashworthiness barrier crash tests are conducted as follows. A vehicle traveling longitudinally forward at any speed, up to and including 30 mph (used in English units to conform to the FMVSS specifications;

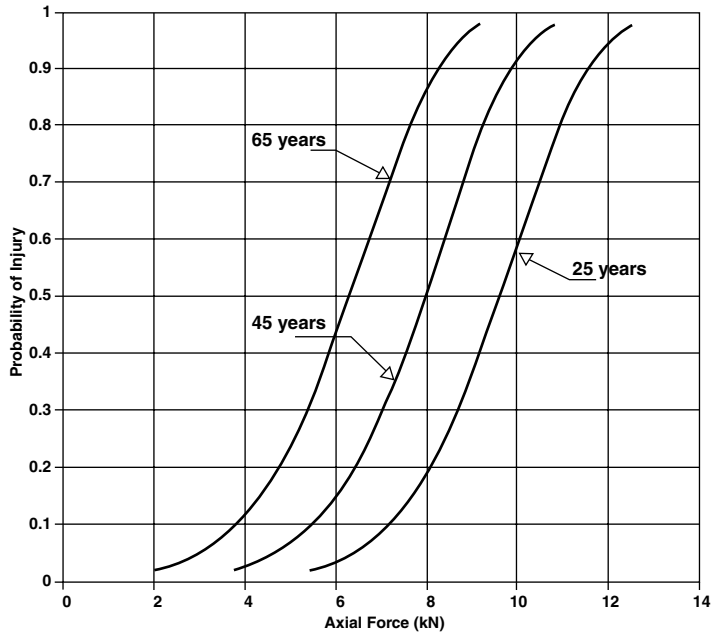

FIGURE 6.32 Probability distribution for foot/ankle injury as a function of the dynamic axial force. The probability curves are shown for three distinctively different ages.

1.6 kph = 1 mph), is impacted into a fixed collision barrier that is perpendicular to the line of the vehicle or at any angle up to 30¡ in either direction from the perpendicular to the line of travel of the vehicle. The anthropomorphic manikin is placed in each front outboard designated sitting position and should meet the following injury criteria.

1. All portions of the test dummy shall be contained within the outer surfaces of the vehicle passenger compartment during the entire test.
2. The resultant acceleration of the center of gravity of the head of the anthropomorphic manikin is obtained from the following equation.

$$(t_2 - t_1)\left[\frac{1}{(t_2 - t_1)}\int_{t_1}^{t_2} a(t)dt\right]^{2.5} < 1000$$

   The HIC shall not exceed 1000, where a is the resultant acceleration expressed as a multiple of G, and t_1 and t_2 are any two points in time during the crash of the vehicle which are separated by not more than 36 msec time intervals.
3. The resultant acceleration at the center of gravity of the upper thorax, calculated from the output of the thoracic instrumentation shall not exceed 60 G, except for intervals whose cumulative duration is not more than 3 msec.
4. The compression-deflection of the sternum relative to the spine shall not exceed 3 in.
5. The compressive force transmitted axially through each upper leg of the anthropomorphic manikin shall not exceed 2250 lbs (10 kN).

Flat (full) barrier tests involve a vehicle crashing into the center of the perpendicular barrier such that the loading is across the full front of the vehicle. In contrast, angle barrier tests involve a vehicle crashing into the center of a barrier set at an angle such that the loading is concentrated to either the left or the right side of the front of the vehicle. Offset barrier tests involve a vehicle crashing into the edge of a perpendicular barrier, with the degree of offset depending on the amount of overlap between the vehicle and the barrier. The new car assessment program (NCAP) was initiated in 1978 with the primary purpose

of partially fulfilling one of the requirements of Title 2 of the motor vehicle information and cost savings act of 1972 (Hackney et al., 1994). In contrast to the FMVSS 208 standards, wherein the frontal impact tests are conducted at an impact velocity of 30 mph, the tests under the NCAP program are conducted at a higher velocity, wherein the vehicles are towed head-on into a fixed rigid barrier at 35 mph. The ultimate goal of the NCAP is to improve occupant safety by providing market incentives for manufacturers to voluntarily incorporate better crashworthiness into their vehicles rather than solely by regulatory directives. Two instrumented anthropomorphic test devices simulating 50th percentile adult males are seated in the front driver and the front right passenger seats, and restrained with appropriate systems. Similar to the FMVSS 208 tests, information such as the HIC chest acceleration and upper leg forces are measured in the NCAP test. The higher velocity of 35 mph chosen in the NCAP tests is meant to provide a level of impact severity sufficiently higher than the FMVSS 208 requirement so that differences in frontal crashworthiness performance among the vehicles can be readily observed. This increased velocity represents a 36% increase in the kinetic energy during the frontal impact. In the 35-mph NCAP test, the average "delta v" (change in velocity) is 40 mph including the rebound velocity from the barrier. In contrast, in a 30-mph FMVSS 208 test, the average "delta v" is 33 mph. It has been indicated that NCAP conditions approximate real-world crash scenarios encompassing a major segment of the frontal crash safety problem and that there is a significant correlation between the NCAP results and real-world fatality risks for restrained drivers (Hackney et al., 1994). Recently, the NCAP program has been expanded into the side-impact testing mode, which is outside the scope of the this chapter.

The Insurance Institute for Highway Safety (IIHS) routinely conducts 40-mph frontal crash tests to demonstrate the differences between a 30-mph FMVSS 208, a 35-mph NCAP test, and the more severe 40-mph frontal crash test. In the IIHS test, the vehicles are evaluated in terms of the structural performance (e.g., crush profiles of the front end), injury measures from the 50th percentile in the male Hybrid III dummy in the driver's seat, and the kinematics of the anthropomorphic manikin.

6.10 Summary

An overview of the biodynamic response of the human body secondary to vehicular frontal impact is given in this chapter. Biodynamic studies with particular reference to experimental studies and human tolerance data are discussed for the head, face, neck, thorax, abdomen, and the upper and lower extremities. The existing Federal Motor Vehicle Safety Standard specifications for frontal impact are also provided. It is hoped that this presentation will provide an understanding of the topic.

Acknowledgment

This study was supported in part by DOT NHTSA Grant DTNH-22-93-Y-17028, PHS CDC Grant R49CCR-507370, and the Department of Veterans Affairs.

References

(1992a). Driver deaths down substantially in cars equipped with air bags. *Status Report, Insurance Institute for Highway Safety* **27**(12).

(1992b). Evaluation of the effectiveness of occupant protection: Interim Report, U.S. Department of Transportation, National Highway Traffic Safety Administration.

(1995). *Code of Federal Regulations*. Washington, DC: National Highway Traffic Safety Administration.

AIS (1990). *The Abbreviated Injury Scale*. Arlington Heights, IL: American Association for Automotive Medicine.

Augenstein, J. S., Digges, K. H., Malliaris, A. C., Lombardo, L. V., Stratton, J., Nunez, D., Byers, P., Quigely, C. V., Young, P. E., Andron, J., Murtha, M., Craythrone, K., Zych, G., and Halem, M. (1995). Liver injuries associated with 2-point belt restraints in frontal crashes. *39th Annual American Association of Automotive Medicine*, Chicago IL, 193-212.

Backaitis, S. H. (1995). *Biomechanics of Impact Injury and Injury Tolerances of the Thorax-Shoulder Complex*. (Vol. PT-45). Warrendale, PA: Society of Automotive Engineers.

Backaitis, S. H. and Mertz, H. J. (Eds.) (1994). *Hybrid III: The First Human-Like Crash Test Dummy*. (Vol. PT44). Warrendale, PA: Society of Automotive Engineers.

Backaitis, S. H. and Roberts, J. V. (1987). Occupant injury patterns in crashes with air bag equipped government sponsored cars. *Proceedings 31st Stapp Car Crash Conference*, New Orleans, LA, 251-266.

Backaitis, S. H. and St. Laurent, A. (1986). Chest deflection characteristics of volunteers and Hybrid II dummies. *Proceedings 30th Stapp Car Crash Conference*, San Diego, CA, 157-166.

Begeman, P. and Aekbote, K. (1996). Axial load strength and some ligament properties of the ankle joint. *Injury Prevention Through Biomechanics Symposium*, Detroit, MI, 125-135.

Begeman, P., Aekbote, K., Levine, R., and King, A. (1994). Human ankle response in internal and external rotation. *Proceedings 4th Annual Injury Prevention Through Biomechanics Symposium*, Wayne State University, 63-73.

Begeman, P. and Prasad, P. (1990). Human ankle response in dorsiflexion. *Proceedings 34th Stapp Car Crash Conference*, Orlando, FL, 39-53.

Begeman, P. C., Balakrishnan, P., Levine, R., and King, A. I. (1993). Dynamic human ankle response to inversion and eversion. *Proceedings 37th Stapp Car Crash Conference*, San Antonio, TX, 83-93.

Braakman, R. (1972). Depressed skull fracture: Data, treatment, and follow-up in 225 consecutive cases. *J. Neurol. Neurosurg. Psychiatry* **35**: 395.

Burgess, A., Dischinger, P., O'Quinn, T., and Schmindhauser, C. (1995). Lower extremity injuries in drivers of airbag-equipped automobiles: Clinical and crash reconstruction correlations. *J Trauma* **38**, 509-516.

Cesari, D. and Boquet, R. (1990). Behaviour of human surrogates thorax under belt loading. *Proceedings 34th Stapp Car Crash Conference*, Orlando, FL, 73-81.

Cesari, D. and Bouquet, R. (1994). Comparison of Hybrid III and human cadaver thorax deformations loaded by a thoracic belt. *Proceedings 38th Stapp Car Crash Conference*, Ft. Lauderdale, FL, 65-76.

Committee on Trauma Research, Commission on Life Sciences, National Research Council, and Medicine. (1985). Injury in America: A Continuing Public Health Problem . Washington, DC: National Academy Press.

Crandall, J. R., Klisch, S. M., Klopp, G. S., Sieveka, E., Pilkey, W. D., and Martin, P. (1994a). Research program to investigate lower extremity injuries. *International Congress and Exposition*, Detroit, MI, 19-30.

Crandall, J. R., Pilkey, W. D., Klopp, G. S., Pilkey, B., Morgan, R. M., Eppinger, R. H., Kuppa, S. M., and Sharpless, C. L. (1994b). A comparison of two and three point belt restraint systems. *Advances in Occupant Restraint Technologies: Joint AAAM - IRCOBI Special Session*, Lyon, France.

Cusick, J. F., Yoganandan, N., Pintar, F. A., and Gardon, M. (1996). Cervical spine injuries from high velocity forces: A pathoanatomical and radiological study. *J Spinal Disords* **9**(1), 1-7.

Dimasi, F., Eppinger, R. H., Gabler, H. C., III, and Marcus, J. H. (1991). Simulated head impacts with upper interior structures using rigid and anatomic brain models. *Auto and Traffic Safety* Technical Paper, 20-31.

Dimasi, F. P., Eppinger, R. H., and Bandak, F. A. (1995). Computational analysis of head impact responses under car crash loadings. *Proceedings 39th Stapp Car Crash Conference*, San Francisco, CA, 425-438.

Ehler, V. E., Eickhoff, G., and Pursian, M. (1976a). Zur Festigkeit und Elastizitat Druckbelasteter Menschlicher Weichteilbedeckter Kopfe. *Anat Anz* **140**, S139.

Ehler, V. E., Weber, J., Weber, J., and Steffin, C. (1976b). Der menschliche schadel unter dem einfluss vertikal im bereich der ossa parietalia eingeleiteter statischer drucklasten. *Anat Anz* **140**(S301).

Eiband, A. M. Human tolerance to rapidly applied accelerations: a summary of the literature, NASA Memorandum 5-19-59E: NASA Lewis Research Center, Cleveland, OH.

Eppinger, R. H. (1976). Prediction of thoracic injury using measurable experimental parameters. *Sixth International Conference on Experimental Safety Vehicles*, Washington, DC, 770-779.

Eppinger, R. H. (1989). On the development of deformation measurement system and its application toward developing mechanically based indices. *Proceedings 33rd Stapp Car Crash Conference*, Washington, DC, 209-268.

Evans, F. G., Lissner, H. R., and Lebow, M. (1958). The relation of energy, velocity, and acceleration to skull deformation and fracture. *Surg Gynecol Obstet* **107**, 593-601.

Fildes, B., Lenard, J., and Lane, J. (1995). Lower limb injury in frontal crashes. *International Conference on Pelvic and Lower Extremity Injuries*, Washington, DC.

Gennarelli, T. A. (1981). Mechanistic approach to the head injuries: Clinical and experimental studies of the important types of injury, Head and Neck Injury Criteria: A Consensus Workshop, (pp. 20-25). Washington, DC: National Highway Traffic Safety Administration.

Gurdjian, E. S. (1975). *Impact Head Injury, Mechanistic, Clinical and Preventive Correlations*. Springfield, IL: Charles C Thomas.

Gurdjian, E. S., Lissner, H. R., Evans, F. G., Patrick, L. M., and Hardy, W. G. (1961). Intracranial pressure and acceleration accompanying head impacts in human cadavers. *Surg Gynecol Obstet*, 185-190.

Gurdjian, E. S., Lissner, H. R., and Patrick, L. M. (1962b). Protection of the head and neck in sports. *JAMA* **182**(5), 509.

Gurdjian, E. S., Lissner, H. R., and Patrick, L. M. (1962a). Protection of the head and neck in sports. *JAMA* **182**(5), 509-512.

Hackney, J. R., Kahane, C. J., and Quarles, V. R. (1994). The new car assessment program -- historical review and effect. , 75-89.

Haffner, M. (1987). Trauma assessment device development program: Thorax-abdomen development task. Preliminary goals and design requirements statement. Contract Communication. Washington, DC: National Highway Traffic Safety Administrations, US Department of Transportation.

Hardy, C. H. and Marcal, P. V. (1973). Elastic analysis of a skull. *ASME Transactions*, 838-842.

Harris, G. F., Yoganandan, N., Schmaltz, D., Reinartz, J., Pintar, F. A., and Sances, A., Jr. (1993). A biomechanical impact test system for head and facial injury assessment and model development. *J Biomed Eng* **15**, 67-73.

Hodgson, V. R. and Thomas, L. M. (1971). Breaking strength of the human skull vs. impact surface curvature (HS-800-583). Springfield, VA: US Department of Transportation.

Holub, D. P., Boynton, M., Yoganandan, N., and Pintar, F. A. (1995). Foot and ankle fractures in motor vehicle accident victims. *International Conference on Pelvic and Lower Extremity Injuries*, Washington, DC, 349-353.

Huelke, D. F., Moore, J. L., Compton, T. W., Samuels, J., and Levine, R. S. (1994). Upper extremity injuries related to air bag deployments. *In-Depth Accident Investigation: Trauma Team Findings in Late Model Vehicle Collisions*, Warrendale, PA, 55-64.

Jamieson, K. G. (1974). Surgical lesions in head injuries: Their relative incidence, mortality rates and trends. *Aust NZ J Surg* **44**(3), 241.

Jamieson, K. G. and Kelly, D. (1974). Traffic injuries in Brisbane hospitals over one decade. *Aust NZ J Surg* **44**(2), 150.

Jamieson, K. G. and Yelland, J. D. (1972). Depressed skull fractures in Australia. *J Neurosurg* **37**, 150.

Kallina, I. (1995). Injuries of the lower leg: Significance for the occupant-assessment in tests - injury prevention. *Pelvic and Lower Extremity Injuries Conference*, Washington, DC,

Katz, E., Grosch, L., and Kassing, L. (1987). Chest compression response of a modified Hybrid III with different restraint systems. *Proceedings 31st Stapp Car Crash Conference*, New Orleans, LA, 245-249.

Kleinberger, M. (1993). Application of finite element techniques to the study of cervical spine mechanics. *Proceedings 37th Stapp Car Crash Conference*, San Antonio, TX, 261-272.

Kroell, C. K., Schneider, D. C., and Nahum, A. M. (1971). Impact tolerance and response to the human thorax. *Proceedings 15th Stapp Car Crash Conference*, Coronado, CA, 84-134.

Kroell, C. K., Schneider, D. C., and Nahum, A. M. (1974). Impact tolerance and response to the human thorax II. *Proceedings 18th Stapp Car Crash Conference*, Ann Arbor, MI, 123-142.

Kumaresan, S. and Radhakrishnan, S. (1996). Importance of partitioning membranes of the brain and the neck in head injury modelling. *Med and Biolog Eng and Computing* **34**, 27-32.

Kumaresan, S., Radhakrishnan, S., and Ganesan, N. (1995). Generation of geometry and discretization of closed human head for finite element analysis. *Med and Biolog Eng and Computing* **5133**(13), 349-353.

Kuppa, S. M., Olson, M. B., Yeiser, C. W., Taylor, L. M., Morgan, R. M., and Eppinger, R. H. (1997). RAID -- An investigative tool to study airbag/upper extremity interactions (245-257). Warrendale, PA: Society of Automotive Engineers.

Lau, I. V. and Viano, D. C. (1986). The viscous criterion -- bases and applications of an injury severity index for soft tissues. *Proceedings 30th Stapp Car Crash Conference*, San Diego, CA, 123-142.

Lissner, H. R., Lebow, M., and Evans, F. G. (1960). Experimental studies on the relation between acceleration and intracranial pressure changes in man. *Surg Gynecol Obstet*, 329-338.

Liu, Y. K. and Dai, Q. G. (1989). The second stiffest axis of a beam-column: Implications for cervical spine trauma. *J Biomech Eng* **111**(2), 122-127.

Maiman, D. J. and Yoganandan, N. (1991). Biomechanics of cervical spine trauma. In P. Black (Ed.), Clinical Neurosurgery, (Vol. 37, pp. 543-570). Baltimore, MD: Williams and Wilkins.

McElhaney, J. H. and Myers, B. S. (1993). Biomechanical aspects of cervical trauma. In A. M. Nahum and J. W. Melvin (Eds.), Accidental Injury: Biomechanics and Prevention, (pp. 311-361). New York: Springer-Verlag New York Inc.

McElhaney, J. H., Stalnaker, R. L., and Roberts, V. L. (1972). Biomechanical aspects of head injury. In W. F. King and H. J. Mertz (Eds.), Human Impact Tolerance, (pp. 406). New York: Plenum Press.

Melvin, J. W. (1985). Advanced Anthropomorphic Test Device (AATD) Development Program. Phase 1: Concept Definition : U.S. Department of Transportation, National Highway Traffic Safety Administration.

Melvin, J. W. and Evans, F. G. (1971). A strain energy approach to the mechanics of skull fracture. *Proceedings 15th Stapp Car Crash Conference*, Coronado, CA, 666.

Melvin, J. W., Fuller, P. M., and Roberts, V. L. (1969). Frangible head form development Phase I: A six month study of the effects of localized impact on tissue (NP-47-356319). Ann Arbor, MI: Highway Safety Research Institute.

Mertz, H. J. (1967). The kinematics and kinetics of whiplash. Unpublished Dissertation, Wayne State, Detroit, MI. 370 pp.

Mertz, H. J. and Patrick, L. M. (1967). Investigation of the kinematics and kinetics of whiplash. *Proceedings 11th Stapp Car Crash Conference*, Anaheim, CA, 267-317.

Mertz, H. J. and Patrick, L. M. (1971). Strength and response of the human neck. *Proceedings 15th Stapp Car Crash Conference*, Coronado, CA, 207-255.

Messerer, O. (1880). Uber Elasticitat und Festigkeit der Menschlichen Knochen. Stuttgart, Germany.

Morgan, R. M., Eppinger, R. H., Haffner, M. P., Yoganandan, N., Pintar, F. A., and Sances, A., Jr. (1994). Thoracic trauma assessment formulations for restrained drivers in frontal impact. *Proceedings 38th Stapp Car Crash Conference*, Ft. Lauderdale, FL, 12-34.

Morgan, R. M., Eppinger, R. H., and Hennessey, B. C. (1991). Ankle joint injury mechanism for adults in frontal automotive impact. *Proceedings 35th Stapp Car Crash Conference*, San Diego, CA, 189-198.

Nahum, A., Gatts, J. D., Gadd, C. W., and Danforth, J. (1968). Impact tolerance of the skull and face. *Proceedings 12th Stapp Car Crash Conference*, Detroit, MI, 302.

Nightingale, R. W., McElhaney, J. H., Richardson, W. J., and Myers, B. (1996). Dynamic responses of the head and cervical spine to axial impact loading. *J Biomech* **29**(3), 307-318.

Patrick, L. M., Lissner, H. R., and Gurdjian, E. S. (1963). Survival by design: Head protection. *Proceedings 7th Stapp Car Crash Conference*, New York, 483-499.

Pintar, F. A. (1986). Biomechanics of Spinal Elements. Unpublished Doctoral Dissertation, Marquette University, Milwaukee, WI. 222 pp.

Pintar, F. A., Maiman, D. J., and Yoganandan, N. (1996a). Clinical and Experimental Biomechanics of the Spine. In G. T. Tindall, Cooper, P R, Barrow, D L (Ed.), The Practice of Neurosurgery, (pp. 2347-2356). Baltimore, MD: Williams and Wilkins.

Pintar, F. A., Myklebust, J. B., Yoganandan, N., and Sances, A., Jr. (1986). Biomechanical properties of the human intervertebral disc in tension. *ASME*, New York, NY, 38-39.

Pintar, F. A., Sances, A., Jr, Yoganandan, N., Reinartz, J. M., Maiman, D. J., Suh, J. K., Unger, G., Cusick, J. F., and Larson, S. J. (1990a). Biodynamics of the total human cadaver cervical spine. *Proceedings 34th Stapp Car Crash Conference*, Orlando, FL, 55-72.

Pintar, F. A., Schlick, M. B., Yoganandan, N., and Maiman, D. J. (1996b). Instrumented artificial spinal cord for human cervical pressure measurement. *Bio-Med Mat and Eng* **6**(2), 219-229.

Pintar, F. A., Yoganandan, N., Maiman, D. J., and Sances, A., Jr. (1995a). Cervical spinal bony injury and the potential for cord injury. *5th Symposium on Injury Prevention Through Biomechanics*, Detroit, MI, 161-169.

Pintar, F. A., Yoganandan, N., Sances, A., Jr , Reinartz, J., Harris, G., and Larson, S. J. (1990b). Kinematic and anatomical analysis of the human cervical spinal column under axial loading. *SAE Transactions* **98**(6), 1766-1789.

Pintar, F. A., Yoganandan, N., Voo, L. M., Cusick, J. F., Maiman, D. J., and Sances, A., Jr. (1995b). Dynamic characteristics of the human cervical spine. *SAE Transactions* **104**(6), 3087-3094.

Pintar, F. A., Yoganandan, N., Voo, L. M., Droese, K., Reinartz, J., Schlick, M., and Hollowell, J. P. (1995c). Spinal cord injury potential using an experimental biomechanical model. *Proceedings American Association Neurological Surgeons Annual Meeting*, Orlando, FL, 278.

Prasad, P. and Chou, C. C. (1993). A review of mathematical occupant simulation models. In A. M. Nahum and J. W. Melvin (Eds.), Accidental Injury: Biomechanics and Prevention, (pp. 102-150). New York: Springer-Verlag New York Inc.

Prasad, P. and Mertz, H. J. (1985). The position of the United States Delegation to the ISO Working Group 6 on the use of HIC in the automotive environment (851246). , Warrendale, PA,

Rice, D. P. and MacKenzie, E. J. (1989). *Cost of Injury in the United States. A report to Congress*.

Roberts, D., Donnelly, B., Severin, C., and Medige, J. (1993). Injury mechanisms and tolerance of the human ankle joint (Grant #R494CCR203615 01, 365 pp): Report to the Centers for Disease Control.

Ruan, J. S., Khalil, T. B., and King, A. I. (1993). Finite element modeling of direct head impact. *Proceedings 37th Stapp Car Crash Conference*, San Antonio, TX, 69-81.

Ruan, J. S., Khalil, T. B., and King, A. I. (1994). Dynamic response of the human head to impact by three-dimensional finite element analysis. *J Biomech Engr* **116**, 44-50.

Sances, A., Jr. and Yoganandan, N. (1986). Human head injury tolerance. In A. Sances, Jr., D.J. Thomas, C.L. Ewing, S.J. Larson, F. Unterharnscheidt (Ed.), Mechanisms of Head and Spine Trauma, (pp. 189-218). Goshen, NY: Aloray.

Saul, R. A., Backaitis, S. H., Beebe, M. S., and Ore, L. S. (1996). Hybrid III dummy instrumentation and assessment of arm injuries during air bag deployment. *Proceedings 40th Stapp Car Crash Conference*, 85-94.

Schneider, D. C. and Nahum, A. M. (1972). Impact studies of facial bones and skull. *Proceedings 16th Stapp Car Crash Conference*, Detroit, MI, 186.

Schneider, L. W. (1989). Design requirements and specifications: Thorax-abdomen development task. Interim report. Trauma assessment device development program (DOT HS 807 511). Ann Arbor, MI: US Department of Transportation, National Highway Traffic Safety Administration.

Schneider, L. W., Ricci, L. L., Salloum, M. J., Beebe, M. S., Rouhana, S. H., and Neathery, R. F. (1992). Design and development of an advanced ATD thorax system for frontal crash environments: Primary concept and development. (Final Report UMTRI-92-22-1). Washington, DC: US Department of Transportation.

Shea, M., Edwards, W. T., White, A. A., III, and Hayes, W. C. (1991). Variations of stiffness and strength along the human cervical spine. *J Biomech* **24**(2), 95-107.

Stapp, J. P. (1955). Tolerance to abrupt deceleration (Agardograph No. 6), Collected Papers on Aviation Medicine, (pp. 122-169): London: Butterworth.

Stapp, J. P. (1961). Human tolerance to severe, abrupt deceleration. In O. H. Gauer and G. D. Zuideme (Eds.), Gravitational Stress in Aerospace Medicine, (pp. 165-188). Boston: Little, Brown.

States, J., Huelke, D., Dance, D., and Green, R. (1987). Fatal injuries caused by underarm use of shoulder belts. *J Trauma* **27**(7), 740-745.

Stover, S. L. and Zeigler, H. E. (1976). Head injury in children and teenagers: functional recovery correlated with the duration of coma. *Arch Phys Med Rehabil* **57**, 201.

Thomas, P., Charles, J., and Fay, P. (1995). Lower limb injuries - the effect of intrusion, crash severity and the pedals on injury risk and injury type in frontal collisions. *Proceedings 39th Stapp Car Crash Conference*, Coronado, CA, 265-280.

Unterharnscheidt, F. and Higgins, L. (1969). Traumatic lesions of brain and spinal cord due to nondeforming angular acceleration of the head. *Tex Rep Biol Med* **27**(1), 127.

USDHHS. (1989). *Healthy People 2000 - National Health Promotion and Disease Prevention Objectives*. Washington, DC: U.S. Government Printing Office.

Versace, J. (1971). A review of the severity index. *Proceedings 15th Stapp Car Crash Conference*, New York, 771-796.

Viano, D. C. and Lau, I. V. (1988). A viscous tolerance criterion for soft tissue injury assessment. *J Biomech* **21**(5), 387-399.

Voo, L. M., Kumaresan, S., Yoganandan, N., Pintar, F. A., and Cusick, J. F. (1997). Finite element analysis of cervical facetectomy. *Spine* **22**(9), 964-969.

Walker, A. E., Caveness, W. F., and Critchley, M. (1969). *The Late Effects of Head Injury*. Springfield, IL: Charles C Thomas.

Yamada, H. (1970). *Strength of Biological Materials*. Baltimore, MD: Williams and Wilkins.

Yoganandan, N., Boynton, M., and Pintar, F. A. (1997a). Axial impact biomechanics of the human foot-ankle complex. *J Biomech Engr* (In Press).

Yoganandan, N., Haffner, M., Maiman, D. J., Nichols, H., Pintar, F. A., Jentzen, J., Weinshel, S., Larson, S. J., and Sances, A., Jr. (1990). Epidemiology and injury biomechanics of motor vehicle related trauma to the human spine. *SAE Transactions* **98**(6), 1790-1807.

Yoganandan, N., Haffner, M., and Pintar, F. A. (1996a). Facial injury: a review of biomechanical studies and test procedures for facial injury assessment. *J Biomech* **29**(7), 985-986.

Yoganandan, N., Halliday, A., Dickman, C., and Benzel, E. (1997b). Practical anatomy and fundamental biomechanics. In E. Benzel (Ed.), Spine Surgery: Techniques, Complication Avoidance, and Management. New York, NY: Churchill Livingstone.

Yoganandan, N., Kumaresan, S., Voo, L., and Pintar, F. (1996b). Finite element applications in human cervical spine modeling. *Spine* **21**(15), 1824-1834.

Yoganandan, N., Kumaresan, S., Voo, L., and Pintar, F. (1997c). Finite element model of the human lower cervical spine. *J Biomech Eng* **119**(1), 87-92.

Yoganandan, N., Kumaresan, S., Voo, L., Pintar, F., and Larson, S. (1996c). Finite element modeling of the C4-C6 cervical spine unit. *Med Eng Phy* **18**(7), 569-574.

Yoganandan, N., Maiman, D. J., Pintar, F. A., Ray, G., Myklebust, J. B., Sances, A., Jr, and Larson, S. J. (1988a). Microtrauma in the lumbar spine: A cause of low back pain. *Neurosurgery* **23**(2), 162-168.

Yoganandan, N., Morgan, R. M., Eppinger, R. H., Pintar, F. A., Sances, A., Jr, and Williams, A. (1996d). Mechanism of thoracic injury in a frontal impact. *J Biomech Engr* **118**, 595-597.

Yoganandan, N., Morgan, R. M., Eppinger, R. H., Pintar, F. A., Skrade, D. A., and Sances, A., Jr. (1995a). Thoracic deformation and velocity analysis in frontal impact. *J Biomech Engr* **117**, 48-52.

Yoganandan, N., Myklebust, J. B., Ray, G., and Sances, A., Jr. (1987). Mathematical and finite element analysis of spinal injuries. *CRC Review Biomed Eng* **15**(1), 29-93.

Yoganandan, N., Myklebust, J. B., Wilson, C. R., Cusick, J. F., and Sances, A., Jr. (1988b). Functional biomechanics of the thoracolumbar vertebral cortex. *Clinical Biomechanics* **3**, 11-18.

Yoganandan, N., Pintar, F. A., Arnold, P., Reinartz, J., Cusick, J. F., Maiman, D. J., and Sances, A., Jr. (1994a). Continuous motion analysis of the head-neck complex under impact. *J Spinal Disord* **7**(3), 420-428.

Yoganandan, N., Pintar, F. A., Boynton, M., Morgan, R. M., and Eppinger, R. (1996e). Dynamic axial tolerance of the human foot-ankle complex. *Proceedings 40th Stapp Car Crash Conference*, Albuquerque, NM, 207-218.

Yoganandan, N., Pintar, F. A., Cusick, J. F., Reinartz, J., Sances, A., Jr, and Maiman, D. J. (1994b). Cervical spine injury mechanism under vertical impact. *ASME - BED* **28**, 339-340.

Yoganandan, N., Pintar, F. A., Kumaresan, S., Haffner, M., and Kuppa, S. (1997d). Impact Biomechanics of the human thorax-abdomen complex. *I J Crashworthiness* 2(2): 219-228.

Yoganandan, N., Pintar, F. A., Kumaresan, S., Sances, A., Jr, and Haffner, M. (1996f). Response of human lower thorax to impact. *40th Annual Association for the Advancement of Automotive Medicine Conference*, Vancouver, BC, Canada, 33-43.

Yoganandan, N., Pintar, F. A., Maiman, D. J., Cusick, J. F., Sances, A., Jr, and Walsh, P. R. (1996g). Human head-neck biomechanics under axial tension. *Med Eng Physics* **18**(4), 289-294.

Yoganandan, N., Pintar, F. A., Reinartz, J., and Sances, A., Jr. (1993). Human facial tolerance to steering wheel impact: A biomechanical study. *J Safety Res* **24**(2), 77-85.

Yoganandan, N., Pintar, F. A., and Sances, A., Jr. (1991a). Biodynamics of steering wheel induced facial trauma. *J Safety Res* **22**, 179-190.

Yoganandan, N., Pintar, F. A., Sances, A., Jr, and Maiman, D. J. (1991b). Strength and motion analysis of the human head-neck complex. *J Spinal Disord* **4**(1), 73-85.

Yoganandan, N., Pintar, F. A., Sances, A., Jr, Reinartz, J., and Larson, S. J. (1991c). Strength and kinematic response of dynamic cervical spine injuries. *Spine* **16**(10), 511-517.

Yoganandan, N., Pintar, F. A., Sances, A. J., Walsh, P. R., Ewing, C. L., Thomas, D. L., and Snyder, R. G. (1995b). Biomechanics of skull fracture. *J Neurotrauma* **12**(4), 659-668.

Yoganandan, N., Pintar, F. A., Skrade, D., Chmiel, W., Reinartz, J. M., and Sances, A., Jr. (1994c). Thoracic biomechanics with air bag restraint. *SAE Transactions* **102**(6), 2597-2607.

Yoganandan, N., Sances, A., Jr, and Pintar, F. A. (1989). Biomechanical evaluation of the axial compressive responses of the human cadaveric and manikin necks. *J Biomech Eng* **111**(3), 250-255.

Yoganandan, N., Sances, A., Jr , Pintar, F. A., Larson, S., Hemmy, D., Maiman, D., and Haughton, V. (1991d). Traumatic facial injuries with steering wheel loading. *J Trauma* **31**(5), 699-710.

Yoganandan, N., Skrade, D., Pintar, F., Reinartz, J., and Sances, A., Jr. (1991e). Thoracic deformation contours in a frontal impact. *Proceedings 35th Stapp Car Crash Conference*, San Diego, CA, 47-63.

Yoganandan, N., Voo, L., Pintar, F. A., Kumaresan, S., Cusick, J. F., and Sances, A., Jr. (1995c). Finite element analysis of the cervical spine. *CDC Injury Prevention Through Biomechanics*, Detroit, MI, 149-155.

Zhou, Q., Rouhana, S. W., and Melvin, J. W. (1996). Age effects on thoracic injury tolerance. *Proceedings 40th Stapp Car Crash Conference*, Albuquerque, NM, 137-148.

7

Techniques and Applications of Finite Element Analysis of the Biomechanical Response of the Human Head to Impact

Jesse S. Ruan
Ford Motor Company

Chun Zhou
Wayne State University

Tawfik B. Khalil
Wayne State University

Albert I. King
Wayne State University

The biomechanical response of the human head to mechanical impacts along with its injury mechanisms was studied by finite element analysis. In this chapter, the large deformation, explicit, finite element techniques are briefly described. Their applications to the dynamic response of the human head to impact are presented in terms of model development, model prediction of injury-producing parameters, and parametric studies.

Detailed finite element models of the human head were developed to incorporate the macroanatomical features of the average adult head. The models have been used to study injury mechanisms of the human head undergoing direct and indirect impacts. It was shown that the sites of injury and injury severity may correspond to the computed skull stresses and strains, intracranial pressures, and brain stresses and strains, provided that injury tolerance to these parameters is known. It is concluded that there is potential for head injury prediction and assessment by finite element analysis.

7.1 Introduction

Simulating the head impact events and the biomechanical response of the human brain to dynamic loading plays a key role in understanding brain injury mechanisms. A validated head model can provide a rational basis for injury prevention, treatment, and establishing injury criterion for safety design. It has been a long-term goal of head injury researchers to explain clinical experiences with sound physical mechanisms and to establish predictive means to reduce the incidence of head trauma. To attain this goal, experimental modeling and mathematical modeling of head injury have been the two parallel methods used by biomechanical head injury researchers.

In experimental modeling, animals, cadavers, physical models, and anthropomorphic dummies are used. Experimental modeling of head injury yields measured force, acceleration, displacement, stress, and strain related to initiation of head injury. These data help the bioengineer in understanding the human response and tolerance to impact and also permit the development of mathematical models. Living animal models also provide useful pathological and physiological information related to mechanical loading. However, the repeatability of the experimental models is difficult to achieve and a parametric study with experimental models may be virtually impossible. In addition, impact experiments using animals raises ethical issues.

Mathematical modeling of head injury, on the other hand, applies the principles of mechanics and numerical analysis to define the problem, formulate the solution, and predict the potential of injuries. Mathematical models furnish the head trauma analysts with powerful tools to extrapolate major experimental findings in animals and other surrogates to the human and to establish the relationship between neurological deficit and mechanical dosage.

Developing representative head models requires a thorough understanding of the mathematical process involved in producing head injury and of its relationship to physiological and pathological tissue damage from experimental animal data. Mathematical head injury models, once validated, can help us in quantifying mechanical parameters related to a specific impact event and can be used repeatedly in a wide variety of loading conditions to predict injury. Thus, such a model can be used as a tool to study the formulation of a head tolerance limit and enhance our understanding of head injury mechanisms in such a way that more detailed information can be obtained by parametric studies.

It is currently feasible and desirable to develop sophisticated head injury models to incorporate more anatomical details of the human head, utilizing nonlinear, large deformation, finite element techniques, and a constitutive representation of head tissues. Accordingly, a second-generation mathematical model of the human head has been developed. The three-dimensional model simulated essential anatomical features (scalp, layered skull, partitioning membranes, gray and white matter, bridging veins, etc.) of the human head, which are important to the dynamic head response to direct/indirect impact or acceleration (linear or angular) loads. Model responses have been compared with experimental data to establish the necessary confidence level in model accuracy. The primary emphasis of the model was on the injury mechanisms and the assessment of head impact severity on the basis of the head tissues' mechanical response and their failure criteria.

7.2 Literature Review of Finite Element Head Models

The development of a validated mathematical human head model has challenged many head injury investigators due to the complex geometry, highly nonlinear material of the head tissues, and the difficulty of the numerical computations. It is not easy to develop a model that can faithfully duplicate the experimental results and clinical findings. Since the first mathematical head injury model proposed by Anzelius in 1943, numerous such models have been reported using closed-form formulation or finite element analysis. In this section, a literature review of finite element head models is given.

Two-Dimensional Finite Element Models

Several two-dimensional finite element models have been reported to simulate the human brain, animal brain, and physical surrogates. The model geometry ranged from midsagittal to coronal sections of the human and animal brains. Both elastic and viscoelastic materials have been considered to simulate the brain tissues. The loading conditions included direct and indirect or rotational impacts. Brain pressures and strains have been used as parameters for injury-potential assessment.

Shugar and Katona (1975) developed a plane strain model of a midsagittal section of the human head represented by a shell and fluid. They predicted a quadratic pressure gradient with the contrecoup pressure about twice as large as the coup pressure. Pressure contours were provided to visualize the pressure distribution in the brain. Khalil and Hubbard (1977) used the finite element method to model the head as an axisymmetric spherical fluid-filled shell. The model simulated the scalp, skull, and brain, including a multilayered skull. They found a linear pressure gradient in the fluid, with compression near the point of impact (coup) and tension on the opposite side (contrecoup). Pluche et al. (1985) proposed a two-dimensional finite element model to simulate a midsagittal section of the human head. The model included the skull, cerebrospinal fluid, and brain. After many computer runs were made by this model, the authors concluded that the neck restraint and skull deformation were important in head injury simulation.

A two-dimensional finite element model of a rhesus monkey head was proposed by Lee et al. (1987) to study the mechanism of traumatic subdural hematoma. The model was a rigid shell containing an elastic material that simulated the brain. The model predicted higher shear stress (hence strain) at the vertex where the parasagittal bridging veins were located. The authors deduced from the model prediction that subdural hematoma might have occurred. They concluded that for a Poisson's ratio of 0.475 for the brain material, both rotational and translational acceleration contributed equally to the deformation of the bridging vein (vertex in the model), and for a Poisson's ratio of 0.49, angular acceleration contributed more to the deformation of the bridging vein than translational acceleration.

Ueno et al. (1989) used a 2-D finite element model of a human brain based on a photograph of a sagittal section of the brain in conjunction with Lee et al.'s rhesus monkey model to scale experimental animal data (Abel et al., 1978) to the human level by a scaling law based on the mass of two models. Ueno et al. (1991) developed a 2-D ferret brain model subjected to a direct impact to the brain at a controlled velocity and stroke. A fairly good agreement between simulated and experimental pressure-time histories was reported.

Cheng et al. (1990) developed a two-dimensional finite element model representing a coronal section of the brain to study the diffuse axonal injury (DAI) problem. Model results were compared with experiments that were carried out at the University of Pennsylvania (Margulies, 1987). The effects of the skull/brain interface boundary, partitioning by a falxlike partition, load magnitude, brain size, and pulse duration on the levels of shear strain were studied by parametric variations. It was shown that the skull/brain interface and the geometry and partition of the brain had considerable influence on brain response to inertial loading.

In simulating the physical model of Margulies (1987), Lee (1990) developed two-dimensional full-cylinder and half-cylinder models. The models were subjected to an angular acceleration. The relationship between shear strains in the gel material that represented the brain and the linearly elastic properties of the brain was studied parametrically. The no-slip boundary condition at skull-brain interface was also investigated.

Ruan et al. (1991a) formulated three finite element models, an axisymmetric model, and a plane strain model of the coronal section of the human head, with and without the falx and cerebral tentorium, respectively, to study the side impact response of the head. The responses of the models were compared with previously published data and were found to be in good agreement. A parametric study addressed the effects of brain material properties on pressure response and the effects of the interior membrane on side impact response. The model prediction indicated that the cerebral membrane played an important role in the stresses produced in the brain.

A finite element model of the human head in the sagittal plane was devolved by Willinger et al. (1992) to perform a modal analysis. Based on the vibration mode of head model, the author concluded that a global vibration motion of the brain within the skull was responsible for the contrecoup injury mechanism.

A plane strain model of a parasagittal section of an average human head was created by Chu et al. (1994) to study the mechanisms of cerebral contusion. The model response was compared with previous experimental cadaver data (Nahum et al., 1977). The investigators found that the presence of a foramen magnum had only minor effects on the calculated pressure and believed that cerebral contusion was due to shear stress rather than pressure gradients in the brain.

Zhou et al. (1994) analyzed a 2-D porcine model to study the DAI problem. The model was used to simulate the porcine test performed at the University of Pennsylvanian (Ross et al., 1994). It was found that locations of high-shear strains predicted by the model matched the sites in the brain where DAI was found.

Three-Dimensional Finite Element Models

The models cited above are concerned with two-dimensional idealizations. More geometrically complex humanlike models require three-dimensional finite element simulations. Ward and Thompson's model (1975) was one of the first finite element models that approximated the three-dimensional anatomy of the brain, including the falx cerebri and tentorium. The discretized mesh of the brain had 877 degrees of freedom. However, the skull was assumed to be rigid. The model results included the natural frequencies from the first to the sixth mode with and without the interior membrane present in the model. Subsequent models by Ward and others (Ward et al., 1980; Nahum et al., 1977, 1980) predicted the pattern of pressure variation in the brain and showed that the dura, falx cerebri, and tentorium were important structures affecting brain response. Model responses were compared with experimental cadaver data.

Later, Ward et al. (1978) proposed two brain models representing the baboon and the small primate (rhesus or cynomolgus monkey) brains in addition to the early human brain model (Ward and Thompson, 1975). The models included the internal folds of the falx and tentorium. Each model was subjected to the same skull acceleration in an attempt to establish response relationships between species. Model responses were compared with experimentally derived head injury data and correlated well with test results. It showed that the location and magnitude of the maximum stresses were different in humans and animals. This finding led to a conclusion that scaling the response between specimens is inadvisable.

Shugar (1977) developed a 3-D model that closely approximated the geometry of the human skull and brain. A three-layered skull and a homogeneous brain were modeled. His results included shell strain near the impact site and around the foramen magnum at the base of the skull. A nearly linear pressure gradient in the brain was predicted. No experimental data comparison was given by this model. A 3-D monkey brain model was also developed in the same study.

The model proposed by Hosey and Liu (1982) simulated a layered skull, dura, cerebrospinal fluid (CSF), brain, spinal cord, cervical column, and cerebral membranes: falx and tentorium. The model predicted that there were pressure differences across the membranes. However, because of the geometric complexity of the model, a detailed parametric study was not provided at the time the model was developed. Also, no model comparisons with experimental data were made although such data were available at that time.

With the development of faster computers and explicit, nonlinear, large deformation finite element techniques, several three-dimensional models have been reported. Tong et al. (1989) simulated the physical model tests conducted at the University of Pennsylvania. The physical model was a simple half-cylinder containing a brainlike gel and was designed to study diffuse axonal injury (DAI). The model was used to estimate the material properties of brainlike gel used in the physical model. A comparison of mesh deformation between the finite element model and physical model was given. Strain contours induced in the model with sliding boundary interface between the brain and skull and with friction levels

of 0.07, 0.22, and 0.7 were given. The model showed significantly higher strains at the tip of the anatomic partition (presumably the falx).

More recently, DiMasi et al. (1991) developed a 3-D brain model to study diffuse axonal injury by assuming that DAI is related to brain strains. The model predicted shear and normal strains in the brain in response to head impact with an automotive A-pillar. Only a portion of the brain was modeled. It included the upper cerebral cortex with longitudinal fissure, which provided the distinctive sagittal and coronal geometric features and the surrounding dura including the falx. The dura and cortex were enclosed by a rigid skull to simulate direct-impact events with a padded and an unpadded A-pillar. Although the model could estimate brain strains in an impact event, it was insufficient to evaluate directional loading effects through simulated impacts simply because the skull was not modeled.

Mendis (1992) developed 3-D models of a baboon and a human head in an attempt to extrapolate animal data to the human.

A three-dimensional human head model simulating three-layer skull, cerebrospinal fluid, and brain was developed by Ruan et al. (1991b, 1992, 1994) to study in more detail the coup/contrecoup response in the brain. This model was validated against cadaveric intracranial pressure reported by Nahum et al. (1976, 1977). The model predicted higher skull stresses and negative intracranial pressures at the contrecoup site from occipital impacts than from frontal impacts. This finding afforded a biomechanical explanation of the clinical observation that occipital impacts cause more severe contrecoup injury than frontal impacts.

Also, the viscoelastic response of the human brain to impact has been investigated by Ruan et al. (1993a) using a 3-D finite element human head model. The model was developed based on their previous model (Ruan et al., 1992, 1994) by the addition of the scalp, dura mater, and falx partition. Model meshes were also refined in order to improve model accuracy. The viscoelastic behavior of the brain in shear was characterized by a short- and long-term shear modulus and a time decay factor. The values of these parameters were scaled from the literature (Galford and McElhaney, 1970). The study showed that the viscoelasticity of the brain had an insignificant effect on intracranial pressure. It also showed a complicated shear stress distribution in the brain. Unlike pressure, the shear stress time history did not follow that of the impact force. When the impact force was reduced to zero at the end of the pulse, the shear stress was not reduced. Using the same model, Ruan et al. (1993b) studied the human head response to different impacts (impact locations, impactor mass, and velocity) by having a rigid cylinder impact the head model directly. The study demonstrated the variation of human head response to different impacts, and the HIC (head injury criterion) was found to be generally proportional to the impact force, intracranial pressure, linear acceleration, and skull stress. The authors pointed out that the HIC appeared to be a reasonable index of injury severity in a direct-impact situation.

Zhou et al. (1994) developed a 3-D porcine finite element model and compared the dynamic response of this model with Ruan et al.'s human model. The porcine model showed a similar pressure and shear response to that of the human. A three-dimensional human head model including the skull, brain (white and gray matter), CSF, ventricles, falx cerebri, tentorium cerebelli, and bridging veins was proposed by Zhou et al. (1995). The new features of this model include differentiation of the white and gray matter of the brain and the modeling of the bridging veins. The authors found that higher shear stresses were produced in the white matter and hence DAI can occur in areas of high shear.

Summary

The state of the art in finite element modeling of head injury in the early 1980s was delineated by Khalil and Viano (1982). After that time, the development in finite element modeling of head impact was advanced by many authors. More recently, an extensive review of finite element modeling of head impact from the early 1980s to date has been conducted by Sauren and Claessens (1993). They pointed out that more realistic boundary conditions allowing relative motion between the brain and skull have been successfully achieved during the last decade, but the boundary conditions at the head-neck junction need further investigation. The utilization of nonlinear viscoelastic models was hampered by the lack of

TABLE 7.1 Brief Description of Finite Element Models

Authors	Geometry	Constitutive	Major Model Features
Shugar and Katona (1975)	Human (2-D)	Elastic Viscoelastic	Layered skull and brain of sagittal section of human head; localized shell strain and quadratic pressures gradient of the fluid were predicted by a sine-squared input load
Khalil and Hubbard (1977)	Axisymmetric (2-D)	Elastic Viscoelastic	Scalp, layered skull, and brain of axisymmetric model; localized shell strain and a linear pressures gradient of the fluid were predicted by a sine-squared input load
Pluche et al. (1985)	Human (2-D)	Elastic	Sagittal section of human head simulating skull, brain, and CSF; linear and angular acceleration, stresses/strains were output from many computer runs
Lee et al. (1987)	Monkey (2-D)	Elastic	Sagittal section of rhesus monkey head with rigid skull; input is the idealized acceleration of Abel (1978); shear strain is major output
Ueno et al. (1989)	Human (2-D)	Elastic	Sagittal section of human head; scaling law is applied to scale animal data to human
Cheng et al. (1990)	Cylinder (2-D)	Viscoelastic	Rigid cylinder filled with gel; simulate tests of U. of Pennsylvania with velocity input
Lee (1990)	Cylinder (2-D, 3-D)	Viscoelastic	Rigid cylinder filled with gel; simulate tests of U. of P. with nodal displacement input
Ruan et al. (1991)	Human (2-D)	Elastic	Coronal section of human head; impact force is input; modal analysis and parametric studies on neck boundary and the properties of the brain and skull were performed
Willinger et al. (1992)	Human (2-D)	Elastic	Sagittal section of human head; rigid skull with brain, modal analysis was performed
Chu et al. (1994)	Human (2-D)	Elastic	Sagittal section of human head; simulate Nahum's et al. test with displacement input
Zhou et al. (1994)	Porcine (2-D)	Elastic	Porcine brain and skull; simulate porcine test of U. of P.; shear stress was output

constitutive properties from experimental data. As a summary, Table 7.1 gives a brief description of the finite element models that can be found in the head injury research literature.

7.3 Overview of Explicit Finite Element Analysis

The explicit finite element techniques have been used for many years for crashworthiness analysis to simulate buckling and large deformation of physical structures. It is highly suited to solve impact types of problems. In the last decade, several commercial finite element codes have been introduced and are available for most users. The computations in this study were performed by a commercial code — PAMCRASH.

The finite element equations of motion in an explicit analysis are written as:

$$\mathbf{M}\mathbf{x} = \mathbf{f}^e - \mathbf{f}^i \tag{7.1}$$

where, **M** is the mass matrix, **x** is the acceleration matrix, $\mathbf{f}^e$ and $\mathbf{f}^i$ the nodal force matrices derived from external forces and the internal element resistances.

The solution of Eq. (7.1) is obtained by the central difference integration method:

$$x_{n+1/2} = x_{n-1/2} + \Delta t x \tag{7.2}$$

$$x_{n+1} = x_n + \Delta t x_{n+1/2} \tag{7.3}$$

TABLE 7.1 Brief Description of Finite Element Models (continued)

Authors	Geometry	Constitutive	Major Model Features
Ward and Thompson (1975)	Human (3-D)	Elastic	Rigid skull with brain, dura, and brain stem; pressure gradient in the brain was predicted with an acceleration pulse input, pressure was compared with cadaveric test
Ward et al. (1978)	Monkey (3-D)	Elastic	Rigid skull and brain of rhesus and baboon; pressure gradient was predicted with an acceleration pulse, different frequency response was found between human and animal
Shugar (1977)	Human, monkey (3-D)	Elastic	3-layer skull, subarachnoid space, and brain of human and rhesus heads; localized shell strain and nearly linear pressure gradient were predicted with a half sine loading
Hosey and Liu (1982)	Human (3-D)	Elastic	3-layer skull, dura, CSF, brain, spinal cord, and cervical column of human; pressure gradient in the fluid was predicted with a half sine loading input
Tong et al. (1989)	Cylinder (3-D)	Viscoelastic	Rigid cylinder filled with gel; simulate tests of U. of P. with prescribed nodal motion
Dimasi et al. (1991)	Human (3-D)	Viscoelastic	Two hemispheres with rigid skull; simulate human head impact to an A-pillar
Ruan et al. (1994)	Human (3-D)	Elastic	3-layer skull, brain, CSF, and facial bone; impact force from Nahum's test, pressure gradient was predicted, parametric studies on properties of the skull, brain & CSF
Mendis (1992)	Human, baboon (3-D)	Viscoelastic	Baboon model; simulate Gennarelli's (1982) tests, human model for injury criterion
Ruan et al. (1993)	Human (3-D)	Viscoelastic	Scalp, 3-layer skull, dura, flax, brain, CSF, and facial bone; simulate Nahum's et al. test, parametric studies on the impact severity of several impact conditions
Zhou et al. (1994)	Porcine (3-D)	Viscoelastic	Compare the response of porcine head model with Ruan's human head model
Ueno et al. (1995)	Ferret (3-D)	Elastic	Half ferret brain; simulate cortical impact test, stress in tissue level was output
Willinger et al. (1995)	Human (3-D)	Elastic	Skull, brain, CSF, falx of human head; modal analysis was performed

where, Δt is the time step, $\mathbf{x}_n$ and $\mathbf{x}_{n+1}$ are the displacements, and $\mathbf{x}_{n-1/2}$ and $\mathbf{x}_{n+1/2}$ are the velocities.

In the explicit codes, the stress tensors are actually calculated from the velocity gradient tensors because the strain rate is considered in the constitutive relations. The advantage of explicit methods is that they take much less computer time as they do not involve the solution of sets of coupled equations in order to obtain nodal accelerations. Their drawback is that they are conditionally stable. A very small time step is required. If the time step is too large, the solution will grow without bounds.

In an explicit analysis, time increments are very small (typically 100 to 1000 times smaller than in an implicit analysis), and the deformation takes place in a very small time interval; thus, small displacement approximations are justified during one time step. In an implicit analysis, however, the solution of nonlinear sets of equations requires iterations and convergence criteria, and the stiffness matrix needs to be inverted at every time step. This is time consuming, especially when the problem involves large systems. Since no matrix inversion is involved in the explicit method, a smaller portion of the computer memory is required than in the implicit method. Explicit analysis can trace a fast dynamic transient, but it cannot solve a static problem as an implicit analysis can. The disadvantage with explicit methods (smaller time step requirement) becomes insignificant in crashworthiness simulation due to the short duration of the crash.

7.4 Finite Element Modeling of The Human Head

Basic Consideration

The impact response of the head depends on its geometry, loading conditions, mass distribution, and material properties. Therefore, a working finite element model of the head should have the correct geometry and appropriate material properties to successfully simulate the dynamic events of a head impact. Unfortunately, the complex head structures, the irregular geometry of the brain, the virtually unknown material properties of the brain, and the many loading conditions make the modeling of the head a very challenging task. Therefore, simplification in head geometry and idealization in the constitutive relationship of head tissues have been made which compromise the accuracy and objectivity of the models.

Mechanical Structures of the Head

The head consists of the scalp, skull, meninges, cerebrospinal fluid (CSF), brain tissue, and blood vessels. The brain is enclosed in the cranial cavity, which consists of the cranial bones. The brain floats within the cranial cavity in the CSF. The skull is covered by the scalp. The cerebral membranes coat the inner surface of the cranial cavity and the brain.

The scalp helps absorb and distribute external traumatic forces and facilitates the slip-off of tangential impacts to the head. The thickness of the scalp ranges from 5 to 7 mm. The scalp is usually modeled by elastic membrane elements. To better account for contact mechanics, it can be modeled by viscoelastic solid elements in impact areas.

The skull is the main structure supporting and protecting the brain. Its thickness varies from 4 to 7 mm at different locations to snugly accommodate the brain to provide reinforcement of the cranium. The somewhat spheroidal shape of the cranium allows it to provide maximum protection against the indentations produced by external impacts with the minimum of structural mass or substance. The length and breadth of a male adult cranium are about 198 mm and 156 mm, respectively, and the intracranial volume is between 1400 and 1500 ml. To better depict the impact response, the skull should be modeled as a three-layered structure consisting of the inner and outer tables of compact bones on either side of the diploe or cancellous bone. The skull is usually treated as an elastic material.

The three membranes known as the meninges envelope the brain and the spinal cord. The outer layer is the dura mater and the inner is the pia mater; the arachnoid is located between the two. The dura mater is a tough, fibrous membrane with a thickness of about 1 mm. The falx cerebri, a fold of the dura mater that projects into the longitudinal fissure, and the tentorium cerebelli, a fold of the dura mater forming a shelf supporting the posterior cerebral hemispheres, divide the cranial cavity into three compartments, adding considerable support to the brain in various motions of the head. The meninges can be modeled by elastic or viscoelastic membrane elements.

The subarachnoid space and the ventricles of the brain are filled with the cerebrospinal fluid (CSF). The CSF provides a special environment in which the brain floats, cushioning it against hard blows and sudden movements. The volume of the CSF is about 140 ml. The specific gravity of the CSF is about 1.008 in the adult. The CSF is modeled by solid elements with a very low shear modulus and a high bulk modulus to simulate incompressibility. Note that higher shear modulus should be used for the CSF layer covering the outer surface of the brain to account for the trabeculae connecting the arachnoid and pia mater.

The brain can be divided structurally and functionally into five parts: cerebrum, cerebellum, midbrain, pons, and medulla oblongata. Inside the brain there are four ventricles: two lateral ventricles, the third ventricle, and the fourth ventricle. The average length of the brain is about 165 mm and its greatest transverse diameter is about 140 mm. Because of size differences, its average weight is 1.36 kg for the male and a little less for the female. The specific gravity of the brain averages 1.036. The distinct structural features of the brain are its inhomogeneity and irregularity. The cortex is made up of a layer of gray matter with an average thickness of 2.5 mm. The subcortical white matter is composed of vast numbers

of fibers that interconnect various cortical areas and project to and from the brain stem and spinal cord. The brain was treated as an incompressible fluid in early continuum models and as near incompressible, homogeneous elastic/viscoelastic solids in finite element models until 1994. Recent modeling efforts have shown that the differentiation in material properties between the gray and white matter in a finite element model of the brain improves model prediction of diffuse axonal injury (DAI) location.

The bridging veins are the terminations of the superficial cortical veins. They cross the subdural space and empty into the dural venous sinuses. Therefore, they are particularly prone to injury, producing subdural hematomas. The parasagittal bridging veins are composed of the veins that drain into the superior sagittal sinus. There is usually a free segment of vein, 10 to 20 mm in length, in the subdural space between the vein's exit from its bed in the subarachnoid space and its entrance into the sinus. The bridging veins can be modeled by elastic/viscoelastic string elements.

Material Properties

Most of the experimental data on material properties of the head tissues were obtained during the period of 1968 to 1971 and were reviewed by Goldsmith (1972). The greatest amount of information has been obtained for the skull (Haynes et al., 1969; Hubbard, 1971; McElhaney et al., 1970; Melvin et al., 1970a,b; Robbins and Wood, 1969; Roberts and Melvin, 1969; Wood, 1971) because its mechanical properties are similar to those of conventional engineering materials and can be easily measured by standard test apparatus and routines. Material properties of the brain tissues are difficult to measure. Considerable experimental studies have been done in the measurement of material properties of the brain (McElhaney et al., 1969; Estes and McElhaney, 1970; Fallenstein et al., 1969; Galford and McElhaney, 1970; Mertz et al., 1970; Shuck et al., 1970; Shuck and Advani, 1972; Arbogast et al., 1995). However, the considerable variation in the test data shows that the material properties of the brain have not been finally established.

It is well recognized that biological tissues are inhomogeneous, anisotropic, and nonlinear. Yet, approximations have been made for the sake of model development. Finite element head models are generally based on small deformations of elastic or viscoelastic materials. In addition, linearity, homogeneity, and isotropy are assumed. The material constants selected for the head models should be considered as approximate values with some limitations on their use. Since effective constants for high strain rate events have not been determined, parametric studies have been conducted to determine which material constants can provide the best correlations with cadaveric test data.

In finite element model testing, Khalil and Hubbard (1977) noted that skull strains and intracranial pressures depended slightly on the flexural properties of the skull when membrane stiffness was held constant. Variations in the skull elastic modulus produced a significant inverse effect in skull strains and a slight effect on intracranial pressure. Ruan et al. (1991a) pointed out that the spatial distribution of intracranial pressures are affected by Young's modulus and the thickness of the skull, and that the zero-point pressure can move along the impact axis as a function of the skull stiffness. Ruan et al (1994) also found that the skull von Mises stress increased as Young's modulus of the skull increased. The positive pressure in the brain decreased and its absolute negative pressure increased as skull stiffness increased to 10 times its base value.

Studies have shown that brain response is more sensitive to changes in Poisson's ratio (ν) than to changes in Young's modulus (E). Ward et al. (1980) found that an appropriate value for ν seemed to depend on the head acceleration pulse duration: the shorter the acceleration pulse, the higher the value for ν. When the acceleration pulse durations were less than 2.5 ms, a ν of 0.499 for the human and 0.4999 for the monkey gave the best results. When the duration was 6.5 to 8 ms, a ν of 0.49 for the human and 0.499 for the monkey were the best. Between 2.5 and 6.5 ms the value of ν varied linearly. For longer pulse durations of more than 8 ms, a ν of 0.48 for the human gave good results. Khalil and Hubbard (1977) also pointed out that variations in Poison's ratio significantly affected intracranial pressure. Ruan et al. (1994) showed that positive intracranial pressure increased and absolute negative intracranial pressure decreased when the bulk modulus was increased. They concluded that a reasonable bulk modulus for the brain and CSF should be between 2.19 to 219 MPa.

TABLE 7.2 Material Properties Used in Linear Elastic Head Models

Ref.	Compact Bone			Spongy Bone			Brain				
	ρ	E	n	ρ	E	n	ρ	E	n	K	G
Shugar (1975)	1.43	13.8	0.25	0.143	1.38	0.25	0.672	0.0103	0.5	2.1	3.45
Shugar (1977)	1.4	5.66 12.28	0.22				1.04			2.19	
Ward (1975)							1.04	0.0667	0.48		
Ward (1982)		4.46	0.21					0.650	0.48-0.499		
Khalil and Hubbard (1977)	3.0	17.94	0.35	1.7	0.725	0.05				2.19	
Hosey and Liu (1982)	1.41	4.46	0.21				1.04	0.0667	0.499		
Lee et al. (1987)							1.0		0.49		80.0
Chu (1991)	2.027	6.5	0.2				1.0	0.250	0.49		
Ruan (1991a)	1.41	6.5	0.22				1.04	0.0667	0.48-0.4999		
Ruan (1991b)	3.0	12.2	0.22	1.75	5.66	0.22				2.19	1680
Trosseille et al. (1992)							1.0	0.240	0.49-0.499		
Willinger et al. (1992)		5.0	0.2					0.675	0.48		

ρ = density (ton/m^3); E = Young's modulus (GPa); ν = Poisson's ratio; K = bulk modulus (GPa); G = shear modulus (kPa).

TABLE 7.3 Material Properties of the Brain Used in Linear Viscoelastic Models

Ref.	G_∞ (kPa)	G_0 (kPa)	β (1/s)	K (MPa)
Khalil and Viano (1977)	16.2	49.0	145	
Galbraith and Tong (1988) (gel)	5.512	11.02	200	
Cheng et al. (1990) (gel)	7.51	35-70	50-300	
Lee (1990) (gel)	2.87-18	26.9-110	50	1.25-5.44
DiMasi et al. (1991)	17.237	34.474	100	68.948
Ruan (1994)	168	528	35	2.19

G_∞ = long term shear modulus; G_0 = short term shear modulus; β =decay factor; K = bulk modulus.

Material properties used in the linear elastic head models are summarized in Table 7.2 and those for the linear viscoelastic head models are listed in Table 7.3.

Mesh Generation

The finite element mesh of a model significantly influences the accuracy of model results. The first important thing to do is to keep the geometric representation as close as possible to the original structure. Care must be taken to ensure that the mesh is fine enough, with elements distributed in a proper manner.

The geometry of the head can be obtained using images from X-rays, CT scans, and MR scans. With the development of computer imaging techniques, it is expected that the accuracy of head geometry data will continue to improve.

The order of model development is as follows: head injury model -version 93, head injury model — version 94, and brain injury model — version 95. The geometries of these models were taken from an atlas of sectional anatomy of the head and photographs of brain slices made at the Bioengineering Center. The mesh was generated with the aid of preprocessor code, such as MENTAT, PATRAN, HYPERMESH.

The process of mesh generation of three-dimensional models was painstaking and time consuming. Coronal and transverse sections of the brain were digitized point by point manually and the profile points were then used as starting points to generate boundary lines that divide different structural components

of the section. Each section was then meshed with surface elements, and then elements between any two neighboring sections were generated by connecting corresponding points. Difficulty was encountered when the structure of two connecting sections changed abruptly. It was very hard to find a way to generate elements between those sections, and the boundaries between the gray and white matter changed greatly from section to section. It was actually impossible to keep to the original boundaries in the model.

The mesh was first generated in the more regular transverse sections of the middle part of the brain, then on the top and the coronal sections of the frontal and basal area, followed by the mesh in the coronal sections of the occipital region. The most difficult part to mesh was the brainstem region because of the presence of the foramen magnum. The brain was modeled with 6-node and 8-node elements with one point quadrature. The brain was covered with a membrane element layer representing the pia mater and a solid element layer representing the CSF. The tentorium separated the cerebrum and cerebellum and there was a layer of CSF between the two. The scalp, modeled by a layer of shell elements, 6 mm thick, covered the cranial bones. In the head injury model, the dura covered the entire inner surface of the inner table except at three sinus areas where the two layers of dura (endosteal layer and meningeal layer) separate: the endosteal layer continues on the interior surface of the inner table while the meningeal layer joins with its counterpart coming from the other side of the skull to form the falx cerebri and tentorium cerebelli. In the brain injury model, the dura on the inner surface of the skull was considered as part of the inner table to reduce element numbers; only the dural separations at the sinuses and fissures were modeled. The dura mater was modeled as membrane elements.

The skull was modeled by three-layered, 8-node solid elements in the head injury models. To save computer time, the skull in the brain injury model was modeled as a single layer of solid elements with an effective material property. The facial bones were modeled with solid elements in the head injury models and with shell elements in the brain injury model. They were given an overall shape and an approximate mass of the face.

The bridging veins were not included in the head injury model. However, in the brain injury model, ten pairs of parasagittal bridging veins were modeled with string elements that can only sustain a tensile load.

Head Injury Model — Version 93

This three-dimensional finite element human head model was developed by Ruan et al. (1993a, b). It included the scalp, three-layered skull, cerebrospinal fluid (CSF), dura mater, falx cerebri, and brain. It contained 6080 nodes and 7351 elements, with 1760 for the brain, 2800 for the skull, 896 for the CSF, 864 for the scalp, 896 for the dura mater, and 135 for the falx cerebri. It simulated a 50th percentile male human head. The total mass of this model was 3.077 kg with 1.25 kg contributed by the intracranial contents. The material properties of this model were assumed to be homogeneous, isotropic, and linearly elastic/viscoelastic. Their values were found from the literature. Model validation was accomplished by simulating a cadaveric test conducted by Nahum et al. (1976, 1977). Computed pressures at five locations in the brain were compared to test data. The model was used to study the dynamic response of the human head to a direct impact (Ruan et al., 1993a). The effects of the viscoelasticity of the brain on intracranial response were also studied (Ruan et al., 1993b).

Head Injury Model — Version 94

This model was an improvement of the previous version and was completed by Ruan in 1994. The outside geometry of the skull was not changed. However, the intracranial contents were remeshed by adding several sinuses, falx cerebri, and cerebral tentorium. A simple neck to extend the brainstem to the spinal cord was also included in this model. Figure 7.1 is the midsagittal sectional view of the model. Figure 7.2 shows that the brain is divided by a longitudinal fissure and a transverse fissure into left and right hemispheres and the cerebellum. The neck and spinal cord were extended to C-7. The head model consisted of 7205 nodal points and 9146 elements. Its total mass was 5.059 kg (the average male head mass is 4.55 kg without the neck). There was no sliding interface between model components. Blood vessels and bridging veins were not included in this model. Table 7.4 lists the element type, number of

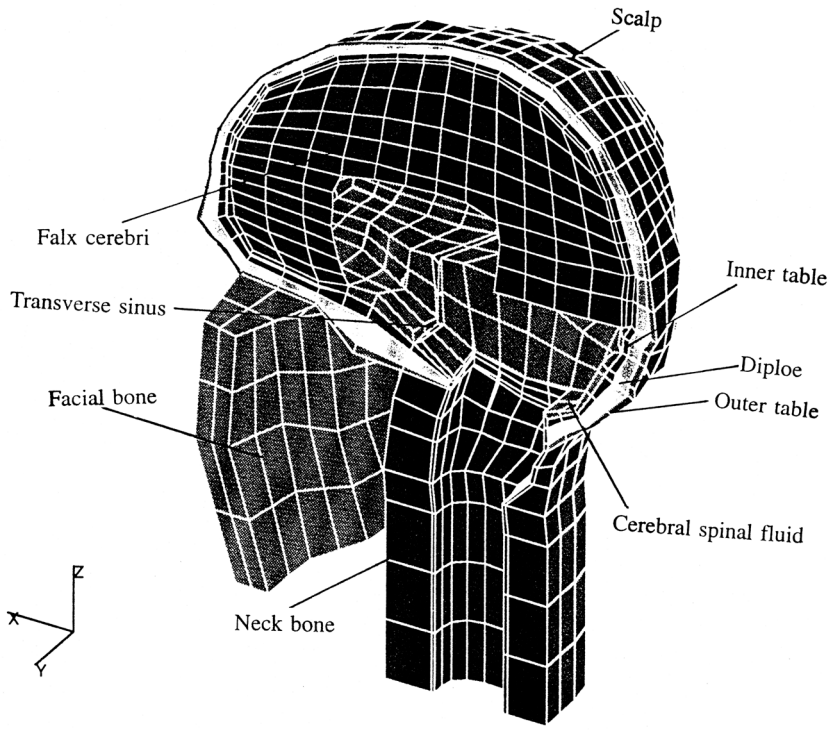

FIGURE 7.1 Finite element human head model — midsagittal view. The intracranial contents such as hemispheres and cerebellums, sinuses, fissures, brain stem, and cervical cord were removed.

elements, and mass for each anatomical component of the head model. Table 7.5 lists material properties used in this model. Figure 7.3 shows the impact configurations of this human head model. The results of these impact conditions will be discussed later.

This model was also validated against pressure data measured by Nahum et al. (1977). An impact from a cylinder with a mass of 5.23 kg and an initial velocity of 6.33 m/s was delivered to the model in the frontal bone in the midsagittal plane in an anterior-posterior direction as in Nahum et al.'s (1977) tests. The pressures measured were those in the frontal lobe adjacent to the impact area (coup), immediately posterior and superior to the coronal and squamosal suture, respectively, in the parietal bone, inferior to the lambdoidal suture in the occipital bone (one in each side), and at the posterior fossa in the occipital bone (contrecoup). The model closely duplicated the impact force of the test, as shown in Fig. 7.4. Pressures predicted by the model matched the experimental data well, as shown in Fig. 7.5. More data comparisons between model predictions and experiment results can be found in Ruan (1994).

Brain Injury Model — Version 95

This model was developed by Zhou et al. in 1995. As shown in Fig. 7.6, it consisted of the scalp, skull, dura, falx, tentorium, pia, CSF, venous sinuses, ventricles, cerebrum (gray and white matter), cerebellum, brainstem, and bridging veins. The overall geometry of the model represented a 50th percentile male human head. The head consisted of 17,656 nodes and 22,995 elements. Its total mass was 4.37 kg with the brain being 1.41 kg. Details of the model can be found in Zhou (1995).

One of the distinctive features of the model is the differentiation of the gray and white matter. The irregular boundaries between the gray and white matter were simulated in the model, but were greatly simplified. Different material properties were used for the gray and white matter. The inhomogeneous nature of the brain can be better simulated with these geometrical and constitutive descriptions.

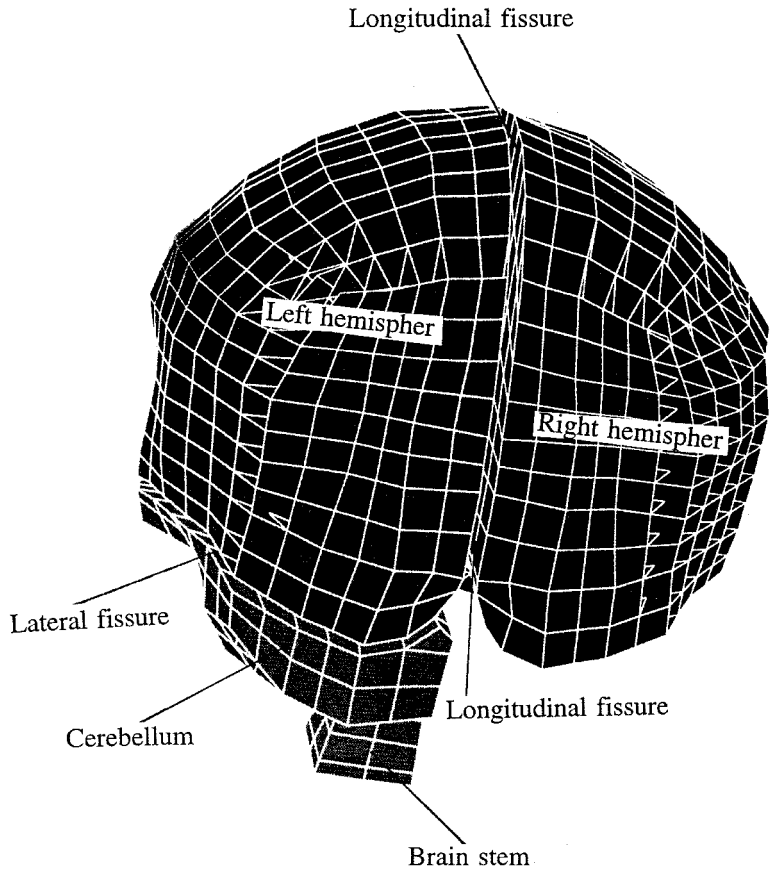

FIGURE 7.2 Cerebral hemispheres, fissures, and brain stem. The sinuses were located along the fissures between the dura and the fissures and provided a path for the cerebral spinal fluid.

TABLE 7.4 Finite Element Components of the Head Model

Head Tissue	Number of Element	Element Type	Mass (kg)
Skull (3 layers)	2554	Solid	1.754
Brain and spinal cord	1928	Solid	1.42
Cerebral spinal fluid	1235	Solid	0.183
Dura mater	1010	Membrane	0.123
Falx cerebri	286	Membrane	0.022
Tentorium cerebelli	300	Membrane	0.021
Scalp	1111	Shell	0.53
Sinus and fissure	342	Solid	0.056
Neck bone	140	Solid	0.49
Facial bone	240	Solid	0.46

Another new feature is the inclusion of the ventricles in the model. The corners of the ventricles are common sites of diffuse axonal injury (DAI). Without ventricular representation in the model, stress concentrations around ventricles could not be produced in our previous study (Zhou et al., 1994).

A third new feature is the modeling of ten pairs of parasagittal bridging veins with string elements. It was the first attempt to simulate bridging veins in a human head finite element model. With these bridging veins, their impact response can be analyzed and the mechanisms of subdural hematoma can be investigated by computer modeling.

TABLE 7.5 Material Property of the Head Tissues

Head Tissue	Bulk Modulus (Pa)	Shear Modulus (Pa)	Density (kg/m3)	Poisson Ratio
Outer table	3.26×10^9	2.24×10^9	3.00	0.22
Inner table	3.26×10^9	2.24×10^9	3.00	0.22
Diploe	1.75×10^9	1.10×10^9	1.75	0.24
Facial bone	3.26×10^9	2.24×10^9	3.00	0.22
Neck bone	1.75×10^9	1.10×10^9	1.75	0.24
Brain	2.19×10^9	5.28×10^5 (short) 1.68×10^5 (long)	1.04	0.49996
CSF	2.19×10^7	5.0×10^5	1.04	0.4887
Dura mater[a]	3.15×10^7		1.133	0.45
Falx[a]	3.15×10^7		1.133	0.45
Tentorium[a]	3.15×10^7		1.133	0.45
Scalp[a]	1.67×10^7		1.20	0.42

[a]Young's Modulus replace bulk and shear for shell and membrane elements.

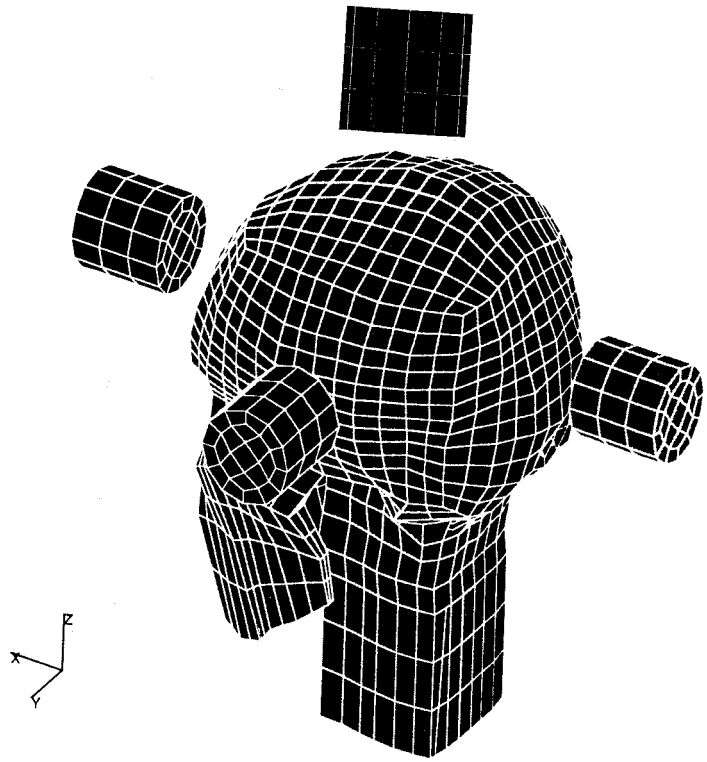

FIGURE 7.3 Impact configuration of the head model.

Material properties for the model were reported in Zhou et al. (1995). Most of them were the same as those for Ruan's model except that different material properties were used for the gray and white matter. In this study, viscoelastic material properties were used for the brain:

$$G_0 = 41 \text{ kPa}, G_\infty = 7.6 \text{ kPa}, \beta = 700 \text{ s}^{-1} \text{ for white matter,}$$

$$G_0 = 34 \text{ kPa}, G_\infty = 6.3 \text{ kPa}, \beta = 700 \text{ s}^{-1} \text{ for gray matter}$$

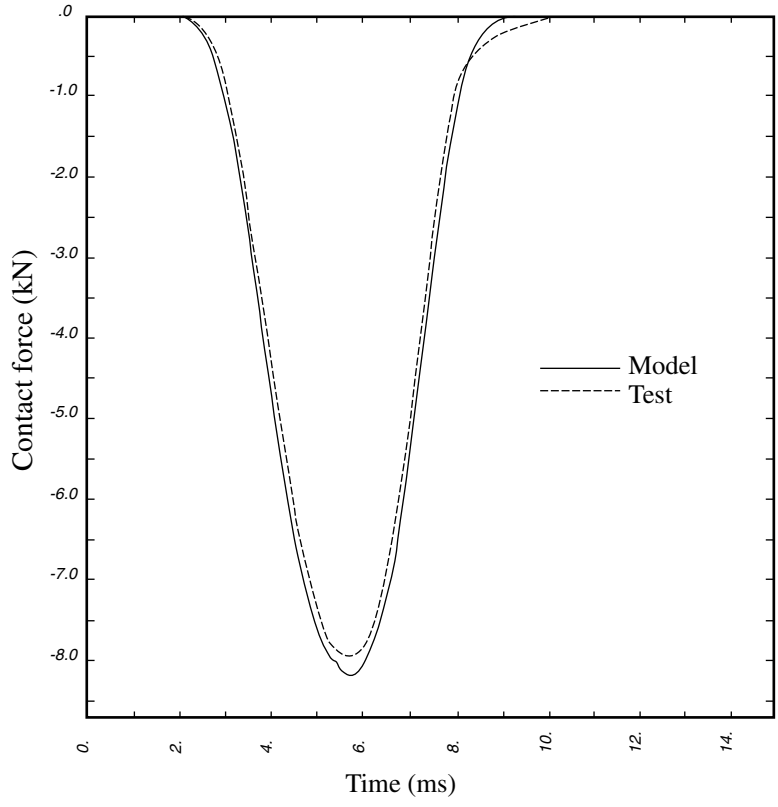

FIGURE 7.4 Impact force comparisons — frontal impact.

where G_0 is the short-term shear modulus, G_∞ is the long-term shear modulus, and β is decay factor. The shear relaxation behavior is described by:

$$G(t) = G_\infty + (G_0 + G_\infty)e\text{-}\beta t \tag{7.4}$$

We assumed that the white and gray matter had the same decay factor but that the shear modulus of the white matter was higher than that of the gray matter. The only justification for this assumption is that white matter should be stronger and tougher because it is composed of axonal fibers and gray matter is composed of nerve cell bodies. A bulk modulus (K) of 2.19 GPa was used for both materials.

The frontal impact simulating the test condition described by Nahum et al. (1977) was used to validate the inhomogeneous brain model. The impact contact force is shown in Fig. 7.7. Experimental data by Nahum et al. (1977), shown in Fig 7.7, were left-shifted 2 ms to align the peaks. The peak impact force was 7.90 kN for the test and 7.92 kN for the model, occurring at around 3 ms. Figure 7.8 is a comparison of coup/contrecoup pressure between model and experiment. The peak coup pressure was 144 kPa for the test and 149 kPa for the model, and the corresponding peak contrecoup pressures were –53 kPa and –64 kPa. The higher pressures predicted by the model could be due to the slight differences in impact force and the lack of precise information regarding the exact location of the pressure transducers used. Pressure gradients were high at the coup/contrecoup sites. Despite these variations, the model predicted coup/contrecoup pressure time histories that roughly matched those obtained experimentally. This is by no means a full validation of the model but we have compared the model against available data.

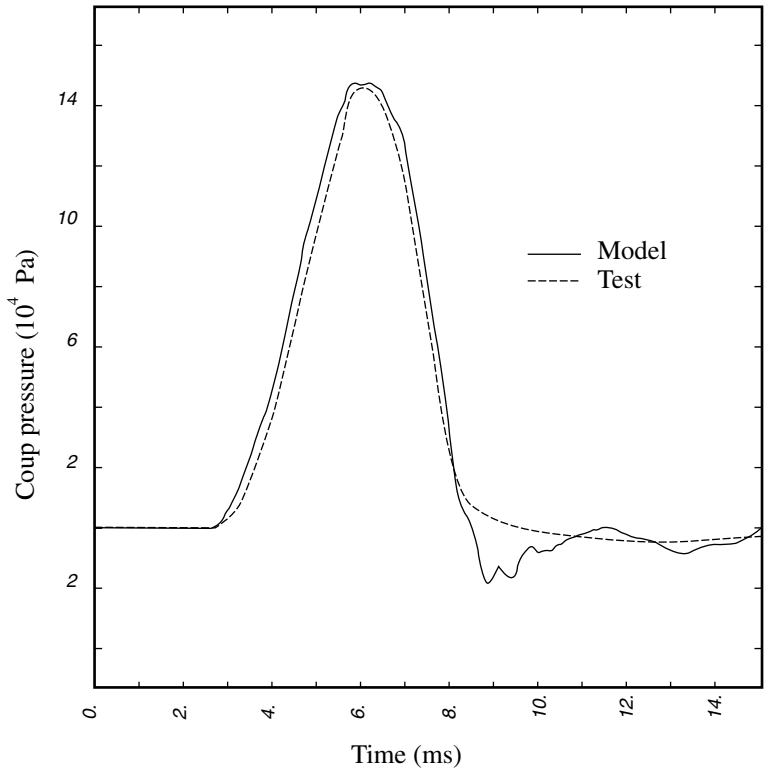

FIGURE 7.5 Coup pressure comparisons — frontal impact.

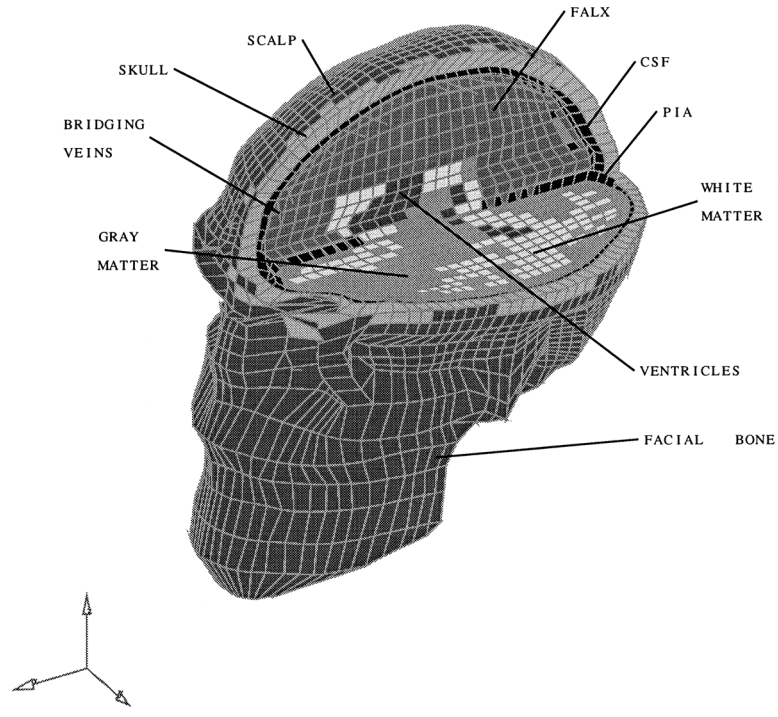

FIGURE 7.6 The 3-D human brain model V95: overview.

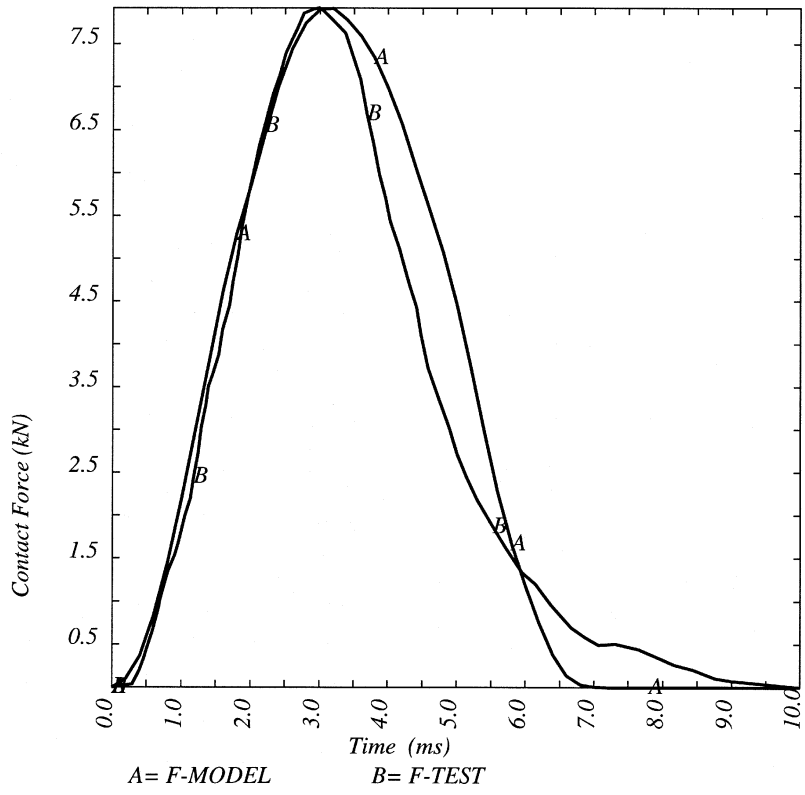

FIGURE 7.7 Validation of the human brain model V95: comparison of impact force.

7.5 Simulation Results and Discussion

Physically, when the head is struck by an external force the skull deforms and a state of stress/strain is induced throughout the head. If the stress in the skull exceeds its strength, fracture of the skull may occur and brain damage can result due to the fracture. Brain tissue can also be damaged due to a sudden skull-brain translational and/or rotational impulse even though the skull is not fractured or deformed. Under a direct impact condition, pressure is generated in the brain near the impact site and tensile stress is generated at the opposite site of the impact. As a result of the transit of the pressure waves, zero pressure will occur within the impacted medium. On the other hand, consider a closed cylindrical tube filled with an incompressible fluid and impacted by a force. The fluid will be accelerated by pressure from the impacted end of the tube resulting in tension at the opposite end of the tube. For a deformable body, the zero-pressure point can be located at any point along the axis of impact depending on the stiffness of the system and material properties of the medium (Kopecky and Ripperger, 1969; Ruan et al., 1991a). Brain trauma can result from large changes in intracranial pressures and from the tensile and shear strains. Shear strain is also considered as being responsible for diffuse axonal injury (DAI) due to the shearing effect of the neural tissues (Strich, 1956, 1961). Both positive and negative shearing are equally important for DAI, unlike intracranial pressure, for which the negative pressure is considered to be more injurious than the positive one. In the following discussion, we will use intracranial pressure, skull von Mises stress and tensile strain, and intracranial tensile and shear strains as parameters to quantify model predictions and to measure the severity of the impact. Intracranial pressure and skull von Mises stress are defined by:

$$p = 1/3(\sigma_1 + \sigma_2 + \sigma_3) \tag{7.5}$$

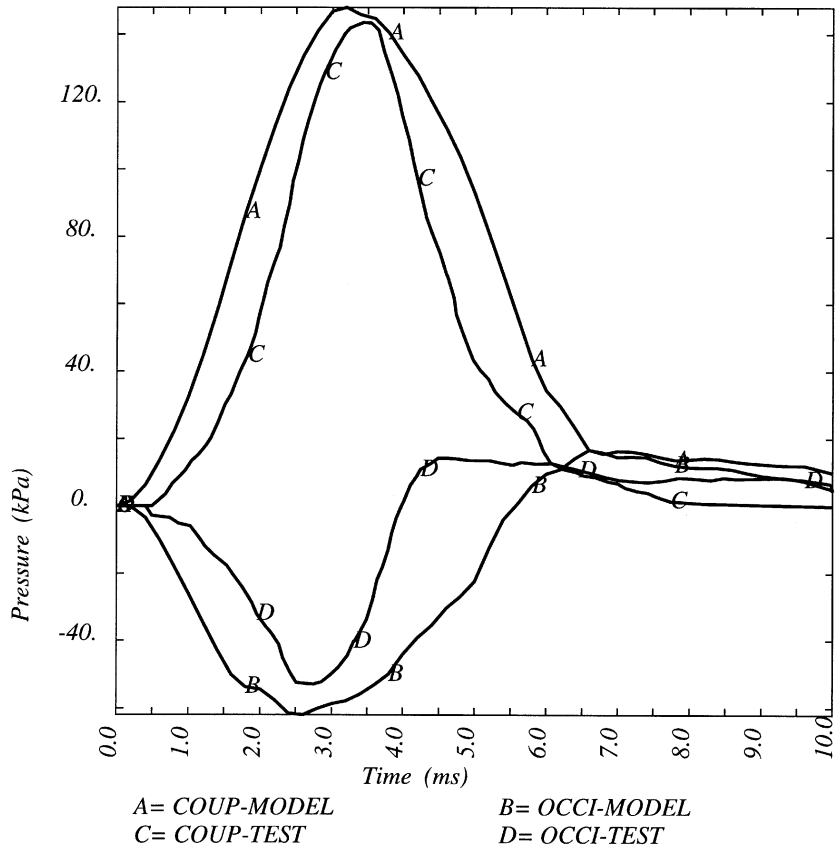

FIGURE 7.8 Validation of the human brain model V95: comparison of coup/contrecoup pressures.

(7.6)

where p is the pressure in the brain, σ is skull von Mises stress, σ_1 i = 1, 2, 3 are the principal stresses.

Intracranial tensile strains in the x, y, and z directions are ε_x, ε_y, and ε_z. Intracranial shear strain is defined by τ_{max}, the maximum shear strain.

In the following, the head injury model — version 94 was used to investigate head impact responses to the direct frontal, occipital, side and crown impact by a cylinder. The head injury model — version 93 was used to simulate a head-to-tested A-pillar impact. The brain injury model — version 95 was used to study brain responses to a sagittal angular acceleration of the head.

Frontal Impact

After model validation, a parametric study for frontal impact was performed using head injury model — version 94. It consisted of simulations involving variations in impactor mass and velocity. The impactor mass and velocity were reduced by 25% and 50%, respectively, while maintaining the original shape, to study their effects on the intracranial response. The time history of contact forces, coup-contrecoup pressures, maximum brain shear stresses, and head accelerations were plotted but only contact forces and the coup-contrecoup pressures are shown in Figs. 7.9 and 7.10. In these figures, a 25% reduction in mass is denoted by a solid line, a 50% reduction in mass by a dotted line, a 25% reduction in velocity by a solid-dotted line, and a 50% reduction in velocity by a dashed line.

In comparison with the baseline simulation in frontal impact, the impact force was reduced by about 5% when the impactor mass was reduced by 25%, and by about 15% when the impactor mass was

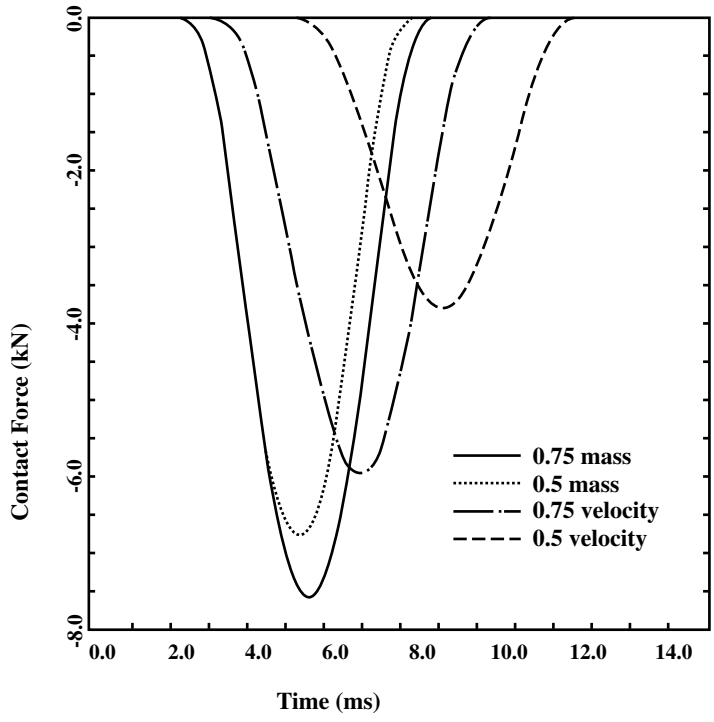

FIGURE 7.9 Impact force in frontal impacts.

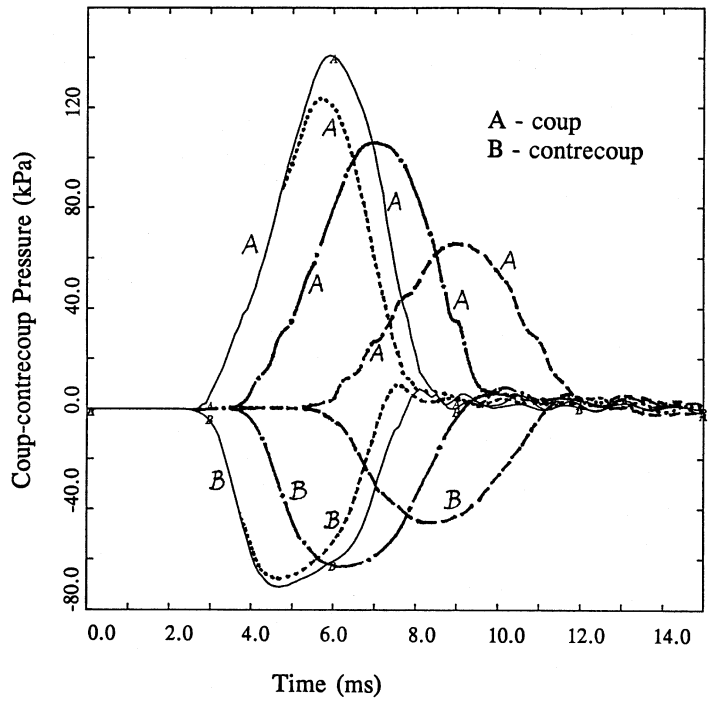

FIGURE 7.10 Coup-contrecoup pressure in frontal impacts.

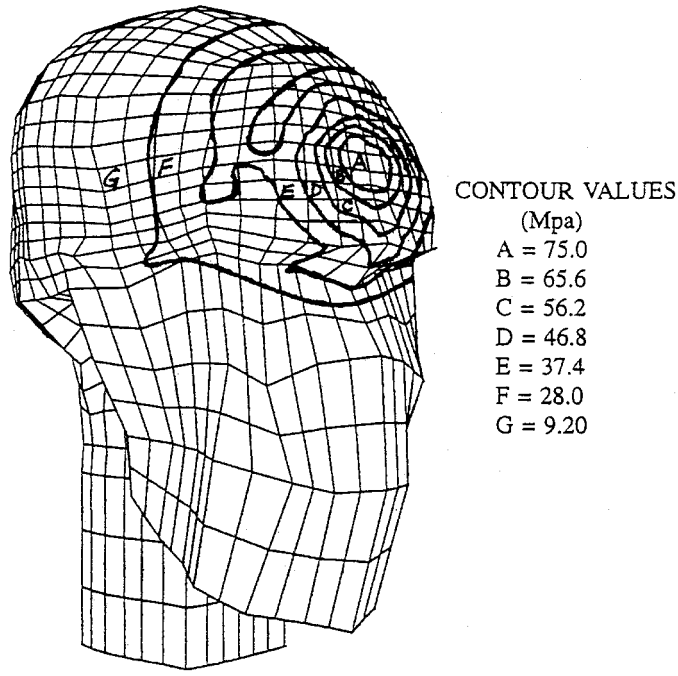

FIGURE 7.11 Skull von Mises stress contour at 6 ms — frontal impact.

reduced by 50%. The impact force was lowered by about 25% when the impactor velocity was reduced by 25%, and by about 53% when the impactor velocity was reduced by 50%. The effect of impactor mass on head response was not as large as that of impactor velocity. This is understandable because impactor energy varies linearly with impactor mass, but varies with the square of impactor velocity. Coup pressure, maximum shear stress, and head acceleration showed the same reduction as impact force when impactor mass and velocity were reduced. However, contrecoup pressure did not seem to follow the same trend. When the impactor mass or velocity was reduced by 25%, contrecoup pressures did not change as much (Fig. 7.10) as the impact force, maximum intracranial shear, and head acceleration. Impactor velocity reduction resulted in a larger increase in impact duration than did a reduction in impactor mass. Since head response is more sensitive to impact velocity, in the design of a head protection device, controlling the impact velocity is more important than impact mass.

Contour plots for skull von Mises stress, intracranial pressure, and tensile and shear strains from the baseline model of frontal impact (used for model validation) are shown in Figs. 7.11 through 7.14. Significant skull von Mises stress is localized in the impact area. It decays quickly from the impact point throughout the rest of the skull, indicating dominant bending stresses. The skull can be fractured if these stresses exceed the tolerance of the cranium bone. Segments of fractured skull could lacerate the brain and cause contusion (Gurdjian and Gurdjian, 1976). Skull tensile strain contours (not shown) indicated that large strains were found at the base of the frontal bone near the ethmoid bone. In clinical observations, skull fracture is frequently found in these areas (Gurdjian, 1975).

Intracranial pressure was uniformly distributed across the brain (side to side), except at the dural separations between the hemispheres and the cerebellum, with compression at the impact point and tension at a point opposite to the impact, as shown in Fig. 7.12. Pressure distribution was disrupted by the falx and tentorium at these areas.

Figure 7.13 shows spatial distributions of tensile strain (ε_x) in an anterior-posterior direction. As shown in this figure, compressive strain is seen at the impact site and tensile strain at the contrecoup site. The maximum compressive strain (4.5%) was located in the basal area of the frontal lobe. Large tensile strains (ε_x) were also seen in the brainstem. Since the longitudinal fissures were included in the model and they

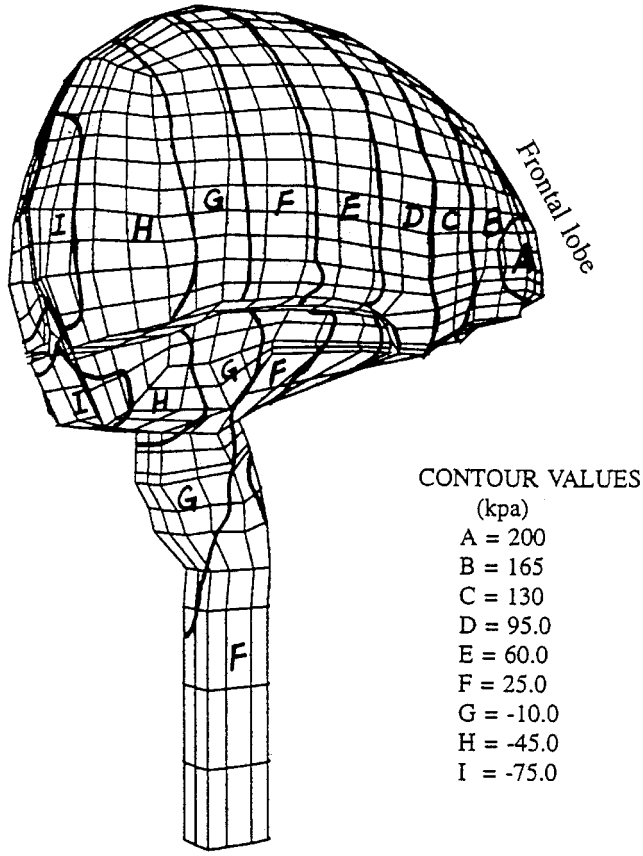

FIGURE 7.12 Intracranial pressure contour in frontal impact.

were filled with CSF, cerebral deformation was more easily transmitted to the corpus callosum through these fissures, resulting in compressive strains (ε_x) of over 4% in the corpus callosum. The contour of brain strain ε_y (not shown) from frontal impact showed that the brain, including the corpus callosum, was pulled away from the falx which was at the center line of impact. Maximum tensile strain ε_y (4%) was located in the frontal lobe in the white matter and in the corpus callosum. The strain contour for ε_z was also localized in the impact area and showed that the white matter was stretched in a superior-inferior direction. The principal shear strain (τ_{max}) contour is shown in Fig. 7.14. The highest principal shear strain (4.5%) was located close to the white matter and corpus callosum. Note that the second largest principal shear strain (3%) also occurred at the dorsolateral part of the rostral brainstem.

It has long been hypothesized that strain is the mechanism of concussion and diffuse axonal injury (DAI). These strains can cause diffuse injury of the white matter (Strich, 1956, 1961) and stretch the axonal nerve system, since DAI is sustained at the moment of injury and not a secondary event (Adams et al., 1982), and it was also produced in a laboratory animal subjected to direct impact (Lighthall et al., 1990).

High tensile and shear strains were predicted at both the corpus callosum and the dorsolateral area of rostral brainstem. These strains may be responsible for diffuse axonal injury, if strain is indeed a mechanism of DAI. It has been reported in the head injury literature that DAI was characterized by the presence of foci of hemorrhage in the corpus callosum and in the dorsolateral area of rostral brainstem (Adams et al., 1977, 1982, 1983; Gennarelli et al., 1982). Evidence of axonal injury has been found by Pilz (1983) in a study of 324 cases that the corpus callosum was involved in 79%, and the brainstem in over 80% (internal capsule in 89%, midbrain in 76%, pons in 92%). The model predictions in this study

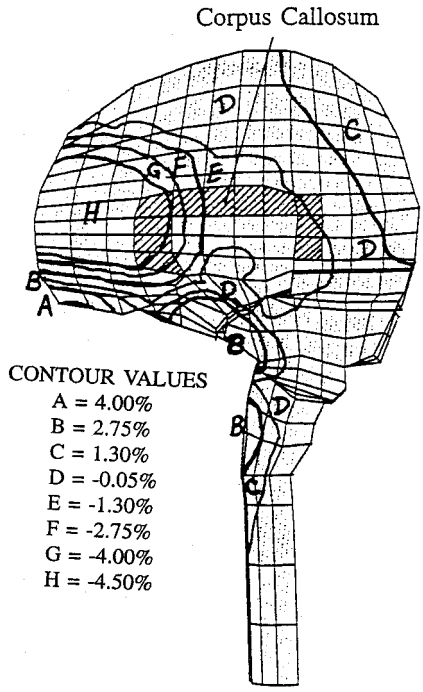

FIGURE 7.13 Brain tensile strain (ε_x) contour at 6 ms — frontal impact.

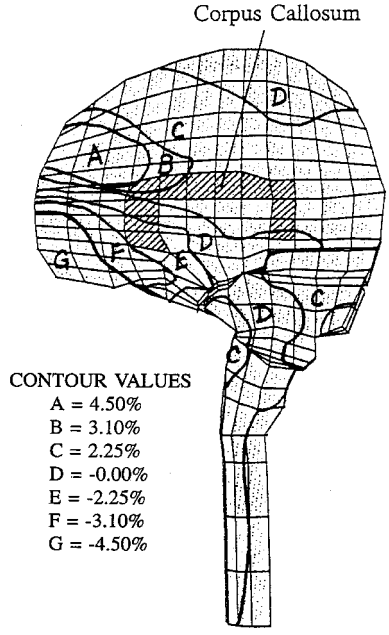

FIGURE 7.14 Brain principal shear strain contour at 6 ms — frontal impact.

support these findings. Since DAI has also been found in ferret brain exposed to direct impact (Lighthall, 1988; Lighthall et al., 1990), the mechanism of DAI should also take into account the direct impact effects.

Occipital Impact

To simulate an occipital impact, the cylinder was positioned to impact the head in the occipital region using head injury model — version 94. The impact direction was from posterior to anterior in the

midsagittal plane and the impact was delivered to the scalp at the occipital bone. The impactor mass and velocity were the same as in the baseline frontal impact. The impact force and acceleration responses from occipital impact were essentially similar in shape to those obtained from frontal impact and are, therefore, not shown. Intracranial pressure (also not shown) was varied linearly as positive pressure at the coup site (occipital lobe) to negative pressure at the contrecoup site (frontal lobe), except at the falx/tentorium partition area, where the pressure was disrupted by these partitions. Peak negative pressure was generated at the frontal lobe near the base toward the anterior skull. The brain in this area can be lacerated by the tensile stress and sustain a contrecoup contusion. Coup-contrecoup pressure time histories followed the impact pulse, reaching a peak magnitude at 5 ms. However, shear stress (not shown) did not follow the impact pulse. This was also true in the frontal impact case (see Ruan et al., 1993b). Skull von Mises stress and tensile strain, ε_x, (both not shown) were localized in the impact area and decayed quickly from the impact point throughout the rest of the skull, similar to those in frontal impact.

In comparison with the frontal baseline impact, the occipital impact force was lower than that of frontal impact (6.8 kN vs. 8.1 kN). As a result, head acceleration was also lower in occipital impact than that in frontal impact (180 G vs. 220 G). Consequently, skull von Mises stress was 46 Mpa in occipital impact and 85 Mpa in frontal impact. However, the contrecoup pressure due to an occipital impact was –108 kPa, which was higher in magnitude than the –92 kPa due to a frontal impact. Tensile strain (ε_x) at the contrecoup site was about 2.0% due to an occipital impact, which was higher in magnitude than 1.2% due to a frontal impact. This is consistent with clinical observations that contrecoup injuries are found more frequently from an occipital impact than from a frontal impact, since both negative pressure and tensile strain can lacerate the brain matter in this area. We have previously pointed out (Ruan et al., 1993b, 1994) that the higher contrecoup pressure from occipital impact could be due to a difference in the oval shape of the frontal and occipital bones as well as due to the presence of the anterior fossa adjacent to the frontal bone.

Side Impact

In order to perform a side impact simulation, the cylinder was relocated to impact the left and right parietal/temporal regions, respectively. The two impact simulations were from left to right and then from right to left in the coronal plane. The loading was directed to the scalp of the parietal/temporal bone above the ear. The impactor mass and velocity were the same as these in the baseline frontal impact. Head acceleration and intracranial pressure time histories (not shown) from side impact also followed that of the impact pulse; however, that of the shear stress did not, which was the case in frontal and occipital impact simulations. The absolute value of the coup pressure from side impact was about three times that of the contrecoup pressure. This is probably due to the effect of the falx partition. In a previous study (Ruan et al., 1994), the falx cerebri was not included in the analysis and the absolute values of coup and contrecoup pressures were about the same in side impact. The falx cerebri appeared to reduce the contrecoup pressures in side impact. Hence, the falx cerebri seemed to protect the brain laterally from contrecoup injury.

In both left- and right-sided impacts, a compressive pressure wave was propagated from the impact site and reflected back as a tensile pressure wave on the contralateral side. Peak tensile and shear strains (not shown) occurred in the area of impact. The second largest shear strain was found in the brainstem. The tensile and shear strains in this area can cause brainstem contusions and diffuse axonal injury, if these strains are a mechanism for these types of injury. Skull von Mises stress and tensile strain distributions (both not shown) were highest on the impacted side. These stresses and strains are localized in the impact area and spread from the impact point to the rest of the skull, which again is an indication that bending stress is dominant at the impact point.

Crown Impact

Since the foramen magnum was modeled in the study, the whole head as a system was open when it was subjected to a crown impact. Therefore, the dynamic response from a crown impact should be different

TABLE 7.6 Summary of Results from Different Impacts

Impact condition	Impact mass (kg)	Impact velocity (m/s)	Impact force (kN)	Coup pressure (kPa)	Contrecoup Pressure (kPa)	Maximum shear (kPa)	Head acceleration (G)	HIC
Frontal baseline	5.23	6.33	8.1	255	-92	75	212	1574
Frontal 0.75 mass	3.92	6.33	7.4	235	-84	31	198	1212
Frontal 0.5 mass	2.62	6.33	6.6	220	-72	27	175	783
Frontal 0.75 velocity	5.23	4.75	5.9	190	-76	23	154	689
Frontal 0.5 velocity	5.23	3.165	3.7	112	-54	12	97	235
Occipital	5.23	6.33	6.9	232	-108	29	185	1115
Left side	5.23	6.33	7.6	245	-85	47	210	1553
Right side	5.23	6.33	7.7	253	-87	48	215	1593
Crown	5.23	6.33	6.4	195	-15	29	164	1060

from those of other impact locations. By keeping the same impactor mass and velocity as in other impact situations, the head was impacted by the cylinder on the crown with the scalp in place. The impact duration of 8 ms in crown impact was longer than that of other impact situations (6 ms). Contrecoup pressure (not shown) in crown impact is lower because the contrecoup side of the brain contains an opening. Brain pressures were linearly distributed from the crown to the brainstem. Negative pressure was found in the spinal cord, the contrecoup site in a crown impact situation. The maximum tensile strain was located in the brainstem area. The maximum shear strain was also located in the brainstem and spinal cord. These strains can be responsible for brainstem contusions.

The impact force and head acceleration were both lower in crown impact than those in frontal and side impacts. As a consequence, skull von Mises stress (not shown) is lower than those from frontal and side impacts. Under the same impact conditions, crown impact seemed to produce fewer injuries.

Summary of Results from Different Impact Locations

Cross-sections of the human head are very different when viewed from the front, rear, side, and top. If we consider the skull as being represented by many spring-mass systems, the stiffness of the skull would be different for each of the impact configurations discussed above because it is a combination of all the springs involved. In addition, the radius of curvature of the skull is different from place to place; in some areas it is much more rounded, while in others it is much flatter. Hence, the reaction forces are different when the skull is struck at different places by a flat surface. Furthermore, the brain assumes the shape of the interior of the skull and is expected to respond differently to dynamic loading from different directions.

Table 7.6 is a summary of the impact forces, coup and contrecoup pressures, maximum brain shear stresses, and head accelerations for all the impact simulations using head injury model — version 94. The head injury criterion (HIC) was also calculated for all the impact cases that were studied and is also included in Table 7.6. Figure 7.15 illustrates the impact severity vs. all the impact conditions that we have investigated. It is seen that, in general, intracranial pressure, shear stress, and head acceleration have the same trend to predict injury severity as does HIC. However, the correlations between shear stress and HIC and between contrecoup pressure and HIC are not as good as those between coup pressure and HIC and head acceleration and HIC.

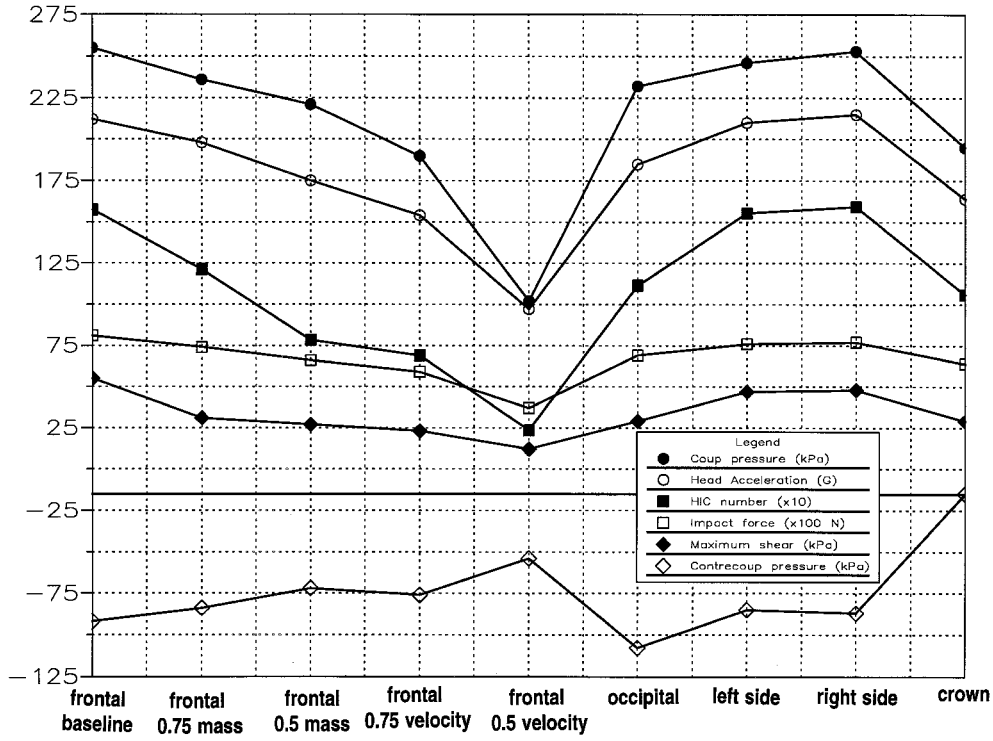

FIGURE 7.15 Mechanical parameters vs. impact conditions.

Human Head to A-Pillar Impact Simulations

One application of the finite element human head model is to perform a head-to-tested A-pillar impact simulation. In this simulation, the head injury model — version 93 was given an initial velocity to impact the tested A-pillar and the neck restraint was neglected. Figure 7.16 shows a model simulation setup.

Both padded and unpadded tested A-pillars were simulated in the study. For the padded case, a Dytherm foam of 1-in. thickness was added to cover the outside of the tested A-pillar at the impact area. The impact velocity was set at 15 mph (6.7056 m/s), 20 mph (8.94 m/s), and 25 mph (11.176 m/s) for both padded and unpadded cases. Totally, six runs were made.

Since the head model is deformable, stress/strain and pressure within the head tissues can be obtained as a simulated result. However, these responses were not included because we are only looking for the effects of impact speed and padding on the head impact response. Table 7.7 summarizes the peak impact force, peak head acceleration at the center of gravity, and HIC for padded and unpadded impacts at impact velocities of 15, 20 and 25 mph.

The results from padded impacts for 15, 20, and 25 mph are shown in Figs. 7.17 and 7.18, which are linear head acceleration and impact force plots. Figures 7.19 and 7.20 show those from 15-, 20-, and 25-mph unpadded impacts.

Head angular acceleration cannot be obtained directly from the output in these simulations, although the head model did rotate during simulation. However, the angular acceleration can be estimated if we consider the head as a rigid body. In this way, the angular acceleration for the padded and unpadded impact cases were estimated at 11,405 rad/s^2 and 14,765 rad/s^2, respectively. It should be kept in mind that since the head model is deformable, the estimated angular accelerations do not reflect the kinematics of the head during impact.

Although these results are preliminary and they have not been validated against experimental data, we can observe that the head responds differently to padding the velocity of impact. This is shown in

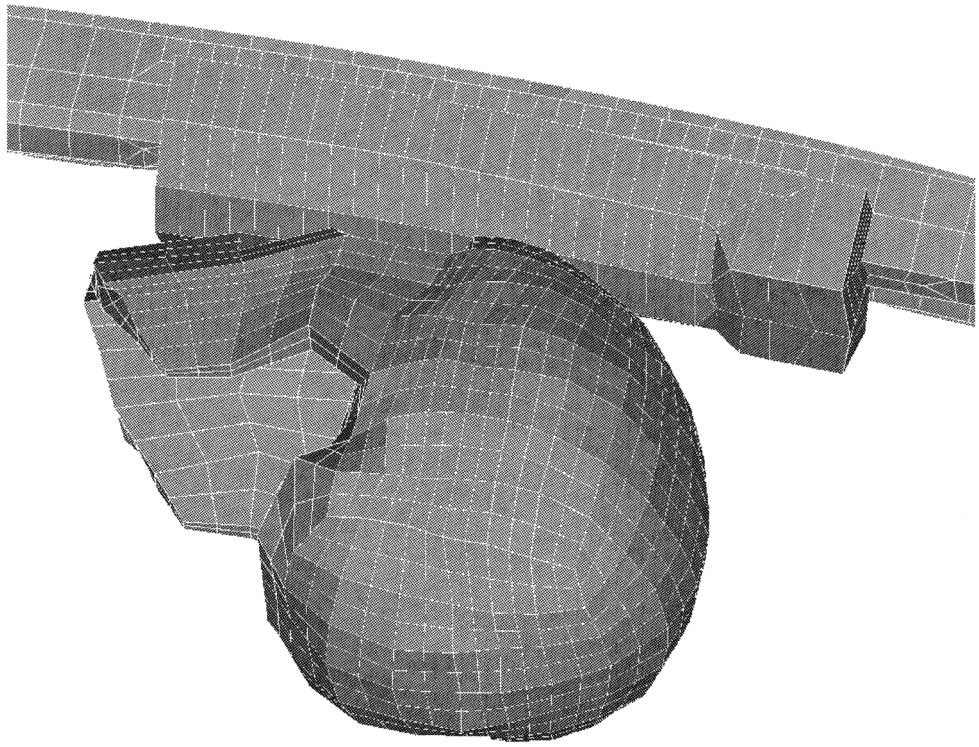

FIGURE 7.16 Human head — A-pillar impact.

TABLE 7.7 Peak Impact Force, Peak Head Acceleration at C.G. and HIC

	Padded			Unpadded		
Impact Velocity (mph) / (m/s)	Impact Force (N)	Acceleration at C.G. (G)	HIC	Impact Force (N)	Acceleration at C.G. (G)	HIC
(15) / (6.706)	6,000	175	766	6,900	210	920
(20) / (8.94)	8,350	260	1819	9,500	290	1947
(25) / (11.18)	9,520	295	2670	12,000	375	3509

Figs. 7.17 through 7.20 and in Table 7.7. In general, impact force, head acceleration, and HIC are lower in padded impacts than unpadded impacts. The higher the impact velocity, the higher are the impact force, head acceleration, and HIC.

Response of the Brain to Sagittal Angular Acceleration

Shear deformation of the brain due to head rotation has long been postulated as a major cause of brain injury because of the very low shear stiffness of brain tissue (Holbourn, 1943). Animal, physical, and finite element models have been used to investigate brain response due to rotational impacts. But three-dimensional finite element simulations of rotational impacts are rare, and little information on the distribution of shear stress/strain of the human brain due to rotational impact is available. In this section, the brain injury model — version 95 was exercised to investigate elastic and viscoelastic responses of the brain to an impulsive sagittal plane rotation of the head. An angular acceleration pulse taken from Abel's monkey test data (1978) was scaled to provide input for the human brain. The scaling method used maintained an approximately equal shear strain level in the brain and equal displacement of the head.

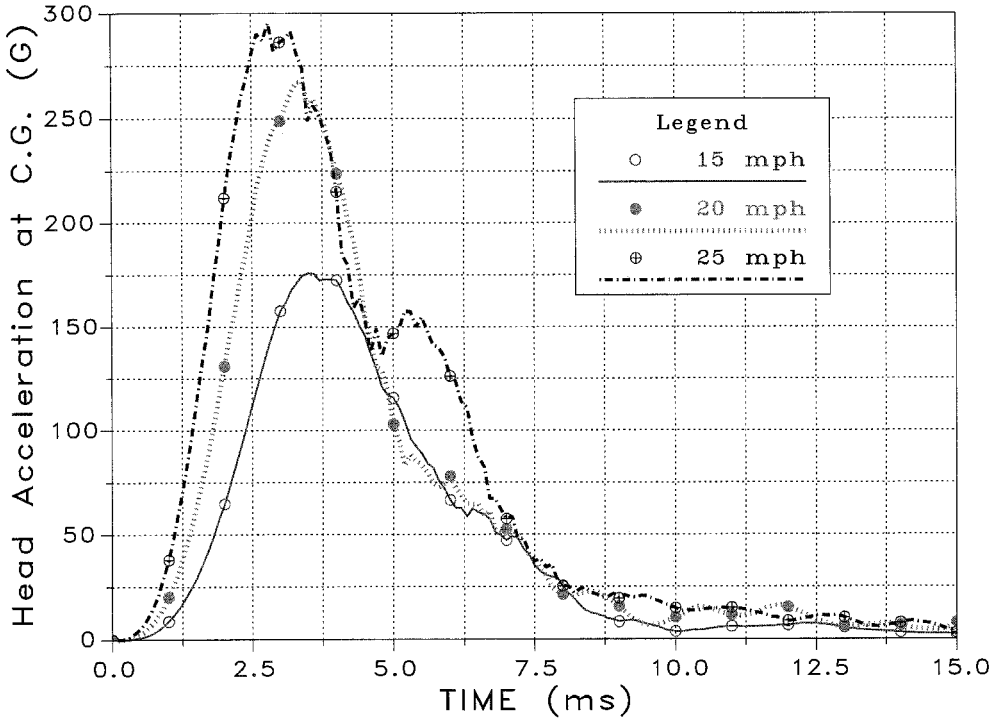

FIGURE 7.17 Head acceleration in three different impact speeds for padded impacts.

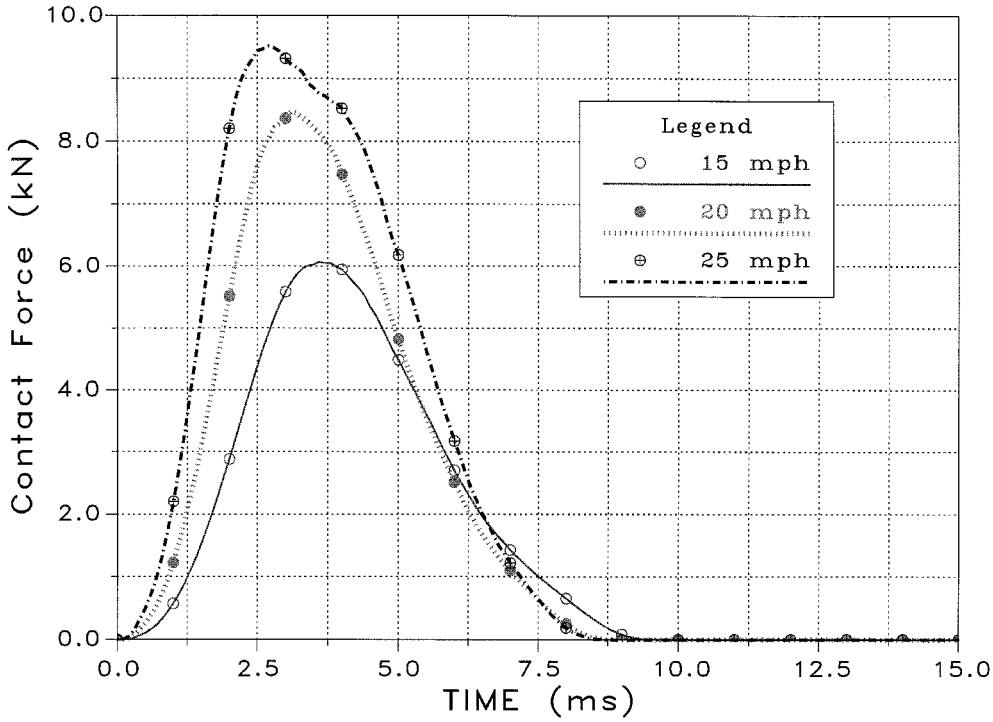

FIGURE 7.18 Impact force in three different impact speeds for padded impacts.

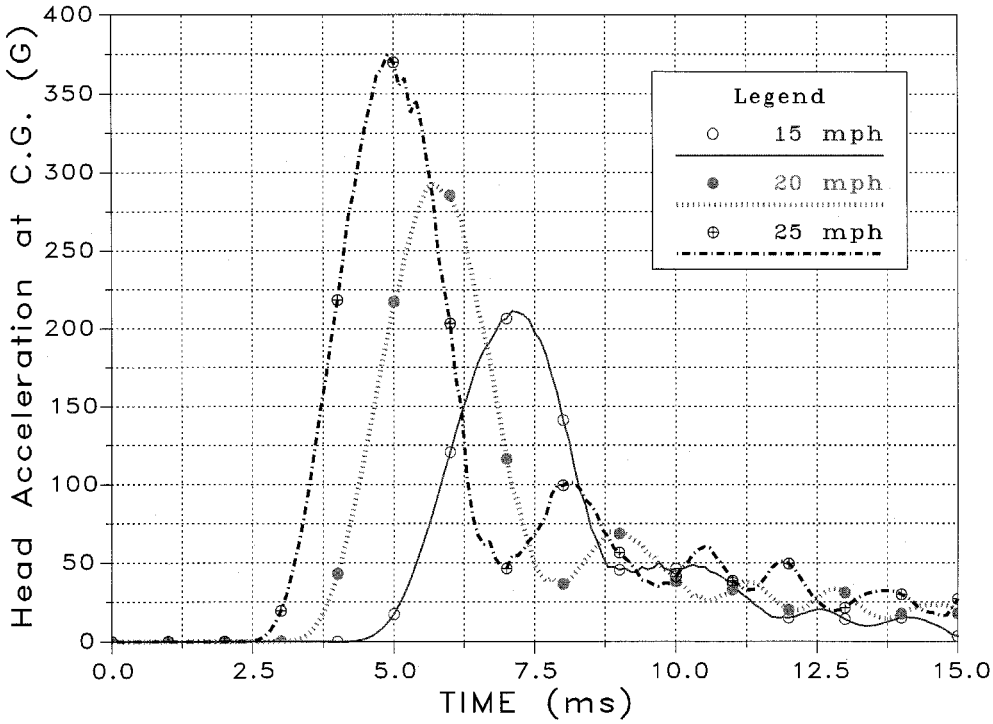

FIGURE 7.19 Head acceleration in three impact speeds for unpadded impacts.

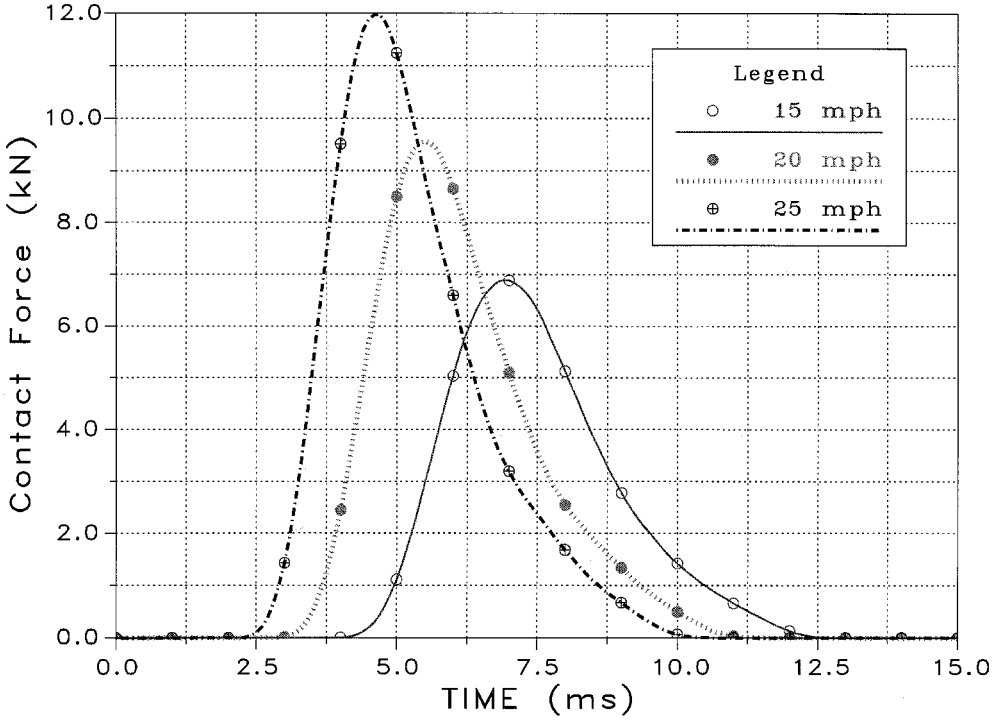

FIGURE 7.20 Impact force in three impact speeds for unpadded impacts

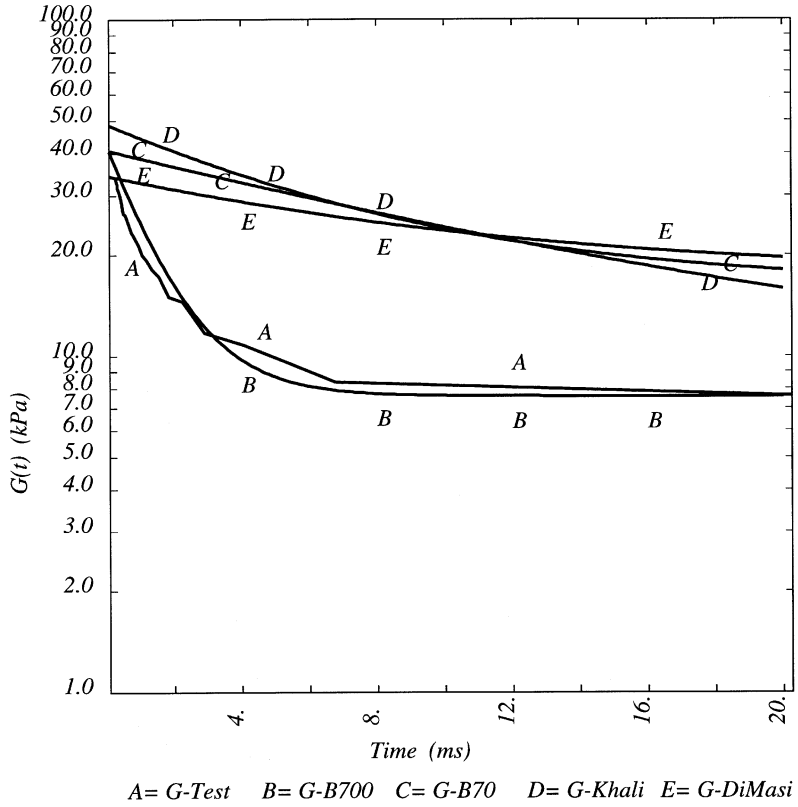

FIGURE 7.21 Shear relaxation functions for the brain.

Responses of the brain to impulsive sagittal rotational accelerations were obtained. The influence of the brain material properties on model response was also investigated.

In Fig. 7.21, curve A is the exponential relaxation function from Shuck and Advani's test data (1972), while curve B is based on our curve fitting for white matter with $\beta = 700\ s^{-1}$. curve C, used as the upper bound of the relaxation function, is for $\beta = 70\ s^{-1}$; curve D is taken from Khalil and Viano (1977); and curve E is from DiMasi et al (1991).

The deduced viscoelastic moduli from curve A were used to make a baseline run. In addition, five more runs were performed with different brain material parameters to study the influence of brain material properties on model response. In case B-70 β was changed to 70 s^{-1} from the baseline value to get results for the upper bound. Case SG50 assumed a 50% higher shear modulus for the white matter than that of the gray matter with $\beta = 700\ s^{-1}$. Case SG50-B70 was the upper-bounds case for case SG50 with $\beta = 70\ s^{-1}$. Case E-MAX was the elastic analysis assuming the shear modulus of G_0 used for the baseline. Case E-MIN was the elastic analysis assuming the shear modulus of G_∞ used for the baseline. The material properties used in this study are listed in Table 7.8.

To extrapolate impact test results obtained from animals to humans, a scaling relationship must be established. Ommaya et al. (1967) applied Holbourn's scaling law

$$\Theta_1 = \Theta_2(M_2/M_1)^{2/3} \tag{7.7}$$

where Θ = angular acceleration, M = brain mass, to predict a concussion threshold for man from monkey test data. Margulies et al. (1985) also used this scaling law in their physical model tests. This kind of scaling is not complete. For dynamic problems, scaling of time should also be considered.

TABLE 7.8 Material Properties of the Brain Used for Parametric Study

	G0 (kPa)		G_ (kPa)		β (s-1)
Base	41	34	7.6	6.3	700
B-70	41	34	7.6	6.3	70
SG50	51	34	9.5	6.3	700
SG50-B70	51	34	9.5	6.3	70
E-MAX	G = 41	G = 34			
E-MIN			G=7.6	G=6.3	
	white	gray	white	gray	

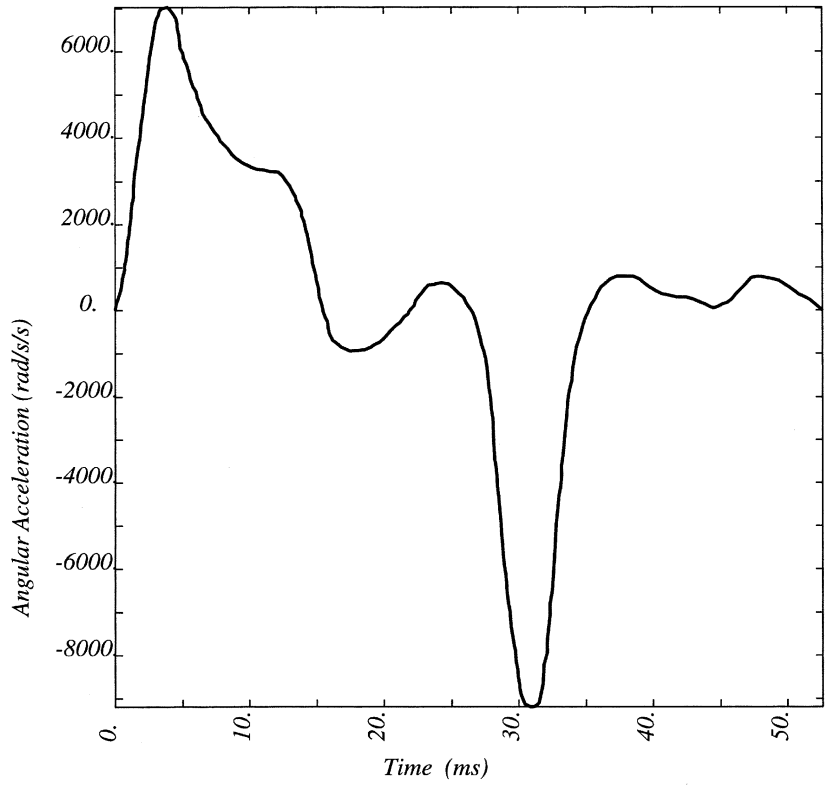

FIGURE 7.22 Angular acceleration impulse scaled from Abel's data.

If the brain is idealized as a sphere with a radius R, it can be shown that to have the same stress level in two different sizes of the brain, the scaling for rotational acceleration is

$$\Theta_1/\Theta_2 = (R_2/R_1)^2 = (M_2/M_1)^{2/3} \tag{7.8}$$

Time scaling is established by the requirement of having the same rotational displacement.

$$t_1/t_2 = R_1/R_2 = (M_1/M_2)^{1/3} \tag{7.9}$$

In this study, the scaling was done according to the above equations, assuming that R = 68 mm for the human brain and R = 26 mm for the rhesus monkey brain. The angular acceleration pulse was taken from Abel et al. (1978). The input angular acceleration impulse scaled from Abel's tests data is shown in Fig. 7.22. A peak angular acceleration of 7030 rad/s^2 occurred at about 4 ms, and the peak angular deceleration of 9192 rad/s^2 was reached at about 32 ms. These values are well within the common range

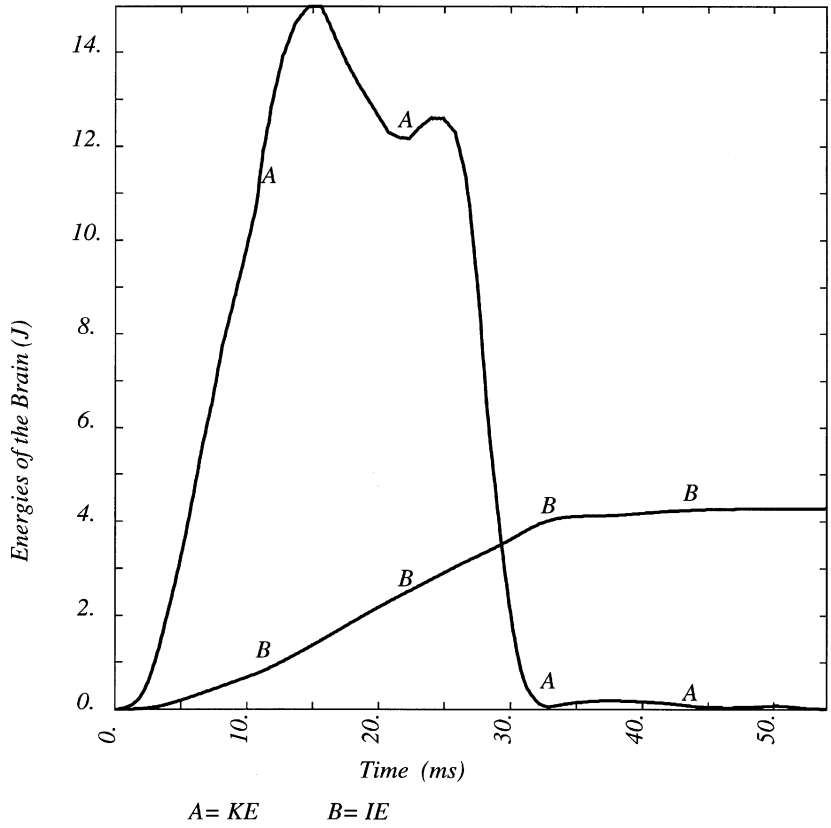

FIGURE 7. 23 Energies imparted to the brain due to rotations.

of angular acceleration magnitudes sustained by the human head in field accidents. The head was forced to rotate in the sagittal plane about a lateral +Y-axis (right to left). The maximum angular displacement was about 60° (same as that in the tests).

Figure 7.23 shows the kinetic energy (curve A) and strain energy (curve D) imparted to the brain due to a sagittal rotational impact. The kinetic energy followed the angular velocity of the head but the strain energy was not released right away after the impact.

Figures 7.24 and 7.25 show the shear stresses and strains developed in the genu of the corpus callosum. The peak shear stress was 8.81 kPa and the corresponding peak shear strain was 0.289 for the baseline case. Note that the stress-time histories are not of the same shape as those for strain because of viscoelasticity. The first peak shear stress occurred at about 4 ms for curve A in Fig. 7.28, while the first peak shear strain occurred at about 7 to 8 ms for curve A in Fig. 7.25.

When $\beta = 70\ s^{-1}$, the peak shear stress increased to 18.5 kPa and the corresponding peak shear strain decreased to 0.256. Similar changes were seen from case SG50 to case SG50-B70, the peak shear stress increased from 10.6 kPa to 21.8 kPa and the corresponding peak shear strain decreased from 0.281 to 0.242. Therefore, the decay factor has a great influence over the magnitude of the peak shear stress, and less influence over the magnitude of the peak shear strain. Note that changes in the decay factor do not change the shear deformation pattern.

When the shear modulus for the white matter was changed from about 20% higher than that of the gray matter to 50% higher, the peak shear stress increased from 8.81 kPa to 10.6 kPa, and the corresponding peak shear strain decreased from 0.289 to 0.281, which was not significant.

The results of the elastic analysis case E-MAX, using the shear modulus of G_0 for the baseline case, formed the upper bounds for the peak shear stresses and lower bounds for the peak shear strains. The

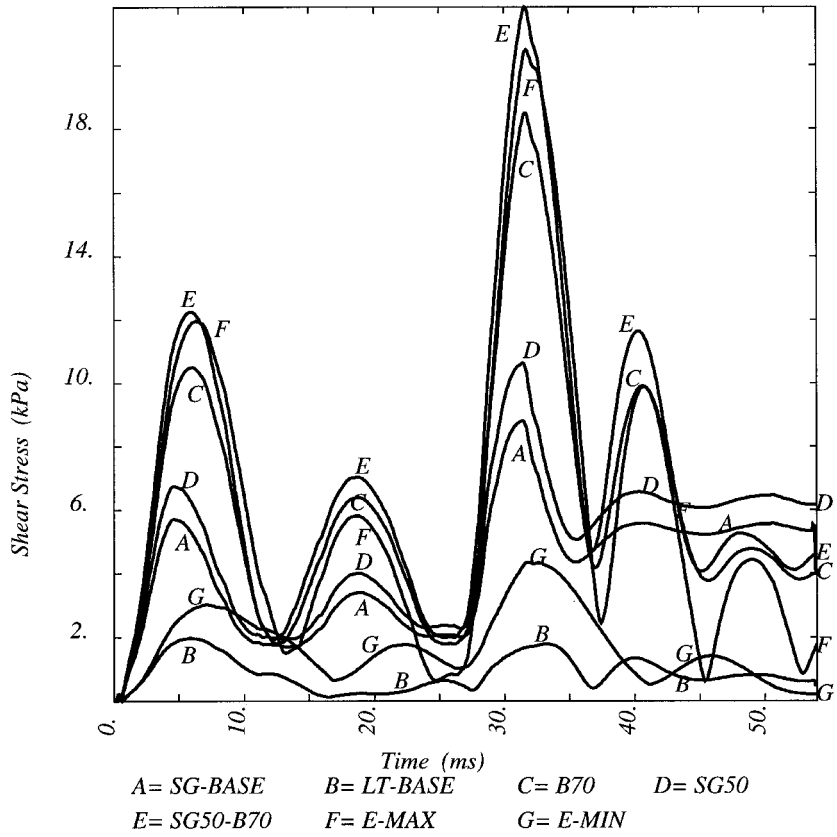

FIGURE 7.24 Shear stresses in the genu due to rotations.

results of case E-MIN, using the shear modulus of G_∞ for the baseline case, formed the lower bounds for the peak shear stresses and upper bounds for the peak shear strains. The responses of the viscoelastic cases were basically located within the corridor formed by case E-MAX and case E-MIN. Curve E for case SG50-B70 was not covered by the corridor because the shear modulus of the brain for case SG50-B70 was beyond the range of the elastic shear modulus used. The results of the elastic and viscoelastic analyses showed a similar trend. However, the peak time for viscoelastic analysis was ahead of that for elastic analysis. If we are only interested in a limit analysis, the elastic analysis can provide a reasonable estimate of the shear response of the brain if the range of the shear moduli for the brain are known.

Shown in Fig. 7.26 are the axial strains of the central bridging veins which sustained the highest stretch in the sagittal rotational impact. The material properties of the brain showed influence over the stretch of the parasagittal bridging veins. The central bridging vein experienced a strain of 0.383 for the baseline case. When $\beta = 70\ s^{-1}$, the axial strain decreased from 0.383 to 0.33 for case B70, and from 0.376 for case SG50 to 0.32 for case SG50-B70. The difference between case SG-BASE and case SG50 was not significant. The elastic cases also formed upper bound of 0.43 (case E-MIN) and lower bounds of 0.32 (case E-MAX). The results showed that when higher shear moduli were used for the brain, the axial strains of the bridging veins decreased.

Shown in Fig. 7.27 are the axial strains of the parasagittal bridging veins due to sagittal rotation (case BASE). The backward-facing bridging veins of the frontopolar (A), the anterior frontal (B), and the middle frontal (C) were in tension during the deceleration phase, while the forward-facing bridging veins from the posterior frontal (D) to the occipital (J) were under higher tensile strains during the acceleration phase. These results indicated that the bridging veins would rupture during the acceleration phase. In particular, the posterior frontal to the occipital veins would be at a higher risk of rupture. These results

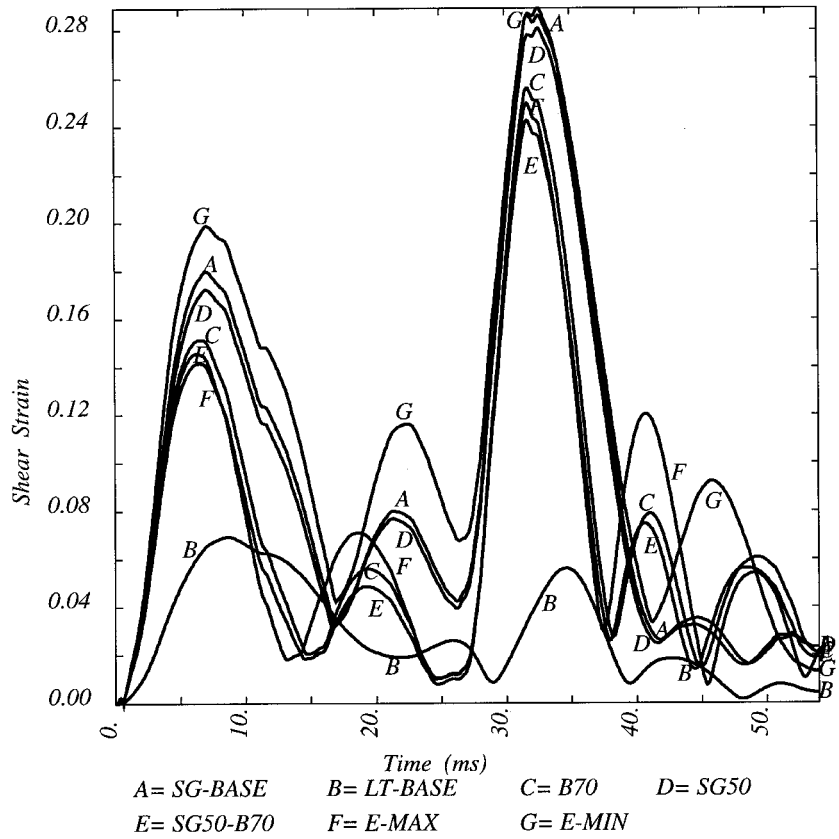

FIGURE 7.25 Shear strains in the genu due to rotations.

are consistent with the findings in the animal tests by Abel et al. (1978) in which subdural hematomas originating in the parasagittal bridging veins were found in 16 out of the 40 experiments. However, these results also tend to support Lee and Haut's (1989) arguments that subdural hematoma in the animal tests by Gennarelli and Thibault (1982) could have occurred during the acceleration phase.

Shear stress contours in a parasagittal section at 32 ms are shown in Fig. 7.28. There were some variations with different material properties of the brain used in the model. However, the shear stress distribution patterns were virtually the same. They predicted roughly the same locations with high shear stresses, and so major injury sites and injury types could be predicted by the model with the material properties used. High shear stresses occurring in the genu of the corpus callosum, midbrain, thalamus, and brainstem predicted a higher risk of DAI in these areas. Shear stress contours in a coronal section through the level of the anterior commissure at 32 ms are shown in Fig. 7.29. High shear stresses in the corpus callosum, septum pellucidum, and the inferior horns of the lateral ventricles can be observed. Shear stress contours in the coronal section through the thalamus and brainstem revealed high shear stresses in the midbrain, cerebral peduncle, and hippocampus (Fig. 7.30).

7.6 Conclusions

Human head finite element models have been developed to study the biomechanical response of the head in direct and indirect impacts. The models have been partially validated against available cadaveric experimental data in terms of head impact force, intracranial pressures, and head acceleration at the center of gravity. Further model validations in a wide range of different loading conditions need more test data to further assure model accuracy.

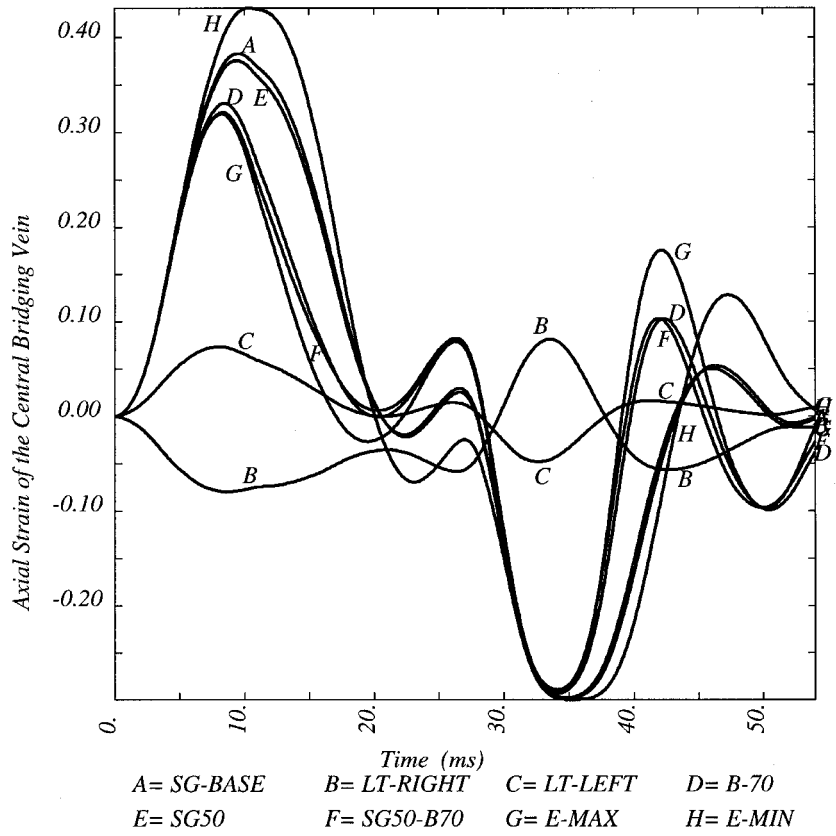

FIGURE 7.26 Stretch of the central bridging veins due to rotations.

The material properties of the head tissue are very important model parameters and affect model response greatly. Since consistent information about material properties of the brain is not well established, more research effort is needed to measure the material property of the brain.

Anatomical details such as the layered skull, membranes, CSF, bridging veins, white matter, gray matter, and ventricles are important in studying the injury mechanisms of the human head. Hence, these components should be included in the model.

It has been demonstrated that the injury site and injury severity can be predicted from the computed skull and brain stresses and strains. From a mechanical point of view, skull von Mises stress and tensile strain, intracranial pressures, brain shear, and principal strains can be used as indicators for skull fracture, coup-contrecoup injury, and DAI. However, it should be emphasized that the model results shown are preliminary and are only valid for the cases investigated where the model responses were compared with experimental data.

Impact injury severity vs. impact locations, impactor mass, and impactor velocity can be found from a parametric study in direct impact. In the rotational impact simulation, the model confirmed the hypothesis that intracranial strains are likely to be responsible for DAI since rotational acceleration induces larger shear and principal strains in the brain than direct impact.

A new scaling method, based on the equal stress and displacement requirement, was introduced to scale animal data to the human. The scaling method used to convert test data from living animals and other surrogates to the human appears promising, and finite element models may be useful in the establishment of human tolerance to head impact.

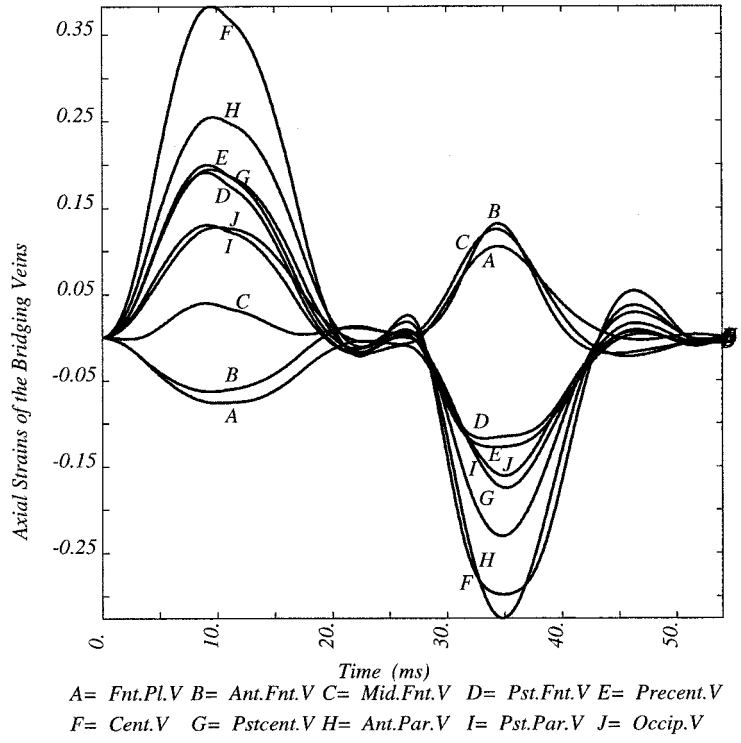

FIGURE 7.27 Stretch of the bridging veins due to sagittal rotation.

FIGURE 7.28 Shear stress contours at 32 ms due to sagittal rotation: parasagittal section, case BASE.

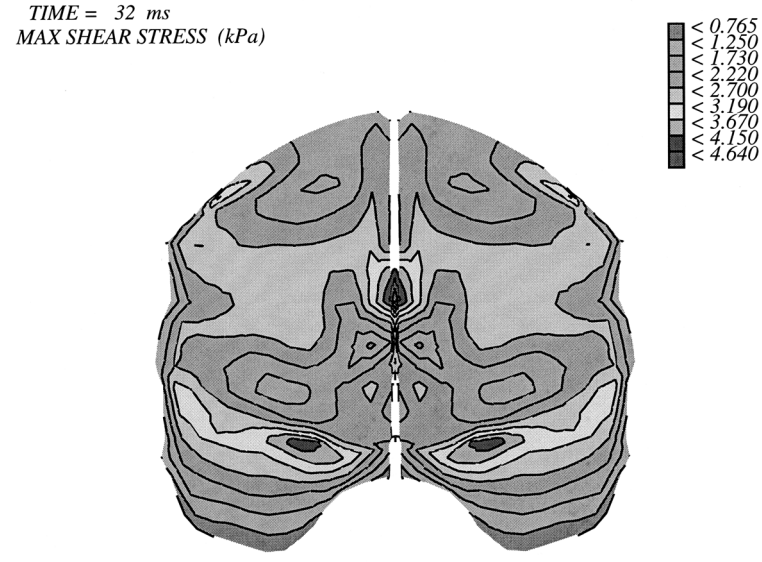

FIGURE 7.29 Shear stress contours at 32 ms due to sagittal rotation: coronal section in the forebrain, case BASE.

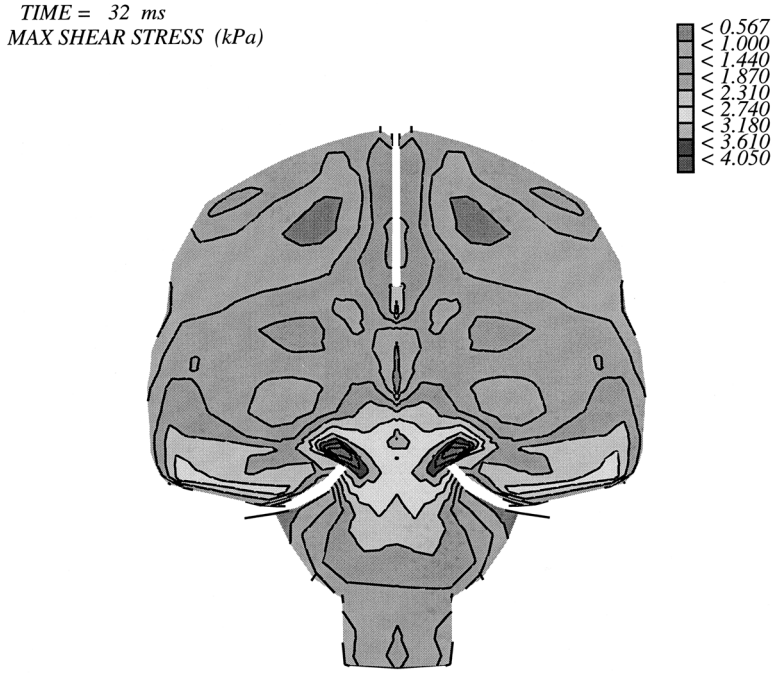

FIGURE 7.30 Shear stress contours at 32 ms due to sagittal rotation: coronal section in the midbrain, case BASE.

References

Abel, J. M., Gennarelli, T. A., and Segawa, H., 1978, Incidence and Severity of Cerebral Concussion in the Rhesus Monkey Following Sagittal Plane Angular Acceleration, *Proc. 22nd Stapp Car Crash Conf.*, SAE Paper No. 780886.

Adams, J. H., Mitchell, D. E., Graham, D. I., et al, 1977, Diffuse Brain Damage of Immediate Impact Type. Its Relationship to Primary Brain-stem Damage in Head Injury, *Brain*, Vol. 100, pp. 489-502.

Adams, J. H., Graham, D. I., Murray, L. S., and Scott, G., 1982, Diffuse Axonal Injury Due to Nonmissile Head Injury in Humans: An Analysis of 45 Cases, *Ann. Neurol.*, Vol. 12, pp. 557-563.

Adams, J. H., Graham, D. I., and Gennarelli, T. A., 1983, Head Injury in Man and Experimental Animals: Neuropathology, *Acta Neurochirurgica*, Suppl. Vol. 32, pp. 15-30.

Anzelius, A., 1943, The Effect of An Impact on A Spherical Liquid Mass, *Acta Pathol. Microbiol. Scand.*, Suppl., Vol. 48, pp.153-159.

Arbogast, K. B., Meaney, D. F., and Thibault, L. E., 1995, Biomechanical Characterization of the Constitutive Relationship for the Brainstem, *Proc. 39th Stapp Car Crash Conference*, SAE Paper No. 952716.

Belytschko, T., Tsay, C. S., 1983, A Stabilization Procedure for the Quadrilateral Plate Element with One-point Quadrature, *Int. J. Numer. Methods Engrg.*, Vol. 19, pp. 405-419.

Belytschko, T., Lin, J. I., and Tsay, C. S., 1984a, Explicit Algorithms for the Nonlinear Dynamics of Shells, *Computer Methods in Applied Mechanics and Engineering*, Vol. 42, pp. 225-251.

Belytschko, T., Ong, S. J., Liu, W. K., and Kennedy, J. M., 1984b, Hourglass Control in Linear and Nonlinear Problems, *Computer Methods in Applied Mechanics and Engineering*, Vol. 43, pp. 251-276.

Belytschko, T. and Bindeman L. P., 1991, Assumed Strain Stabilization of the 4-node Quadrilateral with 1-point Quadrature for Nonlinear Problems, *Computer Methods in Applied Mechanics and Engineering,* Vol. 88, pp. 311-340.

Cheng, L. Y., Rifai, S., Khatua, T., and Piziali, R. L., 1990, Finite Element Analysis of Diffuse Axonal Injury, in *Vehicle Crashworthiness and Occupant Protection in Frontal Collisions*, SAE paper No. 900547.

Chu, C. S., Lin, M. S., Huang, H. M., and Lee, M. C., 1994, Finite Element Analysis of Cerebral Contusion, *J. Biomech*, Vol. 27, pp. 187-194.

DiMasi, F., Marcus, J., and Eppinger, R., 1991, Three-Dimensional Anatomic Brain Model for Relating Cortical Strains to Automobile Crash Loading, *Proc. 12nd Intern. Tech. Conf. on Exp. Safety Vehicle*, Paris, France, pp. 617-627.

Estes, M. S. and McElhaney, J. H., 1970, Response of Brain Tissue to Compressive Loading, ASME Paper No. 70-BHF-13.

Fallenstein, G. T. and Hulce, V. D., 1969, Dynamic Mechanical Properties of Human Brain Tissue, *J. Biomech.*, Vol. 2, pp. 217-226.

Galford, J. E. and McElhaney, J. H., 1970, A Viscoelastic Study of Scalp, Brain, and Dura, *J. Biomech.,* Vol. 3, pp. 211-221.

Gennarelli, T. A., Thibault, L. E., 1982, Biomechanics of Acute Subdural Hematoma, *J. Trauma,* Vol. 22, pp. 680-686.

Gennarelli, T. A., Thibault, L. E., and Adams, J. H., et al, 1982, Diffuse Axonal Injury and Traumatic Coma in the Primate, *Ann. Neurol.* Vol. 12, pp. 564-574.

Goldsmith, W., 1972, Biomechanics of Head Injury, *Biomechanics, Its Foundations and Objectives* ed. by Fung, Y. C., Perrome, N., and Ankliker, M., Prentice-Hall, Englewood Cliffs, N.J., pp. 585-608.

Gurdjian, E. S., 1975, *Impact Head Injury,* Thomas Publishing Company, Springfield, Ill.

Gurdjian, E. S. and Gurdjian, E. S., 1976, Cerebral Contusions: Re-evaluation of the Mechanisms of Their Development, *J. Trauma*, Vol. 16, pp. 35-51.

Hallquist, J. O., Goudreau, G. L., and Benson, D. J., 1985, Sliding Interfaces with Contact-impact in Large-scale Lagrangian Computations, *Computer Methods in Applied Mechanics and Engineering*, Vol. 43, pp. 107-137.

Haynes, R. H., McElhaney, and J. H. and Fogle, J. L., 1969, Mechanical Properties of Skull, *Proc. 6th Annual Rocky Mountain Bioengineering Symp.,* Laramie, Wyo., pp. 62-66.

Holbourn, A. H. S., 1943, Mechanics of Head Injuries, *Lancet*, Vol. 2, pp. 438-441.

Hosey, R. R. and Liu, Y. K., 1982, A Homomorphic Finite Element Model of the Human Head and Neck, *Finite Element in Biomechanics,* Gallagher, R. H., Simon, B. R., Johnson, T. C., and J. F., Gross, eds., Wiley, pp. 379-401.

Hubbard, R. P., 1971, Flexure of Layer Cranial Bone, *J. Biomech.*, Vol. 4, pp. 251-263.
Khalil, T. B. and Hubbard, R. P., 1977, Parametric Study of Head Response by Finite Element Modeling, *J. Biomech.*, Vol. 10, pp. 119-132.
Khalil, T. B. and Viano, D. C., 1977, Impact Response of a Viscoelastic Head Model, *General Motors Research Publication* GMR-2380.
Khalil, T. B. and Viano, D. C., 1982, Critical Issues in Finite Element Modeling of Head Impact, *Proc. 26th Stapp Car Crash Conf.*, SAE Paper No. 821150.
Kopecky, J. A. and Ripperger, E. A., 1969, Close Brain Injury: An Engineering Analysis, *J. Biomech.*, Vol. 2, pp. 29-34.
Lee, E. S., 1990, A Large-strain, Transient-dynamic Analysis of Head Injury Problems by the Finite Element Method, Ph.D. dissertation, Georgia Institute of Technology, October, 1990.
Lee, M.-C. and Haut, R. C., 1989, Insensitivity of Tensile Failure Properties of Human Bridging Veins to Strain Rates: Implications in Biomechanics of Subdural Hematoma, *J. Biomech.*, Vol. 22, pp. 537-542.
Lee, M. C., Melvin, J. W., and Ueno, K., 1987, Finite Element Analysis of Traumatic Subdural Hematoma, *Proc. 31st Stapp Car Crash Conf.*, SAE Paper No. 872201.
Lighthall, J. W., 1988, Controlled Cortical Impact: A New Experimental Brain Injury Model, *J. Neurotrauma*, Vol. 5, pp. 1-16.
Lighthall, J. W., Goshgarian, H. G., and Pinderski, C. R., 1990, Characterization of Axonal Injury Produced by Controlled Cortical Impact, *J. Neurotrauma*, Vol. 7, pp. 65-76.
Margulies, S. S., Thibault, L. E., and Gennarelli, T. A., 1985, A Study of Scaling and Head Injury Criteria Using Physical Model Experiments, *Proc. 1985 International IRCOBI Conference on the Biomechanics of Impacts*, pp. 223-234.
Margulies, S. S., 1987, Biomechanics of Traumatic Coma in the Primate, Ph.D. dissertation, University of Pennsylvania.
McElhaney, J. H., Stalnaker, R. L., Estes, M. S., and Rose, L. S., 1969, Dynamic Mechanical Properties of Scalp and Brain, *Proc. 6th Annual Rocky Mountain Bioengineering Symp.*, Laramie, Wyo., pp. 67-73.
McElhaney, J. H., Fogle, J. L., Melvin, J. W., Haynes, R. R., Roberts, V. L., and Alem, N. M., 1970, Mechanical Properties of Cranial Bone, *J. Biomech.*, Vol. 3, pp. 495-511.
Melvin, J. W., Robbins, D. H., and Roberts, V. L., 1970a, The Mechanical Behavior of the Diploë Layer in Human Skull in Compression, *Developments in Mechanics.,* Vol. 5, Proc. 11th Midwest Mech. Conf., pp. 811-818.
Melvin, J. W., Fuller, P. M., and Barodawala, I. T., 1970b, The Mechanical Properties of the Diploë Layer in the Human Skull, *Presented at 1970 SESA Spring Meeting*, Huntsville, Ala.
Mendis, K., 1992, Finite Element Modeling of the Brain to Establish Diffuse Axonal Injury Criteria, Ph.D. dissertation, Ohio State University.
Mertz, H., McElhaney, J. H., and Ommaya, A. K., 1970, A Comparison of the Elasticity of Live, Dead and Fixed Brain Tissue, *J. Biomech*. Vol. 3, pp. 453-458.
Nahum, A. M., Smith, R., and Ward, C. C., 1977, Intracranial Pressure Dynamics During Head Impact, *Proc. 21st Stapp Car Crash Conf.*, SAE Paper No. 770922.
Nahum, A. M., Ward, C. C., Raasch, E., Adams, S., and Schneider, D., 1980, Experimental Studies of Side Impact, *Proc. 24th Stapp Car Crash Conf.*, SAE Paper No. 801301.
Ommaya, A. K., Yarnell, P., Hirsch, A. E., and Harris, E. H., 1967, Scaling of Experimental Data on Cerebral Concussion in Sub-human Primates to Concussion Threshold for Man, *Proc. 11th Stapp Car Crash Conference*, SAE Paper No. 670906.
Pilz, P., 1983, Axonal Injury in Head Injury, *Acta Neurochirurgica*, Suppl. Vol. 32, pp. 119-123.
Pluche, R., Lantz, S. A., and King, A. I., 1985, Finite Element Model of the Head, *Head Injury Prevention, Past and Present Research,* Wayne State University, pp. 235-256.
Robbins, D. H. and Wood, J. L., 1969, Determination of Mechanical Properties of the Bones of the Skull, *Exp. Mech.* Vol. 9, pp. 236-240.

Roberts, V. L. and Melvin, J. W., 1969, The Measurement of the Dynamic Mechanical Properties of Human Skull Bone, *Appl. Poly. Symp.*, Vol. 12, pp. 235-247.

Ross, D. T., Meaney, D. F., Sabol, M. K., Smith, D H., and Gennarelli, T. A., 1994, Distribution of Diffuse Axonal Injury Following Inertial Closed Head Injury in Miniature Swine *Exp. Neurol.*, Vol. 126, pp. 291-299.

Ruan, J. S., Khalil, T. B., and King, A. I., 1991a, Human Head Dynamic Response to Side Impact by Finite Element Modeling, ASME *J. Biomech. Engrg.*, Vol. 113, pp. 276-283.

Ruan, J. S., Khalil, T. B., and King, A. I., 1991b, Intracranial Response of a Three-dimensional Human Head Finite Element Model, *Proceedings of first Injury Prevention through Biomechanics Symposium*, Wayne State University, pp. 97-103.

Ruan, J. S., Khalil, T. B., and King, A. I., 1992, Finite Element Analysis of the Human Head to Impact, *ASME 1992 Advances in Bioengineering,* BED-Vol. 22, pp. 249-252.

Ruan, J. S., Khalil, T. B., and King, A. I., 1993a, On the Impact Response of a 3-D Human Head Model, ASME 1993 Bioengineering Conference, BED-Vol. 24, eds. Langrana, N. A., Friedman, M. H., and Grood, E. S., pp. 530-533.

Ruan, J. S., Khalil, T. B., and King, A. I., 1993b, Finite Element Modeling of Direct Head Impact, *Proc. 37th Stapp Car Crash Conf.*, SAE Paper No. 933114.

Ruan, J. S., Khalil, T. B., and King, A. I., 1994, Dynamic Response of the Human Head to Impact by Three-Dimensional Finite Element Analysis, ASME *J. Biomech. Engrg.*, Vol. 116, pp. 44-50.

Ruan, J. S., 1994, Impact Biomechanics of Head Injury by Mathematical Modeling, Ph. D. dissertation, Wayne State University, September, 1994.

Sauren, A. A. H. J. and Claessens, M. H. A., 1993, Finite Element Modeling of Head Impact: The Second Decade, *Proc. 1993 International IRCOBI Conference on the Biomechanics of Impacts,* pp. 241-254.

Shuck, L. Z., Haynes, R. R., and Fogle, J. L., 1970, Determination of Viscoelastic Properties of Human Brain Tissue, ASME Paper No. 70-BHF-12.

Shuck, L. Z. and Advani, S. H., 1972, Rheological Response of Human Brain Tissue in Shear, *J. Basic Engrg.*, pp. 905-911.

Shugar, T. A. and Katona, M. G., 1975, Development of Finite Element of Head Injury Model, *J. ASCE*, Vol. 101, pp. 223-239.

Shugar, T. A., 1977, A Finite Element Head Injury Model, Report No. DOT HS-289-3-550 TA, Vol. I.

Strich, S. J., 1956, Diffuse Degeneration of the Cerebral White Matter in Severe Dementia Following Head Injury, *J. Neurol. Neurosurg. Psychiatry*, Vol. 19, pp. 163-185.

Strich, S. J., 1961, Shearing of Nerve Fibers as a Cause of Brain Damage due to Head Injury, *Lancet*, Vol. 2, pp. 443-448.

Tong, DiMasi, Eppinger, Marcus, and Galbraith, C., 1989, Finite Element Modeling of Head Injury Caused by Inertial Loading, *Proc. 12nd Intern. Tech. Conf. on Exp. Safety Vehicle*, pp. 617-627.

Trosseille, X., Tarriere, C., Lavaste, F., Guillon, F., and Domont, A., 1992, Development of a F.E.M. of the Human Head According to a Specific Test Protocol, *Proc. 36th Stapp Car Crash Conf.*, SAE Paper No. 922527.

Ueno, K., Melvin, J. W., Lundquist, E., and Lee, M. C., 1989, Two-Dimensional Finite Element Analysis of Human Brain Impact Responses: Application of a Scaling Law, *Crashworthiness and Occupant Protection in Transportation Systems,* Ed. Khalil, T. B., ASME AMD-Vol. 106/BED-Vol. 13, pp. 123-124.

Ueno, K., Melvin, J. W., Rouhana, M. E., and Lighthall, J. W., 1991, Two-dimensional Finite Element Model of the Cortical Impact Method for Mechanical Brain Injury, *Crashworthiness and Occupant Protection in Transportation Systems,* ASME AMD-Vol. 126/BED-Vol. 19, pp. 121-147.

Ward, C. C. and Thompson, R. B., 1975, The Development of a Detailed Finite Element Brain Model, *Proc. 19th Stapp Car Crash Conf.*, SAE Paper No. 751163.

Ward, C. C., Nikravesh, P. E., and Thompson, R. B., 1978, Biodynamic Finite Element Models Used in Brain Injury Research, *Aviation, Space, and Environmental Medicine*, January, pp. 136-142.

Ward, C. C., Chan, M., and Nahum, A. M., 1980, Intracranial Pressure — A Brain Injury Criterion, *Proc. 24th Stapp Car Crash Conf.*, SAE Paper No. 801304.

Willinger, R., Kopp, C. M., and Cesari, D., 1992, New Concept of Contrecoup Lesion Mechanism, Modal analysis of a finite element model of the head, *Proceedings of the 1992 International IRCOBI Conference on the Biomechanics of Impacts*, pp. 283-297.

Wood, J. L., 1971, Dynamic Response of Human Cranial Bone, *J. Biomech.*, Vol. 4, pp. 1-12.

Zhou, C., Khalil, T. B., and King, A. I., 1994, Shear Stress Distribution in the Porcine Brain due to Rotational Impact, *Proc. 38th Stapp Car Crash Conf.*, SAE Paper No. 942214.

Zhou, C., Khalil, T. B., and King, A. I., 1995, A New Model Comparing Impact Responses of the Homogeneous and Inhomogeneous Human Brain, *Proc. 39th Stapp Car Crash Conference*, SAE Paper No. 952714.

Zhou, C., 1995, Finite Element Modeling of Impact Response of an Inhomogeneous Brain, Ph.D. dissertation, Wayne State University.